University of Southampton

Faculty of Engineering and Physical Sciences

School of Engineering and the Environment

Applications of Advanced Imaging and Simulation Methods in Analysing Delamination Fracture in Fibre Reinforced Composite Materials

by

Keiran Max Ball

ORCID - 0000-0003-2628-0891

Thesis for the degree of Doctor of Engineering

September 2023

University of Southampton

Abstract

Faculty of Engineering and Physical Sciences

School of Engineering and the Environment

Doctor of Engineering

Applications of Advanced Imaging and Simulation Methods in Analysing Delamination Fracture in Fibre Reinforced Composite Materials

by

Keiran Max Ball

The Mode I interlaminar fracture toughness plays a key role in improving the impact resistance of carbon fibre reinforced polymer composites due to the contribution of damage response mechanisms determined in part by the relative competition between interlaminar and intralaminar crack paths. In turn, the resultant damage tolerance and resistance after impact can be attributed to the ability of the composite to suppress the initiation and propagation of delamination damage under the impact site. Keeping a crack in the toughened interlayer of a composite can reduce the extent off impact damage and improve the residual strength properties. However, the mechanisms that determine whether a crack stays in the toughened interlayer or transitions to weaker interface regions are uncertain. This study focuses on the damage response mechanisms that contribute to the interlaminar fracture toughness of particle-toughened carbon fibre reinforced polymer composites at the meso to macroscale. The double cantilever beam experimental test and complementary imaging methods are used to quantify the toughness response of different material systems and map the underlying mechanisms which may be contributing to the change in toughness response. Computational modelling is used to investigate the relationship between mesoscale interlayer geometry variation, relative strength values, critical strain energy release rate, and stochastic cohesive damage parameter variability. The results demonstrate that interlayer geometry is a factor in determining the crack path and the toughness response during Mode I loading. The relative competition between crack initiation mechanisms in potential crack paths is another key factor that determines interlaminar to intralaminar crack path transition, where a comparatively small difference in adhesive or cohesive interface strength *i.e.* less than ten percent is enough to facilitate the transition. Additionally, this work shows the three-dimensional characteristic behaviour of crack transition, where the presence of tow gaps; agglomerations of toughening particles or conversely the sparsity of them can lead to local thickening and thinning of the interlayer aligned with the direction of the fibres respectively, which can increase the likelihood of crack path transitions in a plane orthogonal to the dominant crack growth direction. Overall, the work presented in this thesis provides mechanistic insight into how previously identified microscale variations in particle-toughened composites lead to mesoscale architectural variations in interlayer geometry which in turn contribute to the interlaminar to intralaminar crack path transitions. Furthermore, through the work presented in this thesis and previous research, a link between these identified crack path transitions and the resulting toughness response mechanisms has been postulated and used to provide mechanistic theories as to the knock-on to the overall R-curve response under carefully defined conditions. This work suggests that by increasing the uniformity and thickness of the interlayer, the crack transition can be mitigated, improving the predictability of the crack path, and the system's toughness response.

Table of Contents

Table of Contents ..... **i**

Table of Tables ..... **vi**

Table of Figures ..... **vii**

Research Thesis: Declaration of Authorship ..... **xviii**

Acknowledgements ..... **xix**

List of Acronyms ..... **xx**

Nomenclature ..... **xxii**

Chapter 1 Background, Aims and Objectives **1**

1.1 Background and Research Questions 1

1.2 Aims and Objectives 2

1.3 Thesis Structure 3

Chapter 2 Literature Review **5**

2.1 Damage in CFRP's 5

2.1.1 Impact 8

2.1.2 Delamination Failure 9

2.1.3 Mode I 10

2.1.4 Damage Response Mechanisms in Epoxy Resin Systems 12

2.1.4.1 Particle Toughening 13

2.2 Crack Path during Mode I Delamination 14

2.2.1 Toughness Variation with Crack Path 15

2.2.2 Mesoscale effects determining a crack path 16

2.3 Computational Modelling 17

2.3.1 Cohesive Zone Model 17

2.3.2 eXtended Finite Element Method (XFEM) 20

2.3.3 Damage Initiation Criterion 21

2.3.4 Mixed-mode Fracture Criteria 22

2.3.5 Modelling crack transition 24

2.3.5.1 Micromechanical contributions to crack path transition 24

2.3.5.2 Combined Crack Modelling Approach 25

2.4 X-ray Computed Tomography 27

2.4.1 Micro-focus Computed Tomography Overview 27
2.4.2 Operation of Micro-focus Computed Tomography 27
2.4.3 Creating an Image 28
2.4.3.1 Attenuation 28
2.4.3.2 Reconstruction of an Image 28
2.4.4 Noise and Imaging Artefacts 30
2.4.4.1 Noise 30
2.4.4.2 Angular Undersampling 30
2.4.4.3 Ring Artefacts 31
2.4.4.4 Movement Artefacts and Centre of Rotation Error 31
2.4.4.5 Beam Hardening 31
2.4.5 Image Resolution 32
2.4.6 Advances in XCT Imaging of Fibre Reinforced Composites 32
2.5 Conclusions 34

Chapter 3 Delamination Path Transitions in Particle-Toughened Fibre Reinforced Polymer Composites 37

3.1 Introduction 37
3.2 Materials and Test Method 38
3.2.1 Computed Tomographic Scanning 40
3.2.2 Fractography 40
3.2.3 Scanning Electron Microscopy 41
3.3 Results 42
3.3.1 Toughness and R-curve Response 42
3.3.1.1 Untoughened Systems 42
3.3.1.2 Particle Toughened Systems 42
3.3.2 X-ray CT 48
3.3.3 Fractographic Imaging 49
3.3.4 Optical Macroscopy 49
3.3.5 Optical Microscopy 50
3.3.6 Scanning Electron Microscopy 51
3.3.7 Untoughened Material Systems 51
3.3.8 Toughened Material Systems 52

3.4 Discussion 58
3.4.1 Underlying Damage Response Mechanisms 58
3.4.2 Micro-Mechanistic Contribution to Crack Path Transition 59
3.4.3 Influence of Meso-Scale Architecture on Crack Path Transition 60
3.4.4 Specimen Scale Crack Path Transition Behaviour 61
3.4.5 Toughness Response of DCB Specimens 61
3.5 Conclusions 63

Chapter 4 *In situ* Analysis of Crack Path Transitions of Mode I Loaded Particle toughened Carbon Fibre Reinforced Polymer Composites Using 3D X-ray Computed Tomography 65

4.1 Introduction 65
4.2 Materials and Test Methodology 67
4.2.1 Laboratory Based X-ray Computed Tomography *In Situ* Method 67
4.2.2 Scanning Electron Microscopy 71
4.2.3 Fracture Surface Analysis: Trigger Region Mapping 71
4.2.4 Synchrotron Radiation Computed Tomography 72
4.3 Results 73
4.3.1 Fracture Surfaces 73
4.3.2 Surface Fractography and XCT 74
4.3.3 SRCT 77
4.4 Discussion 83
4.4.1 Macro-scale crack transition 83
4.4.2 Interlayer architecture 84
4.4.3 Mechanistic insight into crack transitions 84
4.5 Conclusions 86

Chapter 5 An Investigation of the Mechanisms Contributing to Crack Path Transitions in Unidirectional Carbon Fibre Reinforced Polymer Composites Using a Combined eXtended Finite Element and Cohesive Zone Model Methodology 89

5.1 Introduction 89
5.2 Materials and Methods 91
5.2.1 Image Processing 91
5.2.2 Model Implementation 91

5.2.3 XFEM and Cohesive Element Implementation 92
5.2.4 Model Geometry 93
5.2.5 Determining cohesive element parameters 96
5.2.6 Parametric Investigation and Stochastic Variation 97
5.2.7 Key properties and variables 99
5.3 Results 102
5.3.1 Crack Transition Behaviour 102
5.3.2 Crack Distribution 107
5.3.2.1 Interface Strength at 80% of Interlayer Strength 111
5.3.2.2 Interface Strength 90% of Interlayer Strength 115
5.3.2.3 Interface Strength 95% of Interlayer Strength 120
5.3.2.4 Interface Strength 100% of Interlayer Strength 124
5.3.2.5 Interface over Strength 100% of Interlayer Strength 128
5.3.2.6 Stochastic Distribution of Interface and Interlayer Strength 132
5.3.3 Change in Interlayer Toughness with Varying Interlayer Geometry 134
5.3.4 Stochastic Influence on Rate of Crack Transition 135
5.4 Discussion 136
5.4.1 Damage Distribution during Crack Propagation 136
5.4.2 Toughness Response with Increasing or Varying Interlayer Thickness 138
5.5 Conclusions 140
Chapter 6 Summary, Conclusions, and Further Work 141
6.1 Summary 141
6.1.1 DCB Testing and Toughness Characterisation: 141
6.1.2 *In situ* Observation of Crack Path Transitions: 143
6.1.3 Finite Element Modelling using Advanced Failure Modelling 144
6.2 Conclusions 144
6.3 Further Work 147
6.3.1 Linking Length Scales 147
6.3.2 Isolating the Effect of Meso-Scale Interlayer Features On Delamination Path and Toughness 147
6.3.3 Expanding Modelling Capability 148
Appendix A Delamination Resistance Experiments 151

A.1 Experimental Setup 151
A.2 Delamination Resistance Plots 152

Appendix B *In situ* Investigation of Crack Path Transitions 155

B.1 Mapping Transition Regions 155
B.2 *In situ* Mode I loading Method 156

Appendix C Modelling of Crack Path Transitions 157

C.1 Obtaining Geometric Laminate Properties 157
C.2 Mesh Independence Study 159
C.3 Example Scripts and Input Files to Reproduce Model 161

List of References 163

Table of Tables

Table 1 Mixed-mode fracture criteria 22

Table 2 Material systems by particle, matrix and fibre type. 40

Table 3 The Strain Energy Release Rate values for each material system at specific crack propagation lengths. 48

Table 4 Summary of fractography results for each of the six materials systems analysed..... 54

Table 5 Scan settings 68

Table 6 A summary of the different interlayer geometries modelled, with the corresponding constants to fully describe the variation in interlayer thickness 96

Table 7 Model variations where the normal initiation stress of each cohesive layer varies relative to the interlayer. 99

Table 8 Material properties used in the 3D DCB scale FE model. 101

Table of Figures

Figure 1 CFRP predicted market growth [4, 7]. Global CF demand is broken down by sector [4], and key drivers have been identified [4]. Airbus A350 XWB© [8], where more than 50% of the weight is CFRP, and there is a reported 10 – 12 % fuel efficiency increase for a 20 % weight saving [9]. 1

Figure 2 Varying length scales of a composite system, from individual material constituents to component scale parts [45-51].....7

Figure 3 Subsurface damage initiated by a low-velocity impact event. Schematic of cracks caused by an impact (Top) [61] and a corresponding slice of a CT image showing the damage caused on a real sample [26]. 9

Figure 4 Delamination Modes [68], in-plane opening a), in-plane shear b) and out-of-plane shear c). 10

Figure 5 Schematic of the Mode I wedge-driven loading rig [80].....11

Figure 6 Schematic diagram of toughening mechanisms proposed for thermoplastic-modified epoxies: (1) crack pinning, (2) particle bridging, (3) crack path deflection, (4) particle yielding, (5) particle-yielding induced shear banding, and (6) microcracking [112]. 14

Figure 7 Plastic yield zone interaction with interleaf boundaries for different thicknesses (a) adhesive failure of resin and fibre and (b) cohesive failure of the resin. (Yasaee *et al.*) [121].....16

Figure 8 Schematic showing crack bridging tractions in the cohesive zone [132] 18

Figure 9 Different shapes of the cohesive traction-separation law [133]: (a) exponential [131], (b) polynomial [134], (c) constant [130], (d) trilinear [135], (e) linear [136] and (f) bi-linear [137].....19

Figure 10 Basic operating method for a micro-focus CT scanning system. 27

Figure 11 Schematic diagram showing the principle of Radon transform analysis of a structured 2D image dataset via pixel summation along different projection angles. c) shows the full sinogram, demonstrating image structure at -45^{o} (Image reproduced with permission from the author) [189]. 29

Table of Figures

Figure 12 Separation of the fracture surfaces. Step 1 shows the insertion of a wedge after DCB testing to propagate the crack. Step 2 shows the insertion of the razor blade beyond the DCB fracture length. Step 3 shows the full delamination of the sample using the razor blade. 41

Figure 13 Force displacement curve for a sample in each of the tested material systems. 43

Figure 14 Delamination resistance curves of each material system where the 95% prediction interval of a second-order polynomial fitted curve is plotted. 44

Figure 15 Delamination resistance curve for material system 1, showing a small increase in toughness with crack propagation, where the 95% prediction interval of a second-order polynomial fitted curve is plotted. 44

Figure 16 Delamination resistance curve for material system 2, showing a modest increase in toughness with crack propagation, where the 95% prediction interval of a second-order polynomial fitted curve is plotted. 45

Figure 17 Delamination resistance curve for material system 3a, showing a small increase in toughness up to around 30 mm of crack growth, followed by a subsequent drop in toughness, where the 95% prediction interval of a second-order polynomial fitted curve is plotted. 45

Figure 18 Delamination resistance curve for material system 3b, showing an initial drop in toughness sustained until around 20 mm of crack growth. The toughness then remains steady until falling again in the final 5 mm of crack growth. The 95% prediction interval of a second-order polynomial fitted curve is plotted. 46

Figure 19 Delamination resistance curve for material system 4, showing an initial drop in toughness over the first 5 mm of crack growth followed by a slight rise over a further 5 mm and then self-similar crack propagation for the remainder. The 95% prediction interval of a second-order polynomial fitted curve is plotted. 46

Figure 20 Delamination resistance curve for material system 5 showing a steady increase in toughness with crack propagation until reaching a self-similar propagation at around 30 mm of crack growth. The 95% prediction interval of a second-order polynomial fitted curve is plotted. 47

Figure 21 Delamination resistance curve for material system 6, showing an initial steady decrease in toughness with crack propagation until levelling and remaining similar after

25 mm of crack growth. The 95% prediction interval of a second-order polynomial fitted curve is plotted. 47

Figure 22 Cross-section through each materials system showing the distinct interlayer in the particle-toughened materials with the fibre direction into the page. 48

Figure 23 Fracture surfaces of each material system showing the transition from the interlayer to ply in PT systems. The crack direction is from right to left.....50

Figure 24 Optical microscopy of crack surfaces highlighting the incidence of both inter- and intralaminar propagation. The crack direction is from right to left. 51

Figure 25 SEM overview of the 'finger' regions where the ply and interlayer interface. The crack direction is from the right to the left of each image. 55

Figure 26 SEM image of the interlayer region of each Material system. The crack direction is from the right to the left of each image.....56

Figure 27 SEM image of the fracture along an intralaminar path through the ply. The crack direction is from the right to the left of each image. 57

Figure 28 SEM zoomed image of toughening particles within the interlayer of the particle-toughened system. The crack direction is from the right to the left of each image. 58

Figure 29 Manual apparatus parts description. The M5 bolt is rotated to push the wedge into the specimen. The M5 steel nut locked in position inside the PLA connector allows the displacement of the wedge.....69

Figure 30 The pre-imposed blunt crack and the imaged region relative to coupon length, wedge apparatus, edge and base positions. 70

Figure 31 Schematic of crack transition on the fracture surface of a DCB specimen. Local regions of crack transition from the interlaminar region to the intralaminar region are circled.....72

Figure 32 Comparison of fracture surfaces from three specimens of material system 4 (comparable to material 4 in Figure 23). 73

Figure 33 Mapped trigger regions within the scanned area of specimen Sample 1 shown in Figure 32. a) The fracture surface showing the scanned area, mapped trigger regions and 'beach marks. b) XCT mapping of trigger regions with fibres going into the

page. c) SEM mapping of trigger regions showing the transition from interlaminar to intralaminar fracture. 75

Figure 34 Mapped trigger regions within the scanned area of specimen Sample 2 shown in Figure 32. a) The fracture surface showing the scanned area, mapped trigger regions and 'beach marks. b) XCT mapping of trigger regions with fibres going into the page. c) SEM mapping of trigger regions showing the transition from interlaminar to intralaminar fracture. 76

Figure 35 Mapped trigger regions within the scanned area of specimen Sample 3 shown in Figure 32. a) The fracture surface showing the scanned area, mapped trigger regions and 'beach marks. b) XCT mapping of trigger regions with fibres going into the page. c) SEM mapping of trigger regions showing the transition from interlaminar to intralaminar fracture. 77

Figure 36 XCT images with the fibres going into the page. This figure is for illustrative purposes only to clarify the difference between a TARP in a), and a tow gap in b). 79

Figure 37 SRCT images slices during the crack path transition into the ply across three load steps, where a) is the first slice is approximately 12 mm ahead of the insert, b) is the second slice 15 mm ahead of the insert and c) is the third slice 16 mm ahead of the insert. The reader should note the orientation of the axis for comparison in Figure 38, Figure 39, and Figure 40. 80

Figure 38 SRCT images through orthogonal planes during load step 1, a) shows a slice through section A-A where the crack is travelling from the bottom of the image to the top and debonding toughening particles can be observed ahead of the crack front in the interlayer, and b) shows a slice through section B-B where the crack is travelling from left to right and toughening particles are debonding ahead of the main crack. The reader's attention is drawn to the orientation of the axis relative to Figure 37. 81

Figure 39 SRCT image slices during load step 2, a) shows a section where the crack remains in the interlayer before the bifurcation and secondary crack, b) shows a slice at the bifurcation where the crack transitions to the fibre-interlayer interface, and c) shows a section through the secondary crack, where the crack remains in the ply. The reader's attention is drawn to the orientation of the axis relative to Figure 37. 82

Figure 40 SRCT images slices during load step 3, a) shows a section through the overlapping cracks on either side of the interlayer and b) shows a section where the crack is fully embedded in the upper ply. The reader's attention in drawn to the orientation of the axis relative to Figure 37. 83

Figure 41 Potential crack transition mechanisms at a tow-gap-like feature. 86

Figure 42 Model geometry and boundary conditions. a) shows the lower cantilever is pinned and the upper cantilever is displaced at a rate of 1 mm/min. Furthermore, the ROI is highlighted where crack propagation occurs. b) shows the ROI, showing the toughened interlayer, cohesive interface elements, the first few layers of fibres, and the bulk ply regions of the model. The symmetry conditions are also defined. 92

Figure 43 A cross-section through the interlayer and ply with the fibre direction into the screen, where nominal fibre outlines are shown for clarity. a) is a schematic of a constant thickness interlayer without the inclusion of tow gaps. b) shows a constant thickness interlayer with and without the inclusion of tow gaps. ...93

Figure 44 Slice of a CT image through a sample from material system 4 analysed in Chapter 4 showing the variation in interlayer thickness. The fibres are going into the page. 95

Figure 45 Histogram of experimentally determined interlayer thickness variation, with a minimum value of zero and a maximum value of 57 microns. 95

Figure 46 Interlayer geometry variation. The left shows sinusoidal variation as described by a sine function. The right shows the constant thickness interlayer geometry. 96

Figure 47 Distribution of initiation stress used to assign stochastic cohesive properties. 98

Figure 48 Comparison of different interlayer thickness models where the relative interface strength is 90% of that of the interlayer. A section on the plane of symmetry is shown on the top row and the images show the damage immediately after the pre-imposed crack. For the 10 μm constant thickness interlayer model, the crack transitions to the upper interface where as it propagates and microcracks sequentially initiate in the interlayer but do not propagate further. Section A-A shows that damage transitions to either side of the interlayer and appears to oscillate between the upper and lower interfaces. Likewise, albeit to a lesser extent this behaviour is seen in the 25 μm interlayer thickness model. Finally, in

the 57 µm thick interlayer model, there is some damage distributed within the interlayer as the interface propagates although to a much lesser extent than in the other two models. 104

Figure 49 Comparison of different varying interlayer thickness models where the relative interface strength is 90% of that of the interlayer. A section on the plane of symmetry is shown on the top row and the images show the damage immediately after the pre-imposed crack. For the 10 - 57 µm varying thickness interlayer model the crack transitions to the lower interface as it propagates. Section A-A shows that damage transitions to either side of the interlayer and appears to oscillate between the upper and lower interfaces less frequently than the other two varying thickness models. Similarly, albeit to a greater extent the 12 – 38 µm and 18 – 32 µm varying interlayer models display this oscillation between the upper and lower interface regions with microcracking in the interlayer as they propagate. 105

Figure 50 Comparison of different interlayer thickness models where the relative interface strength is 100% that of the interlayer. A section on the plane of symmetry is shown on the top row and the images show the damage immediately after the pre-imposed crack. In both the 10 µm and 25 µm thickness interlayer models the crack transitions to the interlayer-ply interface. In sections A-A and B-B interlayer crack forms, appearing to bridge between the cracks running along either interface on the opposing side of the interlayer. For the 57 µm thick interlayer model on the symmetry plane where the crack is propagating from right to left the interlayer crack does not transition, although there is evidence of damage to the lower interface which did not become dominant. In section C-C the oscillation between the upper and lower interface is less frequent and an oblique crack appears to be bridging between the upper and lower interface. 106

Figure 51 Comparison of different varying interlayer thickness models where the relative interface strength is 100% that of the interlayer. A section on the plane of symmetry is shown on the top row and the images show the damage immediately after the pre-imposed crack. In the top row of images where the crack is propagating from right to left it can be seen that on the symmetry plane, the crack remains in the interlayer for both the 10 – 57 µm and 12 – 38 µm varying thickness models respectively, where there is some damage in the upper interface of the former. In the 18 – 32 µm varying thickness model, the crack transitions to the lower

interface. In sections A-A, B-B, and C-C the crack propagates along the upper and lower interlayer-ply interfaces with increasing frequency respectively, where interlayer cracks can be seen to bridge between them. 107

Figure 52 Schematic of crack and damage distribution in modelled volumes as an aid to interpreting the results in the following sections. It has been colour coded to match the legend used for the graphs displaying the proportion of the crack in each of the respective layers. This figure is broadly in line with the results shown previously in Figure 38, Figure 39, and Figure 40 in Chapter 4. 110

Figure 53 Proportion of damaged elements in each potential delamination path when the relative interface strength is 80% of that of the interlayer and SDEG > 0. a) Shows the proportion of the crack in each layer at a commonly converged timestep making the results directly comparable. The 10 µm thickness interlayer has the most damage distributed in the interlayer. The presence of tow gaps notably increases the proportion of damage in the interlayer for the 10 – 57 µm varying interlayer thickness model. b) Shows the proportion of the crack at the respective final converged timestep for each model, therefore these proportions are not directly comparable with each other. The tow gaps appear to have a smaller effect on the crack path with an increase in damage in the interlayer in the 10 – 57 µm varying interlayer thickness model. 112

Figure 54 Proportion of damaged elements in each potential delamination path when the relative interface strength is 80% of that of the interlayer and SDEG > 0.9. a) Shows the proportion of the crack in each layer at a commonly converged timestep making the results directly comparable. In the absence of tow gaps the crack is distributed in the interlayer-fibre interface, however, the presence of tow gaps facilitates a small proportion of the crack to be retained within the interlayer for the 10 – 57 µm varying thickness model. b) Shows the proportion of the crack at the respective final converged timestep for each model, therefore these proportions are not directly comparable with each other. The distribution of damage is similar to that mentioned above, however, a small fraction of the crack appears to have transitioned to the interlayer of the 10 µm thick model absent of tow gaps. 114

Figure 55 Proportion of damaged elements in each potential delamination path when the relative interface strength is 90% of that of the interlayer and SDEG > 0. a) Shows the proportion of the crack in each layer at a commonly converged timestep making

the results directly comparable. In the absence of tow gaps, the most damage is distributed in the interlayer for the 57 µm constant thickness model and the proportion decreases when variation is introduced and as the interlayer gets thinner. Notably, the model with the least damage distributed in the interlayer is the 25 µm interlayer thickness model. The presence of tow gaps increased the distribution of damage in the interlayer for all models, particularly the 10 – 57 µm varying interlayer thickness model b) Shows the proportion of the crack at the respective final converged timestep for each model, and therefore these proportions are not directly comparable with each other. The presence of tow gaps appears to enable damage to propagate in the top and bottom plies in two of the constant thickness geometry models. 117

Figure 56 Proportion of damaged elements in each potential delamination path when the relative interface strength is 90% of that of the interlayer and SDEG > 0.9. a) Shows the proportion of the crack in each layer at a commonly converged timestep making the results directly comparable. In the absence of tow gaps the fully developed crack remains entirely in the interlayer for the constant thickness 57 µm interlayer thickness model and a much smaller fraction remains in the interlayer for all the varying interlayer geometry models, whereas the thinner constant thickness interlayer models all see the crack transition out of the interlayer to the interlayer-fibre interfaces. The presence of tow gaps in the 57 µm constant thickness model significantly reduces the proportion of the crack in the interlayer by approximately 65 % b) Shows the proportion of the crack at the respective final converged timestep for each model, therefore these proportions are not directly comparable with each other. The crack remains entirely in the interlayer for the 57 µm thickness interlayer model, in the absence of tow gaps, however, the presence of tow gaps appears to facilitate a significant transition of the crack away from the interlayer. 119

Figure 57 Proportion of damaged elements in each potential delamination path when the relative interface strength is 95% of that of the interlayer and SDEG > 0. a) Shows the proportion of the crack in each layer at a commonly converged timestep making the results directly comparable. The thinner interlayer geometry models see the most damage distributed in the interlayer in the absence of tow gaps. The presence of tow gaps increases the distribution of damage in the interlayer for the 10 – 57 µm varying thickness interlayer. b) Shows the proportion of the crack at the respective final converged timestep for each model, therefore these

proportions are not directly comparable with each other. Notably, there is a greater proportion of damage distributed in the upper and lower plies with and without and presence of tow gaps for the majority of models.....121

Figure 58 Proportion of damaged elements in each potential delamination path when the relative interface strength is 95% of that of the interlayer and SDEG > 0.9. a) Shows the proportion of the crack in each layer at a commonly converged timestep making the results directly comparable. A greater proportion of the crack is distributed in the interlayer for all models, however, the majority of the crack remains in the interlayer-fibre interface, with the exception of the 57 μm interlayer thickness model absent of tow gaps. The presence of tow gaps reduces the proportion of the crack in the interlayer for the constant thickness geometry models and the for the varying thickness geometry models where the standard deviation is greater than one. b) Shows the proportion of the crack at the respective final converged timestep for each model, therefore these proportions are not directly comparable with each other. The crack appears to transition out of the interlayer in all models despite the strength of the interface is 95 % that of the interlayer for all models. 123

Figure 59 Proportion of damaged elements in each potential delamination path when the relative interface strength is equal to that of the interlayer and SDEG > 0. a) Shows the proportion of the crack in each layer at a commonly converged timestep making the results directly comparable. almost 50 % of the damage is distributed within the interlayer of the 10 μm thickness interlayer model with the absence of tow gaps. When tow gaps are present the proportion of damage in the interlayer increases to around 55 %. The same trend is similarly seen in the other models except for the 10 – 57 μm varying thickness interlayer model where damage distribution within the interlayer decreased with the presence of tow gaps. b) Shows the proportion of the crack at the respective final converged timestep for each model, therefore these proportions are not directly comparable with each other. Notably, the proportion of damage in the interlayer increases in the presence of tow gaps for all models as well as damaged elements in the upper and lower ply in all models except for the 10 μm interlayer thickness model regardless of the presence of tow gaps.....125

Figure 60 Proportion of damaged elements in each potential delamination path when the relative interface strength is equal to that of the interlayer and SDEG > 0.9. a) Shows the

proportion of the crack in each layer at a commonly converged timestep making the results directly comparable. Absent of tow gaps, the crack remains in the interlayer for all models. When tow gaps are present there is a limited transition of the crack to the interlayer-fibre interface for the 10 µm interlayer thickness model and a much more significant transition in the 10 – 57 µm varying thickness interlayer, where approximately 70 % of the crack has transitioned to the interface. b) Shows the proportion of the crack at the respective final converged timestep for each model, therefore these proportions are not directly comparable with each other. At the final converged timestep for each model, it is illustrated that for all interlayer geometry conditions when the relative strength of the interlayer and interface are equal, the crack transitions away from the interlayer. 127

Figure 61 Proportion of damaged elements in each potential delamination path when the relative interface strength is 105%, 110% and 120% of that of the interlayer respectively and SDEG > 0. a) Shows the proportion of the crack in each layer at a commonly converged timestep making the results directly comparable. For all models, the relative strength of the interface is greater than the interlayer and all damage remains in the interlayer for all interlayer geometries. b) Shows the proportion of the crack at the respective final converged timestep for each model, therefore these proportions are not directly comparable with each other. For all interlayer geometry models the damage becomes distributed within the interlayer with further load-point opening displacement there is a clear trend for all interlayer geometries that as the strength of the interface increases relative to the interlayer the proportion of damage distributed in the interlayer increases. 129

Figure 62 Proportion of damaged elements in each potential delamination path when the relative interface strength is 105%, 110% and 120% of that of the interlayer respectively and SDEG > 0.9. a) Shows the proportion of the crack in each layer at a commonly converged timestep making the results directly comparable. The crack remains in the interlayer for all models. b) Shows the proportion of the crack at the respective final converged timestep for each model, therefore these proportions are not directly comparable with each other. A small proportion of the crack transitions to the interlayer-fibre interface when the strength of the interface is 1.05 times that of the interlayer for the final converged step of the 25 µm interlayer thickness model and all varying thickness models. When the

strength of the interface is greater than 1.05 times the strength of the interlayer the whole crack remains in the interlayer for all models. 131

Figure 63 Proportion of damaged elements in each potential delamination path when the strength properties of the progressive damage elements in the interfaces and interlayer are stochastic. a) Shows the total proportions of elements with SDEG > 0 due to damage at the final timestep for each respective model. Therefore, models are not directly comparable with each other. b) Shows the proportion of fully damaged elements being capable of supporting less than 90% of their original load-bearing capacity at the final timestep for each respective model. Therefore, models are not directly comparable with each other. It is noteworthy that for stochastic fracture properties, the distribution of the fully developed crack is similar to the total damage distribution. There is also little difference in damage distribution with or without the presence of tow gaps. Damage is distributed in all layers for all the models. 133

Figure 64 Variation in the apparent critical strain energy release rate for each geometric model when the interface stress is 120% of the interlayer strength, where the error bars represent the standard error of the mean. 135

Figure 65 Load Point Opening displacement required for 25% of the crack to transition out of the interlayer 136

Figure 66 potential crack interaction with adjacent fibre-matrix interface regions, showing as the interlayer becomes thicker there may be less interaction with the fibres in the surrounding plies of the interlayer. 137

Research Thesis: Declaration of Authorship

Print name: Keiran Ball

Title of thesis: Applications of Advanced Imaging and Simulation Methods in Analysing Delamination Fracture in Fibre Reinforced Composite Materials

I declare that this thesis and the work presented in it are my own and has been generated by me as the result of my own original research.

I confirm that:

1. This work was done wholly or mainly while in candidature for a research degree at this University;
2. Where any part of this thesis has previously been submitted for a degree or any other qualification at this University or any other institution, this has been clearly stated;
3. Where I have consulted the published work of others, this is always clearly attributed;
4. Where I have quoted from the work of others, the source is always given. With the exception of such quotations, this thesis is entirely my own work;
5. I have acknowledged all main sources of help;
6. Where the thesis is based on work done by myself jointly with others, I have made clear exactly what was done by others and what I have contributed myself;
7. Either none of this work has been published before submission, or parts of this work have been published as the following conference papers:

Ball, K., Lee, Y., Furtado, C., Arteiro, A., Patel, P., Majkut, M., Helfen, L., Wardle, B.L., Mavrogordato, M., Sinclair, I. and Spearing, M., 2022. Gaining mechanistic insight into key factors contributing to crack path transition in particle-toughened carbon fibre reinforced polymer composites using 3D X-ray computed tomography. Energy Reports, 8, pp.61-66.

Ball, K., Lee, Y., Furtado, C. and Arteiro, A., Patel, P., Majkut, M., Helfen, L., Wardle, B.L., Mavrogordato, M., Sinclair, I. and Spearing, M., 2022. 'MODE I CRACK PATH TRANSITIONS IN UNIDIRECTIONAL CARBON FIBRE COMPOSITES ANALYSED USING IN SITU 3D COMPUTED TOMOGRAPHY AND THE EXTENDED FINITE ELEMENT METHOD', Proceedings of the 20th European Conference on Composite Materials - Composites Meet Sustainability (Vol 3). EPFL, Lausanne, June 26-30, 2022. Lausanne, Switzerland: EPFL Lausanne, Composite Construction Laboratory

Signature: .....Date:.....

Acknowledgements

I would like to express my deepest appreciation to each member of my supervisory team: Professor Ian Sinclair, Professor Mark Spearing and Doctor Mark Mavrogordato. It is only with your unwavering support, dedication, and expertise that this project was possible.

I would also like to thank my industrial supervisory team at Solvay for providing key insights and guidance during the project, for project funding, and for supplying materials for testing and imaging.

I am grateful to the µ-VIS X-ray imaging centre, for the provision of tomographic imaging facilities. My particular thanks go to Dr Katy Rankin, Dr Richard Boardman, Dr Sebastian Rosini, and, Dr Mark Mavrogordato. The work in the thesis has benefited from the use of synchrotron facilities at the European Synchrotron Radiation Facility (ID19) under DOI 10.15151/ESRF-ES-569733595 . I would like to thank in particular Dr Lukas Helfen, Dr Marta Majkut, and the team from the Massachusetts Institute of Technology and the Univerity of Porto for their support at the ESRF.

I would like to recognise the support provided by Dr Andrew Robinson head of the Testing and Structures Research Laboratory at which I conducted the mechanical testing of materials used in this thesis. Similarly, I would like to acknowledge the support of all the staff in the EDMC, materials laboratory, and Faculty of Engineering and Physical Sciences whose hard work contributes to the day-to-day running of facilities and makes quality research possible. I also appreciate the funding (under grant number EP/L01582X/1) and support provided by the Centre for Doctoral Training for Sustainable Infrastructure Systems (CDT-SIS). Particularly I would like to thank the staff for their hard work, support, and opportunities presented throughout my time at Southampton, notably Jenny Knight and Professor Paul Kemp.

Finally, a heartfelt thank you goes out to my fiancé and two children who have been on this journey with me. Thank you for your steadfast support and unwavering patience. Truthfully Katie, Max, and Hope, without you this would not have been possible and it has, in many ways, been your journey as much as it has been mine.

List of Acronyms

A-FEM	Augmented-Finite Element Method
ASTM	American Society for Testing and Materials
BS	British Standards
BVID	Barely Visible Impact Damage
CFRP	Carbon Fibre Reinforced Polymer
CNT	Carbon Nanotube
COR	Centre of Rotation
CSERR	Critical Strain Energy Release Rate
CZM	Cohesive Zone Model
DCB	Double Cantilever Beam
FBP	Filtered Back Projection
FE	Finite Element
FEM	Finite Element Model
ILSS	Interlaminar Shear Strength
ISO	International Standards Organisation
LSB	Large-scale Bridgingg
MBT	Modified Beam Theory
OM	Optical Microscopy
PFDM	Phase Field Damage Model
PoU	Partition of Unity
PTFE	Polytetrafluoroethylene
R-Curve	Delamination Resistance Curve
ROI	Region of Interest

SEM	Scanning Electron Microscopy
SERR	Strain Energy Release Rate
SNR	Signal-to-Noise Ratio
SRCT	Synchrotron Radiation Computed Tomography
UD	Unidirectional
VCCT	Virtual Crack Closure Technique
Vf	Volume Fraction
WWFE	World Wide Failure Exercise
XCT	X-ray Computed Tomography
XFEM	eXtended Finite Element Method

Nomenclature

$\bar{\sigma}_{22}$	Transverse normal tensile stress
$\hat{\sigma}_n$	Maximum Mode I traction
$\bar{\tau}_{12}$	Transverse in-plane shear stress average
$\hat{t}_n$	Maximum Mode II traction
$\|\Delta\|$	x-axis intersection from the least squares fit of the graph of the cube root of compliance vs crack length
E'	Equivalent elastic modulus
$E_{1,2,3}$	Elastic modulus in the fibre direction, transverse direction, and through-thickness direction
$F_\alpha(x)$	Asymptotic crack-tip function
$G_{12,13,23}$	Shear modulus components
$G_{I,II,III}$	Strain energy release rate in tensile opening, in-plane shear, and out-of-plane shear respectively
$G_{IC,IIC,IIIC}$	Critical strain energy release rate in tensile opening, in-plane shear, and out-of-plane shear respectively
G_T	Total strain energy release rate
I_0	Intensity of incident X-ray
$K_{I,II,III}$	Cohesive element stiffness components
L_{cl}	Length of Dugdale cohesive strip
$N_I(x)$	Linear shape function
R_p	The radius of the plastic zone according to Irwin's model
a_I	Enriched degree of freedom vector
b_I^α	Enriched nodal degree of freedom vector
u_I	Nodal displacement vector

$\sigma_{I,II,III}$	Direct stress components
$\sigma_{S1,S2}$	Stress in the first and second shear direction respectively
σ_Y^*	Constant in-plane stress along the axis coincident and parallel to the crack tip
σ_n	Stress normal to the plane of the crack front
$\sigma_{principal}$	Maximum principal stress
$\upsilon_{12,13,23}$	Poisson's ratio components
Δx	Specimen thickness
h	Laminate half thickness
$\mathcal{R}(r,\theta)$	Radon transform
I	The intensity of the detected ray
L	Specimen length
P	Load point opening force
R	X-ray spacing
S	Source to detector distance
$W(E)$	Function expressing incident X-ray spectrum
a	Crack length
d	Detector element spacing
$f(x,y)$	2D Fourier transform
n	Number of X-ray photons detected per detector element
r	The perpendicular offset of a line
α	Fitting parameter for the Power Law
β	Fitting parameter for the Power Law
δ	Load point opening displacement
ζ	Fitting parameter for the Bilinear Traction Law
η	Fitting parameter for the B-K Criterion
θ	The angle of an incident ray to the x-axis

κ	Fitting parameter for Linear Interaction traction separation
μ	Attenuation coefficient
ξ	Fitting parameter for the Bilinear Traction Law
φ	Fitting parameter for Linear Interaction traction separation

Chapter 1 Background, Aims and Objectives

1.1 Background and Research Questions

There are many global and domestic pressures facing the composite industry including environmental legislation and targets, changing consumer behaviour, and a downturn in economic activity from the recent common global pressures [1-3]. Whilst the complexity of the situation is somewhat beyond the scope of this report, composites remain attractive in a range of industries including transport, renewable energies, sports equipment and storage (high pressure) vessels [4] due to their high specific strength, high specific stiffness, low density, ease of integration for part consolidation, multi-functionalities, and freedom in design. Research and development are important in providing solutions to increase and optimise the use of composite materials in these industries by improving efficiency in design while also reducing the cost of production of new technologies. Driving factors for the carbon fibre-reinforced polymer (CFRP) market growth and key sectors are identified in Figure 1. For example, the use of composite parts on the Airbus A350 XWB© (extra widebody) resulted in a fuel efficiency saving of around 25% per seat and 20% lower cash operating costs per seat compared to previous long-range competitors such as the Boeing 777 [5]. CFRP's also boast excellent corrosion resistance and superior electrical, dielectric, thermal, mechanical, and magnetic properties when considered alternative shielding materials for suppressing electromagnetic interference [6].

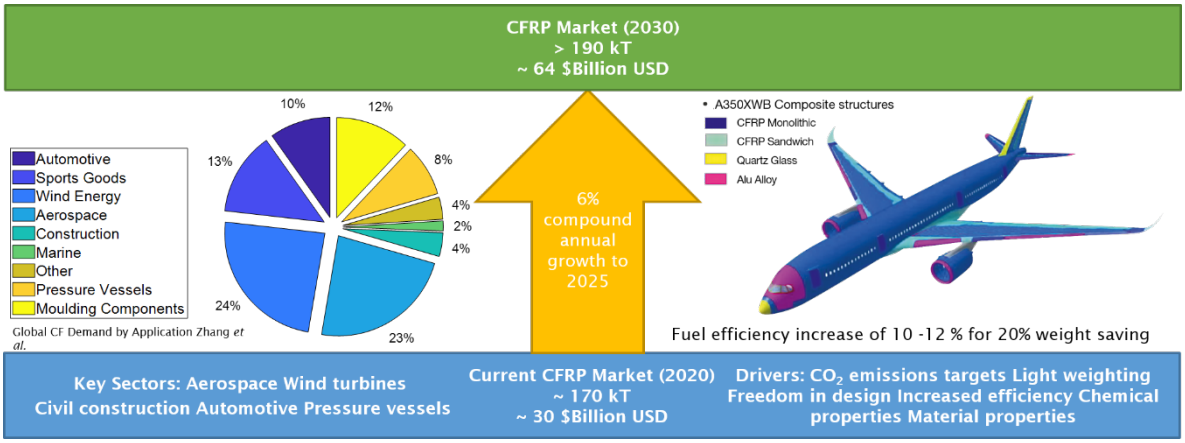

Figure 1 CFRP predicted market growth [4, 7]. Global CF demand is broken down by sector [4], and key drivers have been identified [4]. Airbus A350 XWB© [8], where more than 50% of the weight is CFRP, and there is a reported 10 – 12 % fuel efficiency increase for a 20 % weight saving [9].

Despite the benefits of implementing CFRP's their full potential has not yet been realised due to other considerations such as energy requirements and economic cost of production, production volume and environmental impact, which still need to be addressed to make them viable for a range of industries such as the automotive industry [10, 11]. Among various economic and technical factors contributing to this, it is significant to note an intrinsic susceptibility to impact damage, causing sub-surface delaminations, which can significantly reduce static strength [12]. Barely Visible Impact Damage (BVID) is the name given to subsurface damage and delaminations in a composite that is not visible from the surface, often caused by a low-velocity impact event. The airworthiness regulations state that it must be assumed that BVID is present and that the structure must tolerate this damage at ultimate levels of load without failing [13], thereby leading to significant knockdowns in the design specification which reduce the efficiency of design.

Previous work has identified many ways of increasing the interlaminar toughness of CFRP's to increase the damage tolerance of composite systems. Toughening approaches include, but are not limited to; resin toughening using inorganic fillers, surface modification of fibres, z-pinning and stitching, and multiscale toughening using carbon nano-tubes, and nano and micro toughening particles [14]. In a structure designed for durability, it is often desirable to suppress damage at initiation to preserve the residual strength properties of the part. For example, reducing damage by suppressing delaminations after critical loading events such as impact is most effective by maintaining a crack within the particle-toughened interlayer [15]. Therefore, an appreciation for what damage response mechanisms are occurring is essential as is understanding the controlling length scales, and the effect they have on cracks paths and delaminations within the structure.

1.2 Aims and Objectives

The current project uses a multiscale imaging approach employing a range of complementary imaging techniques to enhance a quantitative mechanistic understanding of delamination processes. X-ray computed tomography (XCT), optical microscopy (OM), and scanning electron microscopy (SEM) is utilised to evaluate the damage response mechanisms of different CFRP systems. The information obtained from the mechanical testing and imaging campaign is used to inform computational models. Collecting such empirical and modelling data allows this project to build upon the previous work carried out at the University of Southampton. This project aims to link the micromechanical damage response mechanisms to the macroscale toughening behaviour of the composite. Additionally, the project aims to utilise existing modelling strategies to obtain mechanistic insight into significant factors determining the crack path through a CFRP and enable material systems to be designed to achieve the desired toughness behaviour.

The primary aim of this project is to provide guidance for the design and manufacturing process of CFRPs in order to achieve the desired damage resistance and damage tolerance. Additionally, it aims to contribute to the more efficient use of CFRP structures in design and certification.

The objectives of this study are to:

• Identify which damage response mechanisms determine the shape of a material system's delamination resistance response (R-curve).

• Determine which damage response mechanisms allow a crack to follow a path in the interlaminar region, fibre-matrix interfacial region or intralaminar region of a composite.

• Establish how a CFRP can be designed or optimised to achieve the desired R-curve response and crack path.

Overall, the research conducted in this project will contribute to the development of more robust and efficient CFRP structures by providing valuable insights into the mechanisms underlying crack path transitions during delamination.

1.3 Thesis Structure

A comprehensive review of the literature is presented. First, it will cover the essential background of the project and then more specific gaps in the literature. The results reported in Chapters 3, 4, and 5 will be submitted for publication and are hence self-contained. Therefore, each results chapter includes a standalone introduction, materials, methods, results, discussion, and conclusion. As a result, there may be some repetition between chapters, particularly in the introduction sections. The report will conclude with a summary of the research presented and a brief synopsis of the main findings and conclusions. Future work resulting from the findings presented in this thesis will be discussed and steps to broaden this investigation will be outlined.

- Chapter 2 – This chapter contains a review of the literature for this thesis. It outlines the fundamental concepts of damage initiation and propagation in particle-toughened CFRP's. Toughening methods are discussed with a focus on the inclusion of interlayering using thermoplastic toughening particles. Work carried out focusing on crack path transitions and resulting damage response mechanisms is reviewed. A review of the modelling strategies used to investigate damage propagation in CFRP's is presented with a focus on combining fracture modelling methods to represent, and understand the factors determining delamination crack path selection. Finally, the fundamentals of

contemporary X-ray CT are explored and novel applications of XCT in the imaging of fibre reinforced composite materials are reviewed.

- Chapter 3 – The first of the technical results chapters presents experimental results aimed at characterising the delamination resistance response of six different toughened unidirectional carbon fibre reinforced epoxy systems during Mode I interlaminar fracture testing. XCT, Scanning Electron Microscopy (SEM), and Optical Microscopy (OM) are used to characterise the effect of interlayering and interlaminar to intralaminar crack path transitions.
- Chapter 4 – The results presented take a more in-depth look at the previously identified interlaminar to intralaminar crack path transitions. *In situ,* high-resolution XCT and Synchrotron Radiation Computed Tomography (SRCT) are used to surmise mechanisms which may play a role in these crack path transitions.
- Chapter 5 – Having identified potential geometric mechanisms contributing to crack path transitions a three-dimensional finite element model (FEM) is used to model crack propagation in a Mode I double cantilever beam (DCB) specimen. The model combines two crack modelling techniques and looks to ascertain the impact of the interlayer architecture, relative interface strength, and how these variables could impact the delamination resistance of a toughened epoxy composite system.
- Chapter 6 – In this chapter, the results presented in this thesis are summarised, key conclusions from the work are outlined and further work which could be carried out in the future as a result of this work is discussed and the main contributions as a result of this work is outlined.

Chapter 2 Literature Review

2.1 Damage in CFRP's

There is no universal definition of failure as it may depend on the application [16]. In general, failure may be considered the point at which a part, mechanism or machine can no longer fulfil its intended purpose. There is an increasing interest in providing robust and accurate tools for predicting failure in composites and allowing for cost-effective designs of components and structures [17]. The first worldwide failure exercise (WWFE) tested various predictive capabilities against experimental evidence [18, 19]. It has since been reported that determining all damage levels and damage modes is essential in optimising lightweight composite components for general use by designers [19-22].

Many damage response mechanisms are reported to act at varying length scales dependent upon the makeup of the CFRP composite system [15, 23-31]. Figure 2 shows the different length scales of CFRP composites; at the nano to microscale, there are the individual material constituents such as fibres and toughening particles. Moving into the tens of μm's, fibre alignment and the interactions between material constituents can be seen. Furthermore, the material architecture can be observed on the mesoscale, such as ply orientation and variation of interlayer thickness. Finally, crack lengths of mm to cm are observed in test size coupons on the macroscale. Hence, predicting the toughness and crack path of CFRP's can become complex due to the interaction of mechanisms between length scales. In some applications of CFRP's, such as aircraft structural components [32], wind turbine blades [33], and composite wheels for Formula One Cars [34], impact damage could present a problem because, despite their desirable properties, composites are particularly susceptible to low-velocity impact damage caused by birdstrikes, debris, and grit being thrown up from the road surface [35]. These impacts can cause a network of intralaminar matrix cracks and interlaminar delaminations [36, 37] below the surface of the impact site, which can significantly reduce the residual compressive strength of the composite [26]. A correlation is reported between the delamination area and the loss in compressive strength [38-40]. There appears to be an intrinsic link between a CFRP's ability to suppress interlaminar delamination initiation and growth, impact damage area and post-impact residual compressive strength [41]. Experimental and modelling work suggest that matrix cracks are the initial damage mode during an impact, delaminations are then initiated from these matrix cracks during impact [42]. It is also suggested that interlaminar shear stresses and in-plane tensile stresses are the dominating stresses causing the initial matrix cracks. Therefore, it may be argued that one way to reduce the extent of delaminations under an impact site (and hence improve the laminates residual

compressive strength) would be to improve the individual loading mode toughness to suppress the initiation of matrix cracks in the first place (*i.e.*, tensile opening corresponding to Mode I loading, and shear corresponding to Mode II and Mode III loading) [42, 43] and then reduce the resulting propagation of the delaminations [44]. The following sections will introduce impact damage and methods being used to improve impact resistance and tolerance.

Individual Material Constituents (Nano – microscale

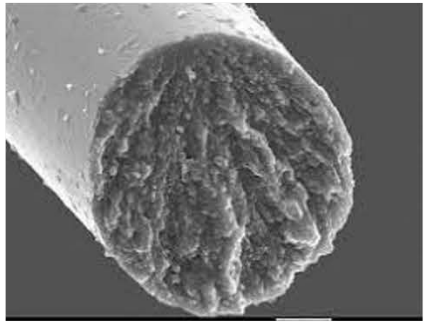

Fibre Ø 5 -7 µm (*Naito et al.*)

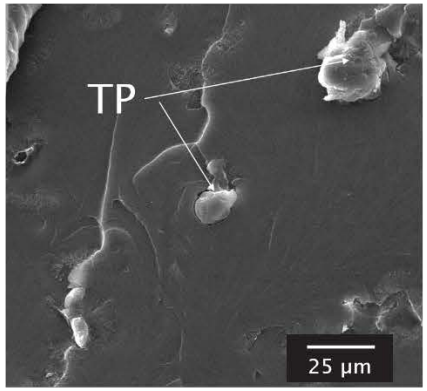

Toughening Particles Ø <5 - 20 µm

Constituent Interactions (microscale)

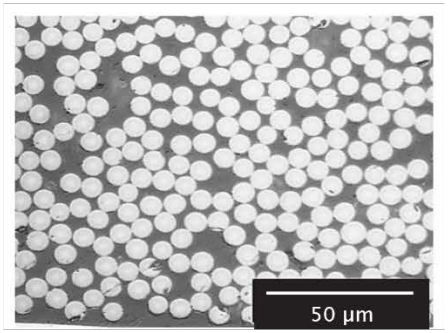

Fibre alignment and dispersion 10's µm (Sebaey *et al.*)

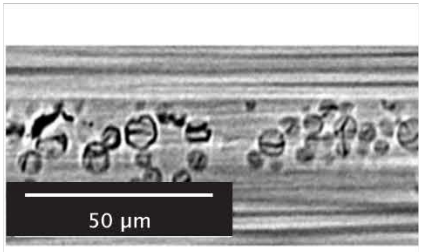

TP damage response mechanisms and interactions 10's µm (Borstnar *et al.*)

Ply orientation and composite architecture (mesoscale)

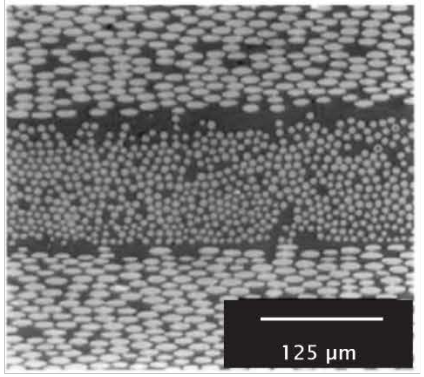

Orientation of adjacent ply's 100's µm (Ye *et al.*)

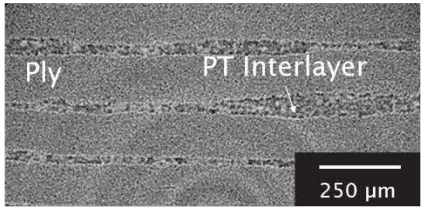

Interlayer thickness variations 100's µm

Test coupon scale (macroscale)

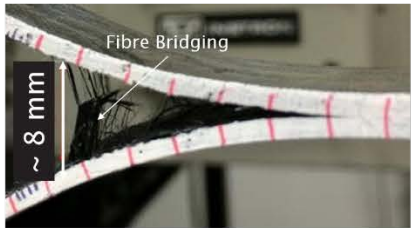

Double cantilever beam (DCB) test showing large scale bridging (LSB) mm's – cm's (Carolan *et al.*)

Failed shear coupon mm's – cm's (Wicaksono *et al.*)

Figure 2 Varying length scales of a composite system, from individual material constituents to component scale parts [45-51]

2.1.1 Impact

In aerospace vehicles, an impact can occur in several ways with varying severity leading to the reduction of residual compressive strength of the laminates [41, 52, 53]. Types of impact include bird strikes, hail, dropped tools during maintenance/inspection, and debris thrown up from a runway during take-off and landing [32, 54]. Therefore, the structure should withstand the initial impact event and continue service in a somewhat damaged state, making both damage resistance and damage tolerance significant. Composites are susceptible to BVID, which manifests as predominantly sub-surface damage making it difficult to detect which can lead to unexpected failure during service [26]. BVID is caused by low velocity, high mass impacts, macroscopically minor dents that may be generated on a composite laminate surface, overlaying significant internal damage, which is, therefore, problematic to detect by standard in-service methods, such as visual inspection [15, 55, 56]. BVID can be detrimental to the compressive strength of the composite and can be responsible for subsequent catastrophic damage and failure in CFRP composites [32].

Subsurface damage caused by an out-of-plane impact can be seen in Figure 3, where a schematic illustration is shown of the damage processes alongside a real sample. During an impact event, matrix shear cracks are reported to initiate in the intraply region [57, 58]. When these matrix cracks reach the ply interface, delaminations are thought to initiate predominantly due to tensile stresses. Delaminations then propagate driven by interlaminar shear stresses, and fibre fracture below the midplane is reported, which initiates due to tensile stresses below the mid-plane of the impact site [58]. It is, therefore, essential to consider interlaminar fracture toughness when modifying a material system to improve impact resistance and tolerance (*i.e.* to suppress the initiation and propagation of delaminations) as discussed at length in a breadth of preceding work [15, 31, 41, 58, 59]. Bull *et al.* reported a reduction in the damaged area under an impact site in particle-toughened laminates compared to untoughened laminates [15, 26, 60] and an increase in compression after impact (CAI) strength of up to 60% for an impact of equal energy (this is in contrast to an impact causing an equivalent indentation) [12, 57].

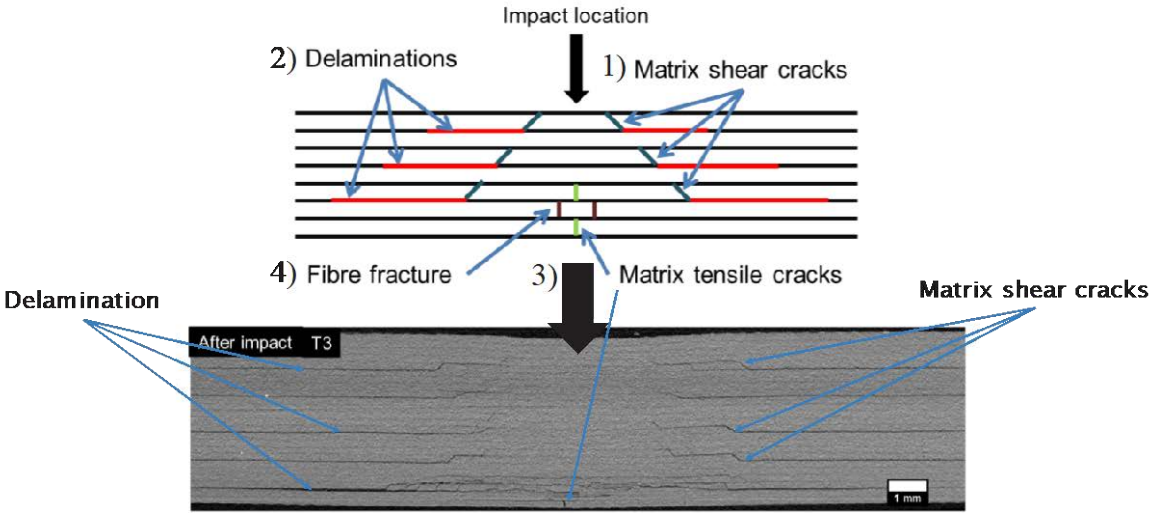

Figure 3 Subsurface damage initiated by a low-velocity impact event. Schematic of cracks caused by an impact (Top) [61] and a corresponding slice of a CT image showing the damage caused on a real sample [26].

Overall, the response of a given laminated CFRP composite to impact depends on various material properties including, but not limited to lay-up sequence, flexural properties, interlaminar shear strength (ILSS) and interlaminar fracture toughness [57]. Increasing the interlaminar delamination resistance is therefore of interest to allow for the optimisation of design and service. In a review by Spearing and Sinclair [62], it was reported that untoughened materials could exhibit three times the damaged area after an impact of given energy than an otherwise equivalent particle-toughened system [15, 41, 62, 63]. It was also shown that the principal effect of toughening was to reduce the extent of delaminations under the impact site, and the order of this toughness correlated with the prevalence of bridging ligament interconnectivity close to the crack tip [62]. Modelling work by Bull *et al.* suggests that residual out-of-plane deformation, interlaminar toughness and the presence of an undamaged cone all play a role in residual compressive strength, in addition to the size of the prior impact damage area [60]. Therefore, among other factors, improving delamination resistance remains an area of continued interest to prevent catastrophic failure.

2.1.2 Delamination Failure

Figure 4 shows the three loading modes which occur in any arbitrarily loaded crack. Figure 4a) shows the in-plane opening, which is propagated by a tensile force pulling the ends of the laminate apart. Figure 4b) shows in-plane shear between two adjacent plies, and Figure 4c) shows the out-of-plane 'tearing' of adjacent plies. Although each delamination mode may be investigated and accounted for individually, it may be expected that all three will apply to some

extent in most practical loading conditions. Whilst well-established tests exist for loading Modes I and II, there is no widely recognised standard for efficient testing in Mode III, although there are proposed methods [64-67].

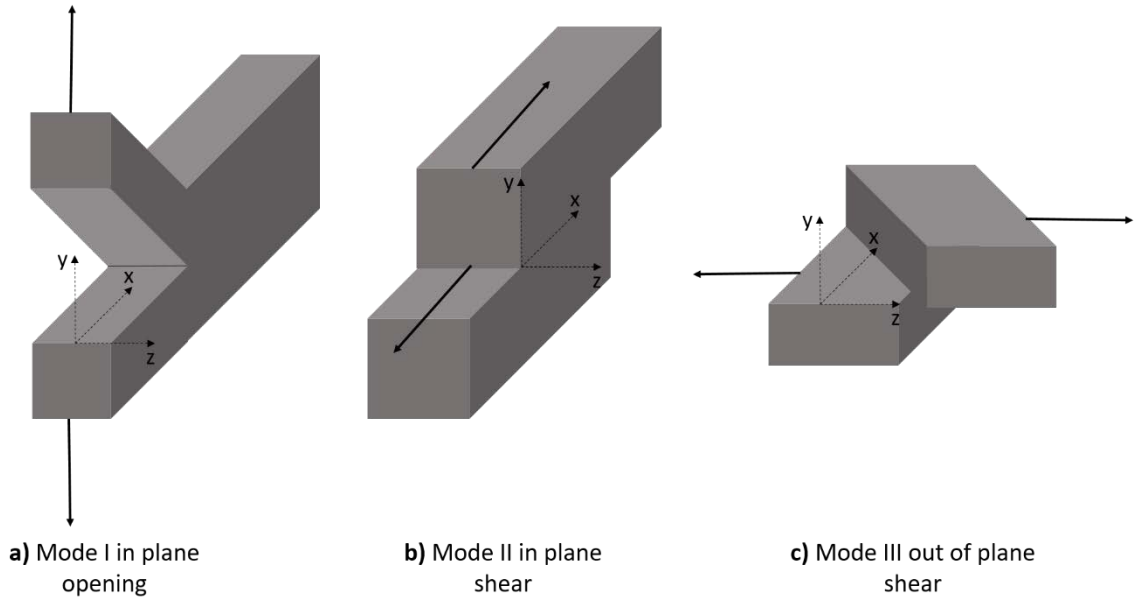

a) Mode I in plane opening

b) Mode II in plane shear

c) Mode III out of plane shear

Figure 4 Delamination Modes [68], in-plane opening a), in-plane shear b) and out-of-plane shear c).

2.1.3 Mode I

While Mode I loading is the focus of this project, it is important to note that other loading modes, such as Mode II and Mode III, may also play a role in determining the overall fracture behaviour of the composite. However, since Mode I delamination is widely recognised to exhibit the lowest fracture energy in most systems and is considered critical [60, 69], this literature review will not explore Mode II and Mode III loading explicitly.

The standard method for testing the Mode I interlaminar fracture toughness of a unidirectional fibre reinforced polymer matrix composite is the DCB test [70, 71], which is employed in research across the field [23, 52, 68, 72-79]. However, despite its widespread use, the standard DCB test may not always be suitable or practical for certain research purposes. As a result, researchers have developed alternative test methods to create Mode I interlaminar delaminations.

To gain a micro mechanistic understanding of delamination in particle-toughened CFRPs a non-standard variation of the DCB test was implemented by Borstnar et al. [31, 49, 80] to allow for *in situ* crack growth analysis using high-resolution XCT. A wedge-driven opening method, was used to propagate the crack and is shown schematically in Figure 5. This method involves a simple displacement-controlled screw arrangement driving a square ram into the laminate and allows for

relatively simple *in situ* mounting to monitor the advance of the delamination crack. While this method provides insight into the microscale response of the material to Mode I delamination, it does not explain how these mechanisms contribute to the larger-scale delamination resistance curve (R-curve) obtained from DCB testing. Furthermore, as the coupon is scaled down from a standard test coupon the results may not be representative of larger-scale test coupons and force-displacement data is not recorded with crack growth. Therefore, it is not clear whether the toughness response is comparable to that produced during the standard test.

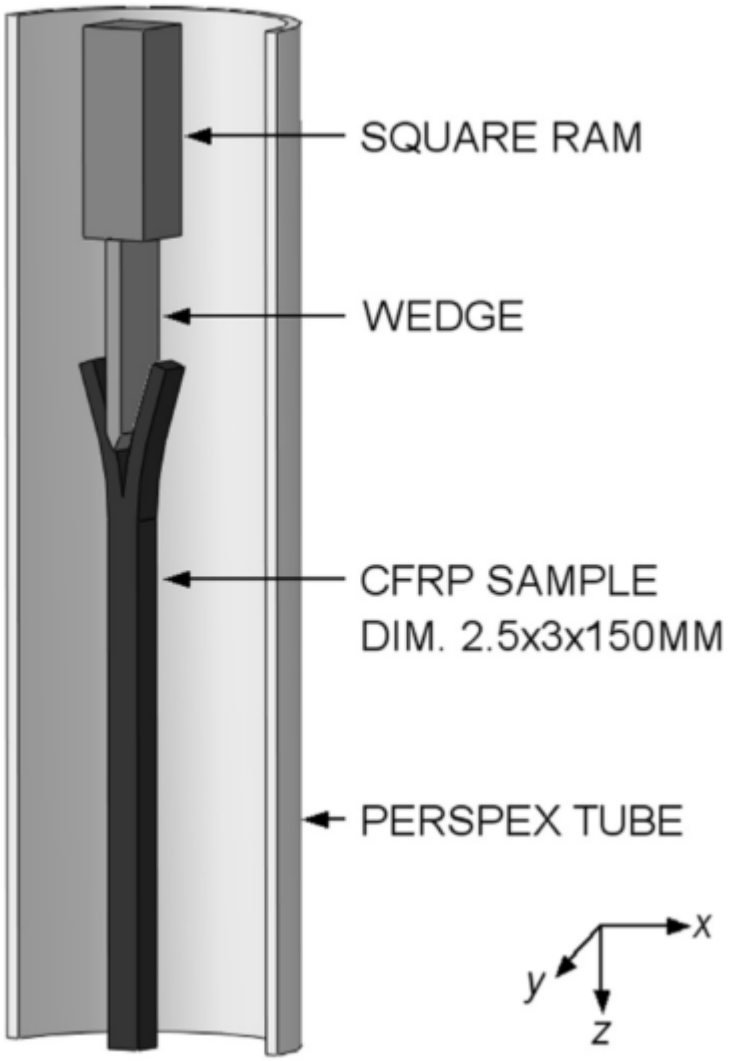

Figure 5 Schematic of the Mode I wedge-driven loading rig [80].

In terms of impact resistance, it has been previously proposed that the fracture toughness of the matrix resin strongly influences the impact response of CFRP laminates [38]. In contrast, the use of high-strength and high-stiffness fibres may not appreciably improve resistance to impact [38]. Therefore, proposed methods aimed at reducing the extent of delaminations under the impact site, which is reported to improve the toughness of the composite [62] tend to focus on matrix

toughening. Proposed toughening strategies to achieve this include but are not limited to the incorporation of Carbon Nanotubes (CNTs) in the composite [68, 81-83] and the toughening of epoxies between plies (interlayering and interleaving) [31, 84]. Additionally, micromechanical damage mechanisms in the vicinity of the crack tip, such as crack front bowing, microcracking, particle cracking, interface separation and crack bifurcation, have been reported to increase the toughness of the material [31, 49, 80, 84].

However, while these strategies have shown promise in improving impact resistance, it is important to note that the effectiveness of a particular toughening approach may depend on various factors, such as the specific composite material being used, the application, and the scale for which the composite is being designed. For example, manufacturing CFRP composites reinforced with CNT's that exhibit consistent material and strength properties continues to be a challenge, even when produced with the same manufacturing process by the same manufacturer [85], making them expensive, difficult to mass produce, and potentially unreliable. Whereas, particle toughening is well-established, however, challenges remain in the optimisation of the process and material characteristics rather than its industrialisation and that is where this review will continue to focus.

2.1.4 Damage Response Mechanisms in Epoxy Resin Systems

Epoxy resins are widely used to form the matrix of carbon fibre composites due to their high strength and adhesive properties [86]. Furthermore, they are relatively easy to process and thermally cure, so they are suitable for making high-quality components. However, their inherent brittleness due to their high crosslink density [87] limits their resistance to crack initiation and propagation [86, 88].

In polymers, as with all common engineering materials, it can be considered that there is an in-elastic process zone ahead of a propagating crack tip that transmits stress to the surrounding area [31]. The corresponding failure will involve a region with some degree of non-linearity [89]. In polymers, similarly to metals, a yield zone may be expected to form at the crack tip, notwithstanding the limits imposed by cross-linking. In the case of shear yielding, it may be considered that the damage zone resembles the plastic zone in metals because slip in metals and shear in polymers are governed by similar yield criteria [90]. Another form of non-linearity in polymers is craze yielding (crazing) associated with triaxial stress states, where microcracks bridged by resin ligaments form ahead of the crack tip in what may be represented as a Dugdale-type strip yield zone [90]. In terms of brittle epoxy resins, it has been reported that crazing may occur similarly to other plastics [91]. Despite contradictory research [92, 93], more recent work by

Henkee and Kramer [94] reported that there is a critical crosslink density at which crazing cannot occur (over 8 x 10^{25} m^{-3}), which was further confirmed by Lee and Yee [95] and is now considered a typical observation of neat thermosetting polymers such as epoxy [96]. Crazing offers one potential explanation for stick-slip crack propagation behaviour (termed 'pop-ins') observed in some studies [97, 98]. Crazes may create a bridged 'plastic zone' where the crack is arrested: when the stress increases, voids begin to form, reaching a critical size, and the crack then jumps forward [99].

2.1.4.1 Particle Toughening

One strategy for increasing the fracture toughness of CFRP composites is to incorporate secondary phases such as rubber particles, thermoplastic particles or hard particles dispersed between plies creating a distinct toughened matrix interlayer [15, 28, 31, 80, 84, 100]. However, incorporating rubber toughening particles has some trade-offs due to the decrease in both strength and stiffness of the epoxy resin matrix [101]. In contrast, the main advantage of using thermoplastics to toughen epoxy resins is that their incorporation does not result in significant decreases in properties such as stiffness and yield strength [102]. Furthermore, findings indicate that including hard particles such as silica nanoparticles can increase laminate strength and stiffness [100].

Toughening is reported in particle-toughened systems due to various mechanisms outlined and shown schematically in Figure 6. Crack pinning impedes the crack front and may lead to local bowing of the crack front between 'crack pins' or 'anchors', arresting the propagation of the crack [103]. Typically crack pinning occurs when the included particles are not smaller than the crack opening displacement [86, 100]. Particle-matrix debonding may relieve stresses by allowing the growth of energy-dissipating shear bands to form between adjacent particles [104-109]. Due to large hydrostatic stresses ahead of the crack front, voids may form [105, 107, 108], allowing the matrix, if it is capable of doing so, to plastically deform with subsequent void growth [110, 111], increasing the work done during failure [107]. Crack face bridging [36, 96, 103, 108, 112] and crack path deflection are also reported as potential toughening mechanisms [86, 103].

Adding thermoplastic modifiers to the brittle epoxy may allow for regions of high plastic deformation of the particles, *i.e.* where the thermoplastics undergo extreme permanent deformation [112]. The deformation, in turn, dissipates energy from the matrix, increasing the toughness of the composite.

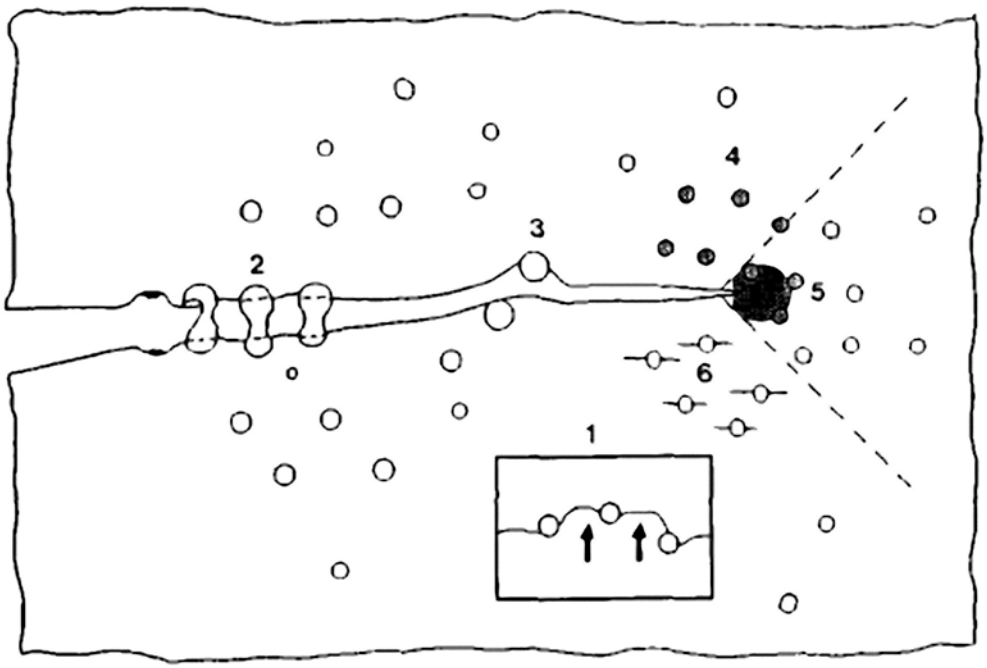

Figure 6 Schematic diagram of toughening mechanisms proposed for thermoplastic-modified epoxies: (1) crack pinning, (2) particle bridging, (3) crack path deflection, (4) particle yielding, (5) particle-yielding induced shear banding, and (6) microcracking[1] [112].

2.2 Crack Path during Mode I Delamination

Predicting the crack path in a carbon fibre composite is problematic due to the interplay of various damage mechanisms and any notional competition for the lowest energy crack path [113]. It has been previously reported that the addition of thermoplastic toughening particles to a CFRPs epoxy interlayer may increase impact damage resistance, residual compressive strength as well as delamination resistance [15, 58, 60, 80]. However, the direct toughening effect from the addition of toughening particles depends on the crack remaining within the toughened interlayer region, rather than taking an alternate crack path into the ply or fibre-matrix interface region [49]. Predicting and quantifying such behaviour is complicated by the structural hierarchy of the composite, *i.e.* fibre diameters are in the order of 5 – 10 µm, microscale toughening particles 5 – 20 µm [80], the ply 100 – 300 µm, the laminate in the range of several millimetres or above and the structural component 0.1 - 100 m [114].

[1] There is a distinction between microcracks and crazes. Crazing has a continuity of material across the craze plane. In contrast, cracks do not possess such continuity, furthermore crazed zones withstand bearing loads as opposed to cracked ones since crazed surfaces are bridged by many fibrils of 5 – 30 nm in diameter

2.2.1 Toughness Variation with Crack Path

Carolan *et al.* [50] and Tsang and Taylor [115] both investigated the use of nanoparticles to increase interlaminar fracture toughness in composites. Tsang and Taylor [115] found that the main mechanism leading to improved toughness in silica-modified epoxy was debonding of the silica nanoparticles and subsequent void growth in the epoxy polymer, in contrast to Carolan *et al.* [50], who reported that fibre-bridging was the dominant mechanism. Sprenger *et al.* [116] who also showed evidence of fibre-bridging offered a possible explanation which could help clarify these apparently conflicting results by reporting that the incorporation of silica nanoparticles in epoxy could lead to fibre-bridging resulting from particle cavitation. The agglomeration of particles near the fibre bed and subsequent delamination along the fibre-matrix interface leads to the cavitation of particles which in turn may then weaken the interface between the fibres and matrix, leading to fibre-bridging [116]. Work by Zeng *et al.* reports improvements in the interlaminar fracture toughness of composites by incorporating either rigid silica or soft rubber nanoparticles added to the matrices by up to 1.3 times and 2.5 times, respectively [117]. Nonetheless, the authors report fibre-bridging in the wake of the crack, where increasing the volume fraction of nanoparticles was reported to decrease the amount of fibre-bridging and the toughness, suggesting the toughening effect may be due to the transition of the crack to intraply and consequent fibre-bridging rather than particle toughening mechanisms. In further work on particle toughening, authors have reported increasing toughness behaviour due to the inclusion of TP's in the interlayer. However, upon further inspection of the results, it is mentioned that this behaviour is actually due to induced fibre-bridging [118]. Thus, while an increasing R-curve may be attributed to particle toughening mechanisms, it may be worth considering whether alternative dominant damage response mechanisms, such as fibre-bridging, could be responsible for the observed increase in toughness over length scales of tens of millimetres and further whether these mechanisms are desirable in specific applications.

Work by Kinloch *et al.* reports that introducing a hybrid toughed matrix using both a nano-silica phase and rubber-phase could increase the toughness of the composite by more than three-fold [119]. There was no mention of directly observed toughening mechanisms in this work. However, a more mechanistic study focusing on increasing interlaminar fracture toughness by dispersing Poly(phenylene oxide) particles reported interlaminar toughness was improved because of several toughening mechanisms. These included particle fracture (crack bridging), crack deflection, crack pinning, and resin hackles [120]. Toughness is also reported to be improved with an optimal loading level of 10 wt% and particle sizes ranging between 10 – 50 µm, increasing the Mode I and Mode II interlaminar fracture toughness by 65 % and 40 % respectively, compared to an untoughened system. When there is no inclusion of toughening particles, the crack is seen to run

along the fibre-matrix interface, which is reported to have a lower G_{IC} and G_{IIC} than the particle loaded systems. Conversely, when particle loading becomes high (15 wt%) or the particle size becomes large (>50 µm), the alignment of the plies became distorted, causing local stress concentrations in the ply, offering an alternative crack path into the weaker interface region. Furthermore, a thicker interlayer showed less crack deflection and arresting of the crack by the hard particles, also seemingly lowering toughness.

2.2.2 Mesoscale effects determining a crack path

Interleaved layers can be formed in a variety of ways, such as by adding short fibres, nanofibres, ductile sheets, or polymer particles to the interlayer region, which increases the thickness of the interlayer. In addition, the introduction of thermoplastic interleaves allows a reported plastic yield zone ahead of the crack tip within the interlayer, thus increasing the toughness of the composite [121]. However, when the plastic yield zone interacts with the fibre-matrix interface, the crack may then take the lowest energy path, as the cohesive strength of the matrix may be expected to be greater than the adhesion between the fibres and matrix, causing a crack to jump to the interface as shown in Figure 7 [121]. Yasaee *et al.* suggested that for a thin interlayer, the toughness may strongly reflect the bond strength between the fibres and matrix [121], rather than the properties of the interlayer *per se*.

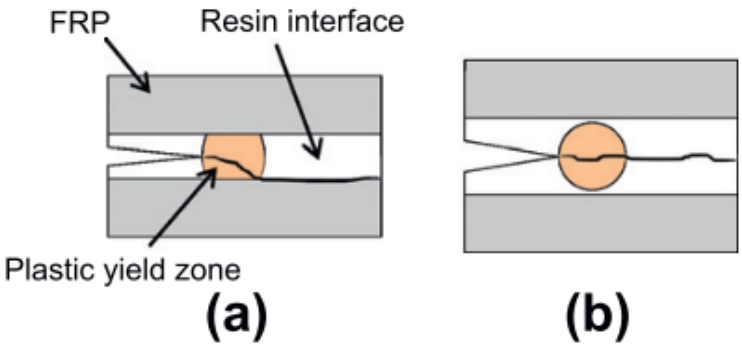

Figure 7 Plastic yield zone interaction with interleaf boundaries for different thicknesses (a) adhesive failure of resin and fibre and (b) cohesive failure of the resin. (Yasaee *et al.*) [121]

When incorporating toughening particles into a system, they may form a distinct interlayer between plies if the particles do not become part of the intraply by being sufficiently small to pass through gaps between fibres [122]. For example, Hayes *et al.* [122] found when comparing various rubber toughening particle sizes (19.2 – 55.6 µm) and concentrations (1.9 wt% and 3.6 wt%) that larger particle sizes increased the interlayer thickness. Additionally, higher

concentrations led to an agglomeration of particles, resulting in areas where the interlayer was much thicker. In contrast, there was an increase in the number of debonds and bridging fibres as the volume fraction and the particle size decreased, and the interlayer thickness became negligible, suggesting an interaction of the crack with the fibres.

2.3 Computational Modelling

When linear elastic fracture mechanics is applied in engineering applications to predict the strength of cracked structures, a knowledge of the crack-tip stress intensity factor as a function of applied load and geometry of the structure is implied [123]. In some cases, exact solutions to the elasticity problem are tabulated [124]. For more complex structures and loading conditions, an exact solution may not be available, so numerical methods (such as the FEM) are used to determine the stress state around the crack-tip. The contour integral method [125] can capture stress intensity factors around the crack tip. The disadvantages of this method are that the mesh must be refined around the crack to sufficiently resolve the stress singularity at the crack-tip [123], and it is not capable of modelling crack propagation. The virtual crack closure technique (VCCT) is a commonly used method for modelling crack growth problems. (VCCT) [126, 127] is a method used to calculate the energy release rates in 2D continuum and 3D solid finite element analysis from the computed forces and displacements. Issues have been reported to arise at bi-material interfaces due to the oscillatory component of a crack tip singularity [128]. Problems such as these with 'conventional' FEM analysis of cracks have been overcome in recent years using enhanced finite element methods, such as the eXtended finite element method (XFEM) [129] based on the partition of unity.

2.3.1 Cohesive Zone Model

Cohesive zone modelling (CZM) operates on principles first reported independently by Dugdale (1960) [130] and later, Barrenblatt (1962) [131], that there is a softening ahead of a crack tip in a given material where a notional crack opening is resisted by cohesive traction forces [132] as shown in Figure 8. The differences were that Dugdale assumed that stress is constant and equal to the yield strength of the material within the softening region, whereas Barrenblatt postulated that the stresses were variable.

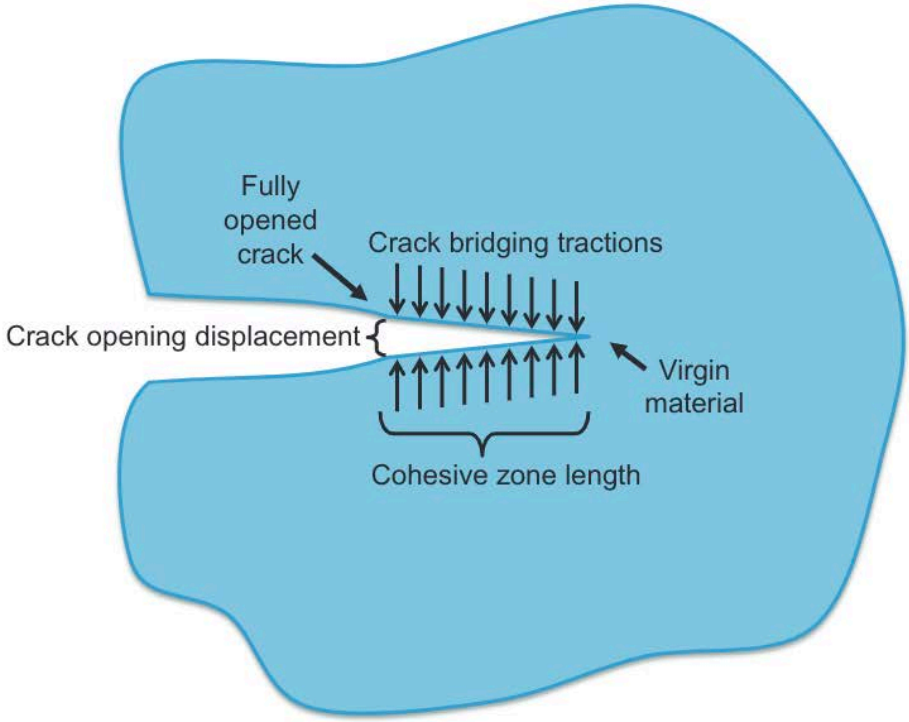

Figure 8 Schematic showing crack bridging tractions in the cohesive zone [132]

CZMs assume a non-linear traction-separation law defines the material response through the fracture process. Complete fracture corresponds to a return to zero traction at some finite crack opening displacement. The area under the corresponding traction-displacement curve is the absorbed energy obtained by the integration of stress. Thus, for a given traction-displacement curve shape, the displacement at failure can be set such that the energy absorbed per unit cracked area is equal to the material's critical strain energy release rate (CSERR), preserving the Griffiths energy balance [132], shown in Figure 9.

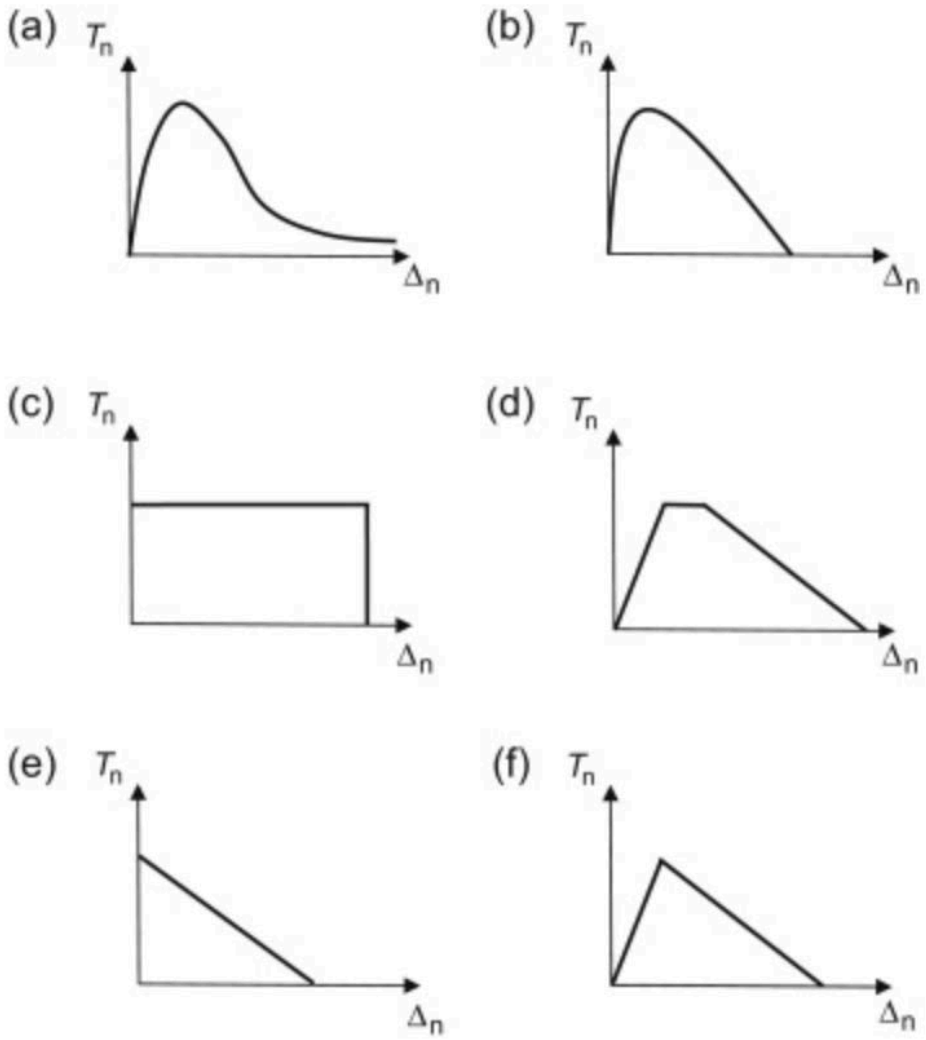

Figure 9 Different shapes of the cohesive traction-separation law [133]: (a) exponential [131], (b) polynomial [134], (c) constant [130], (d) trilinear [135], (e) linear [136] and (f) bi-linear [137].

Therefore, CZM may be used to predict both damage initiation and propagation of a crack. Typically for CFRP, a bilinear traction separation law is chosen [138]. It is necessary to have between two and three interface elements in the cohesive zone to accurately capture the softening ahead of the crack tip [139]. The cohesive zone size must be approximated to obtain an appropriate mesh size with minimal modelling iterations. Irwin's model [140] can calculate an assumed plastic zone around the crack tip as shown in Equation 2-1.

$$R_p = \frac{1}{\pi}\left(\frac{K_I}{\sigma_Y^*}\right)^2 \qquad 2\text{-}1$$

Where K_I is the Mode I stress intensity to propagate the crack in the material and σ_Y^* is the constant in-plane stress along the axis coincident and parallel to the crack tip within the plastic zone, which can be defined for plane stress or plane strain state. This model is valid under small-scale yielding conditions. An alternate theory is the Dugdale model, where yielding is assumed to occur in a narrow strip with zero height along the crack line and is treated as an extended part of the physical crack [141]. According to Dugdale's model, Equation 2-2 shows the length of the plastic zone, which is analogous to craze yielding in epoxy polymers.

$$l_{cl} = \frac{\pi}{8}\left(\frac{K_I}{\sigma_Y^*}\right)^2 \qquad 2\text{-}2$$

Yang *et al*. later proposed an alternative expression for the cohesive zone length for a delamination crack in a relatively slender body, as shown in Equation 2-3 [142].

$$l_{cI} = \left(E_I' \frac{G_{IC}}{\left(\sigma_{I,max}\right)^2}\right)^{1/4} h^{3/4} \qquad 2\text{-}3$$

Where *E'* is an equivalent elastic modulus, $\sigma_{I,max}$ is the peak Mode I stress in the cohesive zone, and *h* is the laminate half thickness.

2.3.2 eXtended Finite Element Method (XFEM)

With the XFEM, a crack arbitrarily aligned with the mesh can be modelled using enrichment functions [143] shown in Equation 2-4. The method uses the partition of unity property of finite elements that the sum of shape functions must be unity [144, 145]. Therefore, by using extra degrees of freedom at selected nodes the near tip, displacement fields can be included near the crack tip and along the faces [143].

$$\boldsymbol{u} = \sum_{I=1}^{N} N_I(x)[\,\boldsymbol{u_I} + H(x)a_I + \sum_{\alpha=1}^{4} F_\alpha(x) b_I^\alpha] \qquad 2\text{-}4$$

Where $N_I(x)$ is a linear shape function, $\boldsymbol{u_I}$ is the nodal displacement vector, and these terms apply to all nodes in the model. $H(x)$ is the Heaviside (jump) function, a_I is the enriched degree of freedom vector, and these terms apply to nodes whose shape function support is cut by the crack interior. $F_a(x)$ is the asymptotic crack-tip function, and b_I^a is the enriched nodal degree of freedom vector. These terms only apply to nodes whose shape function support is cut by the crack tip and only apply in *static* crack analysis; this term is ignored in propagation analysis, and the stress field around the crack tip is not explicitly modelled.

There are limitations to the XFEM, namely, only one crack or discontinuity per element can be modelled using a standard Heaviside enrichment function. However, with special treatment to the Heaviside function, coalescence can be accurately modelled [146]. Although, there are issues when bifurcation or coalescence of cracks occurs in interface elements due to specific functional forms of appropriate enrichment functions not being readily available and an excessively high enrichment level.

XFEM can be used with both the VCCT (XFEM-VCCT) and with CZM (XFEM-CZM) [138]. However, only the XFEM-CZM method will be considered from this point as it is most relevant to the work carried out and due to the following limitations of the VCCT technique: the oscillatory nature of the singular crack-tip stress field introducing numerical instability; and the assumption that the crack always grows in a self-similar manner (which is frequently not the case [142]).

2.3.3 Damage Initiation Criterion

Interface cohesive elements commonly take three forms, discrete non-linear springs connecting adjacent nodes [147] [148], zero thickness (or contact formulation), or solid but thin interface elements, which represent the resin-rich layer in-between plies [132]. A commonly used damage initiation criterion is the quadratic interaction of stresses, where the concept was first introduced by Hashin [149] and was applied to matrix failure by Brewer and Lagace [150] in the following form in Equation 2-5, where it showed an excellent correlation with delamination initiation stress data.

$$\left(\frac{\langle \sigma_I \rangle}{\sigma_I^{max}}\right)^2 + \left(\frac{\sigma_{II}}{\sigma_{II}^{max}}\right)^2 + \left(\frac{\sigma_{III}}{\sigma_{III}^{max}}\right)^2 = 1 \qquad 2\text{-}5$$

Where $\langle \cdots \rangle$ is the McCaulay brackets operator, σ_I the Mode I stress, σ_I^{max} the pure Mode I initiation stress, σ_{II} the resultant shear stress and σ_{II}^{max} the pure Mode II initiation stress. However, it is noted by Hashin that this criterion is not based on physical principles and represents the least complex fit to available data, therefore making it easy to use rather than representative of the actual physics of the system [149].

Alternatively, the maximum stress criterion is a linear, stress-based and failure mode-dependent criterion without stress interaction [151]. Unlike the quadratic criterion, the damage is initiated when the stress exceeds any of the following allowable stresses in Equation 2-6 [152].

$$max\left\{\frac{\langle \sigma_I \rangle}{\sigma_I^{max}}, \frac{\sigma_{II}}{\sigma_{II}^{max}}, \frac{\sigma_{III}}{\sigma_{III}^{max}}\right\} = 1 \qquad 2\text{-}6$$

Yang *et al.* [153] suggested a damage initiation criterion shown in Equation 2-7 for intraply cracks that accounts for the effects of tension normal to the fracture plane and in-plane shear stresses is suggested:

$$\left(\frac{\langle\bar{\sigma}_{22}\rangle}{\hat{\sigma}_n}\right)^2+\left(\frac{\langle\bar{\tau}_{12}\rangle}{\hat{\tau}_s}\right)^2=1 \qquad 2\text{-}7$$

Where $\bar{\sigma}_{22}$ and $\bar{\tau}_{12}$ are the transverse normal tensile stress and in-plane shear stress averaged over an element aligned with the local fibre direction and lying in the laminate plane. The material strength parameters $\hat{\sigma}_n$ and $\hat{\tau}_s$ are the maximum values of the Mode I and Mode II tractions in the respective cohesive laws. It should also be noted that although the form appears to be similar to Hashin's quadratic criterion above, the physical implications are significantly different. Each stress is the local stress at the tip of a cohesive damage zone which includes the constraining effect of neighbouring plies and non-linear shear effects, rather than the global laminar stresses as in Hashin's theory. Furthermore, the material strength parameters are obtained *in situ* for either tunnelling (interior ply) or surface channelling crack (surface ply).

2.3.4 Mixed-mode Fracture Criteria

Delamination onset has been considered to occur when the total strain energy release rate, G_T, (made up of the individual G components) reaches a critical ratio and can be expressed as a mixed-mode ratio in the form of $G_{I,\,II,\,III}/G_T$ [154-156]. When the ratio G_T/G_C reaches unity, the crack or delamination is propagated by either moving the mesh [157] or releasing nodal constraints [158, 159]. There are various ways to predict when a crack will propagate when $G_T \geq G_C$, and many have been previously reviewed by Reeder [160, 161]. Criteria recommended by Reeder are noted here for brevity and are shown in Table 1.

Table 1 Mixed-mode fracture criteria

Criterion Name	Criterion Equation 2D
Linear Interaction [162]	$\frac{G_I}{G_{IC}}+\left[\kappa-1+\varphi\left(\frac{1}{1+\frac{G_{II}}{G_I}}\right)\right]\frac{G_I}{G_{IC}}\frac{G_{II}}{G_{IIC}}+\frac{G_{II}}{G_{IIC}}\geq 1$
Bilinear Interaction [160]	$\frac{G_I-\xi G_{II}}{G_{IC}}\geq 1\ for\ \frac{G_{II}}{G_I}<\frac{\frac{1}{\zeta}G_{IC}+G_{IIC}}{G_{IC}+\xi G_{IIC}}$ $\frac{\zeta G_{II}-G_I}{\zeta G_{IIC}}\geq 1\ for\ \frac{G_{II}}{G_I}>\frac{\frac{1}{\zeta}G_{IC}+G_{IIC}}{G_{IC}+\xi G_{IIC}}$

Power Law [163]	$\left(\frac{G_I}{G_{IC}}\right)^{\alpha} + \left(\frac{G_{II}}{G_{IIC}}\right)^{\beta} \geq 1$
B-K Criterion [164, 165]	$\frac{G_T}{G_{IC} + (G_{IIC} - G_{IC})\left(\frac{G_{II}}{G_T}\right)^{\eta}} \geq 1$

The total strain energy release rate is artificially partitioned into individual components in various ways, and the constants and exponents are to be determined experimentally to obtain a fit for a failure locus plot of G_I vs G_{II}.

The linear interaction criterion is separated into three summed parts: pure Mode I; a mixed-mode term that is governed by an interaction parameter in square brackets; the larger the magnitude, the more one mode affects the other; and a pure Mode II term. The interaction criterion can model an increasing Mode I with Mode II. The values of κ and φ are to be determined experimentally for a given material system. The interaction criterion is complex due to the implicit function of G_{IC} and G_{IIC}.

The bilinear interaction criterion suggests a change in failure mechanism appears to take place in epoxy composites near a 1/1 ratio of G_I/G_{II}. An assumption is made that the response is linear in the two regions of the failure locus curves (*i.e.* either side of the 1/1 ratio). Therefore, the criterion depends on the material parameters ξ and ζ as well as the two pure mode toughness. If $\xi = \zeta = -G_{IC}/G_{IIC}$, the criterion reduces to the Power Law criterion with exponents equal to 1.

The Power Law criterion generalises the linear criterion allowing it to fit a wide range of material systems by determining the relevant exponents α and β. However, this criterion cannot model convex material responses near high Mode I regions of a failure locus curve (*i.e.* the Mode I component increases slightly with introducing a small amount of Mode II).

The B-K criterion measures G_I and G_{II} directly and η is a curve-fitting parameter. The proposed equation is a ratio of the total strain energy release to the critical Mode I CSERR, summed with the ratio of the total CSERR to the mixed-mode critical CSERR. The parameter η is determined for each material system empirically by fitting the curve to experimental data.

For each criterion, the parameters G_I and G_{II} must be partitioned for use in the above equations. There are two analytical ways of doing this, the global approach proposed by Williams [166] is based on beam theory and assumes the applied moments on a beam can be decomposed into the pure Mode I and Mode II components. Pure Mode I occurs when moments are equal and opposite. Pure Mode II occurs when the beam curvatures are equal. The second approach is a

local partitioning approach [167], which is carried out by obtaining the singular stress field distributions at the crack tip and solving for the decomposed stress intensity factors K_I and K_{II}; the relation between the CSERR and stress intensity factor is then used. The mathematical expressions of these approaches are summarised by Conroy *et al.* [168].

These criteria were initially introduced to a Mode I and Mode II domain due to the limitations of standardised test methods [161]. However, there now exists standardised tests for pure Mode I loading (ASTM D5528) using the DCB test [70], pure Mode II loading (ASTM D6671 / D6671M), the End Notch Flexure (ENF) Test (ASTM D7905 / D7905M) [169], mixed-Mode I/II the Mixed-Mode Bending (MMB) Test [170]. However, there are only suggested methods for pure Mode III [171, 172]. The issue remains that there is no reliable test for mixed-mode testing of all three damage modes. Therefore, the 2D criterion needs to be extended for use in 3D. The Power Law is easily extended to 3D by adding an extra G_{III} ratio with another exponent to be fit by empirical means [173].

The B-K criterion has been reported to fit the 2D data well [161], making it an obvious candidate for a 3D model. Due to the lack of three-dimensional mixed-mode data, an assumption is made that the Mode III response is similar to the Mode II response as they are both shear types of loading. Linear interpolation is used to establish the Mode III component of the mixed-Mode term leading to the 3D B-K fracture criterion in Equation 2-8:

$$\frac{G_T}{G_{IC} + \left((G_{IIC} - G_{IC}) \frac{G_{II}}{G_T} + (G_{IIIC} - G_{IC}) \frac{G_{III}}{G_T} \right) \left(\frac{G_{II} + G_{III}}{G_T} \right)^{\eta - 1}} \geq 1 \qquad 2\text{-}8$$

It should further be noted that under pure Mode I, conditions both criteria simplify to Equation 2-9:

$$\frac{G_I}{G_{IC}} \geq 1 \qquad 2\text{-}9$$

2.3.5 Modelling crack transition

2.3.5.1 Micromechanical contributions to crack path transition

One of the significant limitations of XFEM is that it cannot model multiple cracks initiating in a timestep when another crack in the enriched zone is simultaneously propagating. This limitation makes it challenging to model migrating delaminations seen experimentally in multidirectional laminates [174-176] but is also relevant to delamination migration across other interfaces. Successful attempts have been made to resolve this issue by modifying the formulation of the

Heaviside function [177] and by using other more advanced formulations such as the augmented-finite element method (A-FEM) [178].

In work on modelling the crack path of particle-toughened systems during tensile opening loading using A-FEM by Borstnar *et al.* [49], it was reported that the crack propagation path in the interlayer was initiation controlled with the strength of the toughening particles playing a more significant role than their absolute toughness. Weak/debonding particles were reported to reduce stresses at the fibre interface, which prevents the crack from migrating to the fibre interface region and remaining in the PT interlayer. A key finding in this study was that small, closely spaced particles further from the interface region favoured interlaminar fracture, while particle-depleted regions triggered fibre interface failure, resulting in the propagation of the crack along the fibres. In addition, a lower volume fraction of readily debonding particles was reported to increase the stress in the neighbouring ply, triggering fibre interface failure.

These findings are in common with later work by Xie and Koslowsk, who instead used a phase-field damage model (PFDM) to simulate the interlaminar fracture of a particle-toughened CFRP composite in 2D [179]. In PFDM, the surface of the set of discrete cracks is replaced by a phase field. The phase field represents the amount of damage introduced in the material, with a value of 1 when the damage has developed into a crack and less than 1 when it can still bear stress [180]. The elastic constants of the particles were varied, as were surface energies of the particle-matrix and fibre-matrix interfaces to study their effects on the crack path within the interlaminar region. The study shows that failure in the interlayer is a heterogeneous process with a distributed onset of damage ahead of the crack tip, where cracks are initiated at sites ahead of the main crack and crack branching is observed, with further advancement of the crack as they then coalesce. This agrees with findings from Borstnar *et al.* [49] which also suggest a distribution of debonds and microcracks ahead of the crack tip, which then coalesces as the crack is driven, forwards. There is competition between the interfacial failure between the fibre-matrix and particle-matrix interface. Moreover, in particle-depleted regions, the crack is seen to be driven towards the fibre-matrix interface. When the particles are stiffer than the matrix, the fibre-matrix interface becomes a preferential path for the crack by the nucleation microcracks ahead of the crack tip, creating extensive delamination zones, again agreeing with the work by Borstnar *et al. [49]*.

2.3.5.2 Combined Crack Modelling Approach

An alternative way to model multiple delamination paths and coalescence between them is to combine crack modelling techniques such as XFEM and CZM to combine the strengths and

mitigate the weaknesses of both [181-184]. For example, CZM can only be used to model crack growth along a planar path known *a priori*, and it is not suitable for modelling crack growth where the onset and delamination direction in a bulk material is unknown. Conversely, XFEM allows for solution-dependent crack growth allowing initiation and growth in the bulk of the material. The disadvantages, though, are it shows slower convergence and increased simulation time, the crack cannot run along the interface of elements and crack bifurcation and coalescence are not possible [138, 184]. However, by combining the two approaches, cohesive elements can be used to simulate crack growth along the interface regions of the specimen, and XFEM can allow for cracking in finite elements where for example, coalescence between two competing crack paths may occur, or there is damage in the bulk of specimen [184].

A combined cohesive surface – XFEM approach has been reported for modelling a single adhesively bonded lap joint [183]. The bulk adhesive was enriched using XFEM, and the interface between the bulk adhesive and composite was modelled using cohesive elements showing the two numerical regimes could be successfully integrated [183]. The cohesive elements are of zero thickness due to being negligibly thin compared to the bulk adhesive and having differing traction separation properties as the adhesion to the ply is likely to be different to the cohesion of the adhesive. This approach is limited; the crack can transition from the XFEM region to the cohesive surface. However, once propagating in the cohesive surface region, the XFEM crack does not grow. This may be due to crack shielding however, the crack path should be known *a priori* to validate this method.

Work by Cicco and Taheri [184] modelled delamination and crack transition in a DCB specimen under Mode I loading and delamination-buckling of a 3D fibre metal laminate under axial impact loading. The authors used zero-thickness cohesive elements to model interface delamination between the interlayer, and the crack growth in the interlayer was modelled using XFEM. When the combined approach was compared to just using XFEM, it was found to capture crack kinking observed in experiments, which could not be captured by using XFEM exclusively. The authors also found that XFEM was generally the most accurate method of simulating crack growth; however, cohesive elements were deemed preferable in regions where the crack path is known *a priori* to reduce simulation time and increase the convergence rate.

The advantage of using the combined approach over methods such as A-FEM is that the CZM and XFEM and readily available using commercial software packages. Furthermore, it has been shown that it is an effective and computationally efficient method for modelling complex crack interactions and transitions between different potential delamination paths.

2.4 X-ray Computed Tomography

2.4.1 Micro-focus Computed Tomography Overview

The fundamental components of a contemporary XCT scanner are shown in Figure 10. First, an X-ray source produces a cone beam which is then attenuated by a sample, set on a rotating stage. The object is then projected onto a detector where the image is processed, reconstructed (see Section 2.4.3.2) and displayed as a series of slices in the x, y, and z coordinates axis directions, thus forming a 3D representation. In this section, the full operation of an XCT scanner will be explored, including how the X-rays are produced, how they are detected and factors limiting voxel size. Furthermore, the reconstruction and processing of the image will be discussed.

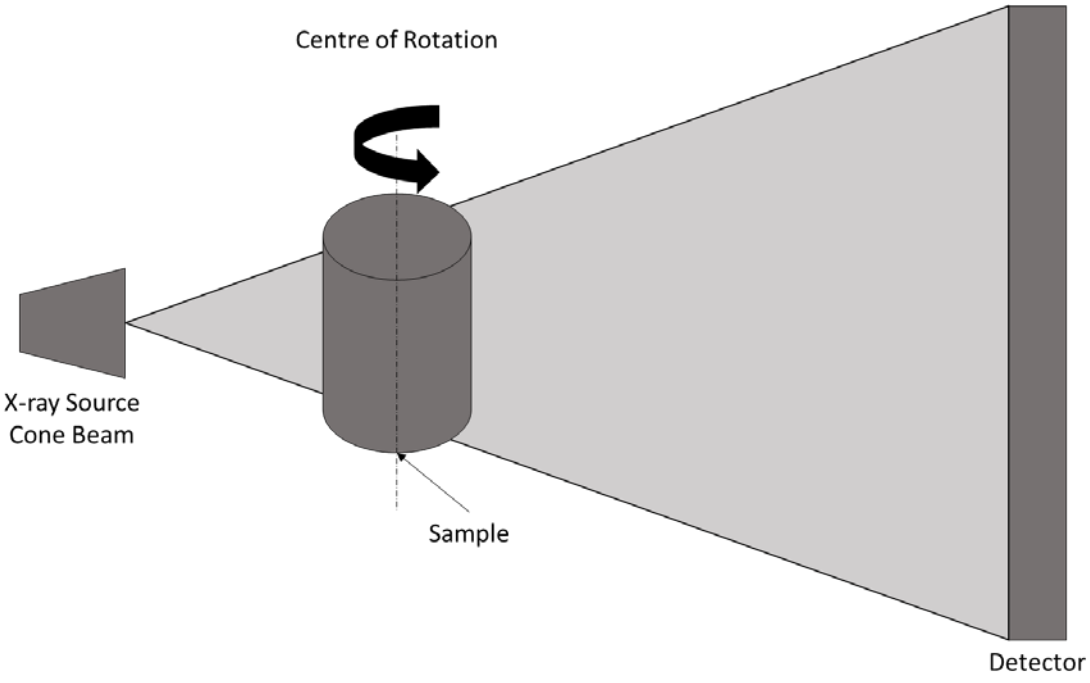

Figure 10 Basic operating method for a micro-focus CT scanning system.

2.4.2 Operation of Micro-focus Computed Tomography

X-rays are produced by accelerating a concentrated high-energy beam of electrons at a rotating or reflective target (commonly tungsten). The target rotates to distribute the heat, so the target does not melt as well as having an internal cooling system to conduct the excess heat away in both cases [185]. At an atomic level, two mechanisms occur during this process. Electrons on the tungsten target are ejected; therefore, electrons with a higher energy level fill these lower energy

holes. The excess energy from this process is then emitted as an X-ray of energy specific to the excess energy emitted from each electron [186]. Also, electrons within the focused beam may interact with the nuclei of atoms in the target, resulting in a deceleration, therefore producing a spectrum of X-rays of varying energies termed Bremsstrahlung X-rays. Therefore, a spectrum of X-rays is produced in laboratory scale X-ray CT machines, with intensity spikes, otherwise known as characteristic X-rays, due to the dominant mechanism of high-energy electrons filling holes [186].

2.4.3 Creating an Image

2.4.3.1 Attenuation

Once produced, X-rays travel through the sample and are absorbed by the different materials/phases. When an X-ray photon interacts with an atom, it will attenuate the primary X-ray beam following the Beer-Lambert Law. Therefore, the absorption can be expressed as a line integral of the attenuation coefficient [187], as shown for a monochromatic X-ray source in Equation 2-10, and the expression for a polychromatic source is shown in Equation 2-11.

Monochromatic $$I = I_o e^{-\mu \Delta x} \quad (2\text{-}10)$$

Polychromatic $$I = I_o \int w(E) e^{-\mu(E)\Delta x} dE \quad (2\text{-}11)$$

Where I_o is the intensity of the incident X-ray, μ is the attenuation coefficient, Δx is the specimen thickness, $w(E)$ is a function expressing the incident X-ray spectrum, and I is the intensity of the X-ray being detected. The detector records the intensity, where each voxel in the reconstructed 3D image represents the average attenuation within that volume of material, based upon the attenuation of each 2D radiograph [188].

2.4.3.2 Reconstruction of an Image

A 3D image is built up by taking a finite number of 2D projections about a 360^o rotation angle. Each pixel has an attenuation related to the material density and thickness at that point and can be represented mathematically as a Radon Transform. A Radon transform performs line integrals in the plane of a 2D image projection, the line integrals are mapped with respect to the position s and angle ϑ shown in Figure 11. Therefore if Beer-Lambert's Law gives the intensity of a line through a sample, by rotating the sample to different angles, a number of line integrals will represent the 2D intensity. It is the Radon transform that maps these line integrals giving the 2D image data. Mathematically, the Radon Transform can be expressed as seen in Equation 2-12.

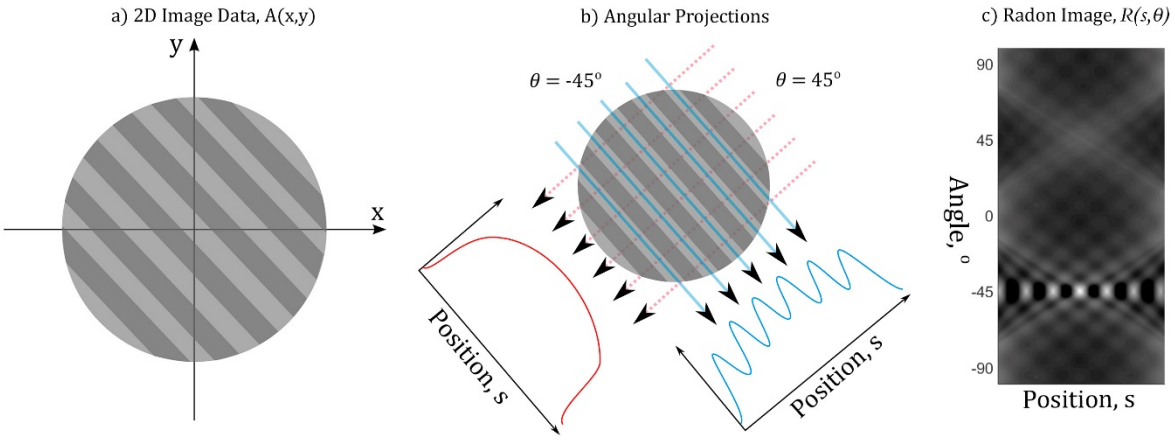

Figure 11 Schematic diagram showing the principle of Radon transform analysis of a structured 2D image dataset via pixel summation along different projection angles. c) shows the full sinogram, demonstrating image structure at -45° (Image reproduced with permission from the author) [189].

$$\mathcal{R}(r,\theta) = \int_{-\infty}^{\infty}\int_{-\infty}^{\infty} f(x,y)\delta(x\cos\theta + y\sin\theta - r)\,dx\,dy \qquad 2\text{-}12$$

Where θ is the angle of the line from the x-axis, and *r* is the perpendicular offset of the line. Therefore, to reconstruct an image, an Inverse Radon Transform must be applied [63]. A commonly used method is a reconstruction algorithm called Filtered Back Projection (FBP). FBP back projects each successive 2D radiograph 'slice' onto the 3D volume [190]. Firstly, the back projection is applied and is defined in Equation 2-13:

$$f(x,y) = \int_{0}^{\pi} f'(x\cos\theta + y\sin\theta)d\theta \qquad 2\text{-}13$$

The inverse transform (back projection) gives a blurred version of the desired image. The image can then be unblurred using a 2D ramp filter. 2D filtering is computationally intensive, so reversing these steps is preferable. Alternatively, reconstruction may directly use the central slice theorem, which states that the 1D Fourier transform with respect to *r* of $\mathcal{R}(r,\theta)$ is equal to the central slice at an angle θ of the 2D Fourier transform of *f(x,y)*, *i.e.* as mathematically shown in Equation 2-14:

$$\mathcal{F}[\mathcal{R}(r,\theta)] = \mathcal{F}_2\left[f_x\cos\theta\,, f_y\sin\theta\right] \qquad 2\text{-}14$$

A disadvantage of this method is that it requires a large number of projections to form a comprehensive set of data. Alternatively, iterative reconstruction tools may be used to compensate for missing data [187]. An iterative algorithm requires multiple reconstructions. Like any iterative technique, an initial solution must be found. Then through sequential iterations, the

solution converges to an adequate output. Iterative methods are computationally much more expensive than FBP, which only requires a single reconstruction.

2.4.4 Noise and Imaging Artefacts

With laboratory-based XCT being more extensively used, it is important to understand artefacts that may arise unique to this imaging method to distinguish them from real features and to optimise the experimental design for image quality [191]. Imaging artefacts arising from limited X-ray flux, polychromatic radiation (laboratory-based systems), finite resolution, discrete sampling, and X-ray scatter will be identified and discussed [191].

2.4.4.1 Noise

Noise is the statistical uncertainty in the image due to the finite number of X-ray photons detected. It also varies across the image, being the greatest (generally) in the centre of the specimen [192]. While not commonly considered an artefact *per se*, noise can significantly impact the quality of the image, resulting in the feature being more difficult to segment, a rough texture on surface-rendered images and small features (relative to the image, *i.e.* a few voxels) not being visible. Therefore, the signal-to-noise ratio (SNR) should be maximised to increase image quality. In practice, this means increasing the number of X-ray photons hitting each detector element, increasing the source-to-object distance while reducing the source-to-detector distance and increasing the spacing between detector pixels (this could be done in practice by binning the detector which averages a set of 2 x 2 pixels to form a single pixel; this also halves the resolution). Mathematically the relationship can be seen in Equation 2-15 and Equation 2-16 [192].

$$R = d\frac{S}{D} \tag{2-15}$$

$$Noise \propto \frac{1}{R\sqrt{n}} \tag{2-16}$$

Where *R* is the ray spacing, *d* is the detector element spacing, *S* is the source-to-object distance, *D* is the source-to-detector distance, and the image noise is proportional to *n*, the square root of the number of X-ray photons detected per detector element.

2.4.4.2 Angular Undersampling

In theory, the number of projections required to sample an object fully should be the maximum specimen dimension in voxels multiplied by $\frac{\pi}{2}$, *i.e.* to fully sample an object that fills a 2000 x 2000 detector would take 3142 projections [193]. This also has implications for scanning an ROI, where the sample width (in voxels) is more than that of the detector, which in turn leads to a greater

number of projections based on the same principle. However, in practice, the number of projections may be reduced with no noticeable effect on the image quality, although reducing the number of projections may increase the SNR, as it reduces the overall exposure. Therefore, if scan time needs to be reduced, reducing the number of frames (averaged) per projection may be preferable.

2.4.4.3 Ring Artefacts

Ring artefacts result from the difference in sensitivities between adjacent detector elements, if these elements remain in the same place for the whole scan they are manifested as circular streaks or rings when back-projected [191]. However, these rings are reinforced more strongly towards the centre of the specimen when projections are summed as the path through the centre sees fewer X-ray photons being detected by each detector element. Ring artefacts can be reduced by moving (shuttling) the sample or the detector. Shuttling means the reinforcement of these artefacts is broken up, reducing the severity of the ring artefacts.

2.4.4.4 Movement Artefacts and Centre of Rotation Error

Movement artefacts can be caused by the movement of the specimen during scanning. This tends to be more of an issue at higher voxel resolutions, where a slight movement accounts for a finite voxel width. Movement artefacts manifest as double edges at 180^{o} degrees from the first projection, and the edges no longer line up.

Centre of rotation (COR) error appears in a similar way superficially as double edges. With COR error, the distance between the double edges is constant around all edges, whereas varying distances or breaks in the double edge would indicate the movement of the sample. COR error is caused by the COR not being correctly determined after scan acquisition, and other artefacts such as beam hardening, movement, and scatter can make finding the COR more challenging [191].

2.4.4.5 Beam Hardening

Beam hardening occurs in laboratory-based XCT due to the polychromatic cone beam and occurs due to the attenuation of lower energy X-rays in the spectrum. Consider a cylindrical sample of uniform density. The path through the centre of the sample is shorter than the path that intersects the edge of the sample. The lower energy X-rays in the spectrum are attenuated more over a greater path length, meaning fewer X-rays are detected at the edge of the sample compared to the centre. This results in a greater hardening of the beam around the edge of the sample resulting in a dishing effect where the specimen appears to be less dense in the centre [191]. Furthermore, if there are highly attenuating features in the specimen, they can cause

streaking, which obscures features and make the distinction between adjacent highly attenuating regions less obvious. Beam hardening can be corrected by linearising the projection data using a calibration curve which can be theoretically or experimentally derived [194, 195]. Alternatively, the best fit to the data can be found through presets included within modern reconstruction software. Secondly, filtering the beam using a filter material [194] (for example, 2 mm of copper) can filter out low-energy X-ray photons hardening the beam. It should be noted that the optimum material used for filtering and its thickness depends on several parameters such as beam power, the density of the specimen, dimensions of the specimen, the XCT enclosure, and manufacturer guidance or specification. Filtering can also increase the SNR due to decreasing the intensity of the beam or increasing the scan time (if exposure or gain is increased to compensate for the reduced SNR).

2.4.5 Image Resolution

There are some important terms to define when determining the resolution of an XCT scan. The spatial resolution describes how far two features in an object need to be separated to be distinguishable in the resulting image [196]. Rueckel *et al. [196]* explored influenceable effects on the spatial resolution of an XCT system. At high magnifications (a voxel size of 3.25 µm), the spatial resolution was strongly influenced by the focal spot enlargement of the X-ray tube depending on the applied tube power. Therefore, at high resolutions (*i.e.* where the voxel size is in the same order of magnitude as the focal spot size), the power applied must be carefully considered as it can become the limiting factor in spatial resolution.

The voxel size is determined by the number of pixels on a detector and the FOV, therefore in laboratory XCT which emits cone beams moving the sample relative to the source and projector can change the magnification and hence the voxel size, whereas for parallel beam CT the beam itself must be narrowed or widened to vary the voxel size. For example, if a sample with a width of 20 mm were to fill the field of view on a 2000 x 2000 pixel detector, the maximum voxels size would be 10 µm. Modern micro-focus CT systems can attain voxel resolutions as low as < 1 µm [63].

2.4.6 Advances in XCT Imaging of Fibre Reinforced Composites

Optimising XCT scanning parameters is essential for obtaining images that can distinguish between (dependent on scan resolution) material constituents such as the resin matrix, individual fibres, and matrix cracks [197-199]. Work by Zwanenburg *et al.,* systematically varied seven XCT parameters resulting in 168 scans [197]. The most significant parameters in improving scan quality

were reported to be voltage and source-to-detector distance. This would suggest where possible, the voltage should be minimised and source to detector distance maximised to improve scan quality, notwithstanding the resulting increase in scan time.

Analysis such as mapping fibre orientation can require high-resolution scans between 5 – 30 µm's depending on whether individual fibres or ply orientations are to be characterised which can significantly limit the FOV [200]. To overcome this limitation XCT scans can be stitched together to cover a larger FOV. It is this method that allowed for the characterisation of the orientation of thermoplastic reinforced with short aligned fibres through the each step of a filament forming process and therefore, allowing critical insight into how the fibre orientation varied through the process [201]. However, this method of stitching and/or concatenating XCT scans can also result in significantly longer scan times and can result in extremely large datasets which may be challenging to process.

Further novel applications include X-ray directional dark-field imaging which is a technique that reveals small-scale structural properties including anisotropic structure orientation, which may be invisible in a conventional imaging system [202]. Smith *et al.,* presented an algorithm allowing for extraction of directional dark-field signals from X-ray speckle-based imaging. The method was found to accurately detect and quantify fibre orientation in CFRPs within one degree. There was also found to be a trade-off between increasing measurement accuracy at the expense of image resolution through varying reconstruction parameters.

XCT can also be used for digital volume correlation (DVC) [203]. DVC is a novel method used to calculate local displacements in 3D images, often obtained from XCT experiments [203]. Schöberl *et al.*, [204, 205] utilised DVC with SRCT to analyse CFRPs under quasi-static tensile loading where Barium Titanate particles were used as fiducial markers. By tracking the displacement of these markers, high-resolution 3D strain measurements during fibre failure events could be visualised allowing for the validation of micromechanical models. This work was the first application of DVC to SRCT imaging of CFRP failure achieving significantly higher resolution than reported in previous literature [206].

2.5 Conclusions

The literature review indicates that predicting failure in composites is essential to optimise lightweight composite components. Predicting the resultant toughness from the crack path and toughness response mechanisms resulting from loading CFRP's can be complex due to the interaction of mechanisms between different length scales. BVID is a significant concern for composites in applications such as aircraft structural components, wind turbine blades, and composite wheels for Formula One Cars as subsurface delaminations can be troublesome to detect, detrimental to the material's compressive strength, and lead to unexpected failure during service. The area of damage is reported to correlate with the loss in residual compressive strength and an intrinsic link between a CFRP's ability to suppress interlaminar delamination initiation and growth, impact damage area, and post-impact residual compressive strength has been suggested. As a result, improving Mode I and Mode II interlaminar fracture toughness of CFRP's remains an area of continued interest to prevent catastrophic failure and improve the efficiency in the design of CFRP composite, particularly in relation to Mode I loading as it exhibits the lowest critical fracture toughness.

To improve the interlaminar fracture toughness of composite systems, secondary phase toughening particles can be dispersed throughout the interlayer, with the fundamental purpose of reducing the delamination damage in the composite. Toughening particles form a distinct interlayer which can vary in thickness depending on particle size and loading. Furthermore, toughening mechanisms are reported to vary depending on the local distribution of particles where small (20 – 50 µm) evenly spaced toughening particles are reported to favour the crack remaining in the particle-toughened interlayer, furthermore increasing the reported G_{IC} and G_{IIC} of the system. The resulting interlayer geometry variation as a consequence of uneven particle loading, large toughening particles, or high *Vf* can cause misalignment of fibres and stress concentrations in the matrix-fibre interface. This is reported to lead to a crack transition to the matrix-fibre interface and reduce the reported interlaminar fracture toughness of the material system.

Predicting the crack path in fibre reinforced composites is complex due to the interplay of various damage mechanisms and the competition for the lowest energy crack path. The addition of toughening particles to a composite's epoxy interlayer may improve impact damage resistance, residual compressive strength, and delamination resistance, but the direct toughening effect depends on the crack remaining within the toughened interlayer region. Understanding and quantifying this behaviour is challenging due to the structural hierarchy of the composite. Some

studies looking at particle toughening using nanoparticles produce seemingly conflicting observations, with some attributing the toughening effect to fibre-bridging and others to toughening particle related mechanisms such as particle fracture, crack deflection, and crack pinning. Another effect of incorporating interleaved layers is increasing the thickness of the interlayer. The introduction of thermoplastic interleaves has been shown to allow for a plastic yield zone ahead of the crack tip, increasing the toughness of the composite, however, if the plastic yield zone can interact with the fibre-matrix interface, the crack could transition to the fibre interface, therefore, for a thin interlayer, the toughness may reflect the bond strength between the fibres and matrix rather than the properties of the interlayer.

Various modelling techniques such as XFEM and CZM have been employed in literature to model progressive damage in CFRPs. One of the significant limitations of the XFEM method is its inability to model multiple cracks initiating in a timestep or the presence of multiple cracks in a single element. This limitation makes it challenging to model the coalescence and bifurcation of delaminations which are seen experimentally. Several methods have been proposed to model complex crack interactions such as the A-FEM and PFDM which have been used to look more specifically into micromechanical contributions to interlaminar fracture strength and toughness under Mode I loading. Both studies suggest that failure in the interlayer is a heterogeneous process with a distributed onset of damage ahead of the crack tip, where cracks are initiated at sites ahead of the main crack and crack branching is observed, with further advancement of the crack as they then coalesce. There is also reported competition between the failure of the fibre-matrix and particle-matrix interfaces and hence the preferential delamination path. Variables affecting crack path transitions were reported to be particle distribution, spacing, and size where optimisation of the parameter could alleviate the stress in the matrix-fibre interface and keep the crack in the interlaminar region of the composite. Furthermore, there is experimental evidence to back up these findings in the form of *in situ* high-resolution XCT.

Alternatively, multiple cracks can be modelled using existing modelling frameworks such as a combined approach using CZM and XFEM. This allowed for the modelling of multiple delamination paths and subsequent coalescence between them. This approach was found to be successful in modelling delamination and crack transition in a DCB specimen under Mode I loading and in delamination-buckling of a 3D fibre metal laminate under axial impact loading. The combined approach was found to capture crack kinking observed in experiments, which could not be captured by using XFEM exclusively. Cohesive elements were deemed preferable in regions where the crack path is known *a priori* to reduce simulation time and increase the convergence rate.

Finally, an overview of XCT as an imaging technique used to visualise CFRPs has been reviewed. Recent advancements in the state-of-art applications have been highlighted, including: optimisation of imaging parameters such as voltage and source-to-detector distance; concatenation and stitching of high-resolution images to characterise fibre orientations with a larger FOV; dark field imaging to reveal structural orientation of samples which may not be visible using conventional means; and high-resolution 3D strain mapping during CFRP failure using DVC in conjunction with SRCT.

The work presented in this thesis aims to progress the analysis carried out identifying the effects of microscale toughening mechanisms. The current work will consider the crack transition in standard interlaminar fracture toughness test specimens. Toughening mechanisms arising from geometric variation of the interlayer caused by factors such as the distribution of toughening particles, resin pockets, and tow gaps will be considered as will the inherent 3D nature of crack propagation. The dominant damage mechanisms at the ply scale of a composite will be analysed using a combined CZM and XFEM approach, making it reproducible in commercial FE software. XCT will also be used to analyse and quantify specifically the interlayer geometry and variation informing the FEM and analysing how these factors affect the crack path and the resulting toughness of a composite system.

Chapter 3 Delamination Path Transitions in Particle-Toughened Fibre Reinforced Polymer Composites

3.1 Introduction

In many applications of composite materials both damage resistance and damage, tolerance are important in maintaining structural integrity and complying with relevant standards. Delamination is a key damage mechanism for laminated composite materials. The interlaminar toughness response of carbon fibre reinforced polymer composites is determined, in part, by the crack path. Furthermore, if the crack path leaves the interlaminar region and enters the adjacent plies, fibre-bridging can result, which can enhance the apparent interlaminar toughness, but also can distort measurements obtained from standard test methods. The incidence of fibre-bridging during the standard Double Cantilever Beam (DCB) test is recognised as a potential artefact of the interlaminar fracture toughness test as it indicates crack propagation in the ply [70]. For this reason, there is a particular emphasis put on the initiation Critical Strain Energy Release Rate (CSERR) for evaluating toughness, as it is considered a better, and more conservative, reflection of the *in situ* toughness of the interlayer, which is most suitable for design and material qualification purposes [207]. However, in many practical applications, it is not only the initiation toughness that is significant for performance but also how the toughness varies with increasing delamination lengths, *i.e.* the delamination resistance curve or R-curve [37, 208, 209]. For example, analysis of compression after impact has shown that the inclusion of toughening particles in the interlayer reduced the extent of delaminations during the initial impact, and, increased the residual strength of the composite compared to the tested untoughened systems by up to 60% upon compression, *via* mechanisms such as particle bridging ligaments [26]. It was also highlighted by Bull *et al.,* that the toughness of the composite system plays a role in damage tolerance after an initial impact, initiating subsurface delaminations [60]. Therefore, an understanding of the mechanisms leading to the often seen (when large-scale bridging is not observed) fall in propagation toughness relative to the critical initiation toughness, resulting from interlayer toughening (or lack thereof), could contribute to improved residual strength properties of composite parts. It is the propagation Strain Energy Release Rate (SERR), which may be viewed as a more accurate reflection of the toughness when delaminations have already been initiated and further propagate, and analysis of the crack path throughout with varying toughness could give a better indication of where the crack would be likely to propagate in real loading situations [210]. So, both the suppression of delamination as well as the ability of a composite to carry load while

damaged are significant, which is similarly reflected in airworthiness standards and considered for civil infrastructure such as wind turbines [211, 212]. It is also well documented that oblique fibre-bridging can lead to rising R-curve behaviour [69, 78]. A reliance on fibre-bridging may not be practicable as crack opening displacements in real applications of concern may not be large enough to facilitate a strong effect and it may not arise in situations where it is expected [210]. It is also worth noting that fibre-bridging may also depend on the orientation of adjacent plies. The variability in toughness due to crack propagation makes the DCB test valuable in studying methods of understanding and potentially controlling the crack path.

In terms of improving materials performance, interleave toughening methods such as the incorporation of thermoplastic toughening particles, may modify the properties of otherwise brittle epoxy matrices as well as introduce additional damage response mechanisms aiming to increase the toughness response and maintain the crack within a toughened interlayer. Toughening mechanisms are well documented in the literature. These include but are not limited to, particle-matrix debonding, particle deformation, particle yielding, crack bridging, and crack pinning [47, 49, 100, 105, 107, 111, 122, 179, 213]. From recent work, a process zone ahead of the crack tip has been identified in particle-toughened systems which can lead to debonding at the interfaces of material constituents such as toughening particles and fibres [31]. Previous work has suggested that it is direct competition in this region beyond the crack tip which is involved in determining the crack path and hence whether the crack propagates in the ply of a composite leading to oblique fibre-bridging, or remains in the particle-toughened interlayer [31, 49].

This study considers Mode I delamination and the effect of local crack paths on the apparent toughness of a material. By carrying out DCB tests on a range of particle-toughened and untoughened materials systems with varying particle, resin and matrix types, toughening mechanisms observed and reported in the literature are examined, to explore the factors affecting the material toughness. X-ray computed tomography (XCT) and crack surface fractography will be used to track crack path progression during the DCB testing. As such, this work aims to link and expand upon previous research carried out on the micromechanical contributions to crack path transitions, dominant damage response mechanisms, and the overall toughness response of a range of CFRP systems [31, 49].

3.2 Materials and Test Method

Particle toughened CFRPs were supplied by Solvay Composite Materials are shown in Table 2, where each material system differs by either the particle, matrix or fibre type. The mean thickness for each material system has also been reported. The materials were cured via a proprietary

aerospace autoclave cycle. DCB specimens were prepared, conforming to ASTM D5528 [70], consisting of a 26-ply unidirectional layup, with a 25 mm wide, 40 µm thick, polytetrafluoroethylene (PTFE) insert placed at the mid-plane in order to control the initiation of fracture. Specimens were a standard size of 254 mm length, 25 mm width x 5 mm thickness. Secondary phase particles were dispersed in the interlayer of several of the materials, where the nominal v_f (volume fraction) is proprietary.

Double cantilever beam tests were carried out in accordance with BS ISO 15024 [71] and ASTM D5528 [70] using an electromechanical tensile testing machine (Instron 5569) with a 5 kN load cell. The wedge opening method was used to introduce the pre-crack for all material systems for consistency and followed the guidance set out in the standards, the crack propagated beyond the insert by ≈ 15 – 20 mm. A minor modification to the test standard was made by using "stirrups" to introduce loads to the samples. A small 3 mm diameter hole was drilled through the width of the specimen along the central plane 45 mm from the end of the insert. Two stirrups were inserted into the specimen supported by a thrust bearing to allow for axial alignment of the sample. This method does not require any parts to be adhered to the specimen, it also does not result in a shortening of the moment arm due to bending and allows for rapid changeover of samples simplifying the preparation process. The crack length was recorded during testing by using a millimetre scale drawn on the side of the sample and recording values of force and displacement at the locations specified by the standards. At least four specimens from each material system were tested. Modified beam theory (MBT) was the chosen data reduction method as only a small variation between data reduction methods was observed, and MBT is reported to give the most conservative values for the widest range of materials systems according to ASTM D5528. The definition of the G_{Ic} used in this work is the deviation from linearity on the load-displacement graph. For the materials tested this did not differ significantly from the visible onset of delamination. The R-curves were produced by plotting all the effective G_{Ic} values for all specimens tested as a function of crack length (to see the R-curves of all specimens tested refer to Appendix A). Specimens of each material showed similar changes in delamination resistance at comparable crack lengths, as well as, initial crack transitions on the fracture surface also occurring at comparable crack lengths. Given that the stress intensity factor, K_I, can be defined in Equation 3-1 as a function of crack length a, opening force, P, and specimen thickness, h. By substituting this into Equation 3-2 which gives the relationship between K_I and G_I, where E_1 is the Young's Modulus in the fibre direction, the expression in Equation 3-3 is derived. Hence a second-order polynomial curve was chosen to fit the data as G_I is proportional to a^2.

$$K_I = 2\sqrt{3}\frac{Pa}{h^{3/2}} \qquad 3\text{-}1$$

$$G_I = \frac{K_I^2}{E_1} \quad 3\text{-}2$$

$$G_I = \frac{12P^2a^2}{E_1h^3} \quad 3\text{-}3$$

Table 2 Material systems by particle, matrix and fibre type.

Material System	Particle Type	Matrix Type	Fibre Type	Mean Specimen Thickness, *h* (mm)
1	Neat resin (Untoughened)	M1	F1	5.184
2	Neat resin (Untoughened)	M2	F1	5.106
3	P1	M1	F1	4.936
4	P1	M2	F1	4.916
5	P1	M1	F2	4.991
6	P2	M1	F1	4.905

3.2.1 Computed Tomographic Scanning

Samples were scanned using Modified 225 kVp Nikon/Xtek HMX. Scanning was carried out using a source energy of 100 kVp and 25 W power using a tungsten target with no filter. A 2048x2048 pixel Perkin Elmer 1621 flat panel detector employing a CsI scintillator was used to detect the X-rays. The detector exposure time was 250 ms. Ring artefact suppression was enabled via the shuttling of the centre of rotation of the sample. Each scan had a voxel resolution of 14.75 µm's, and used 3142 radiographic projections averaging 8 frames per projection. The scans were reconstructed using the filtered back projection method in Metris CT Pro reconstruction software.

3.2.2 Fractography

After mechanical testing and subsequent XCT scanning, the procedure schematically shown in Figure 12 was used to separate the crack surfaces: the first step was to advance the crack 10 mm beyond that of the original test by inserting a wedge into the crack mouth of each specimen. Then a thin razor blade was then inserted in the wake of the new crack tip as the crack surfaces were held open using a wedge, as shown in the second step. The third step was to drive the razor blade

through the sample until split in two. Overview images of the fracture surfaces covering an 80 mm field of view were taken using an optical macroscope. Each image shows the whole fracture surface from right to left. The right hand side of each image is the where the crack initially propagated from the PTFE insert, and the left hand side is the end of experimental crack propagation. This is to assess the crack path across the entire crack extension region (≈70 mm of crack growth including the pre-cracked region,), with an optical microscope then being used to visualise specific features of the fracture surface in greater detail.

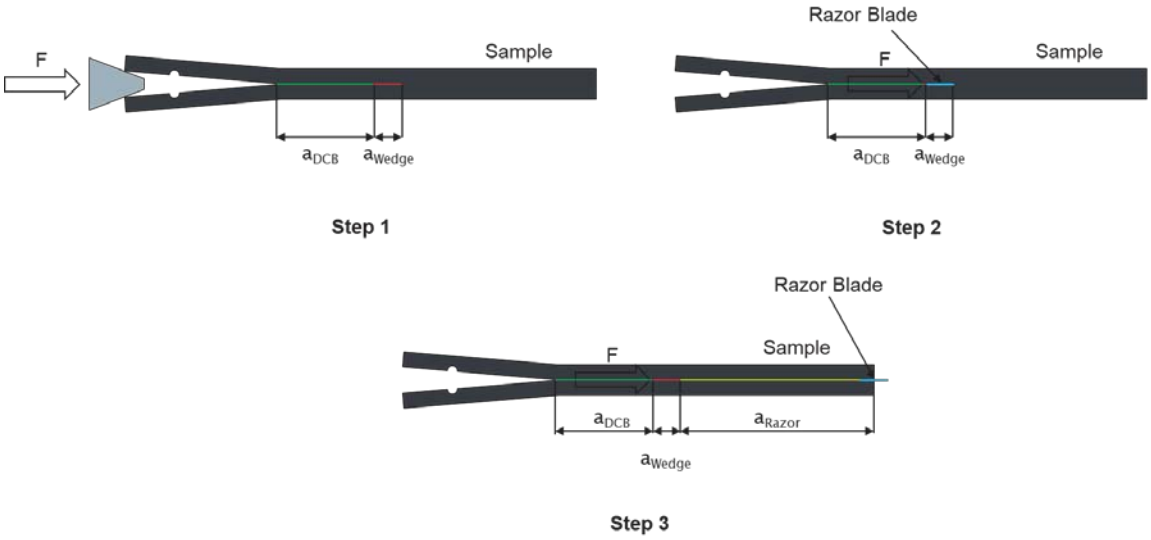

Figure 12 Separation of the fracture surfaces. Step 1 shows the insertion of a wedge after DCB testing to propagate the crack. Step 2 shows the insertion of the razor blade beyond the DCB fracture length. Step 3 shows the full delamination of the sample using the razor blade.

3.2.3 Scanning Electron Microscopy

Once the samples had been imaged by optical means they were prepared for scanning electron microscopy (SEM). One of the fracture surfaces from each specimen was cut into an 80 x 25 mm section using a low-speed diamond saw. The fracture surface was then cleared of contamination and any light debris using compressed air. The samples were then gold-sputtered and scanned using a JEOL JSM7200 LV SEM. A working voltage of 2 kV was used at a working distance of ≈ 35 mm.

3.3 Results

3.3.1 Toughness and R-curve Response

The force displacement curves for all tested material systems are shown in Figure 13, demonstrating the broad range of crack propagation behaviour, with notable pop-in behaviour seen in material 3b. The three broad characteristic R-curve behaviours may be discerned in

Figure 14 and the specific value of the strain energy release rate at crack growth lengths of 0 mm, 10 mm, 25 mm, and 50 mm are shown respectively for each material system in Table 3. Material 5 shows a distinct rising delamination resistance, whilst Materials 1, 2, and 4 show relatively constant fracture resistance, with evidence of a slight rising toughness in Material 2. Materials 3 and 6 show falling toughness. Composite delamination resistance curves are plotted in

Figure 14 averaging the data from all the specimens tested for each material system (*i.e.* in all cases at least three specimens). Only material 3 was seen to exhibit significant variability; with one specimen evidencing an immediate transition of failure from the toughened interlayer (at the starter notch) into the surrounding fibre bed. This immediate transition resulted in a flat R-curve with no distinct drop in toughness during the initial crack propagation. This material is plotted in

Figure 14 and labelled material 3a. The specimens labelled 3b in

Figure 14 exhibited a more gradual transition between the interlayer and the surrounding fibre beds, occurring over some tens of mm of crack growth and forms the focus of the results and discussion from here on in.

3.3.1.1 Untoughened Systems

Materials 1 and 2 which correspond to the two untoughened systems differing by only the matrix show, G_{IC}, values lay within each of their 95 % confidence bounds. Material 1 shows a relatively flat toughness response as shown in Figure 15 whereas material 2 shows a slight increase in toughness with delamination growth as shown in Figure 16.

3.3.1.2 Particle Toughened Systems

Material systems 3 and 4 show similar values of G_{IC} (within the bounds of the 95% confidence intervals of

Figure 14). It is the propagation behaviour which distinguishes them: Material 3 and 4 which differ by the matrix type, show an initial drop in toughness with crack growth, with the drop for Material 3 being greater and more sustained as seen in Figure 18 and Figure 19 respectively.

Distinct 'pop-in' behaviour was observed in Material 3, signified by sudden sequential load drops during crack extension as shown clearly in the force-displacement curve in Figure 13. As noted earlier, this material showed the greatest variability between specimens in terms of toughness response and the crack paths. Furthermore, Material 3 also showed the greatest difference between the initial and final values of G_{IC}. Material 4 showed consistent behaviour between specimens in terms of toughness response and fracture surfaces: after the initial drop in toughness, there is then a small increase before self-similar crack propagation occurs, resulting in the most consistent toughness response of all the material system as shown in Figure 19.

Material system 5 which differs from material systems 3 and 4 by the treatment of the fibres shows a contrasting response. The toughness of the material system increases relatively quickly during the initial delamination growth and then increases gradually throughout crack propagation before levelling off and then growing in a more self-similar fashion as shown in Figure 20.

Material system 6 shares the same matrix and fibre type as material systems 3 and 4, but differs by toughening particle type. It shows a high nominal G_{IC} compared to the other material systems and shows an initial drop in delamination resistance in the first ≈10 mm of crack propagation before becoming relatively flat for the remainder of the propagation as shown in Figure 21.

The performance of all the material systems is relatively similar based on the 95% prediction intervals overlapping.

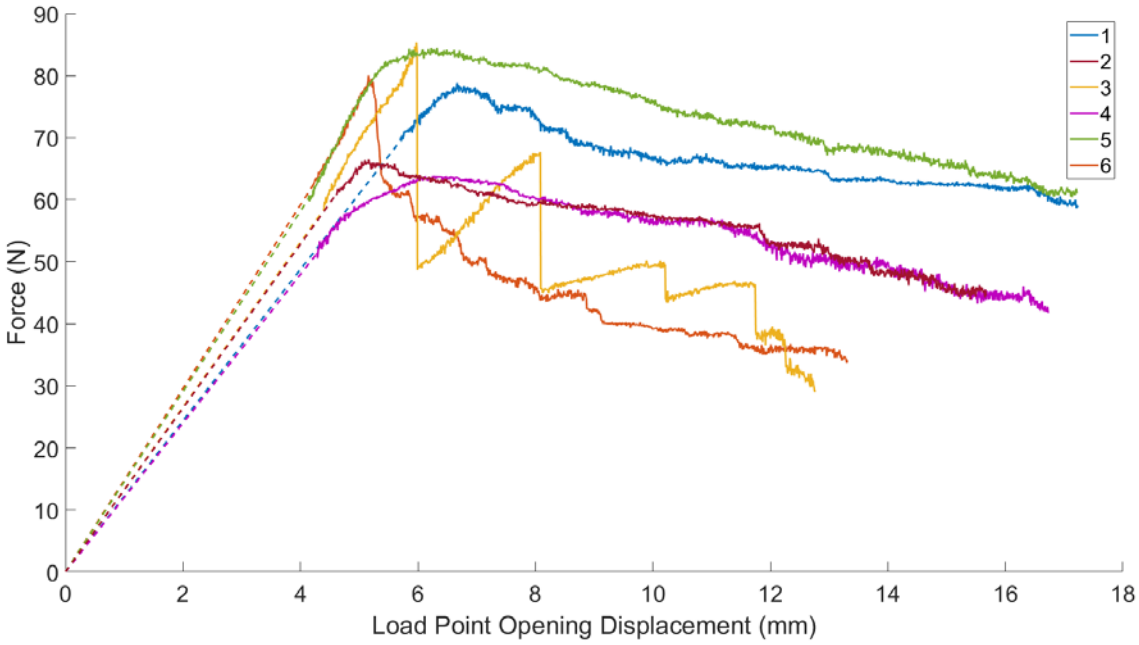

Figure 13 Force displacement curve for a sample in each of the tested material systems.

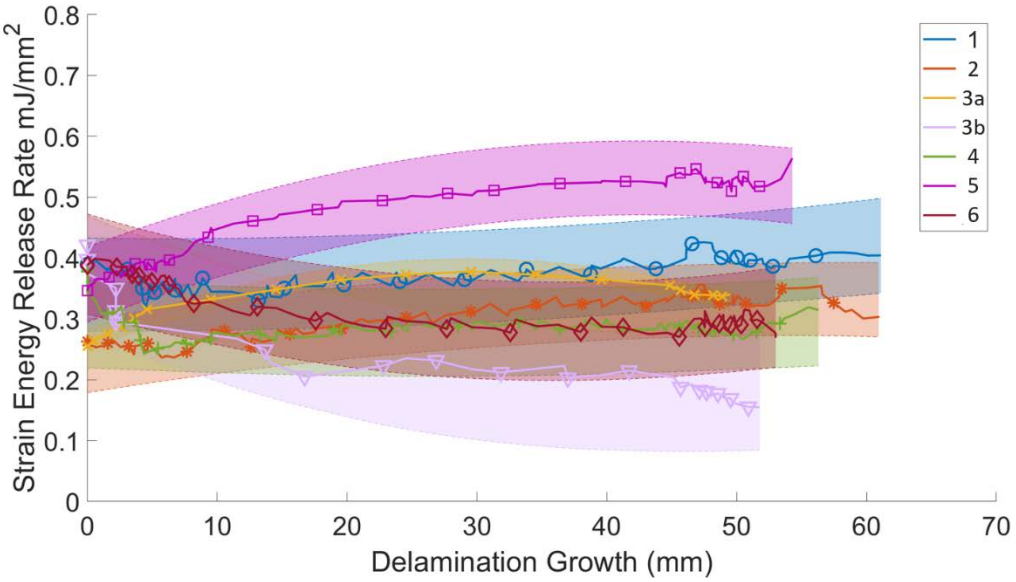

Figure 14 Delamination resistance curves of each material system where the 95% prediction interval of a second-order polynomial fitted curve is plotted.

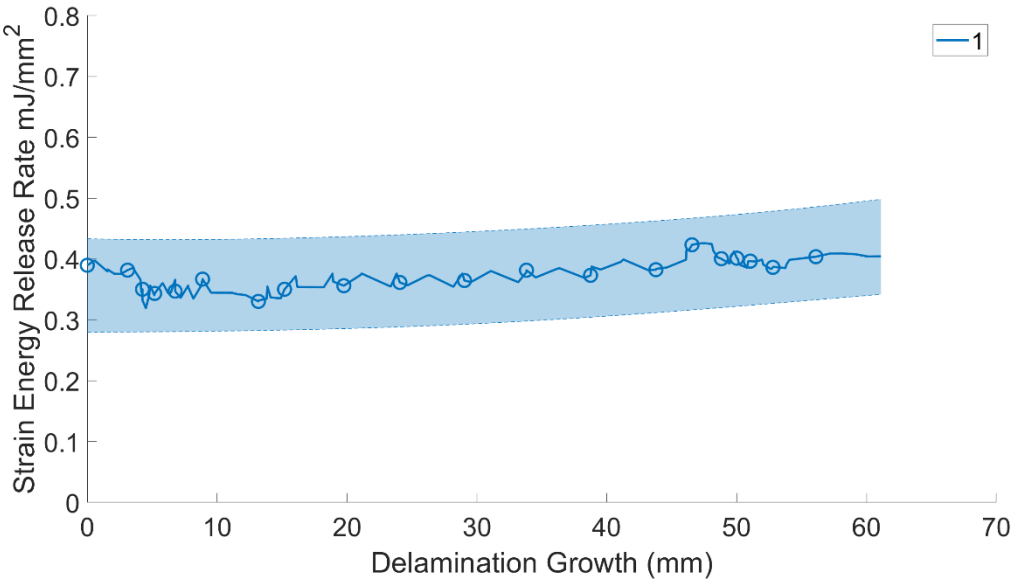

Figure 15 Delamination resistance curve for material system 1, showing a small increase in toughness with crack propagation, where the 95% prediction interval of a second-order polynomial fitted curve is plotted.

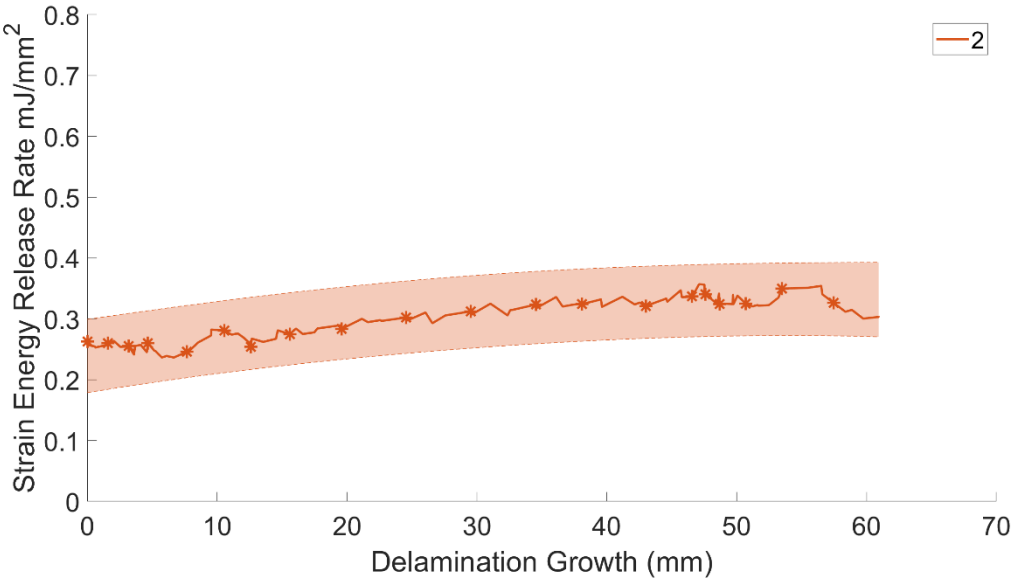

Figure 16 Delamination resistance curve for material system 2, showing a modest increase in toughness with crack propagation, where the 95% prediction interval of a second-order polynomial fitted curve is plotted.

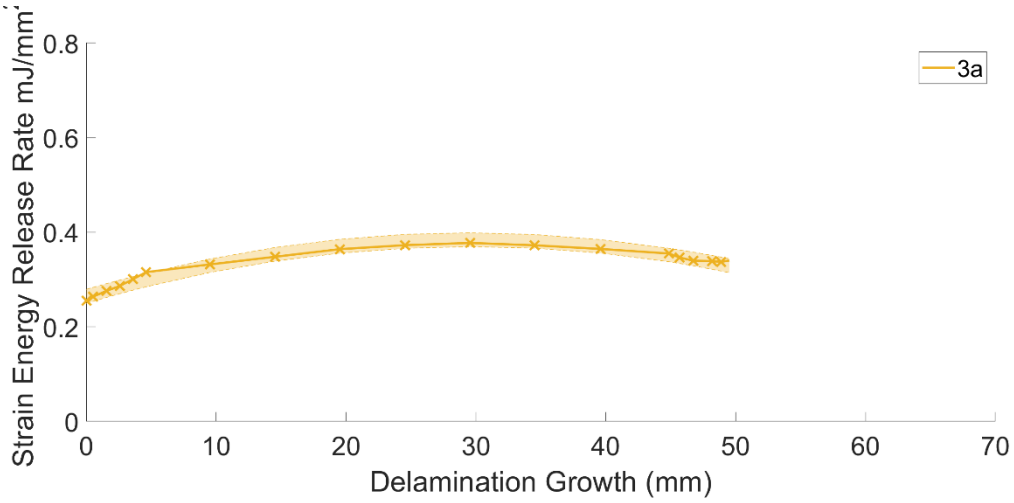

Figure 17 Delamination resistance curve for material system 3a, showing a small increase in toughness up to around 30 mm of crack growth, followed by a subsequent drop in toughness, where the 95% prediction interval of a second-order polynomial fitted curve is plotted.

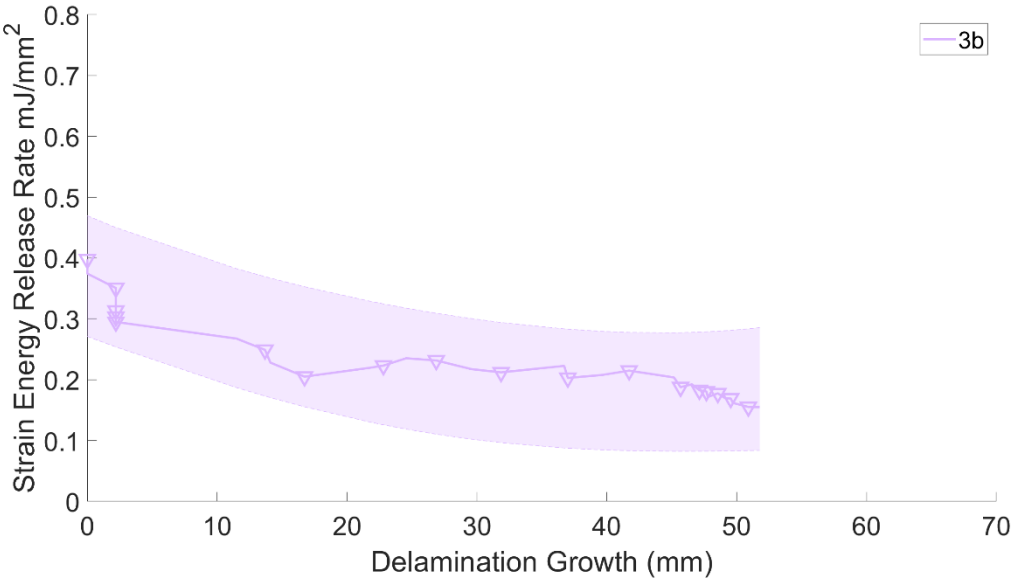

Figure 18 Delamination resistance curve for material system 3b, showing an initial drop in toughness sustained until around 20 mm of crack growth. The toughness then remains steady until falling again in the final 5 mm of crack growth. The 95% prediction interval of a second-order polynomial fitted curve is plotted.

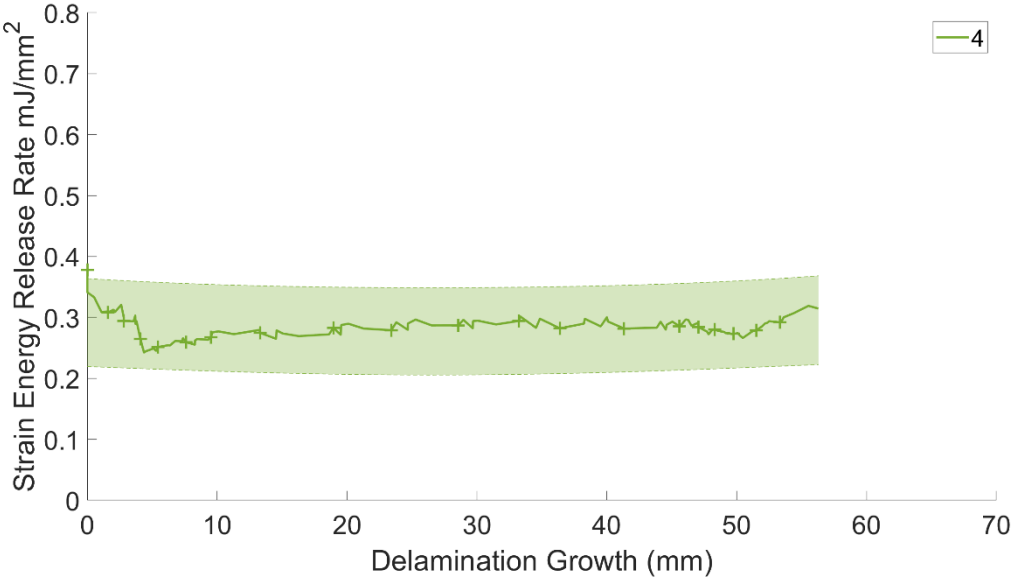

Figure 19 Delamination resistance curve for material system 4, showing an initial drop in toughness over the first 5 mm of crack growth followed by a slight rise over a further 5 mm and then self-similar crack propagation for the remainder. The 95% prediction interval of a second-order polynomial fitted curve is plotted.

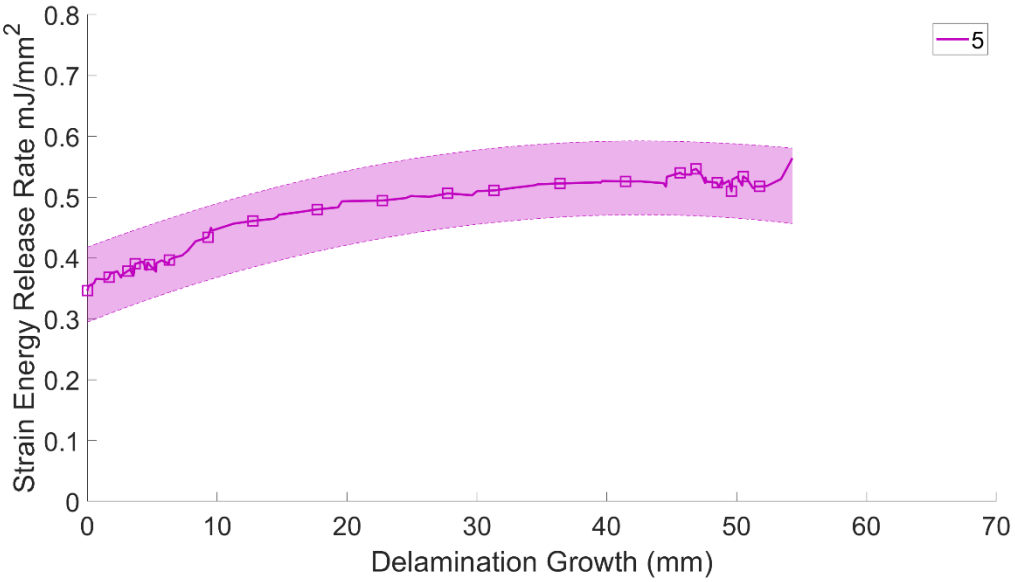

Figure 20 Delamination resistance curve for material system 5 showing a steady increase in toughness with crack propagation until reaching a self-similar propagation at around 30 mm of crack growth. The 95% prediction interval of a second-order polynomial fitted curve is plotted.

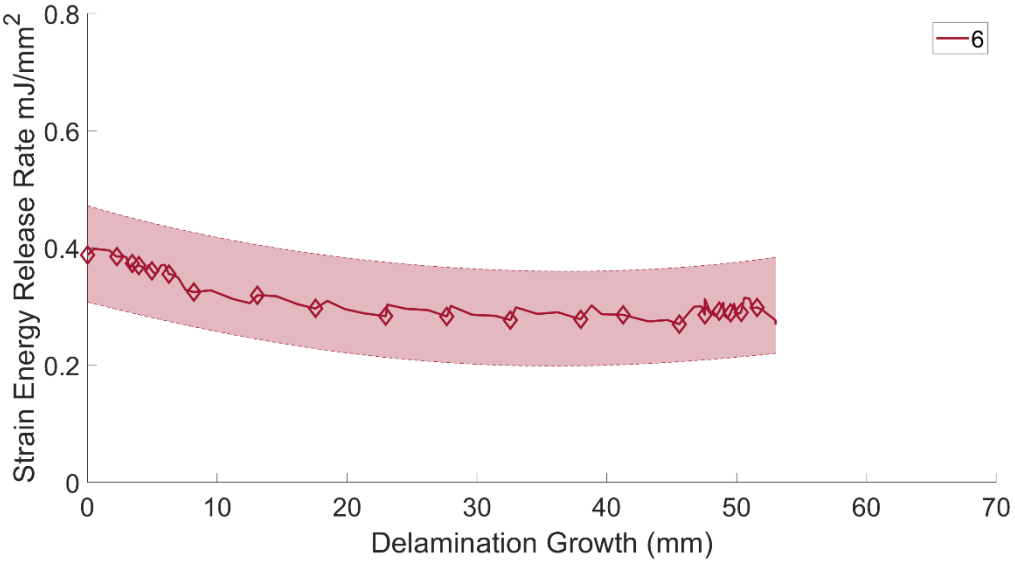

Figure 21 Delamination resistance curve for material system 6, showing an initial steady decrease in toughness with crack propagation until levelling and remaining similar after 25 mm of crack growth. The 95% prediction interval of a second-order polynomial fitted curve is plotted.

Table 3 The Strain Energy Release Rate values for each material system at specific crack propagation lengths.

Material System	Critical Strain Energy Release Rate (mJ/mm^2)	Strain Energy Release Rate at 10 mm Propagation (mJ/mm^2)	Strain Energy Release Rate at 25 mm Propagation (mJ/mm^2)	Strain Energy Release Rate at 50 mm Propagation (mJ/mm^2)
1	0.390	0.345	0.362	0.401
2	0.263	0.281	0.297	0.325
3a	0.255	0.331	0.372	0.337
3b	0.398	0.273	0.232	0.169
4	0.378	0.267	0.287	0.273
5	0.346	0.434	0.505	0.510
6	0.388	0.319	0.285	0.290

3.3.2 X-ray CT

CT scanning reveals distinct interlayers in the particle-toughened systems, attributable to the forced separation of plies by the particle containing regions, see Figure 22. The untoughened systems show an indistinct texture where the ply structure is not visible at this scale/resolution. For the imaging conditions used here, the particle containing interlayers are seen to be distinctly darker than the fibre-containing tows/plies. On this scale (≈15 µm voxel resolution) only large deviations in interlayer geometry can be observed, where for example a tow gap can be clearly visualised in Material 6. Resin-rich pockets are evident in material systems 3, 4, 5, and 6.

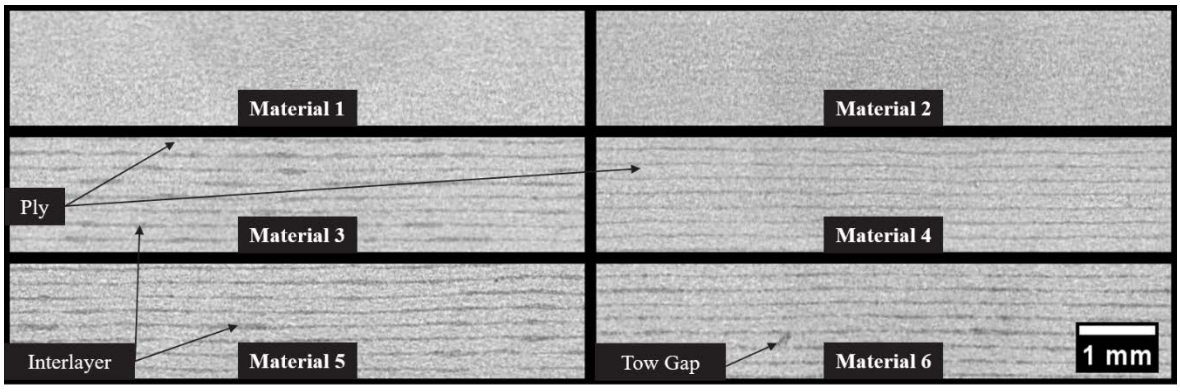

Figure 22 Cross-section through each materials system showing the distinct interlayer in the particle-toughened materials with the fibre direction into the page.

3.3.3 Fractographic Imaging

Results from the fractographic imaging analysis of each material system using optical macroscopy, OM, and SEM is presented in this section. A summary of these findings can be viewed in Table 4. All fracture surfaces were scrutinised carefully, and those included in Figure 23 are as far as possible entirely representative examples. The reader is encouraged to examine the R-Curves for all specimens tested in this chapter and can be found in Appendix A which further evidences the similar delamination response during mode I loading between samples within a given material system.

3.3.4 Optical Macroscopy

A macroscopic overview of each fracture surface can be seen in Figure 23, covering 80 mm of crack propagation beyond the insert. The crack and fibre direction is from right to left, where the end of the insert is just visible on the right of each image. For the toughened materials, in particular, interlaminar and intralaminar fracture are readily identifiable with the lighter and darker regions of the fracture surfaces respectively (confirmed by optical microscopy, see Figure 24). The transition between the two modes is associated with coarse 'finger-like' areas across the surface, which appear to start from small, local regions, referred to, in this work, as 'trigger' regions. With ongoing propagation from the 'trigger' regions, these finger-like structures then spread laterally as the crack continues to propagate. In the untoughened systems, there appear to be some differences in surface fracture texture/appearance, however, this is not as distinct as it is in the particle-toughened systems.

Material 3 has noticeably fewer 'trigger' regions than the other particle-toughened materials, with several fingers which eventually lead to the full transition of the crack from the interlayer to the ply. The transition occurs over an appreciably longer distance in Material 3 than in the other toughened systems (≈70 – 80 mm, as opposed to 30 – 40 mm in the others). The bowed marks seen on the surface of Material 3, termed 'beach' marks, are also of note as these appear to correlate with the pop-ins observed during the testing of this sample.

Distinctively, the surface of Material 5 shows evidence of many bridging fibres, largely absent from the other tests.

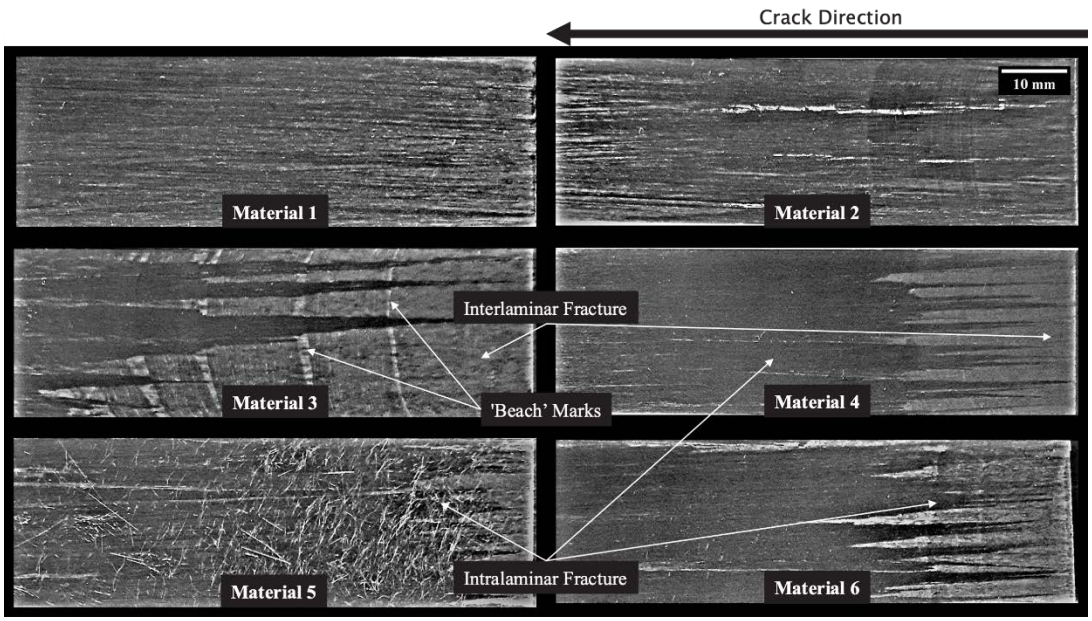

Figure 23 Fracture surfaces of each material system showing the transition from the interlayer to ply in PT systems. The crack direction is from right to left.

3.3.5 Optical Microscopy

Optical microscopy of the crack surfaces is shown in Figure 24. There is a clear distinction between resin and fibre interface failure in Materials 1 and 2. There are regions where the surface of the fibres is visible which are the horizontal (dominant direction) features on the fracture surface. There is no obvious correlation with the macroscopic images in Figure 23. Resin failure in the untoughened materials is characterised by the rougher surface texture. The distinction between the interlayer and fibres is clear in all of the particle-toughened systems. The interlayer is characterised by a rougher topology as a result of the incorporation of toughening particles, whereas the fibres have a distinct horizontal direction and smoother surface. As noted above, these regions correlate to the light (interlayer) and dark (intralayer) regions of the surface overviews in Figure 23.

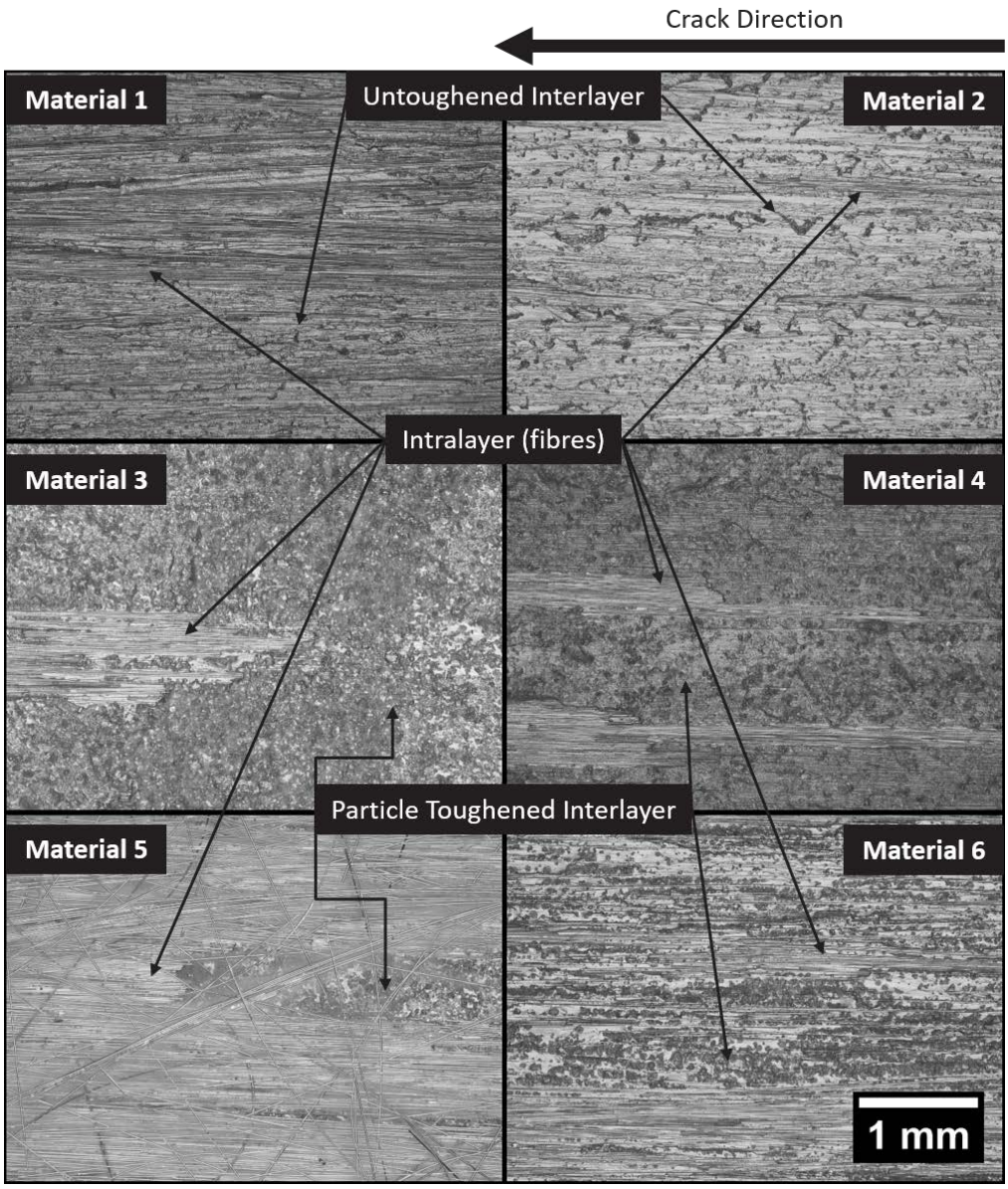

Figure 24 Optical microscopy of crack surfaces highlighting the incidence of both inter- and intralaminar propagation. The crack direction is from right to left.

3.3.6 Scanning Electron Microscopy

SEM images of the fracture surfaces of each material system are shown in Figure 25 to Figure 28 where the crack direction is consistent with the previous figures, propagating from the right of each image to the left.

3.3.7 Untoughened Material Systems

Similar to the optical micrographs there is a clear difference in the fracture surface along the surface of the fibres and in the resin-rich regions shown in Figure 25. Material 1 shows fibre interface failure adjacent to matrix failure in (presumably) resin-rich regions. On the surface of

Materials 1 and 2 river lines can be seen which signify the local crack propagation direction [214]. On the fracture surface of Material 2, resin features, termed scarps, are evident [214].

Using a higher magnification and looking more specifically at the resin-rich fracture region of Materials 1 and 2 in Figure 26, the river lines are identifiable in the resin and appear as shallow channels into the resin. Smaller scarps on the surface of the resin are also evident which are not always in the dominant direction of the fibres. Furthermore, at the bottom of each image for Materials 1 and 2 broken fibres can also be seen showing some bifurcation of the crack between the resin-rich region and fibre interface.

Figure 27 provides a more detailed view of the intralaminar fracture region. Material 1 shows cusps/channels where fibres have been pulled out of the resin and left an imprint. Furthermore, there is clear evidence of fibre breaks on the fracture surface. It is noteworthy that regions of intralaminar fracture in Material 2 are distinctly smaller than those seen in Material 1. Again, there is evidence of fibre breaks where the crack is propagating in the intralaminar region of the composite. There is also a smooth resin-rich region with microcracks on the surface.

3.3.8 Toughened Material Systems

Regions at the interface between interlaminar and intralaminar delamination for each of the particle-toughened systems are shown in Figure 25. There is a clear distinction for all particle-toughened systems between the fibres and toughened interlayer. Material system 3 shows an interlaminar surface where the particles and matrix have been separated, leaving “dimples” where particles have been extracted. It is also notable that the fracture surface is different on either side of the ‘beach’ mark region, with a more pronounced, rougher texture before than after the ‘beach’ mark. Material 4 also shows a rough interlaminar surface, with dimples from missing particles, however, to a lesser extent than in Material 3. There are many fibres pulled free of the fracture surface in Material 5. The interlayer region also appears to exhibit significantly fewer dimples than the other particle-toughened systems. Material 6 has thin regions of interlaminar fracture between regions of intralaminar fracture. Again, the particle-toughened interlayer is rough and dimpled but appears to have a finer texture with more closely spaced, smaller features, than the other systems.

Figure 26 and Figure 28 show more views of the particle-toughened interlaminar fracture surfaces. The region imaged for Material 3 is along the first ‘beach’ mark. Toughening particles are visible on the surface. There are also dimples on the surface where toughening particles have been pulled out of the resin. The roughness of the surface is also notable. Material 4 shows similar features however, the surface is significantly less dimpled. The presence of toughening

particles and particle pull-out is similarly evident for Material 5, however, the interlaminar fracture surface appears smoother than the other material systems. Fibres which have been pulled out of the matrix can also be seen in the foreground of the image. As well as there being some evidence of particle pull-out from the matrix on the fracture surface of Material 6, there also appears to be a significant number of toughening particles which have undergone quite severe plastic deformation and fracture, as further evidenced using a higher magnification in Figure 28.

Adhered resin on the fibre surface (*i.e.* hackles) can be seen on the surface of the fibres of Materials 3 and 4 in Figure 27. Furthermore, there is also evidence of fibre breaks. In the foreground of the fracture surface of Material 5, there are fibres across the field of view, and adhered resin on the fibre surface can be identified. The underlying fibre bed also shows some misaligned and broken fibres. On the intralaminar fracture surface of Material 6, there appear to be toughening particles which have become embedded between fibres. Furthermore, there are cusps where fibres have been pulled out, fibre breaks, and scarps of resin.

Table 4 Summary of fractography results for each of the six materials systems analysed.

Material System	Macroscopic Behaviour	Interlayer Behaviour	Intralaminar Behaviour	Fibre Bridging	Toughening Particle Failure
1	No distinction between resin and fibres	Resin-rich fracture with scarps and river lines. No distinct interlayer	Fibre-matrix debonding and evidence of fibre breakage	Evidence of a small amount	N/A
2	No distinction between resin and fibres	Resin-rich fracture with scarps, river lines and microcracks not aligned in the fibre direction No distinct interlayer	Fibre-matrix debonding and evidence of fibre breakage	Evidence of a small amount	N/A
3	Few trigger regions occur early on, large propagation to full transition, clear 'beach' marks. The full transition occurs at around 70 mm of crack propagation	Rough topology with visible toughening particles. A clear distinction between the 'beach' marks and the surrounding interlayer. Distinct interlayer	Resin hackles on fibres, mostly a 'clean' separation of fibre and matrix with evidence of fibre breakage	Evidence of a small amount	Toughening particles appear to debond from the matrix
4	Significantly more trigger regions than material 3. Where they occur throughout the crack propagation, the full transition occurs at around 20 mm of crack propagation	Rough topology with visible toughening particles. However, the topology appears more even than material 3. Distinct interlayer	Resin hackles on fibres, mostly a 'clean' separation of fibre and matrix with evidence of fibre breakage.	Evidence of a small amount	Toughening particles appear to debond from the matrix
5	Bridged fibres are obvious on the fracture surface over the entire propagation. The full transition appears to occur at around 10 – 15 mm of crack propagation	Significantly smoother topology than materials 3 and 4. Distinct interlayer	Large bundles of fibres at varying depths in the FOV. The underlying ply is also visible with some evidence of resin hackles on fibre surfaces.	Clear large-scale bridging	Toughening particles appear to debond from the matrix
6	Various trigger regions across the fracture surface. The full transition occurs at around 30 mm of crack growth	Rough topology surface with many visible toughening particles. Distinct interlayer	Cusps in matrix from fibre debonding, mounds of resin around and on fibres. Evidence on toughening particles in the ply and around the fibres.	Evidence of a small amount	Toughening particles appear to have plastically deformed and fractured. Evidence of particle crack face bridging.

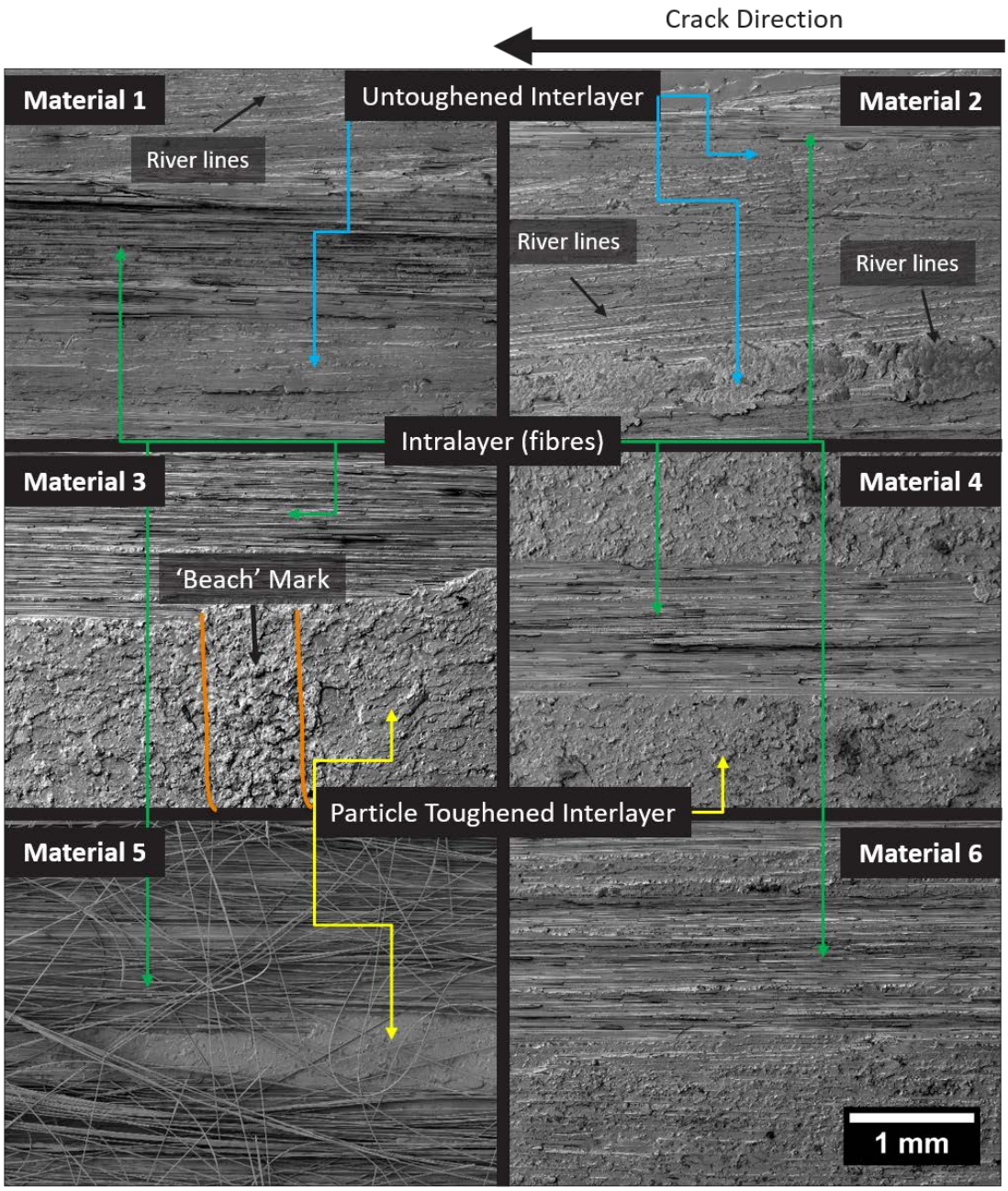

Figure 25 SEM overview of the 'finger' regions where the ply and interlayer interface. The crack direction is from the right to the left of each image.

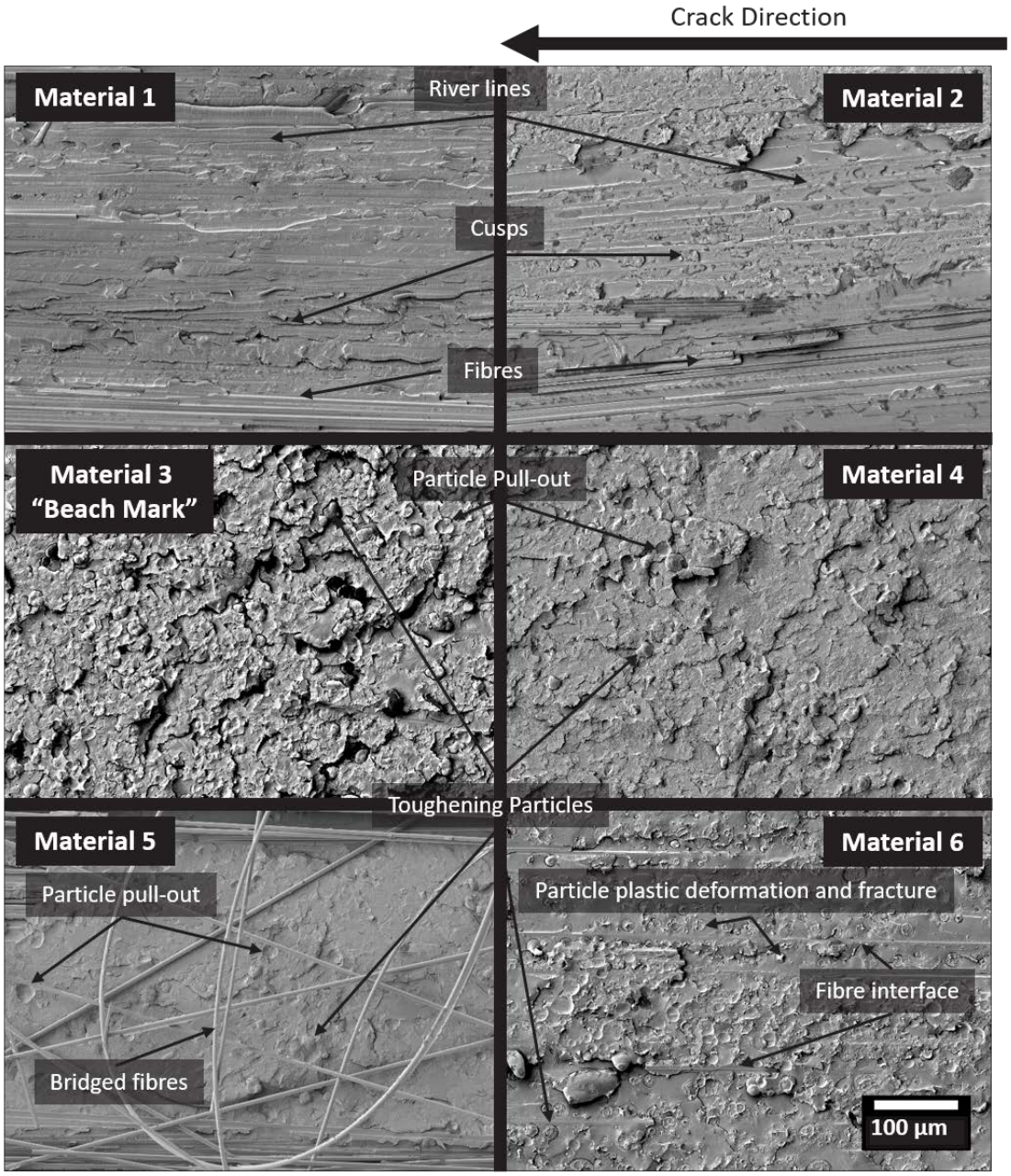

Figure 26 SEM image of the interlayer region of each Material system. The crack direction is from the right to the left of each image.

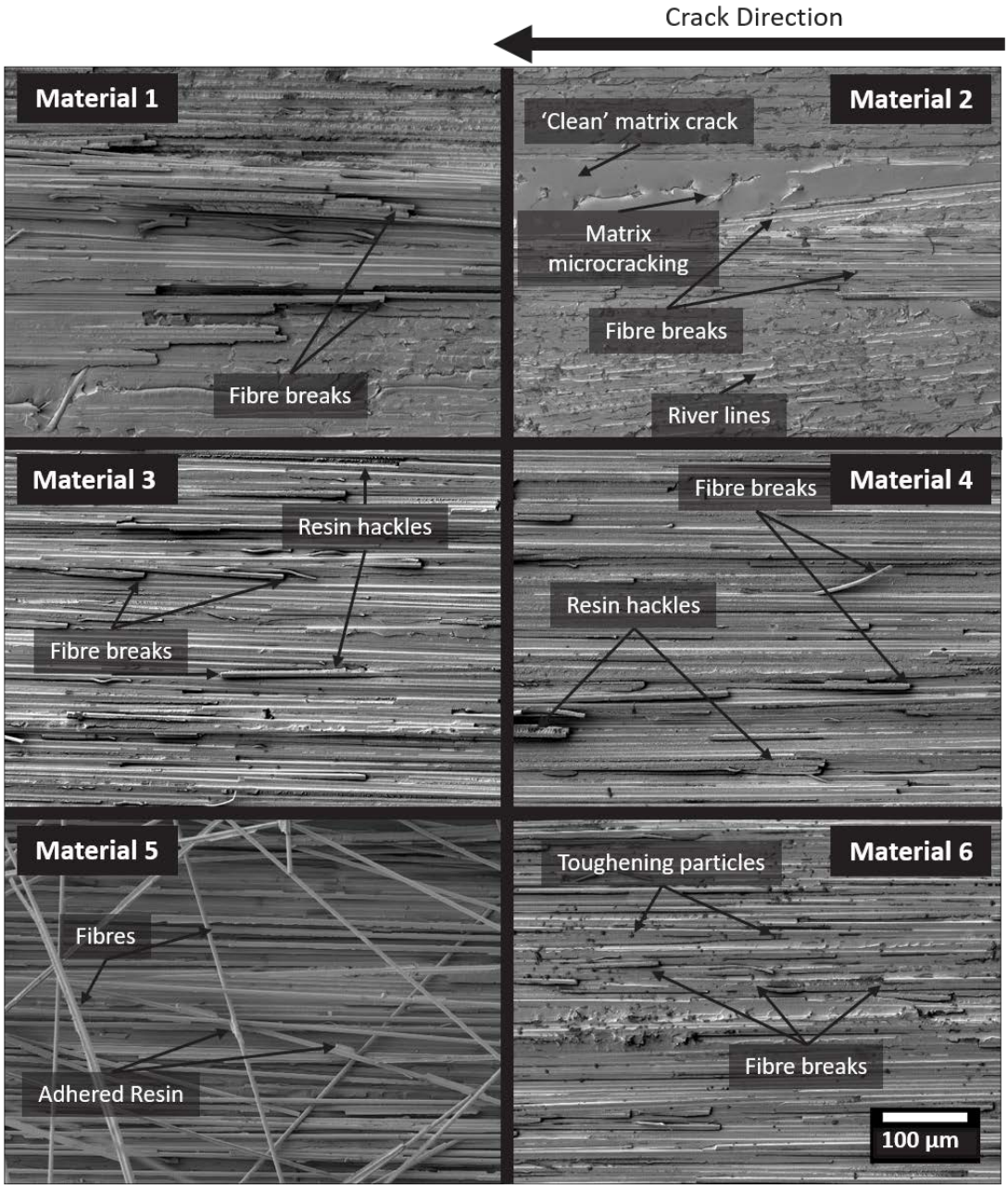

Figure 27 SEM image of the fracture along an intralaminar path through the ply. The crack direction is from the right to the left of each image.

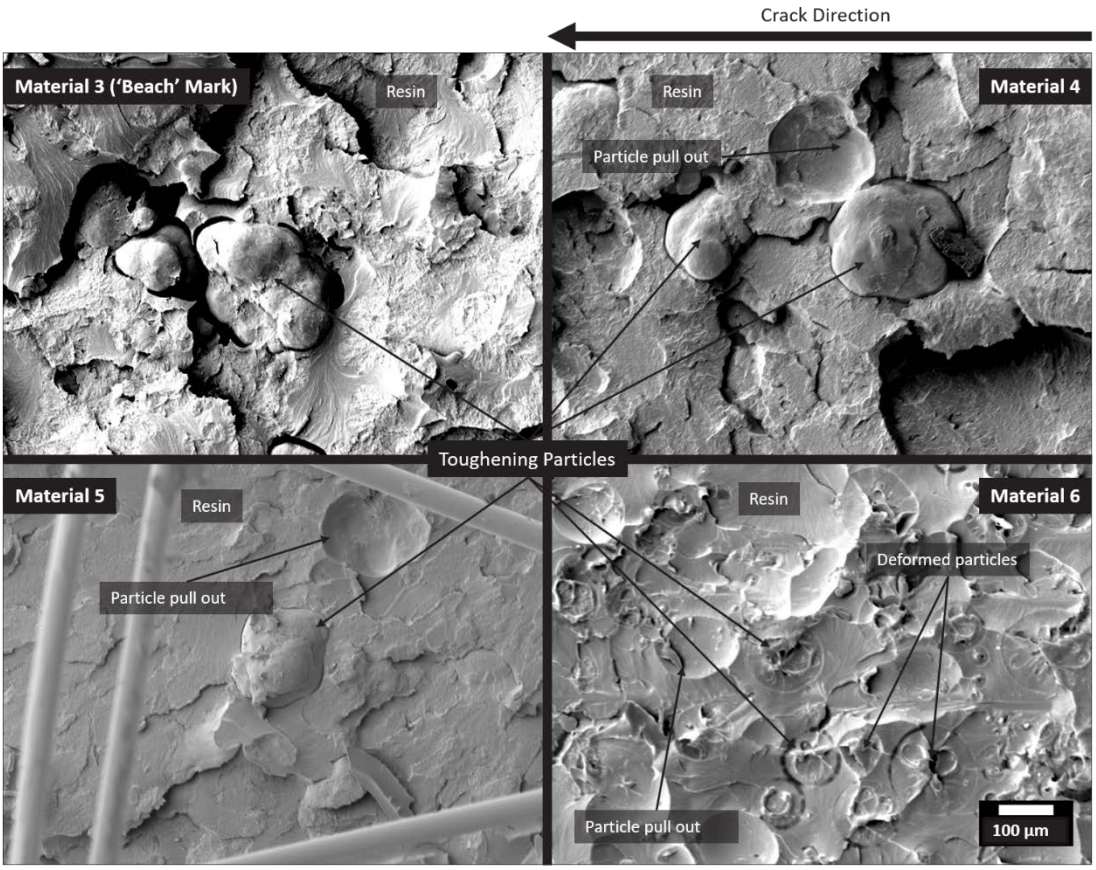

Figure 28 SEM zoomed image of toughening particles within the interlayer of the particle-toughened system. The crack direction is from the right to the left of each image.

3.4 Discussion

3.4.1 Underlying Damage Response Mechanisms

During Mode I delamination of a CFRP system it may be considered that there is a process zone ahead of the crack tip within which deformation and damage processes occur, which may contribute to the macroscopic toughness [31]. In neat resin systems, failure is reported to consist of some degree of nonlinearity due to mechanisms such as shear yielding of the epoxy matrix and crazing ahead of the crack tip [89-91]. In particle-toughened composite systems, the inclusion of thermoplastic toughening particles creates a distinct toughened interlayer between the fibre-containing plies without a significant loss in strength or stiffness from the neat properties [15, 28, 31, 80, 84, 100, 102]. The primary role of the inclusion of toughening particles is to create a more torturous and energy-consuming crack path within the toughened interlayer through various toughening mechanisms, including (but not limited to); particle matrix debonding, plastic deformation, particle crack face bridging, particle yielding, and particle ductile fracture [36, 86, 96, 100, 103-112]. Notably *in situ* synchrotron radiation computed tomography carried out on

similar material systems to those used in this study identified particle-matrix debonding, and particle deformation as playing key roles in maintaining cracks in the particle-toughened interlayer [31, 49]. However, as noted by Yasaee *et al.* the process zone around the crack tip also interacts with the ply and fibre-matrix interface regions [121]. This interaction creates competition between various potential crack paths, between the interlayer and the ply of the composite. Borstnar *et al.,* and later, Xie and Koslowsk [49, 179] illustrated the competition between potential crack paths in the interlayer and fibre-matrix interface, which suggested that the adhesion of the matrix to the toughening particles relative to the fibres was significant. Furthermore, misaligned fibres and crack bifurcation in the ply lead to interaction with the fibres causing fibre-matrix debonding, fibre breakage, and oblique fibre-bridging which may significantly increase the apparent toughness of the composite depending on the relative strength of pull-out tractions [69]. Therefore, when considering damage response mechanisms which contribute to the crack path and the shape of the material system R-curve during Mode I delamination these interactions should be considered fully.

3.4.2 Micro-Mechanistic Contribution to Crack Path Transition

The untoughened interlayer systems in this work appear to have many adjacent regions of resin-rich interlaminar fracture and fibre interface intralaminar fracture. This could be evidence of crack bifurcation along the plane of the crack front. The lack of a distinct interlayer and toughening particles suggests interactions of the crack with fibres will be more likely (than in the other systems), hence the crack path is determined by the debonding of fibres and failure of the matrix. Both untoughened materials show microcracks in the resin where the direction is not necessarily aligned with the fibre direction. This could be evidence of a local shear failure in the resin caused by the non-uniform local geometry and hence stress components and stress distributions which are not normal to the plane of the crack front. The river lines further support this suggestion as they are also not entirely aligned with the fibre direction or the crack direction. The crack appears to separate into different areas of the composite adjacent to one another. Therefore, the crack front is not straight and hence there is a microstructural complexity leading to local mixed-mode separation processes. This local complexity in loading may also contribute to the non-normal fracture direction of microcracks and river lines. It is also clear in both the untoughened systems that there is fibre-matrix interface failure evidenced by the visible fibre surfaces. Cusps in the resin suggest regions where the fibres have been debonded from the matrix and scarps of resin on the surface evidence a degree of local resin-dominated behaviour during crack growth.

As reported in previous studies this work also finds evidence of particle-matrix debonding, particle deformation, particle yielding and fracture. Consistent with the stated use of the same particle

type in Materials 3, 4, and 5 (*i.e.* particle P1), it is evident that the size and geometry of the toughening particles were reasonably consistent. They are somewhat irregular in shape, but approximately spherical. The relative weakness of the P1–matrix interface is evidenced by clear de-bonding and particle pull-out on the fracture surfaces. Material 6 on the other hand, using the P2 toughening particle, showed much greater integrity of the particle-matrix interface, with only occasional debonding. More significantly, a high proportion of fractured particles occurs, indicating that the effective strength of the particle-matrix interface is greater than the strength of the thermoplastic itself. The ductile appearance of the exposed toughening particles suggests a degree of crack face bridging by the particles may have occurred [31].

A common feature of all the material systems in this work is fibre interface crack propagation and fibre breaks in these regions. As such the delamination interacts with the fibres in the ply, leading to some degree of oblique fibre-bridging. Furthermore, features such as resin hackles on the fibre surface suggest the fibres do not cleanly debond from the matrix. Material 5, however, shows fewer features which resemble resin hackles and adhered resin to the fibres, consistent with a lower fibre-matrix interface strength between the F2 fibre and M1 matrix, facilitating the extensive bridging seen in the associated tests.

3.4.3 Influence of Meso-Scale Architecture on Crack Path Transition

The non-uniformity of the particle-toughened interlayer shown in Figure 22 is known to be a result of toughening particle agglomeration and sparsity, creating relatively thick and thin regions respectively. Based on findings from previous studies, the strength of the matrix can be considered greater than that of the fibre-matrix interface then a lack of toughening particles in the vicinity of the crack tip or debonding particles near the fibre-matrix interface will cause a transition of the crack to the lowest energy fracture path [49, 179]. Furthermore, the thinner the interlayer the greater the stress will be at the fibre-matrix interface, increasing the propensity for such a crack path transition. Fritz *et al.* identified similar features in unidirectional epoxy matrix laminates, referred to as tow-aligned resin pockets (TARPs) [215]. Fritz *et al.* postulated that TARPs could be linked to the transition of a crack in and out of the interlayer of the composite, in preliminary results during Mode I loading, although it is recognised that further work is needed to verify this. This present work similarly finds evidence of TARPs correlating with crack path transitions during Mode I loading, however, this study provides no direct evidence at this stage to suggest any causal relationship between these observations.

3.4.4 Specimen Scale Crack Path Transition Behaviour

If it is considered that the aim of introducing toughening particles via interleaving is to increase both the fracture initiation and propagation resistance of the composite, then it would be expected that initiation and propagation should occur within the particle-toughened material. However, fractography shows there is evidence at multiple scales that cracks transition from the toughened interlayer to the fibre-matrix interface and further into the surrounding plies. The 'finger' like structures seen on the fracture surfaces in Figure 23 represents this transition across the whole DCB coupon. For the particle-toughened systems, it appears as though the transition initially occurs at local 'trigger' regions which appear to start as regions in the order of a few fibre widths. As the crack front advances from these points, there is some lateral widening from the initial trigger regions, plus more transitions occurring at new 'trigger' regions. Initial transitions generally occur at relatively short crack lengths within the DCB specimens used here, with some occurring during pre-cracking from the initiating insert. Once a crack has made the transition into the fibrous plies it rarely transitions back to the interlayer of the composite, but instead remains in the neighbouring ply, spreading laterally and/or merging with other transitioned regions, until the entire crack front has entirely left the interlayer. Therefore, although toughening response mechanisms related to the inclusion of toughening particles have been identified, we see that these only play a significant role in the early stages of crack growth, as promoted using DCB tests. As the crack propagates and transitions, fibre-dominated mechanisms such as fibre-matrix debonding, and oblique fibre-bridging become prevalent.

3.4.5 Toughness Response of DCB Specimens

The change in the toughness behaviour of each material system appears to reflect changes in the dominant toughening response mechanisms. The two untoughened materials systems which do not undergo obvious transitions in the crack path produce largely stable R-curves.

Untoughened Materials 1 and 2 are largely stable, with Material 1 having a higher delamination toughness this could be linked to either the matrix toughness in itself, but the preponderance of fibre-matrix failure implies a role of the associated interface strength

Toughened Materials 3, 4, and 5 all use P1 particles, and initially, failure is predominantly interlaminar. They all start with a similar toughness, consistent with this consistent toughening particle largely controlling toughness (initial).

Material 4's toughness drops rapidly over about 10 mm, with a parallel transition to intralaminar failure occurring over approx. 20 mm. After 20 mm, toughness is essentially stable. The initial

drop in toughness is easily explained by the crack leaving the toughened interlayer, but as intralaminar failure starts to occur, so will the availability of fibre-bridging. This could somewhat ameliorate the drop in toughness in that 0 – 20 mm range. After 20 mm of crack extension, the crack is fully intralaminar, and it can be presumed that the build-up of bridging fibres has reached its effective maximum wake (in the order of 10 mm say). The presence of some bridging is implied by the broken fibres on the fracture surface, even if much less extensive than in Material 5. Once Material 4 has propagated about 20 mm, it should be mechanistically similar to Material 2, as there is no longer any role of the interlayer, and this is borne out by the toughness curves, in that Material 2 and 4 are statistically equivalent after 20 mm extension

Material 3 exhibits a prolonged drop in toughness, with seems consistent with the long propagation distance over which the transition to intralaminar failure occurs, specifically the entire test propagation distance. In the absence of complete and sustained intralaminar failure, it is not possible to discern an effective process zone for fibre-bridging effects, although the sustained drop in toughness implies that bridging cannot be particularly effective in this case. In terms of the final propagation toughness level, it is arguable that this could be expected to approach the toughness of Materials 1 (with the same matrix and fibre type). Whilst sustained, self-similar intralaminar failure was not actually achieved in Material 3, it is perhaps confusing that the final recorded toughness levels for Material 3 are distinctly lower than Material 1, the cause of which is unclear. One may tentatively suggest that the morphology of the fibre bed adjacent to the interlayer may be changed to some extent by the presence of the interlayer, and as such, the local toughening mechanism (such as degree of crack tip bifurcation and fibre-bridging) has changed in this case.

Material 5 has the most extensive incidence of fibre-bridging, indicative of a reduced fibre-matrix interface strength for fibre F2. This is consistent with the distance over which the interlaminar to intralaminar failure occurs in this system being the shortest observed here (*circa* 10 mm). The distinctively rising toughness curve is readily explained by the immediate rapid rise in bridging traction, only seemingly to stabilise around 40 – 50 mm of crack growth, implying a similar scale to the bridging process zone.

Material 6 shows a drop in toughness over the initial 20 – 30 mm of crack extensions, in reasonably good correlation with the transition from intralaminar to interlaminar failure. Beyond 20 – 30 mm extension, toughness is largely stable, implying that any bridging process zone is shorter than this. Beyond 30 mm, it may again be expected that toughness of the Material 6 should converge with Material 1 (same fibre and matrix during fibre-matrix dominated failure) but is again seen to fall below Material 1, but not as strong as seen in Material 3. Again, we might

presume that the presence of an interlayer has modified the near-interface bridging and bifurcation behaviour.

3.5 Conclusions

This work presents systematic observations of the toughening mechanisms and delamination crack paths in parametrically varied composite systems tested using double cantilever beam specimens. The observations demonstrate the change in toughness behaviour as the cracks transition into the ply of particle-toughened CFRP composite material systems. It can be seen from the fracture surfaces and optical micrographs that crack transition begins in a region of only several fibre widths, during the initial propagation of cracks where the crack then spreads laterally into the ply in 'finger-like' structures. This crack path transition plays a critical role in determining whether there is a fall or a rise in toughness reflecting the toughness of the dominant damage response mechanism in the ply. Previously work has suggested possible explanations for the transition to the ply such as poor distribution of toughening particles reducing the number readily available for deformation and debonding. The macro effect of this has been demonstrated using X-ray CT where there are clear resin-rich pockets adjacent to much thinner regions of interlayer which could be linked to the agglomeration and sparsity of particles in certain regions. Hence, these resin-rich pockets create an interlayer with a visibly changing thickness, which may be associated with crack path transitions to the ply, notwithstanding that further work needs to be carried out to verify this. If this is the case however, then it may be the case that the change in toughness during the initial crack propagation could reflect the transition from the interlayer to the ply. The toughness response then becomes steady when the crack has fully transitioned, reflecting the strain energy required to propagate through the ply of composite. Furthermore, the use of crack surface fractography in this work reveals the dominant damage response mechanisms during the Mode I DCB experiment and how this is reflected in the toughness response. Fractography provides an effective method to verify the dominant damage response mechanisms during fracture and indicates that the incorporation of interleave films/particles may not provide an effective toughening method over larger lengths scales of tens of mm's and toughening response mechanisms linked to changes in delamination resistance should be verified via fractography.

Material 4 was the only particle toughened material system which did not show a significant drop in toughness with crack propagation and maintained a fairly self-similar crack propagation (flat R-curve) after the first 5 mm of crack growth. It also appeared to have the most even interlayer thickness out of all the particle toughened systems. Therefore, material 4 will be interrogated further using high resolution *in situ* XCT and Synchrotron Radiation Computed Tomography to

capture the crack transitions and ascertain which micro-scale features or damage response mechanisms contribute to the observed crack path transitions during delamination.

Chapter 4 *In situ* Analysis of Crack Path Transitions of Mode I Loaded Particle toughened Carbon Fibre Reinforced Polymer Composites Using 3D X-ray Computed Tomography

4.1 Introduction

Carbon fibre reinforced polymer composites (CFRPs) have long been recognised for their advantageous specific mechanical properties, particularly stiffness and strength, making them desirable for applications such as aircraft, wind turbines, performance road vehicles, and pressure vessels [9, 33, 216, 217]. However, the damage resistance and damage tolerance of composite materials, particularly concerning impact loading, is an established and widely researched problem [15, 35, 42, 52, 60, 218-220]. Low velocity impact, where subsurface crack and delaminations are initiated beneath the impact site with barely visible damage on the surface, can be difficult to detect and predict and, therefore, can be particularly detrimental to structural damage tolerance [58]. Such impact events and damage are common and can be caused by a range of impacts related to service in the aerospace industry, such as dropped tools, bird strikes, and hail [221, 222]. It is widely thought that matrix cracks initiate within plies: these cracks then initiate delaminations when they reach an adjacent ply of differing fibre orientation [56, 58, 223]. It is these delaminations which are reported to be particularly detrimental to the stiffness and strength of the composite where the initial opening of the initiation of the delaminations under impact is reportedly dominated by Mode I loading, and propagation by Mode II loading [43]. Various methods have been proposed to increase damage resistance and therefore overall structural impact resistance and post-impact damage tolerance. These include z-pinning/stitching, and interleave methods, such as particle toughening [15, 52, 108, 214, 224]. Despite the significant improvements in fracture toughness achieved by z-pinning, there are also some major drawbacks, such as the decrease in in-plane mechanical properties, high cost, non-automated production, and lack of certification in certain sectors (such as aerospace) [225]. Thermoplastic toughening particles on the other hand have been widely adopted in industry due to ease of manufacture and reduced detriment to in-plane mechanical properties [102]. The inclusion of toughening particles has been shown to increase Mode I and Mode II delamination toughness, whilst improving compression after impact strength (for an equivalent impact damage area) by up to 100% [15, 60].

Despite the improvements achieved, challenges remain in optimising the effectiveness of thermoplastic toughening. One particular concern is that toughening mechanisms and the increased initiation and propagation toughness associated with the inclusion of toughening particles can only be maintained if the crack propagates within the toughened interlayer. Reductions in toughness have been related to crack transitions from within the toughened layer, into the fibre-matrix interface [49, 84]. Whilst a transition into the adjacent fibre-containing plies may in some cases induce large-scale fibre-bridging (potentially increasing toughness as the crack extends), such bridging is generally considered to be an artefact of Mode I testing in unidirectional composites that is unlikely to occur in multidirectional laminates for structural applications [69, 210, 226]. Hence, investigating the causes of transitions of delamination cracks from the toughened interlayer to the adjacent plies (either at the surface of the fibre bed or into the ply itself) is potentially important for optimising the toughness response of materials for structural applications.

Research conducted by Borstnar *et al.[49],* and later Xie *et al.* [179]*,* used finite element models to interrogate the crack path of a 2D crack through a particle-toughened interlayer over a crack propagation length scale of tens – 100's of microns. Both studies identify particle spacing, particle volume fraction, and relative adhesive bond strengths between the fibre-matrix and particle-matrix interfaces to be factors in determining the crack transition to the weaker fibre-matrix interface. Work by Fritz *et al.* [215]*,* explicitly reported interlayer features in a range of commercial CFRP systems such as tow-aligned resin pockets (or TARPs), sub-micro voids, and misplaced fibres. Although no link has yet been made between these features and damage initiation or propagation, based on previous evidence from the authors it was postulated that such features could act as a precursor to damage initiation. Fritz *et al.* hypothesised that a multiscale microstructural hierarchy could contribute to damage initiation and propagation leading to crack transitions, where the consequence of uneven particle distribution could increase the likelihood of features such as TARPs, which in turn could have an indirect effect on damage initiation within the intralayer or interlayer of the composite [215]. The research presented in this work builds on these previous studies, working at the length scale of fibre tows to identify potentially controlling features of the interlayer architecture, and relating the material response to the macroscopic toughness response of different laminates*. In situ* and *ex situ* imaging of unidirectional particle-toughened CFRP's under Mode I delamination has been carried out and used to identify regions of crack transition from the interlayer to the intralayer (i.e. trigger regions), and map them back to the specimen microstructure.

4.2 Materials and Test Methodology

A particle-toughened CFRP material system was supplied by Solvay Composite Materials. The material was cured using a proprietary aerospace autoclave cycle. Double cantilever beam (DCB) samples were prepared, conforming to ASTM D5528 [70], consisting of a 26-ply unidirectional layup, with a 25 mm wide, 40 µm thick, polytetrafluoroethylene (PTFE) insert placed at the mid-plane in order to create a blunt crack and control the initiation of fracture. Specimens were a standard size of 254 mm in length and a 25 x 5 mm cross-section. Secondary phase particles were dispersed in the interlayer of several of the materials, where the nominal V_f (precure volume fraction) is proprietary. The four samples used in this chapter are from material system 4 where the material constituents were described previously in Chapter 3.

4.2.1 Laboratory Based X-ray Computed Tomography *In Situ* Method

Three specimens of the same material system were tested using a stepped wedge opening of the DCB specimens, similar to the method reported by Borstnar *et al.,* [80]. A wedge was inserted into the initially cracked region of the specimen, without introducing crack propagation beyond the PTFE insert. The specimen was then secured using a 3D-printed polymer base, and secured to the stage of a custom Nikon 450/225 kVp Hutch system using the 225 kVp X-ray source and Perkin Elmer 1621 flat panel detector.

Each specimen was scanned before and during crack propagation to capture the original state of the material, allowing retrospective correlation of damage mechanisms with the undamaged microstructure. Scan settings for laboratory CT imaging of the undamaged and damaged condition are reported in Table 5. Coupons were positioned close to the X-ray source to ensure the highest resolution that would allow coverage of an acceptable width of the specimens while keeping the detector close enough to minimise the scan times. This was found to correspond to a voxel size of 5.2 µm, leading to a region of interest (ROI) of 10.4 mm x 10.4 mm x 10.4 mm for each scan. X-ray power was adjusted to achieve a similar nominal source spot size (*i.e.* ≈5 µm). Approx. 10 mm at the centre of the width of the specimens was imaged, as illustrated in Figure 30. For the undamaged state, longer duration scans have been used to ensure high-quality images of the microstructure. Centre-of-rotation shuttling was used to remove ring artefacts, requiring a stop-start rotation mode that increased the scan times. Subsequently, faster scans were used to distinguish features of interest during crack propagation. Shuttling was not used, along with a halving of the number of collected frames per projection and a slightly lower number of projections, resulting in scan times of approximately 82 minutes each. An area ahead of the insert of 50 mm x 10.4 mm was scanned by concatenating a series of sequential scans along the long

axis of the sample. The displacement of the wedge was controlled via a simple screw device (see Figure 29). The wedge was inserted until the crack was seen to visibly propagate. At this point, the area containing the crack tip was then scanned. This process was repeated until the crack reached the end of the undamaged scan region, typically involving some six to seven propagation steps.

Table 5 Scan settings

	Undamaged 5.2 µm	**Damaged 5.2 µm**
Mag position	62.70	62.70
Detector position	-939.15	-939.15
Energy [kV]	120	120
Power [W]	11	11
Exposure time [s]	500	500
Projections [-]	5000	4800*
Frames per proj. [-]	4	2
Shuttling	On	Off
Scan time [h, min]	5 h	1 h 22 min

HUTCH system, source 225, target material W, detector FP, no filtration.

* value is chosen to keep scanning time below 1 h 22 min for system calibration purposes.

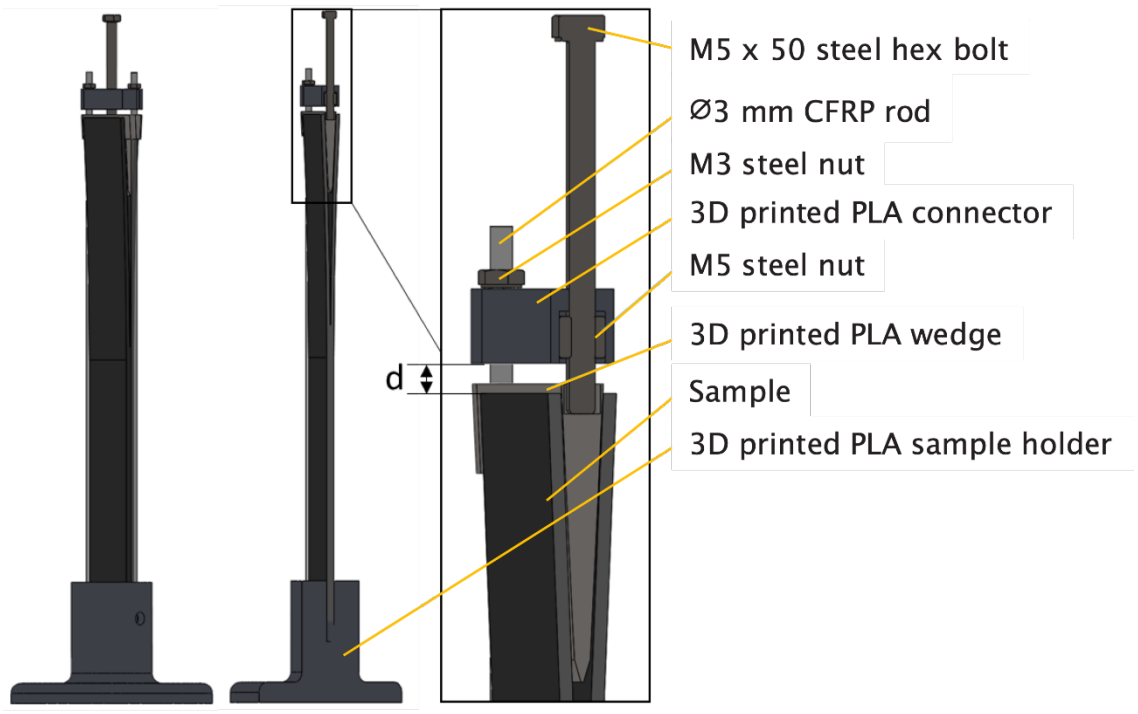

Figure 29 Manual apparatus parts description. The M5 bolt is rotated to push the wedge into the specimen. The M5 steel nut locked in position inside the PLA connector allows the displacement of the wedge.

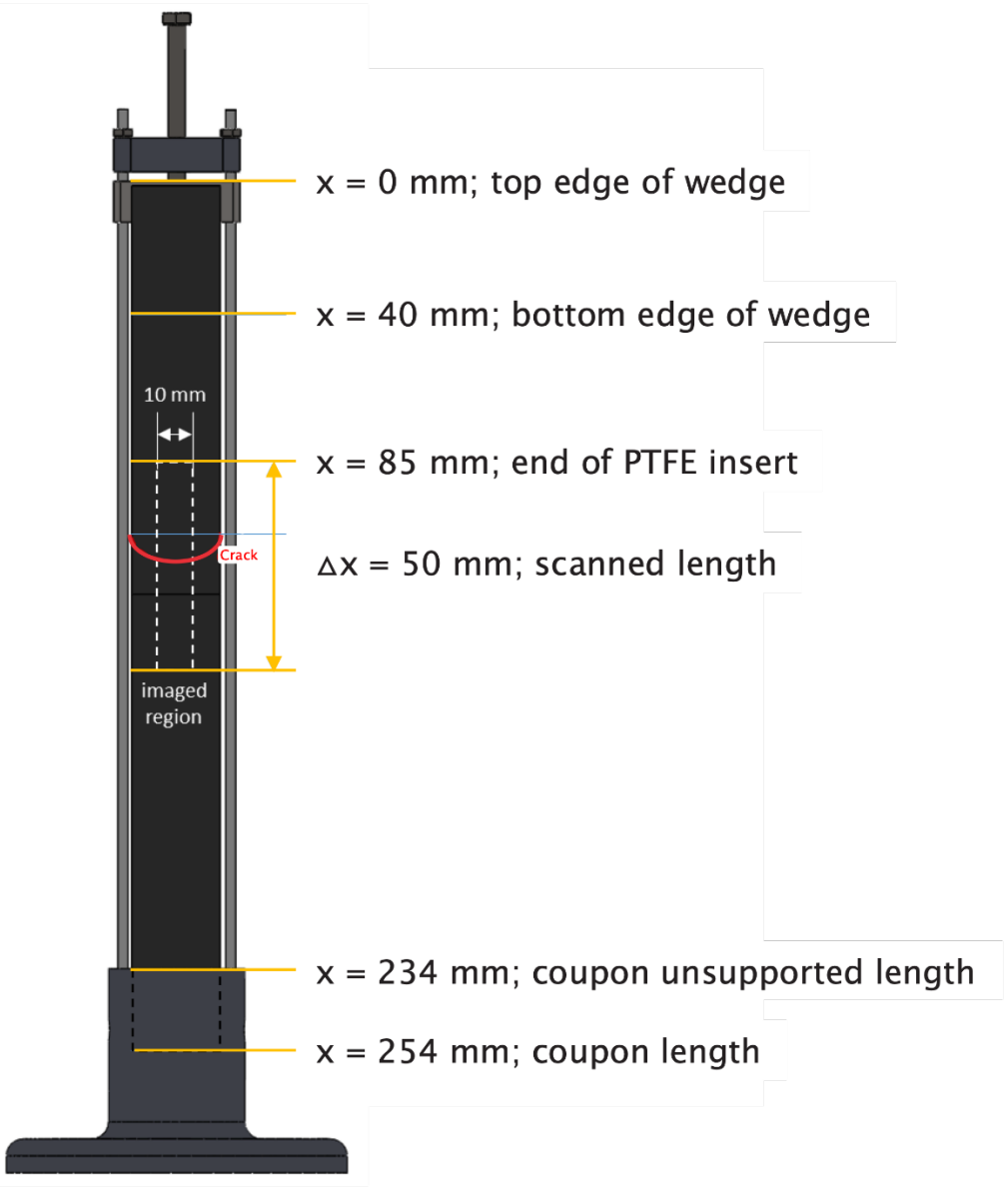

Figure 30 The pre-imposed blunt crack and the imaged region relative to coupon length, wedge apparatus, edge and base positions.

Upon completion of the *in situ* experiment, the specimen was separated using a razor blade to analyse the fracture surface *ex situ.* Optical macroscopy was used to obtain images of the entire fracture surface. From these macrographs, key features were mapped and compared to the undamaged scans. Furthermore, key features were interrogated in more detail using scanning electron microscopy (SEM) to analyse the crack location and crack path transitions within the composite.

4.2.2 Scanning Electron Microscopy

SEM was used to obtain higher resolution and better depth-of-field images of the fracture surface. One side of the fracture surface was cut into a 50 x 25 mm section using a diamond edge low-speed cutting saw at 200 revolutions per minute. The fracture surface was gold sputtered for forty seconds. Each sample was then placed on an aluminium specimen stage, with a piece of conductive tape connecting the gold-sputtered surface to the stage to prevent charging of the fracture surface. The specimens were scanned using a JEOL JSM7200 LV SEM. A working voltage of 2 kV was used at a working distance of ≈ 35 mm.

4.2.3 Fracture Surface Analysis: Trigger Region Mapping

A trigger region is identified here as a location on a fracture surface where the crack transitions from the particle-toughened interlayer into the neighbouring fibre-reinforced ply of the composite; this transition commonly appears to occur in highly localised regions on the macro-scale (regions typically in the order of several fibre widths) creating 'finger-like' structures on the fracture surface as the crack continues to propagate as shown schematically in Figure 31, where the crack direction propagates from right to left. The identified trigger regions were limited to those within the field of view (FOV) of the X-ray CT (XCT) imaging. After removing the region of interest scan artefacts, this equated to an approximately 7.5 mm wide strip (with respect to the centre of the sample), and 50 mm length. A certain proportion of the trigger regions (*circa* 30%) was identified as being immediately adjacent to the PTFE insert and these were therefore not included in the analysis (*i.e.* considered unrepresentative of the material itself). After identifying the trigger regions on the fracture surface for each specimen, SEM was used to characterise the crack transition at each location. Using ImageJ [227] the location of the coordinates of the trigger regions with respect to the end of the insert and the centre of the specimen was measured. Using these coordinates the corresponding regions in the undamaged CT scan volumes could be found and microstructural features related to the crack behaviour.

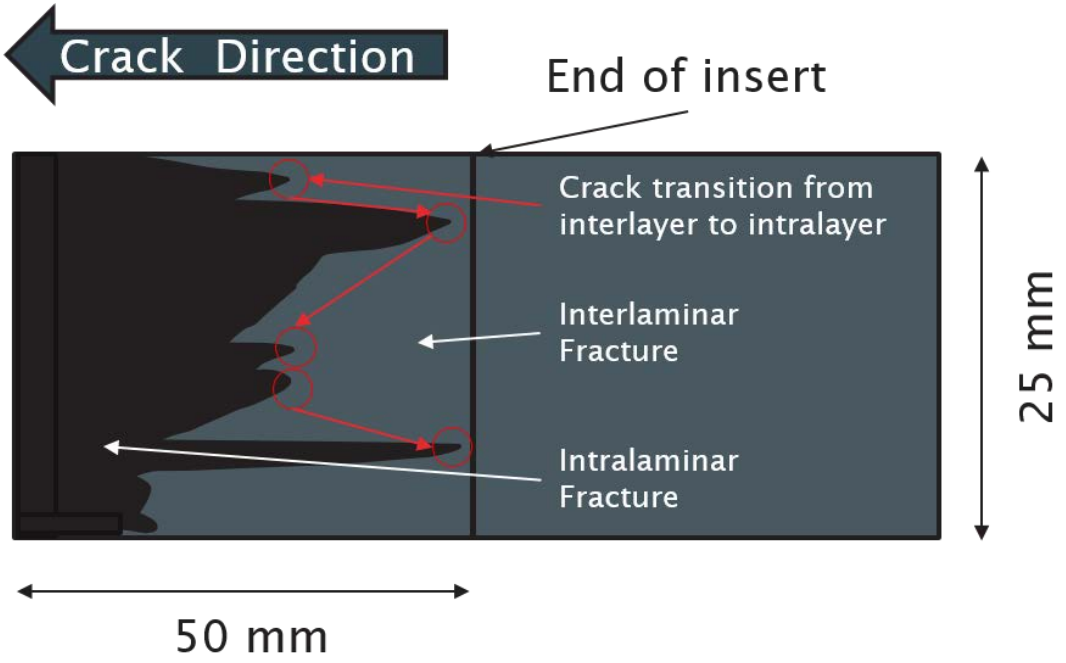

Figure 31 Schematic of crack transition on the fracture surface of a DCB specimen. Local regions of crack transition from the interlaminar region to the intralaminar region are circled.

4.2.4 Synchrotron Radiation Computed Tomography

Phase-enhanced synchrotron X-ray computed tomography was additionally carried out on one specimen at the European Synchrotron Radiation Facility (ESRF) using beamline ID 19, Grenoble, France. The specimen was secured to the rotate stage in an *in situ* loading rig similar to that described previously, but modified for the dimensions of the ESRF rotate stage (refer to Appendix B). The specimen was scanned at a voxel resolution of 0.65 µm, giving a field of view FOV per scan of 1.664 x 1.404 mm using a 2560 x 2160 pixel camera. A beam energy of 19 keV and radiographic exposure time of 30 ms was used, with five thousand projections being taken for a 180^{o} rotation, allowing for ROI "padding" to reduce artefacts caused by scanning a small area of the specimen [228]. The detector was placed at a propagation distance of 55 mm using phase-enhanced contrast in the edge-detection regime [229]. The data was reconstructed using in-house software pyHST (High-Speed Tomography in a Python^{TM} version) [230].

The experimental procedure was similar to that described for the laboratory based *in situ* study with some key differences: the specimen was not scanned before the introduction of damage, as the higher resolution allows for the identification of key features even with the presence of a crack. The crack was propagated beyond the insert and scanned at the crack tip with respect to the central portion of the sample. This process was repeated for three load steps.

4.3 Results

4.3.1 Fracture Surfaces

The fracture surfaces of the three repeat tests are shown in Figure 32, these are comparable to material 4 in Figure 23 as they are from the same material system. The areas of interlaminar fracture, where the crack propagates through the particle-toughened interlayer, can be identified with the lighter grey regions, and the regions of intralaminar fracture with the darker regions. Trigger regions have been circled on each fracture surface. In general, they appear to be highly localised, and then spread laterally as the crack continues to propagate. The number of trigger regions and the crack propagation at which the entire crack transitions to the ply varies somewhat between samples.

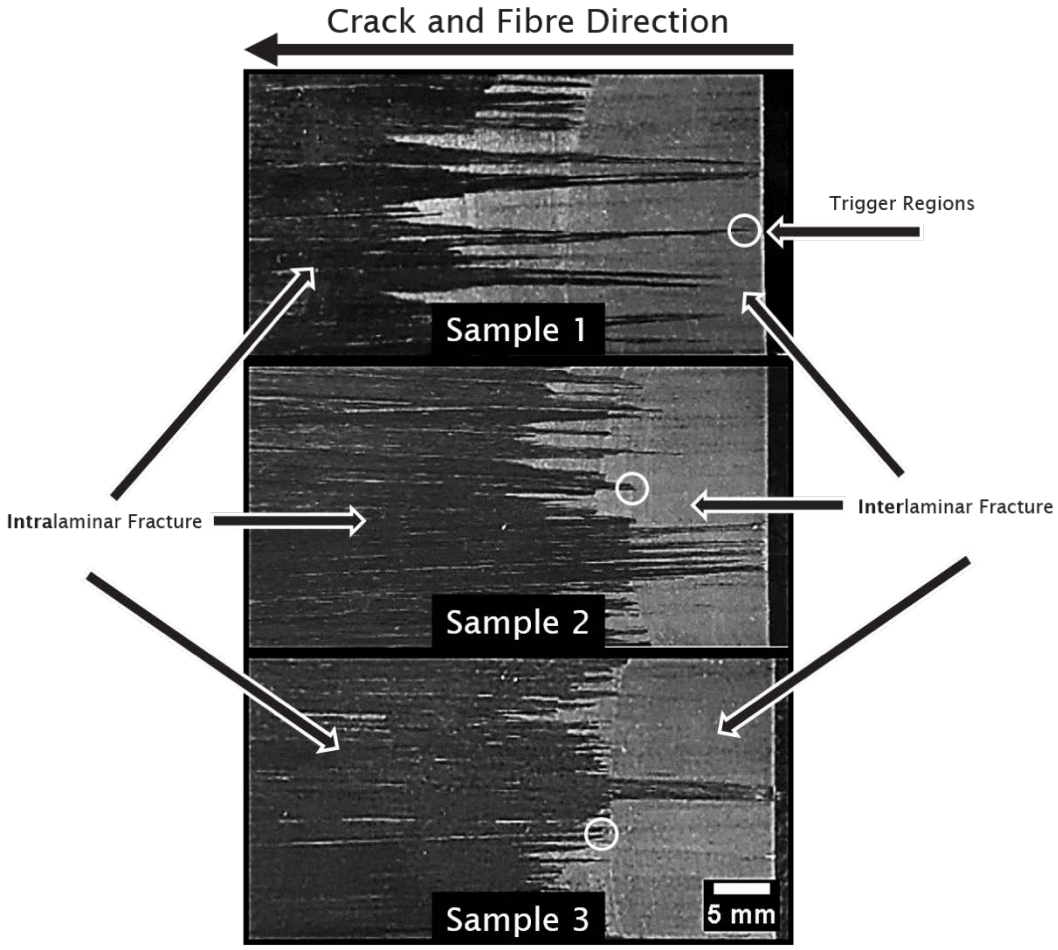

Figure 32 Comparison of fracture surfaces from three specimens of material system 4 (comparable to material 4 in Figure 23).

4.3.2 Surface Fractography and XCT

A total of ten trigger regions were clearly captured in the lab CT datasets, with, two, four, and four captured for Sample 1, Sample 2, and Sample 3 respectively. Each sample showed more regions than this: Figure 33, Figure 34, and Figure 35 show a red shaded area representing the CT scan area and hence only trigger regions within this area have been assessed. 'Beach' marks are also visible on the fracture surfaces of each material system, representing the increments of crack extension.

The two trigger regions identified within the scanner area for sample Sample 1, were seen to correlate to tow gaps in the undamaged XCT scan volumes. The SEM image of trigger region 1 in Figure 33, shows the crack in the particle-toughened interlayer on the right-hand side of the image. The crack appears to make the initial transition into the ply over a crack front region of several fibre widths, spreading out to several 100 μm's, equivalent to tens of fibre widths, and then seeming to stabilise (at that viewing scale). In comparison the second trigger region is more complex, spreading over a somewhat larger area (≈2 – 3 times wider). In all cases, once part of a crack front has made the transition, it stays within the ply until it eventually converges with adjacent transitioned crack regions and the entire crack path falls within the ply of the composite.

Four transition regions have been identified in the ROIs of Sample 2 and Sample 3 as seen in Figure 34 and Figure 35, with local morphologies broadly similar to those, seen in Sample 1. All but the first trigger of Sample 2 were seen to be correlated with tow gaps. Trigger region 1 of Sample 2 correlates with the presence of a TARP. The trigger region associated with the TARP appears to have a different transition morphology: instead of transitioning over the width of a few fibres and spreading, the transition occurs across a single block of fibres simultaneously. The SEM images in Figure 34 have a discernible depth of field at the crack transition regions. When the crack transitions at trigger regions 1, 2, and 3 in Sample 2 it does so in the depth-wise direction of the page, indicating a transition of several fibres into the ply (confirmed by SRCT imaging below). It is noted that the side of the fracture surface observed will of course dictate whether the transition appears into, or out of the page.

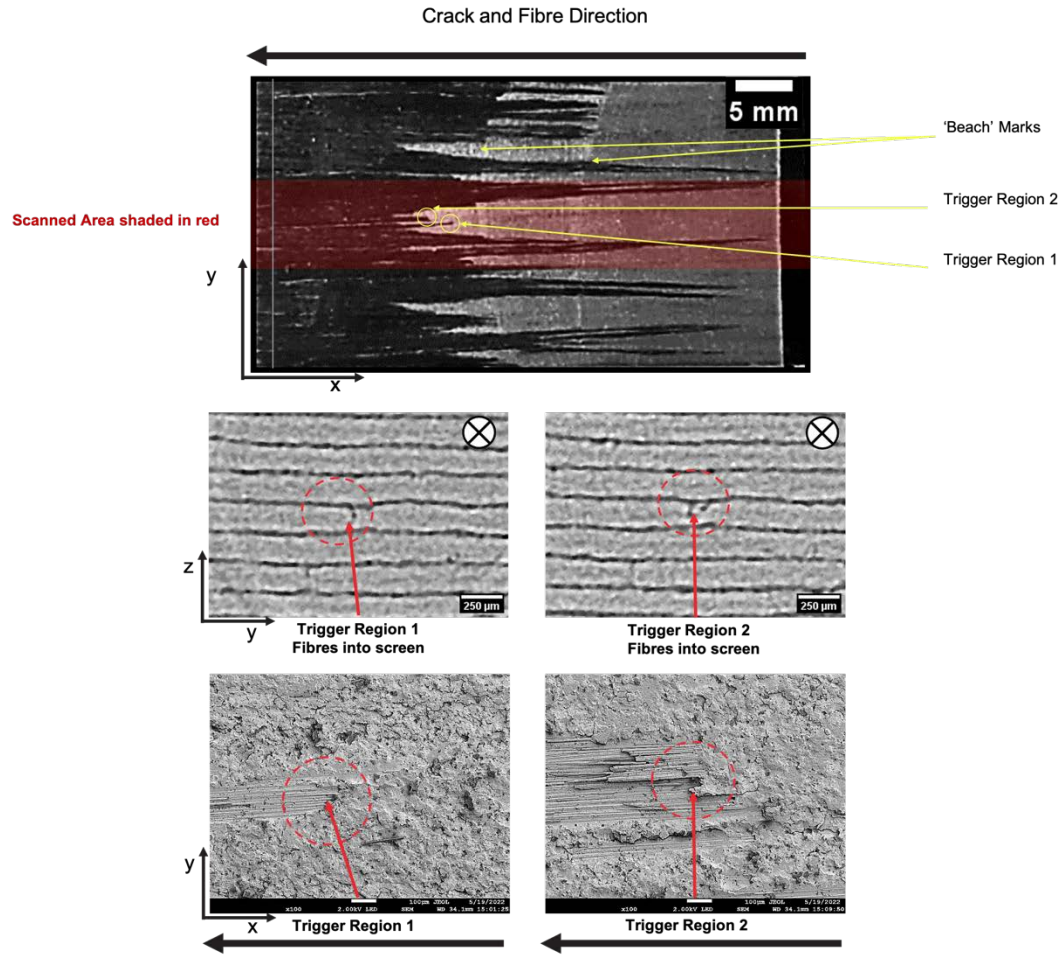

Figure 33 Mapped trigger regions within the scanned area of specimen Sample 1 shown in Figure 32. a) The fracture surface showing the scanned area, mapped trigger regions and 'beach marks. b) XCT mapping of trigger regions with fibres going into the page. c) SEM mapping of trigger regions showing the transition from interlaminar to intralaminar fracture.

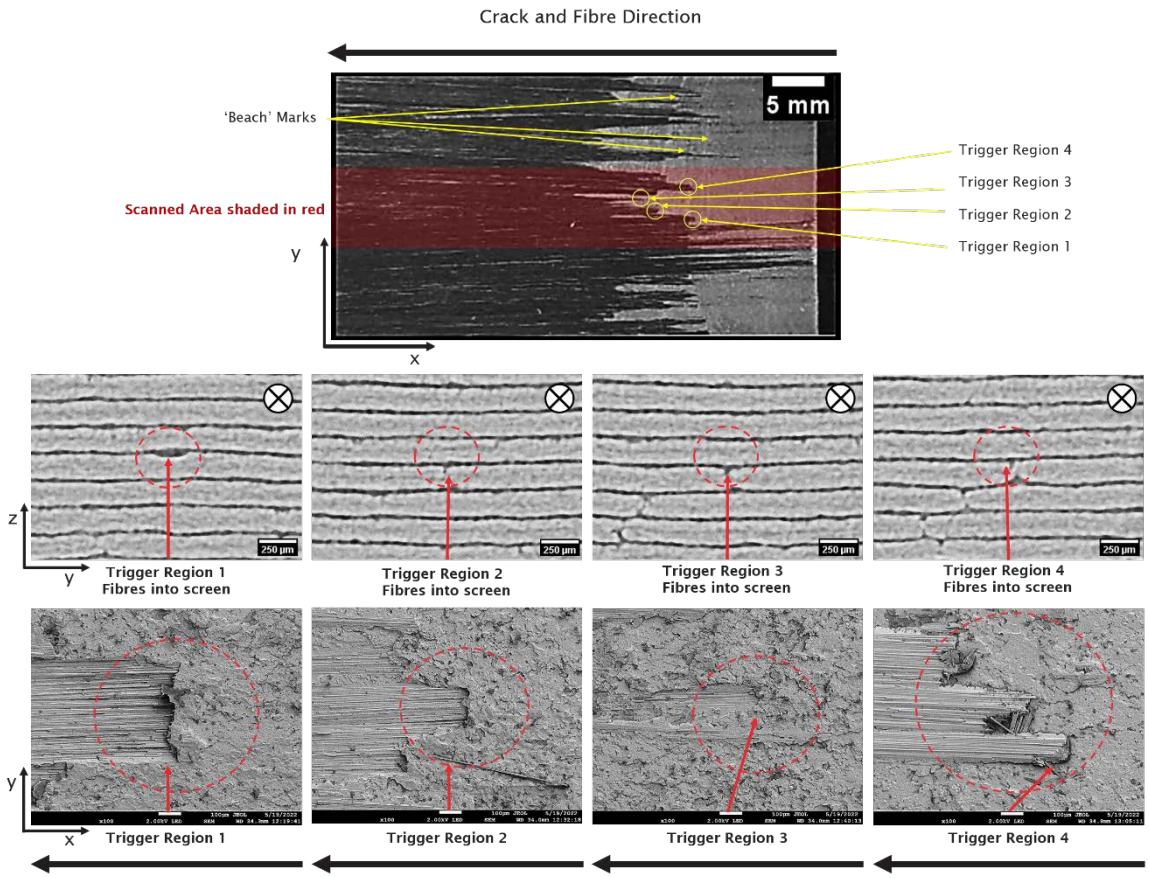

Figure 34 Mapped trigger regions within the scanned area of specimen Sample 2 shown in Figure 32. a) The fracture surface showing the scanned area, mapped trigger regions and 'beach marks. b) XCT mapping of trigger regions with fibres going into the page. c) SEM mapping of trigger regions showing the transition from interlaminar to intralaminar fracture.

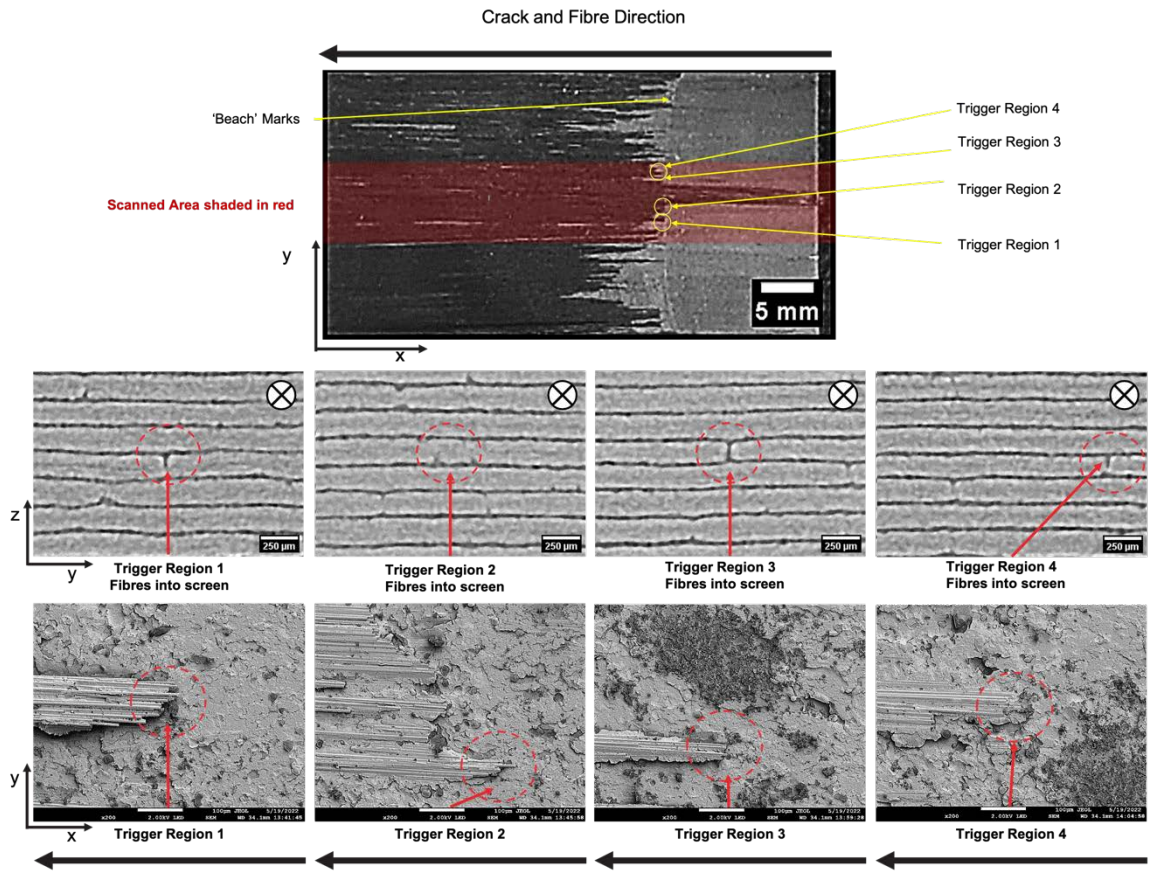

Figure 35 Mapped trigger regions within the scanned area of specimen Sample 3 shown in Figure 32. a) The fracture surface showing the scanned area, mapped trigger regions and 'beach marks. b) XCT mapping of trigger regions with fibres going into the page. c) SEM mapping of trigger regions showing the transition from interlaminar to intralaminar fracture.

4.3.3 SRCT

SRCT scan volume slices through the cross-section of Specimen 4 during crack progression in three load steps are shown in Figure 37. At this 0.65 µm voxel size individual fibres can be distinguished in the ply as well as toughening particles in the interlayer. There are both TARPs and tow gaps present, where the former are regions of significantly increased interlaminar thickness which are also aligned with the direction of the fibres [215] and appear to take on a more rounded morphology (as shown in Figure 36a) whereas the latter is a gap between tows and appears as a resin rich region through the entire thickness of the ply and is aligned with the direction of the fibres (as shown in Figure 36b). Figure 37a shows that for load step 1 the entirety of the crack is in the interlayer within the FOV. As the crack propagates in load step 2, shown in Figure 37b the area around the new crack tip is scanned, it can be seen that on the left-hand side, a secondary crack has initiated within the ply, running alongside the crack within the interlayer. Furthermore,

on the right-hand side of the images, the crack appears to have transitioned into the opposite ply. The third load step shown in Figure 37c shows that the crack has more fully transitioned into the lower ply, with fibres visible within the crack, *i.e.* evidence of fibre-bridging. On the right-hand side of the image, a region of the crack front is within the upper ply, with a small overlap region of simultaneous cracking within both plies.

Figure 38a shows a section through the plane of the crack after the first load step, fragments of resin at the crack tip can be observed as well as particles debonding from the matrix ahead of the main crack. A similar observation can be made in Figure 38b which is in the orthogonal plane where the main crack is propagating from left to right and two particles ahead of the crack tip can be seen to have debonded from the matrix.

Figure 39 shows orthogonal slices at various notable regions at the end of the second load step, Figure 39a shows the region to the left of the secondary crack in Figure 37b, where the crack remains in the interlayer. Figure 39b shows a section which cuts through the bifurcation point where the crack can be seen to transition to the fibre-interlayer interface region where it then propagates. Finally, Figure 39c shows a section where the secondary crack is fully embedded in the lower ply, there is no evidence of bridging fibres in this section as it appears to run cleanly across the fibre-matrix interface.

Figure 40 similarly shows sections at the end of load step 3. Figure 40a is the region where the cracks running along the interfaces on either side of the interlayer overlap and Figure 40b shows a section taken through a plane where the crack is embedded fully in the upper ply, in this section however, it can be seen that there is evidence of fibres bridging the crack opening.

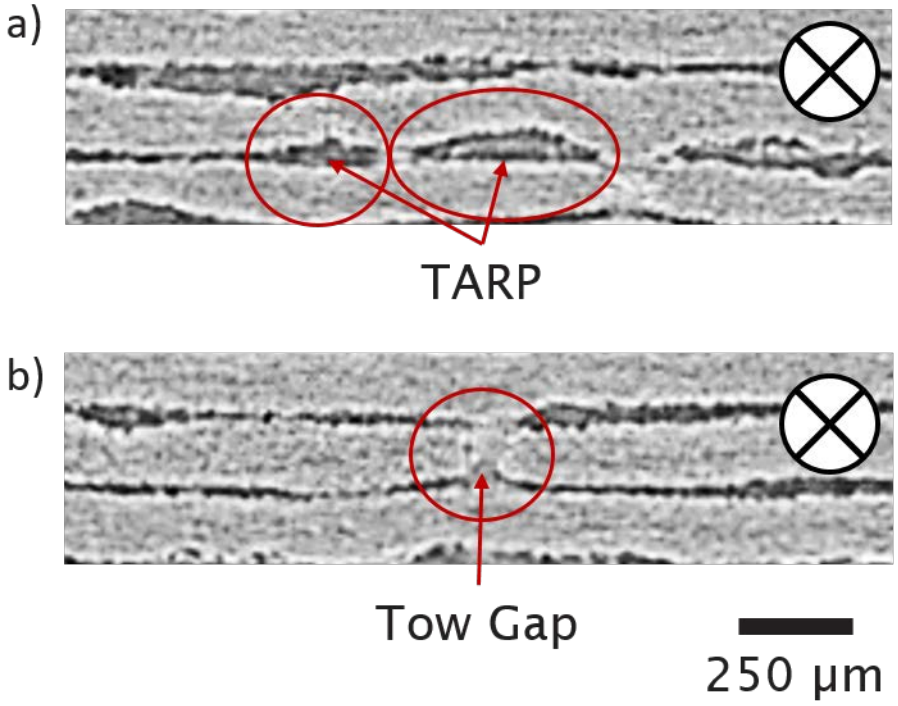

Figure 36 XCT images with the fibres going into the page. This figure is for illustrative purposes only to clarify the difference between a TARP in a), and a tow gap in b).

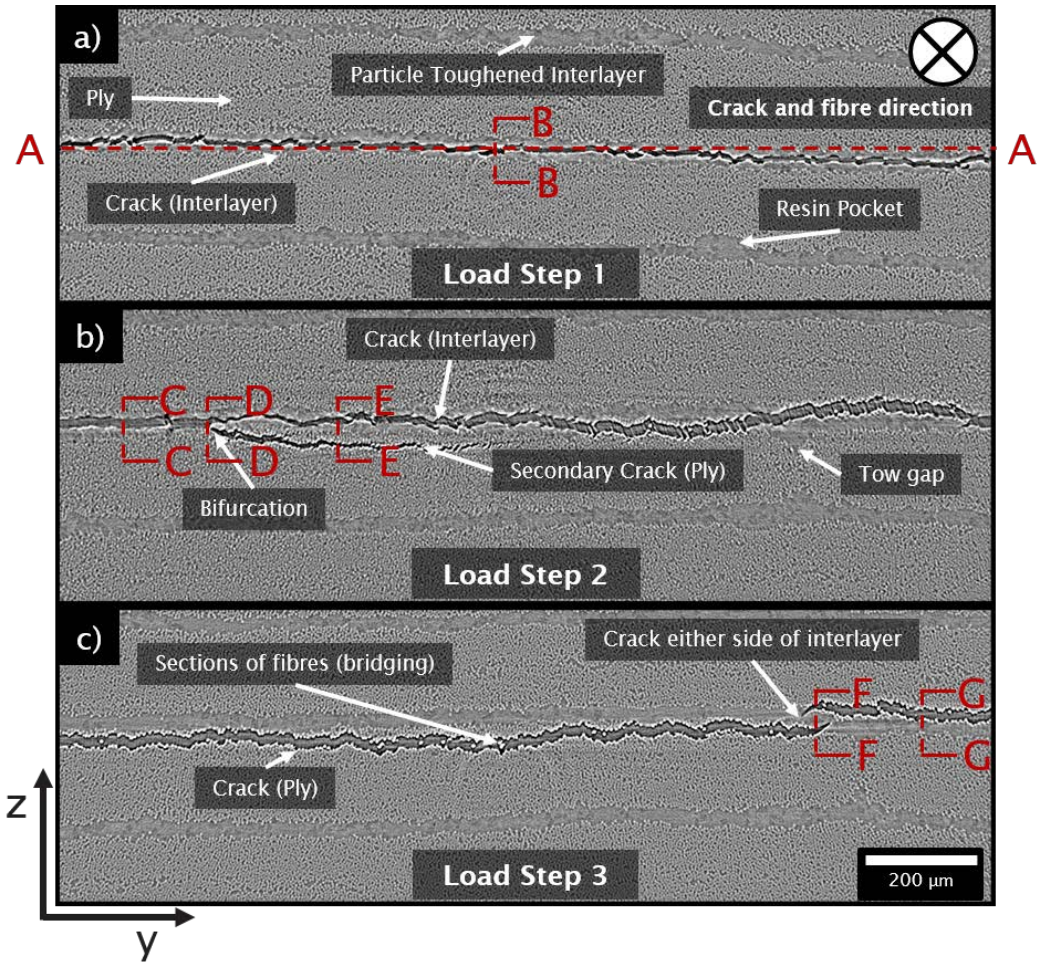

Figure 37 SRCT images slices during the crack path transition into the ply across three load steps, where a) is the first slice is approximately 12 mm ahead of the insert, b) is the second slice 15 mm ahead of the insert and c) is the third slice 16 mm ahead of the insert. The reader should note the orientation of the axis for comparison in Figure 38, Figure 39, and Figure 40.

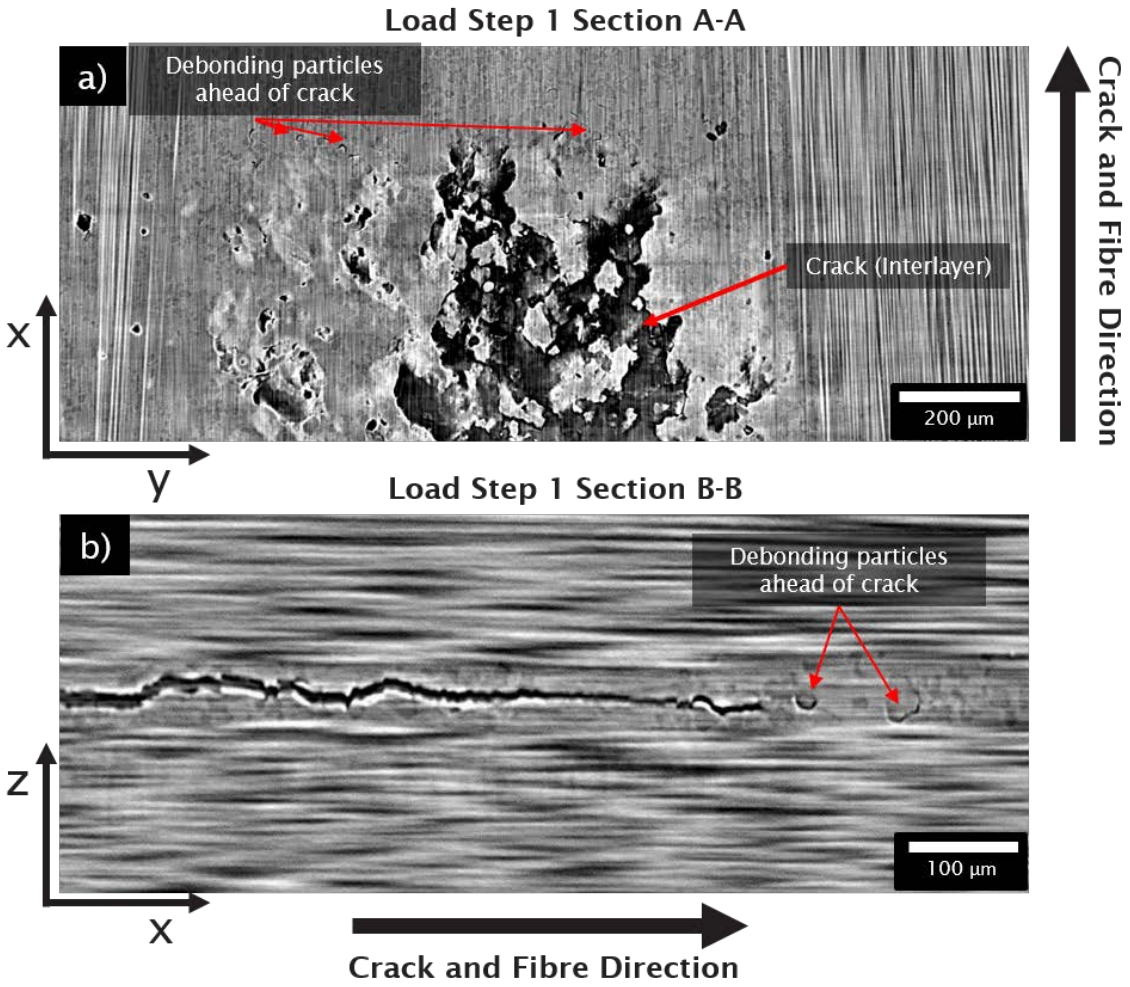

Figure 38 SRCT images through orthogonal planes during load step 1, a) shows a slice through section A-A where the crack is travelling from the bottom of the image to the top and debonding toughening particles can be observed ahead of the crack front in the interlayer, and b) shows a slice through section B-B where the crack is travelling from left to right and toughening particles are debonding ahead of the main crack. The reader's attention is drawn to the orientation of the axis relative to Figure 37.

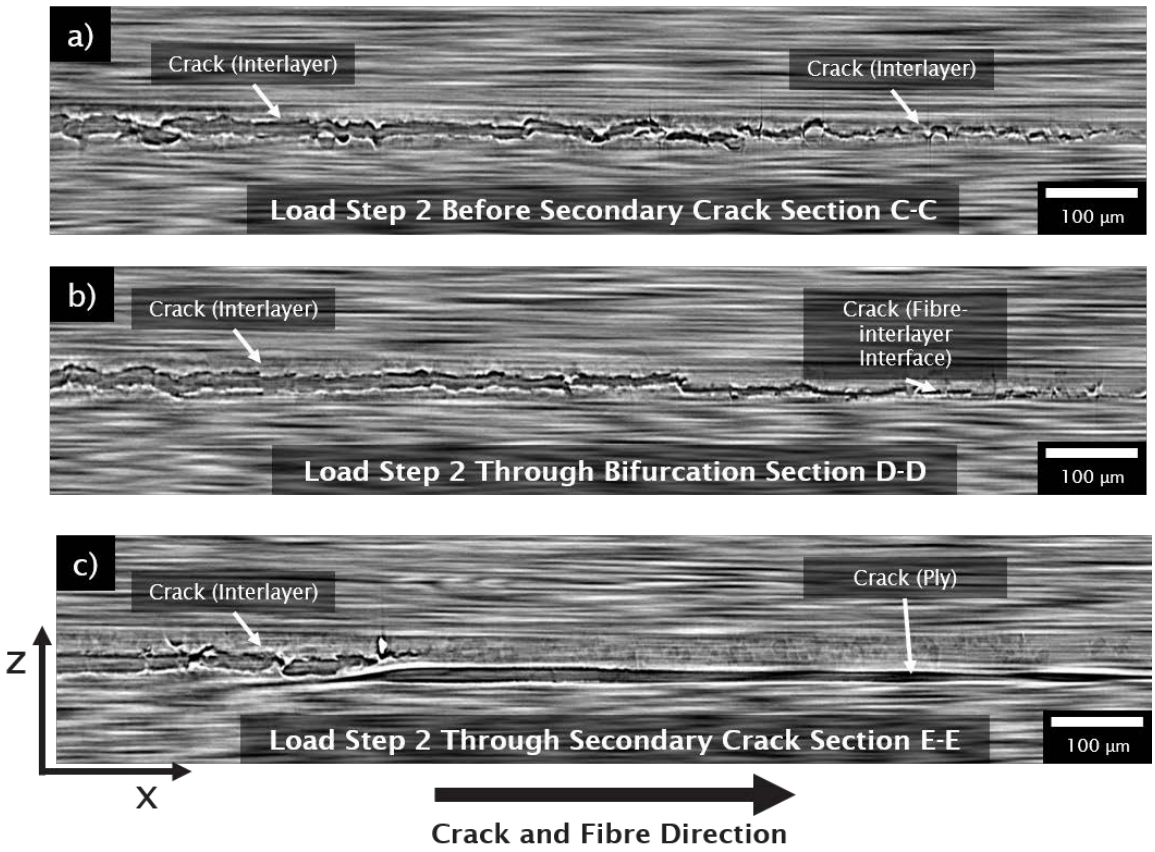

Figure 39 SRCT image slices during load step 2, a) shows a section where the crack remains in the interlayer before the bifurcation and secondary crack, b) shows a slice at the bifurcation where the crack transitions to the fibre-interlayer interface, and c) shows a section through the secondary crack, where the crack remains in the ply. The reader's attention is drawn to the orientation of the axis relative to Figure 37.

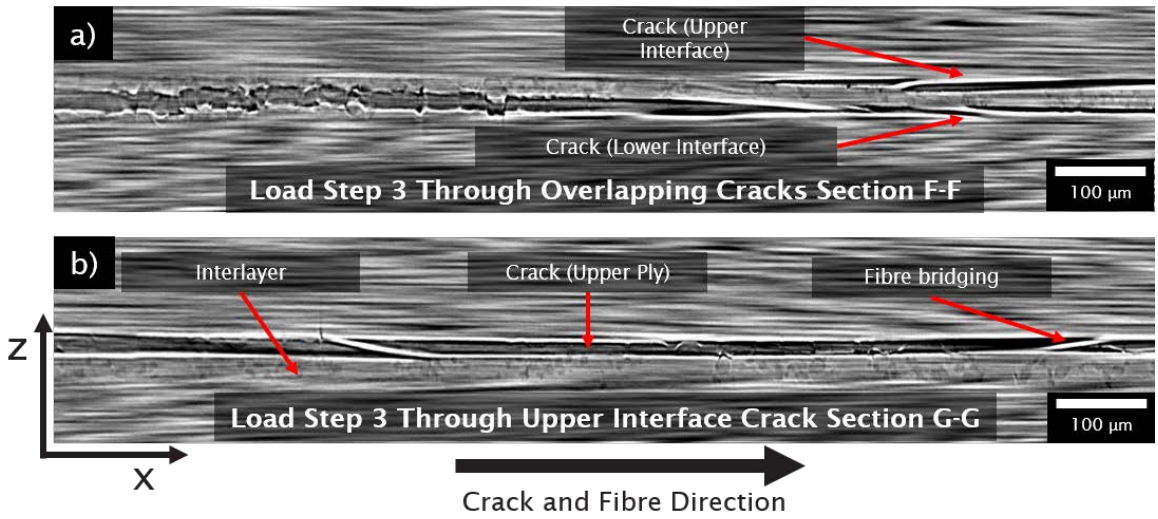

Figure 40 SRCT images slices during load step 3, a) shows a section through the overlapping cracks on either side of the interlayer and b) shows a section where the crack is fully embedded in the upper ply. The reader's attention in drawn to the orientation of the axis relative to Figure 37.

4.4 Discussion

4.4.1 Macro-scale crack transition

There is some distinct variation in the crack path transition behaviour between the three specimens shown in Figure 32. Despite all specimens being from the same material/manufacturer, the rate at which crack transition occurs across the whole specimen width varies, as does the total number of trigger regions across the surface. Furthermore, the lateral crack transition behaviour between specimens is not entirely consistent, with Sample 1 showing the longest 'fingers' and greatest path length to full transition, occurring at around 30 – 35 mm of crack growth. Whereas specimens Sample 2 and Sample 3 have more trigger regions and the full transition occurs at approximately 20 -25 mm of crack growth. As crack transitions appear to be controlled by tow-level features, this behaviour appears consistent with the somewhat stochastic nature of the composite mesostructure, *i.e.* the variable rearrangement of tows during processing, and hence across a sample width of 25 mm, there are many tows and therefore a large scope for variability between samples of the same materials systems.

4.4.2 Interlayer architecture

The mapped transition regions to the undamaged scans in Figure 33, Figure 34, and Figure 35 show that nine out of the ten mapped regions occur at gaps between fibre tows and one occurs around a resin pocket. Therefore, the data available suggests that transitions from the interlayer to the ply occur at inconsistencies or variations with respect to the mean interlayer geometry, in keeping with Fritz *et al's [215]* suggestion that TARPs could be precursors of crack transition both to and from the interlayer. Tow gaps appear to play a more prominent role in the current work, however.

4.4.3 Mechanistic insight into crack transitions

Figure 41 identifies schematically five potential damage mechanism sequences that are consistent with the observations from this work. For all images, the fibres and crack extend into the page, the fibres, and by extension, the ply, are the blue circles, and the idealised circular toughening particles are orange and distributed in the interlayer as shown in Figure 41a. Debonding sites which could arise during Mode I loading at the particle matrix interfaces are shown in Figure 41b by the red interfaces around them. The crack being driven into the page could then develop into mechanism 2 depicted in Figure 41c where the crack remains within the particle-toughened interlayer. Within this depiction, it is assumed that the debonding of toughening particles ahead of the crack path allows the crack to remain within the interlayer without any crack path transition. Although the crack is illustrated in the plane perpendicular to its growth, the extension of the crack into the page is still the dominant mode of extension.

If crack growth into the TARP is considered then a lateral extension of the crack into the ply could be feasible allowing for part of the crack to become embedded as the crack is further extended into the page with loading, as seen in Figure 37, and shown schematically in Figure 41d. Around the tow gap where the toughening particle falls between the fibre tows, the fibres in its vicinity could also debond. The coalescence of this crack with debonded fibres or a lateral extension into the ply could cause the crack to become "trapped" and propagate further within the ply. The intralaminar part of the crack front becomes dominant due to the likely lower strain energy required to propagate a crack along the fibre matrix interfaces compared to within the toughened interlayer.

Mechanism 4 hypothesises that the primary crack front turns into the interlayer. Schematically this mechanism, as shown in Figure 41e, looks similar to that shown in Figure 41d. However, the key difference is that the crack turning in Figure 41e does not rely on the initiation of fibre-matrix

debonds or lateral edging into the ply, but rather is a propagation process where the crack transitions laterally into the ply without overlapping with an interlaminar crack.

The final mechanism is shown in Figure 41f. After the crack becomes “trapped” within the interlayer, further loading causes additional crack propagation. The lower strain energy required to drive the intralaminar portion of the crack causes this to become the preferred path, and no further damage is observed in the interlayer. Considering that once a portion of the crack propagates along the lowest energy path which is assumed to be the fibre-matrix interface in this mechanism, it is unlikely it will transition back to the more energy absorbing path within the toughened interlayer. Therefore, if enough of these local events were to occur across the width of a specimen during crack propagation a greater proportion of the crack front could become embedded in the ply.

Based on the evidence obtained, a likely mechanism for crack transition would seem that the TARPs and tow gaps could be allowing the interlayer crack a route into the ply via lateral propagation perpendicular to the crack growth direction, via turning or coalescence with fibre matrix debonds around the gap. This is in comparison to a uniform interlayer where the crack could be driven into the fibre bed around misaligned fibres. The SRCT image and long fingers of intralaminar growth show that both an intralaminar and interlaminar crack can run concurrently for tens of mm’s and overlap each other during the transition process.

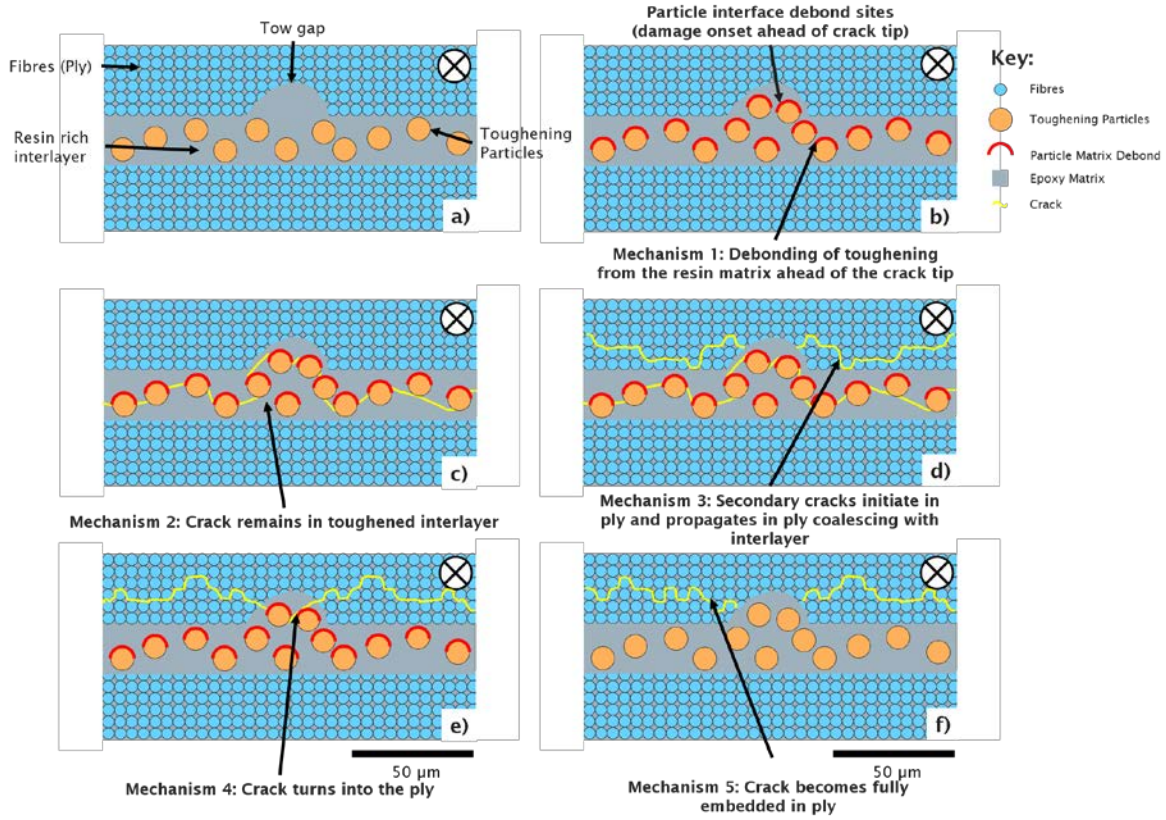

Figure 41 Potential crack transition mechanisms at a tow-gap-like feature.

4.5 Conclusions

Localised “trigger” regions, where the crack transition from the particle-toughened interlayer into the ply, have been identified in this work. Of the 10 such regions identified here, nine were correlated with gaps between the fibre tows and the tenth was associated with a TARP, *i.e.* such mesoscopic features appear to strongly influence crack path transitions, at least in the toughened material system investigated in this work. High-resolution SRCT of crack extension appeared to show an interlaminar and intralaminar cracking growing concurrently. It is then evident that intralaminar cracking subsequently becomes dominant. Furthermore, the results show that a given crack can bifurcate into the plies on both sides of the interlayer at different locations.

Five potential mesoscale mechanisms for crack transition associated with tow gaps have been identified in this research: (1) debonding of the toughening particle-matrix interface. (2) interlaminar crack growth within the interlayer propagating through readily debonded particles ahead of the crack front. (3) lateral crack propagation into the ply where a crack in the interlayer around the tow gap could coalesce with fibre matrix debonds, later becoming the dominant crack growth mechanism. (4) crack turning, where the crack continuously propagates laterally into the ply adjacent to the tow gap with no overlap with the interlayer crack. (5) the intralaminar crack has become dominant and no damage is observed within the particle-toughened interlayer.

The research clearly suggests that “mesostructural” variability influences the macroscopic crack path. It is suggested that if features such as a tow gap could be more carefully controlled then the crack transition behaviour could in turn be influenced. If the goal is to maintain the crack within the particle-toughened interlayer careful control during the lay-up and curing process could reduce the number of tow gaps and increase the likelihood, or increase the crack propagation length over which the crack remains in the interlayer. Furthermore, if the crack transition relies on a transition mechanism around tow gaps or TARPs as suggested by the SRCT results, then work to reduce or control the presence of these features is needed, notwithstanding the potential consequences this may have on fibre-bridging mechanisms. However, it is also clear that particle-toughened composite materials have a hierarchical dependency between length scales. The microscale distribution of resin and toughening particles determine the interlayer architecture. The interlayer architecture then affects the probability of crack transition events to the ply, originating locally at the scale of only a few fibre diameters/spacings. The crack which transitions into the ply becomes “trapped” and with further crack growth over the scale of tens of mm’s this can lead to a full transition of the crack front into the ply. Progressive damage modelling should be applied to better understand the complex mechanistic interactions leading to crack path transitions and the extent to which the mesoscale architecture of the interlayer influences crack path while accounting for relative heterogeneity of material properties within the composite.

Several potential geometric features such as varying interlayer thickness, which could be a result of TARPs due to toughening particle loading (also identified in Chapter 3), and tow gaps have been speculated to be contributing to the majority of crack path transtions observed. However, due to the crack propagating up to several mm’s between XCT and SRCT scans during the *in situ* imaging the exact mechanism(s) leading to these transitions is not certain. Therefore, in the following chapter the FEM will be used to independently scrutinise the relative cohesive and adhesive strength properties of the resin and resin-fibre interfaces from the geometric interlayer features.

Chapter 5 An Investigation of the Mechanisms Contributing to Crack Path Transitions in Unidirectional Carbon Fibre Reinforced Polymer Composites Using a Combined eXtended Finite Element and Cohesive Zone Model Methodology

5.1 Introduction

Carbon fibre reinforced polymer composites (CFRPs) have seen increasing utilisation in various industries, including the aerospace, renewable energy and automotive sectors [4]. However, CFRPs can be susceptible to delamination due to impact damage, reducing their static strength by up to 60% with little or no visible damage to the surface of the part [12]. The incorporation of toughening particles into a CFRP has been shown to inhibit interlaminar crack initiation and propagation, reducing the extent of delamination and the area of damage that may then arise under an impact site (*c.f.* an equivalent untoughened system) [15, 41, 62, 63]. The reduced extent of delamination under and around an impact site, and the ranking of interlayer toughness, has been reported to be inversely related, identified with the prevalence of particle-bridging ligaments within the interlayer for example [62]. During subsequent loading of a part compression after impact (CAI) is widely considered a critical loading condition, where the propagation of delamination under Mode I opening is reported to play a key role [60, 69].

Incorporating thermoplastic toughening particles leads to a reported increase in delamination resistance without significant decreases in matrix strength and stiffness properties [102]. However, uncertainty remains regarding the relative contributions of various toughening mechanisms reported to be enabled by the inclusion of toughening particles. In fibre-reinforced epoxies toughening mechanisms are reported to include; crack pinning [103]; particle bridging [108, 112]; crack path deflection [86, 103]; particle yielding [112]; localised shear yielding [110] and microcracking [112]. Importantly, crack paths along fibre-matrix interfaces at the surface or (just) inside the bounding plies are also reported [31, 231], tending to obviate the influence of a toughening interlayer. Suggested micromechanical factors determining the crack path during delamination may be identified as; particle volume fraction, spatial distribution, spacing and size; relative adhesion between the matrix and toughening particles; the proximity of the crack to the ply interface; the stiffness and strength of the toughening phase [49, 179].

It has been reported that uneven particle distributions can lead to agglomerations, which result in mesoscale variations in interlayer thickness which have not been explored in terms of failure behaviour in toughening particle containing systems [122]. Such heterogeneity will of necessity cause local stress states to vary to some extent and, therefore, may be posited to influence failure mechanisms and corresponding crack paths. The effect of overall interlayer thickness on crack paths and corresponding mechanistic contributions to delamination toughness is not well defined even though several authors suggest a link between interlayer thickness and the delamination resistance of the composite [122, 232-234]. Hayes and Seferis [122] when investigating the toughening of unidirectional (UD) epoxy laminates using rubber toughening particles found that the fracture toughness of the composites was influenced by the particle size distribution, average particle size, and concentration all of which affected the structure and thickness of the interlayer, however, the effects of each of these variables were not effectively separated. Stevanovic *et al.*, [233] used various vinyl-ester (VE) / poly(acrylonitrile-butadiene-styrene) (ABS) blends for interlayer toughening of glass/VE based composites. Dry ABS powder was mixed with liquid resin to achieve interlayer thicknesses within the range of 150 – 500 μm, it was found that Mode I fracture toughness was a function of interlayer thickness in this range and highly influenced by particle content, however, Mode II fracture toughness was independent of interlayer thickness and only moderately influenced by particle content. In the work by Gao *et al.*, [234] where thermoplastic toughening particles were interleaved in UD epoxy prepregs an increase in toughness was observed during Mode II loading and an improvement in compression after impact performance was seen after quasi-static impact tests. The mechanisms by which the toughening effect occurred were reported to be due to crack path kinking and deflection, crack-tip shielding, plastic deformation of thermoplastic particles, and geometrical effects of the interlayer. Therefore, although it is known that interleaving using toughening particles can improve delamination resistance and various micro-mechanical damage response mechanisms can be linked to such increases, the resulting interdependencies on the interlayer geometry and thickness have not yet been independently studied.

The current work employs a combined cohesive zone modelling (CZM), eXtended finite element method (XFEM) approach to investigate the parameters determining mechanisms and transitions in crack paths under Mode I loading, particularly transitions of failure path from within the interlayer to the intraply region; as have been observed experimentally in Chapter 3Chapter 4. An essentially standard 3D double cantilever beam geometry is used to model delamination during Mode I loading. The model is used to examine the effect of interlayer geometric variations. In addition, a parameter sweep of relative micromechanical damage parameters was carried out. Finally, models that account for spatial variation in crack initiation and propagation values are

examined. As such, this work seeks to decouple the interlayer geometry and thickness from potentially confounding variables introduced in micro-mechanical modelling methods, clarifying the influence such geometric variation has on damage response mechanisms, transitions in fracture path, and Mode I fracture toughness.

5.2 Materials and Methods

5.2.1 Image Processing

The interlayer thickness of the three samples from material system 4 analysed in Chapter 4 were measured using ImageJ. A pseudo flat-field correction was carried out to remove greyscale differences across the width of the image resulting from local imaging artefacts associated with specimens with large aspect ratios (10.4 x 10.4 x 5 mm ROI within a 254 x 25 x 5 mm sample). Next, the image was cropped to remove air and any artefacts around the edges of the image which could interfere with later processing steps. Every tenth slice was averaged with the slices in between. For example slices, 1 – 10 were averaged, then slices 11 – 20 *etc.* such that an image stack of 2000 slices would reduce to 200 slices. This was to create greater contrast between the interlayer and ply regions. Finally, a median filter was applied using a pixel radius of 2 to help smooth the image and better define the interlayer-ply boundary. The image was then binarised so that the interlayer had a grey value of 0 and the ply had a grey value of 1 (black and white respectively, this process can be visualised in Appendix C). A macro was then written to measure the thickness of all the interlayers across a 1-pixel width rectangle. This was looped across the entire image slice for every slice in the image stack. This value was then divided by the total number of interlayers measured to provide a more robust measurement of the interlayer thickness. The tow gap widths, however, were measured manually and were found to be of a similar width to the mean interlayer thickness (25 μm).

5.2.2 Model Implementation

A functionally equivalent DCB coupon, with a length of 150 mm, width of 20 mm, and thickness of 3 mm, has been modelled using 3D first-order solid elements in Abaqus2021^{TM}. This is smaller (to make the model more computationally efficient) than the coupons tested in the previous chapters, however, still in line with standard DCB test coupon geometry. The boundary conditions implemented in the model represent the conditions during a DCB test and are shown in Figure 42. The bottom cantilever arm is pinned, and the top cantilever arm is displaced vertically at a constant velocity of 1 mm/min under displacement control. The model takes advantage of the symmetry in a DCB specimen to increase computational efficiency: symmetry is applied to

element faces in the x-z plane as shown in Figure 42 which makes the actual dimensions of the model 150 mm length x 10 mm width x 3 mm thickness. To model crack propagation and transitions in detail, while maintaining reasonable computational cost, a smaller region of interest (ROI) of 3.5 mm length x 10 mm width x 0.3 mm thickness is defined around the crack tip, where a finer mesh is embedded. The precrack length measured from the load-point is 45.5 mm where 0.5 mm is embedded within the finer mesh region and is where the initial XFEM crack is initiated. A full mesh refinement study was carried out where the respective force displacement graphs are shown in Appendix C.

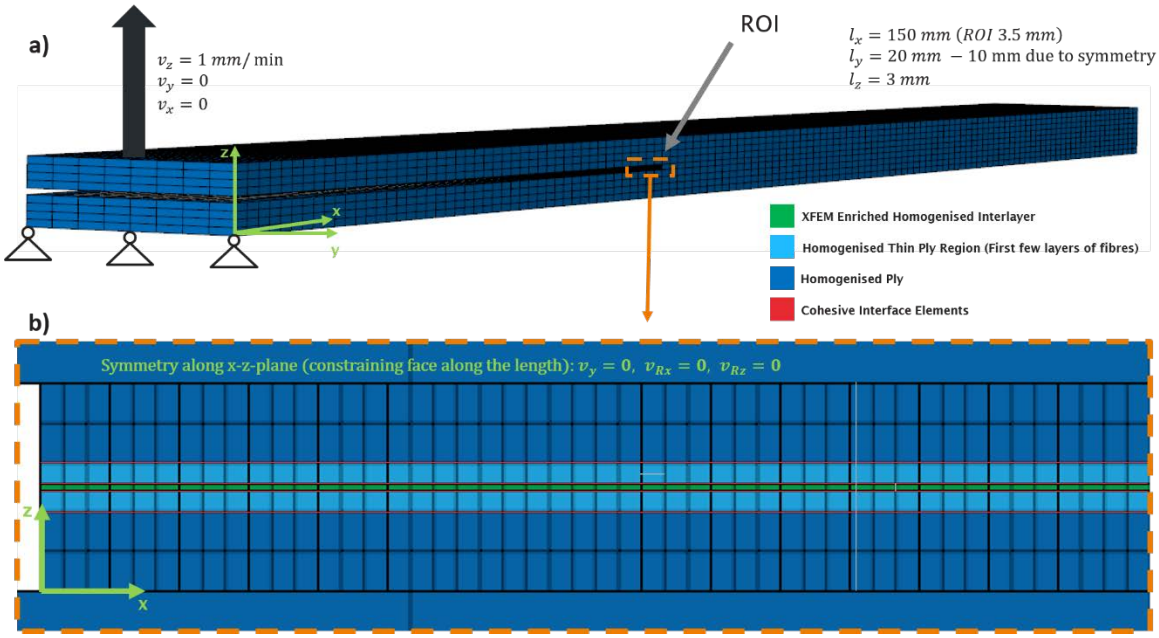

Figure 42 Model geometry and boundary conditions. a) shows the lower cantilever is pinned and the upper cantilever is displaced at a rate of 1 mm/min. Furthermore, the ROI is highlighted where crack propagation occurs. b) shows the ROI, showing the toughened interlayer, cohesive interface elements, the first few layers of fibres, and the bulk ply regions of the model. The symmetry conditions are also defined.

5.2.3 XFEM and Cohesive Element Implementation

A schematic illustration of a section of a constant thickness interlayer model is shown in Figure 43, where the scale bar is chosen to represent the length of an element in the finite element model. Figure 43*a* shows a constant thickness with emulated tow gaps and Figure 43*b* shows a constant thickness section with tow gaps. The shape and dimensions of the tow gaps were chosen such that they could be modelled with a good quality mesh, hence tow gaps in this model have a width of 31.25 µm and connect the interlayer to the outer interface cohesive elements. As mentioned previously the width of the tow gaps was in the same order or magnitude as the interlayer

thickness, hence the chosen is consistent with what is observed via XCT. The spacing of the fibre tows in the models is chosen to be 0.125 mm as to make them occur frequently enough to discern any effect they may have on crack path transitions. As the tow gap spacing is divisible by the element width it allows the tow gaps to be fitted within the model without distorting the mesh.

3D first-order elements were enriched to allow for arbitrary cracking of the solid elements in the interlayer. The maximum principal stress and the quadratic initiation criteria were applied to the interlayer and the cohesive interfaces respectively. Once the initiation criteria are met, the damage then propagates according to a bilinear cohesive traction-separation law. A limitation of XFEM is that it cannot account for more than one crack in a single element, meaning the bifurcation and coalescence of cracks cannot be effectively modelled. For this reason, a combined approach is used where XFEM is used to model delamination in the interlayer and cohesive elements are used to model fracture along the interfaces, allowing for interaction and solution-dependant coalescence between delamination layers.

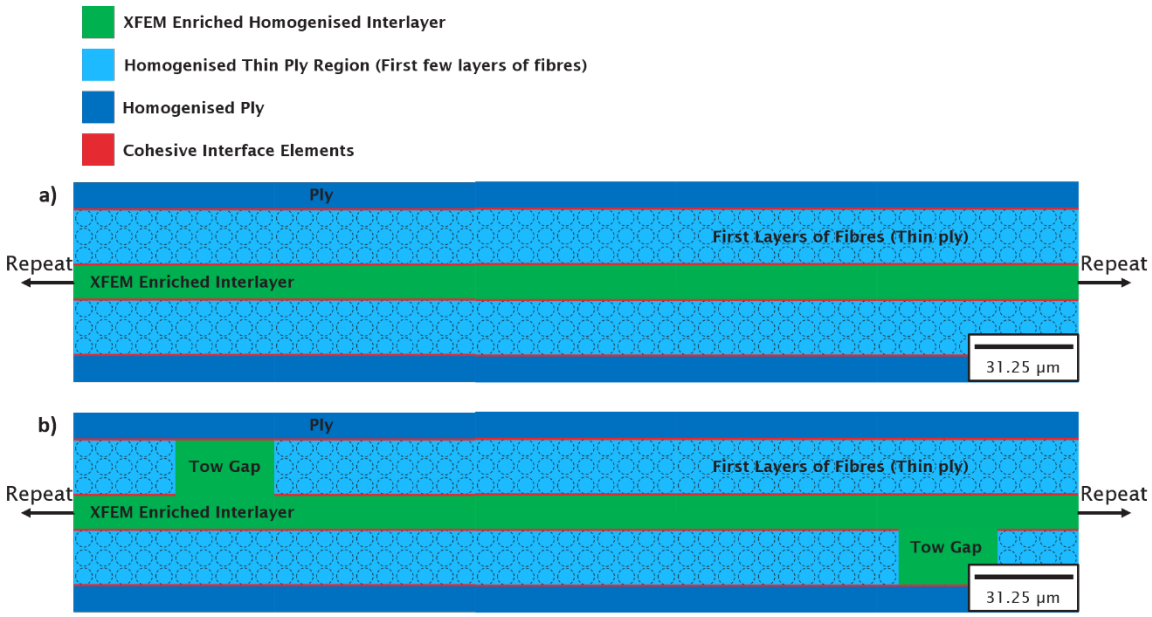

Figure 43 A cross-section through the interlayer and ply with the fibre direction into the screen, where nominal fibre outlines are shown for clarity. a) is a schematic of a constant thickness interlayer without the inclusion of tow gaps. b) shows a constant thickness interlayer with and without the inclusion of tow gaps.

5.2.4 Model Geometry

An XCT image slice through the cross-section of a particle-toughened CFRP is shown in Figure 44, where the fibre direction is into the page. The variation of the interlayer across the width of the

specimen is apparent, with significant variations from relatively 'thin' (< 10 μm) to relatively 'thick' regions (> 50 μm), as well as occasional gaps between fibre tows. To interrogate the potential influences of these geometrical variations, three representations were modelled: (1) constant thickness interlayer models, (2) models with a sinusoidal variation of interlayer thickness, and (3) inclusion of distinct tow gaps (in both the constant and sinusoidal thickness models). Whilst direct, image-based modelling of interlayer geometries could have been adopted (via XCT datasets), the idealisation of the interface geometries was considered more useful, allowing for direct comparison between geometric features and unambiguous identification of parametric influences.

To choose an appropriate range of interlayer thicknesses, the minimum (corresponding to 10 μm) was chosen such that the element aspect ratio would not exceed three for the enriched elements, and the maximum was chosen to be close to the maximum experimentally measured (≈99.9 percentile of the measured range) values and still did not violate a maximum element aspect ratio of three. The period of the sinusoidal variation was estimated from the experimental data shown in Figure 45 by calculating the wavelength between values of 50 μm and 15 μm which represent the range in which 95% of the measured thickness values lie: the peak-to-peak wavelength of the experimental data was calculated by taking a mean value of the peak-to-peak distance as measured on each image slice giving a representative value for the whole sample and, yielding a value of 2.4 mm. In the model, a value of 2.5 mm is used for the wavelength to provide a convenient integer number of wavelengths across the 10 mm width of the specimen. The interlayer geometrical variation can be represented by a sine wave of the form, $Asin(Bx + C) + D$. A schematic of the interlayer geometries is shown in Figure 46, where the parameters of the sine wave are shown. In Figure 46 the cross-section schematics of a varying interlayer model and constant thickness interlayer model are shown side by side. The schematics are not to scale and are illustrative of the parameters used to describe the interlayer sections. The amplitude of the wave is denoted by *A*, the period is denoted by *B*, the phase shift along the horizontal axis is denoted by *C*, and the vertical shift is denoted by *D*. This allows the interlayer to be fully parametrised. Subsequently, in Table 6 the geometries and corresponding constants that fully describe the interlayer variations are shown. There are three constant thickness models of 10 μm, 25 μm, and 57 μm respectively. There are also three varying thickness models: the first varies between the 10 μm and 57 μm, the second varies between 12 μm and 38 μm (*i.e.* one standard deviation below and above the mean respectively), and the third varying model which varies between 18 μm and 32 μm (*i.e.* two standard deviations below and above the mean respectively).

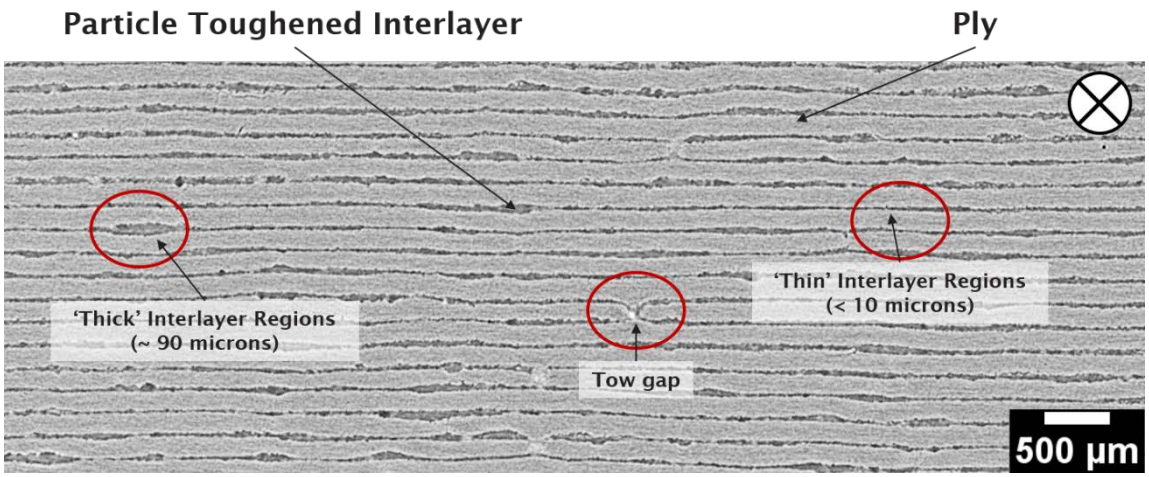

Figure 44 Slice of a CT image through a sample from material system 4 analysed in Chapter 4 showing the variation in interlayer thickness. The fibres are going into the page.

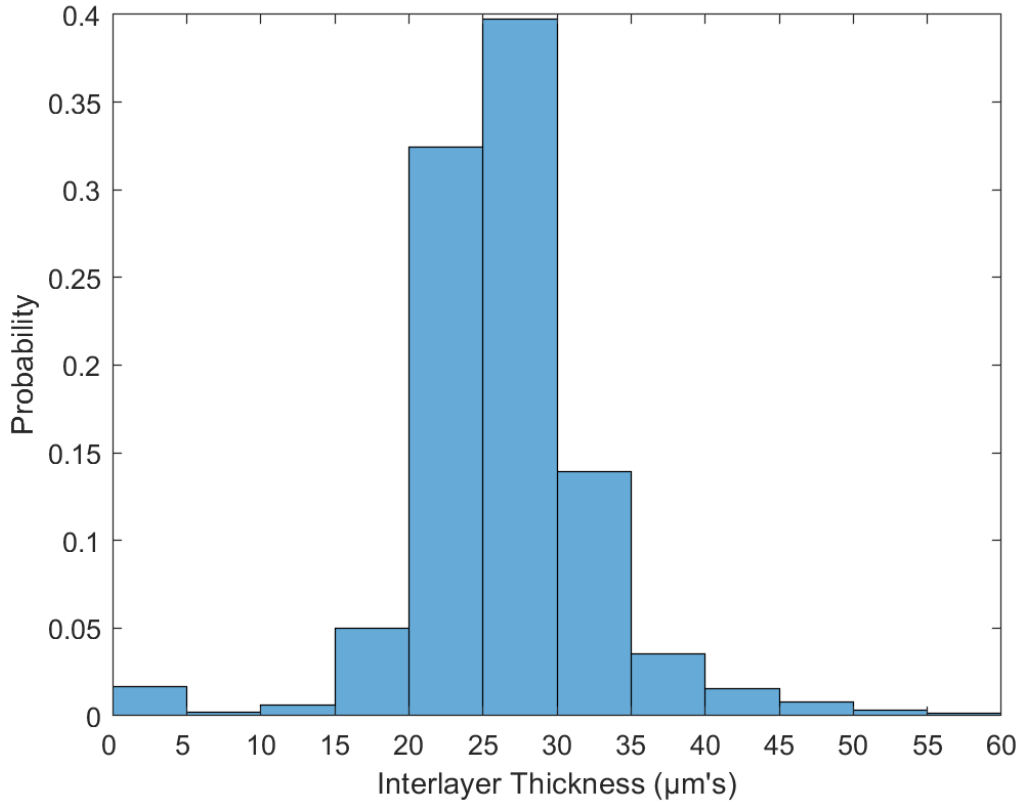

Figure 45 Histogram of experimentally determined interlayer thickness variation, with a minimum value of zero and a maximum value of 57 microns.

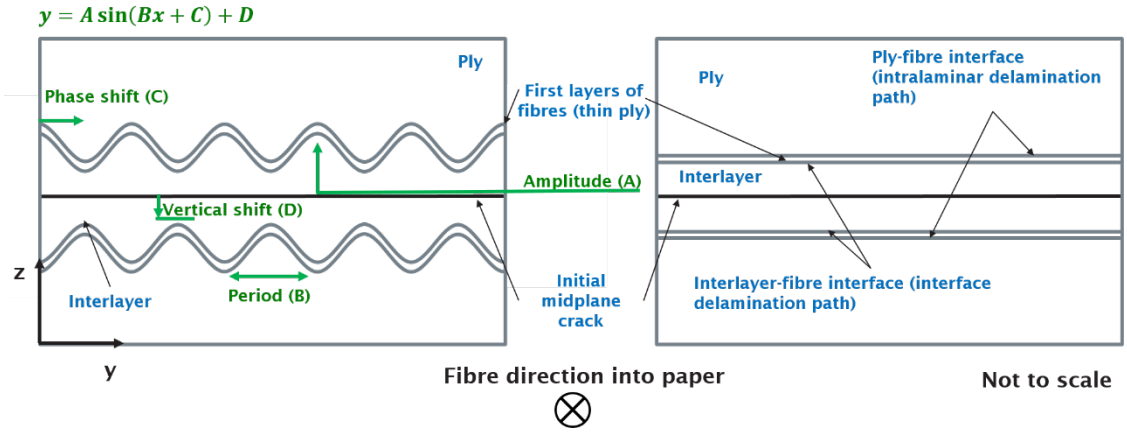

Figure 46 Interlayer geometry variation. The left shows sinusoidal variation as described by a sine function. The right shows the constant thickness interlayer geometry.

Table 6 A summary of the different interlayer geometries modelled, with the corresponding constants to fully describe the variation in interlayer thickness

Geometry Thickness Variation (µm's)	Amplitude (A) (µm's)	Period (B) (mm's)	Phase Shift (C) (Radians)	Vertical Shift (D) (µm's)
10 (Constant)	5	0	$\frac{\pi}{2}$	0
25 (Constant)	12.5	0	$\frac{\pi}{2}$	0
57 (Constant)	28.5	0	$\frac{\pi}{2}$	0
10 – 57 (Varying)	52	2.5	$\frac{\pi}{2}$	± 5
12 – 38 (Varying)	32	2.5	$\frac{\pi}{2}$	± 6
18 – 32 (Varying)	23	2.5	$\frac{\pi}{2}$	± 9

5.2.5 Determining cohesive element parameters

An estimate for the cohesive element length was calculated using the method proposed by Hillborg *et al.* [141] as shown in Equation 5-1, where E is the transverse Young's modulus of the composite, 9.0 GPa, G_{IC} is the CSERR, 0.2 mJ/mm^2, and τ_0 is the maximum value used for the normal interfacial strength of the CE layer, 75.6 MPa.

$$l_{cz} = \frac{EG_{IC}}{{\tau_0}^2} \quad 5\text{-}1$$

This yields the cohesive length of the strongest interface model to be 0.315 mm. A mesh independence study was carried out using element lengths of 0.1 mm, 0.05 mm, 0.03125 mm, 0.025 mm, and 0.02 mm in the refined region of the model, where the aspect ratio between the in-plane and out-of-plane directions was kept at 1 for all models (see Appendix C). This study indicated that a cohesive element length of 0.03125 mm and a viscous regularisation value of 0.0001 gave satisfactory results (within 1% of the finest mesh), and allowed convergence during the coalescence of crack modelling regimes (XFEM and cohesive elements) at the element boundaries. The cohesive stiffness was calculated using Equation 5-2 outlined by Turon *et al.* [235] where α is a scalar constant to be determined, E_3 is the transverse modulus, and *t* is the thickness of the adjacent element layer to the zero-thickness CEs.

$$K = \frac{aE_3}{t} \quad 5\text{-}2$$

The stiffness was chosen such that *K >> E*, but not so stiff that it induced numerical errors. Equation 5-3 proposed by Jalalvand *et al.* was used to validate the stiffness values to ensure, that the whole system's stiffness was not degraded by more than 5% [236, 237]. In Equation 5-3, *n* is the number of rows of cohesive elements, E_1 is the elastic modulus of the material along the fibre direction, *L* is the length of the model which is 150 mm, *K* is the stiffness of the cohesive element and E_1' is the embedded stiffness of the CE in the fibre direction.

$$\frac{E_1'}{E_1} = \frac{1}{1 + \frac{n-1}{L}\frac{E_1}{K}} \quad 5\text{-}3$$

There are 4 layers of cohesive elements representing the interface regions in the model, by substituting in values of n = 4, L = 150 mm, $E_1 = 165{,}000\ MPa, and\ K = 500{,}000\ N/mm^3$. There is a reduction in stiffness of the structure of 0.65 %, which is deemed acceptable.

5.2.6 Parametric Investigation and Stochastic Variation

Table 7 shows the test conditions for model variations. The relative normal initiation stress of the interface and intraply regions were varied relative to the nominal interlayer failure stress across each geometrical condition shown in Table 7. A further condition implemented a stochastic variation of the cohesive properties assigned to the cohesive elements and enriched elements about the nominal failure stress of the interlayer, where the maximum and minimum values were

chosen to vary, with 95% of the distribution contained within ± 20% of the mean, to remain consistent with the parameter sweep values. It is assumed that the initiation parameters of each stochastic layer vary in a simple Gaussian distribution. Values were extracted from a Gaussian distribution with a mean value of 63.0 MPa, and a standard deviation of 5.0 MPa. The values were then randomly assigned to the cohesive and solid enriched elements to reflect variations in the failure stress which might be expected to arise from non-homogenous particle distributions, misaligned fibres or fibre waviness, voids *etc*. The G_{IC} of each element was not varied independently to the stress value, rather a relationship between the values was assumed such that $G_{IC} \propto \sigma_I^2$. To ensure all geometrical models were directly comparable, the assignment of variables was consistent across all geometrical conditions. Variables were assigned using a custom Matlab R2018b code to select values randomly from the given distribution and then collate these values into a .txt format to be directly imported as an Abaqus .inp file (see Appendix C). There are 179,200 cohesive or enriched elements in the model, each assigned independent cohesive properties.

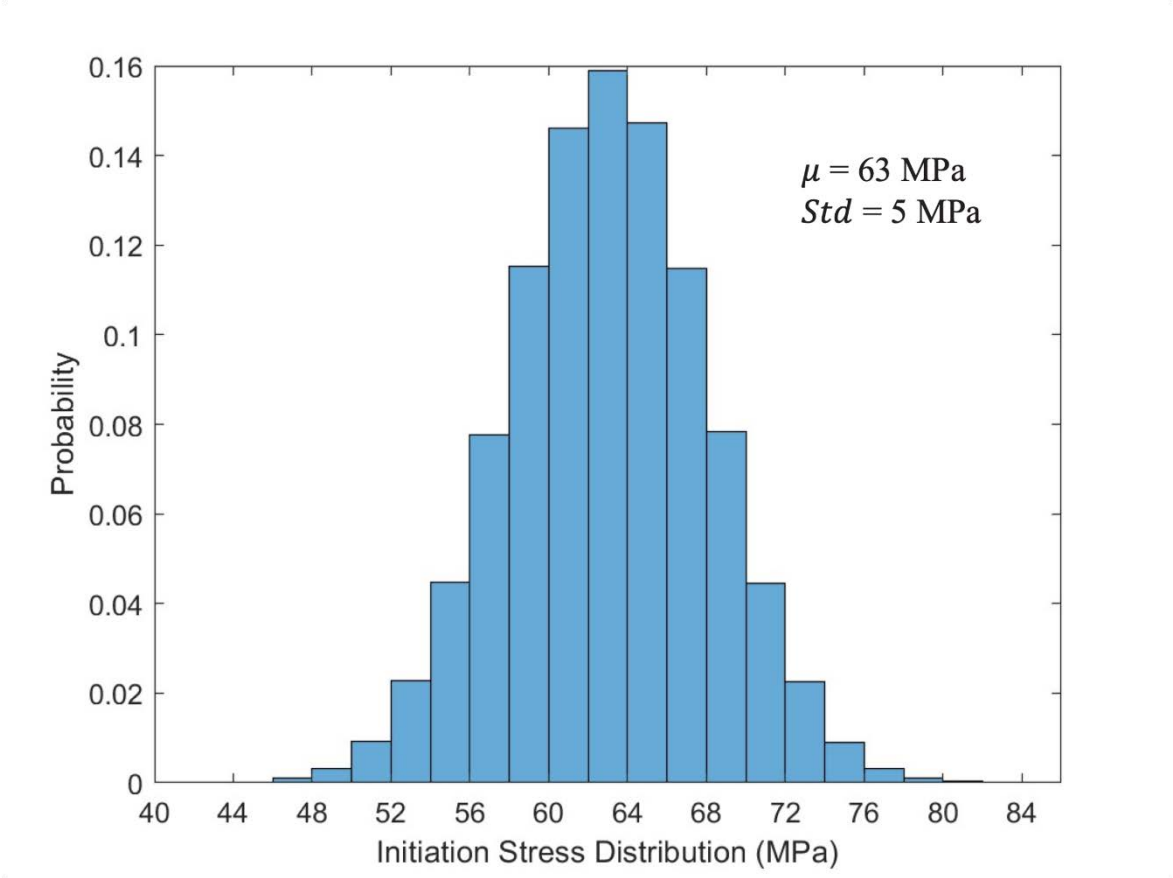

Figure 47 Distribution of initiation stress used to assign stochastic cohesive properties.

Table 7 Model variations where the normal initiation stress of each cohesive layer varies relative to the interlayer.

Model Variation	Interlayer normal initiation stress $\sigma_{n,i}^{Int}$ (MPa)	Interlayer-fibre interface normal initiation stress (MPa)	Intralaminar normal initiation stress (MPa)
80	63	$0.80\sigma_{n,i}^{Int}$	$0.80\sigma_{n,i}^{Int}$
90	63	$0.90\sigma_{n,i}^{Int}$	$0.90\sigma_{n,i}^{Int}$
95	63	$0.95\sigma_{n,i}^{Int}$	$0.95\sigma_{n,i}^{Int}$
100	63	$\sigma_{n,i}^{Int}$	$\sigma_{n,i}^{Int}$
105	63	$1.05\sigma_{n,i}^{Int}$	$1.05\sigma_{n,i}^{Int}$
110	63	$1.10\sigma_{n,i}^{Int}$	$1.10\sigma_{n,i}^{Int}$
120	63	$1.20\sigma_{n,i}^{Int}$	$1.20\sigma_{n,i}^{Int}$
80TG	63	$0.8\sigma_{n,i}^{Int}$	$0.80\sigma_{n,i}^{Int}$
90TG	63	$0.9\sigma_{n,i}^{Int}$	$0.90\sigma_{n,i}^{Int}$
95TG	63	$0.95\sigma_{n,i}^{Int}$	$0.95\sigma_{n,i}^{Int}$
100TG	63	$\sigma_{n,i}^{Int}$	$\sigma_{n,i}^{Int}$
Sto	$\mu = 63$	$\mu_{width} = 63$	$\mu_{width} = 63$
N(μ, Std)	$Std = 5$	$Std = 5$	$Std = 5$
StoTG	$\mu = 63$	$\mu_{width} = 63$	$\mu_{width} = 63$
N(μ, Std)	$Std = 5$	$Std = 5$	$Std = 5$

* denotes the stochastic iteration of the model. Parameters are defined in terms of the normal probability density function *N* as a function of μ the distribution mean and Std^2 the variance of the distribution.

5.2.7 Key properties and variables

Table 8 shows the parameters used for each section of the model. All values are considered reasonably characteristic and representative, being available in the third World Wide Failure Exercise (WWFE III) [22]. The material system IM7/8552 was chosen as the associated data is widely available and it represents an intermediate modulus toughened epoxy system, known to be similar to the material system imaged in this work. The model is split into three key regions shown in Figure 42b: (1) the central interlayer region, (2) a 'thin ply' which represents the first few

fibre layers into the surrounding ply, and (3) the bulk of the ply material, with cohesive elements being introduced along the interface between the interlayer and the thin ply and the thin ply and bulk ply respectively. The definition of a 'thin ply' region was directly driven by experimentally observed failure processes, *i.e* instances where cracking is seen to exit the interlayer, but rather than meeting and growing along the interfaces of the fibres directly adjoining the interlayer, grows into the bulk of the surrounding plies, typically by just a few fibre diameters as discussed in detail in Chapter 4. Each region is defined separately and assigned corresponding properties. The crack starts at the midplane of the interlayer. For the enriched elements (elements in the XFEM region) in the interlayer, it is assumed that an element's load-carrying capacity begins to degrade when $\frac{\langle \sigma_{principal} \rangle}{\sigma_{principal,max}} \geq 1$, where $\langle \cdots \rangle$ are Macaulay brackets to represent the ramp function, and hence the crack within the interlayer can propagate through an arbitrary path. Due to variation in interlayer geometry, it is assumed that a crack at the interface regions (the cohesive elements) could initiate and propagate according to a mixed loading condition described by the quadratic initiation criterion, $\left(\frac{\langle \sigma_n \rangle}{\sigma_{n,max}}\right)^2 + \left(\frac{\langle \sigma_{S1} \rangle}{\sigma_{S1,max}}\right)^2 + \left(\frac{\langle \sigma_{S2} \rangle}{\sigma_{S2,max}}\right)^2 \geq 1.$

Table 8 Material properties used in the 3D DCB scale FE model.

Property	**Symbol**	**Units**	**Interlaminar Region**	**First Layers of Fibres (Thin ply)**	**Ply**
Elastic Modulus	E_1	MPa (N/mm^2)	4080	165,000	165,000
	E_2			9,000	9,000
	E_3			9000	9,000
Shear Modulus	G_{12}	MPa (N/mm^2)	1478	5600	5600
	G_{13}			5600	5600
	G_{23}			2800	2800
Poisson Ratio	ν_{12}	N/A	0.38	0.34	0.34
	ν_{13}			0.34	0.34
	ν_{23}			0.5	0.5
-		-	**XFEM Enriched Interlaminar Region**	**Cohesive Element Interfaces**	-
Cohesive Stiffness	K_I	MPa/mm (N/mm^3)	-	500,000	N/A
	K_{II}		-	500,000	
	K_{III}		-	500,000	
Initiation Maximum Stress	σ_n	MPa (N/mm^2)	63[a,b,c]	63[b,c]	N/A
	σ_{S1}		-	90	
	σ_{S2}		-	90	

Property	Symbol	Units	Interlaminar Region	First Layers of Fibres (Thin ply)	Ply
Mode I Strain Energy Release Rate	G_{IC}	KJ/m^2 (mJ/mm^2)	0.3[c,d]	0.2[c,d]	N/A
	G_{IIC}		0.8	0.8	
	G_{IIIC}		0.8	0.8	

[a] Maximum principal stress value used for interlayer XFEM enriched region

[b] Denotes variable for parameter sweep, where the normal initiation stress was varied by ± 20 %.

[c] Denotes that there is a link between the nominal failure stress variable and G_{IC} in the stochastic implementation of the model

[d] The interface CSERR is lower than the interlayer CSERR to reflect the observations in Chapter 3 and Chapter 4, which suggested that the measured SERR decreased as the crack transitioned from the interlayer to the ply (fibre-matrix interface).

A simple damage propagation criteria shown in Equation 5-4 is employed to account for mixed-mode degradation of the CE's and enriched (XFEM) elements, as used by Yang *et al.* [142].

$$\frac{G_I}{G_{IC}} + \frac{G_{II}}{G_{IIC}} + \frac{G_{III}}{G_{IIIC}} \geq 1 \qquad 5\text{-}4$$

In Equation 5-4 G denotes the strain energy release rate (SERR), and G_C denotes the critical SERR (CSERR) required to propagate the crack under the respective loading mode.

5.3 Results

5.3.1 Crack Transition Behaviour

Two relative material properties have been used to visualise crack path transition and competition when the relative interface strength is 90% of that of the interlayer (see Figure 48 and Figure 49) and when there is no relative strength difference (see Figure 50 and Figure 51). The top row in each figure shows a section through the centre of the coupon, perpendicular to the plane of crack growth, where the crack is moving from right to left as indicated by the arrows. The bottom row in each figure shows the orthogonal plane with the crack growth going into the page, similarly indicated. The black lines and split elements in the (green) interlayer show the XFEM

crack path, and the red elements at the interface between the interlayer and the (light blue) first few layers of homogenised fibres show the damaged cohesive elements.

The constant thickness geometry models show similar transition behaviour in the plane of crack growth. The crack in the interlayer is arrested and the interface crack propagates without any visible re-initiation in the interlayer. However, in the second row showing the orthogonal section planes it can be seen for the 10 µm thickness model there is an interaction between delamination paths where the crack has bifurcated on either side of the interlayer and an oblique crack has caused a coalescence through the interlayer. For the 25 µm thickness interlayer model, it appears that microcracks form in regions where the delaminations running in the adjacent interfaces overlap, however, at this stage do not form a continuous crack between them. A similar observation can be made for the 57 µm thick interlayer model, where there appears to be a microcrack within the interlayer between overlapping interface delamination, but again without a continuous linking crack. In this case, an oblique crack appears to coalesce with the top interface and propagates at an angle towards the bottom interface. Finally, it is also apparent that there is a pattern of crack path oscillation between the two interlayer-ply interfaces for all three models, however, with increasing interlayer thickness the frequency of this oscillation decreases.

Similar behaviour occurs for the varying geometry models in Figure 49, however, rather than the interlayer cracks being located near every interface crack overlap, they only appear to occur when the overlap occurs at the thinner region of the interlayer. Furthermore, as the thickness variation becomes less pronounced the alternation between the upper and lower interface becomes less frequent.

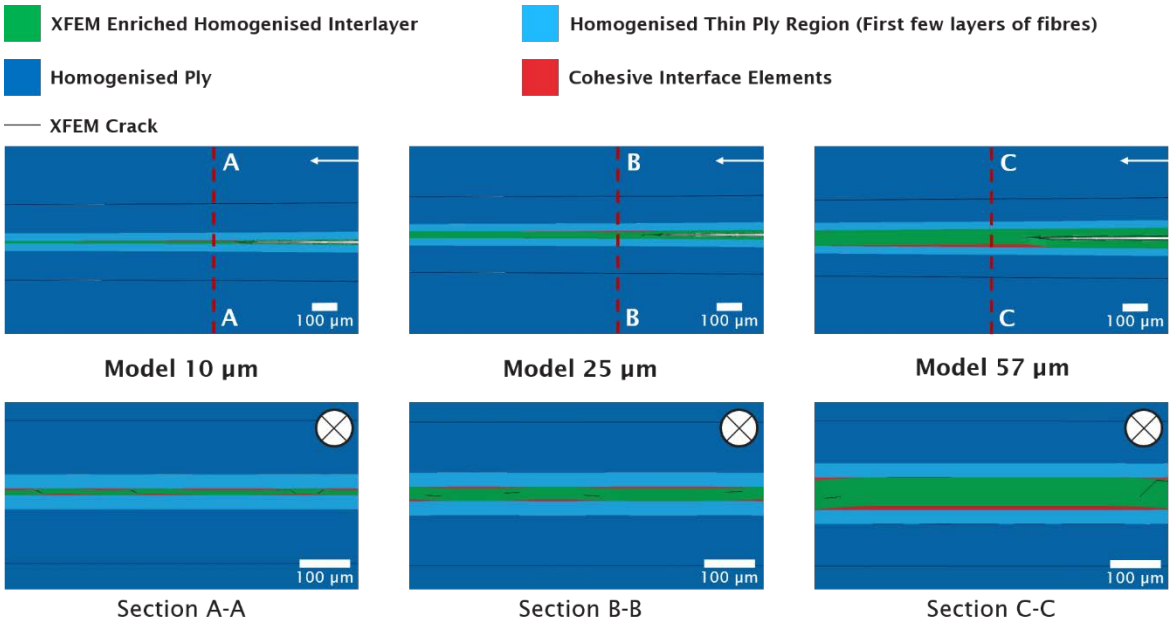

Figure 48 Comparison of different interlayer thickness models where the relative interface strength is 90% of that of the interlayer. A section on the plane of symmetry is shown on the top row and the images show the damage immediately after the pre-imposed crack. For the 10 µm constant thickness interlayer model, the crack transitions to the upper interface where as it propagates and microcracks sequentially initiate in the interlayer but do not propagate further. Section A-A shows that damage transitions to either side of the interlayer and appears to oscillate between the upper and lower interfaces. Likewise, albeit to a lesser extent this behaviour is seen in the 25 µm interlayer thickness model. Finally, in the 57 µm thick interlayer model, there is some damage distributed within the interlayer as the interface propagates although to a much lesser extent than in the other two models.

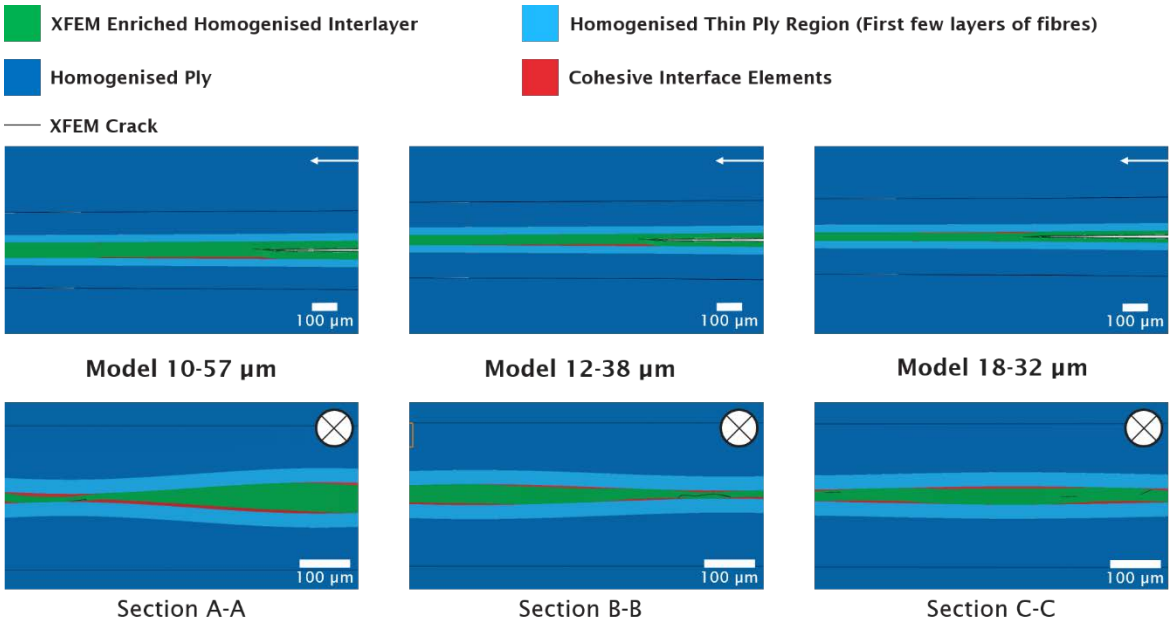

Figure 49 Comparison of different varying interlayer thickness models where the relative interface strength is 90% of that of the interlayer. A section on the plane of symmetry is shown on the top row and the images show the damage immediately after the pre-imposed crack. For the 10 - 57 µm varying thickness interlayer model the crack transitions to the lower interface as it propagates. Section A-A shows that damage transitions to either side of the interlayer and appears to oscillate between the upper and lower interfaces less frequently than the other two varying thickness models. Similarly, albeit to a greater extent the 12 – 38 µm and 18 – 32 µm varying interlayer models display this oscillation between the upper and lower interface regions with microcracking in the interlayer as they propagate.

The second material condition investigated was for an interface strength of 100% relative to the interlayer and both the constant thickness and varying thickness models are shown in Figure 50 and Figure 51 respectively. In Figure 50 in the top row where the crack is propagating from right to left, in the 10 µm thickness interlayer model and 25 µm thickness interlayer model the crack propagates in the interlayer before transitioning to the interlayer-fibre interface, however, after further propagation in the interface, there is a re-initiation in the interlayer followed by further propagation within the interlayer. However, in the 57 µm thick interlayer model, some damage appears to accumulate at the interface but it does not cause a full crack transition. The crack tip does, however, begin to turn towards the upper interface. The orthogonal plane showing the crack propagation direction into the screen on the bottom row clearly shows damage distribution in the interlayer and either side of the interlayer, with an oblique crack in the 25 µm thick

interlayer model running and coalescing in between the delamination paths on either side of the interlayer.

In the varying thickness models, it is evident that a smaller magnitude of variation in the interlayer thickness causes more oscillation of the crack between either side of the interlayer as seen in Figure 51. Furthermore, there is coalescence between the delamination paths on either side of the interlayer which can be seen clearly in the geometry model varying from 18 – 32 µm.

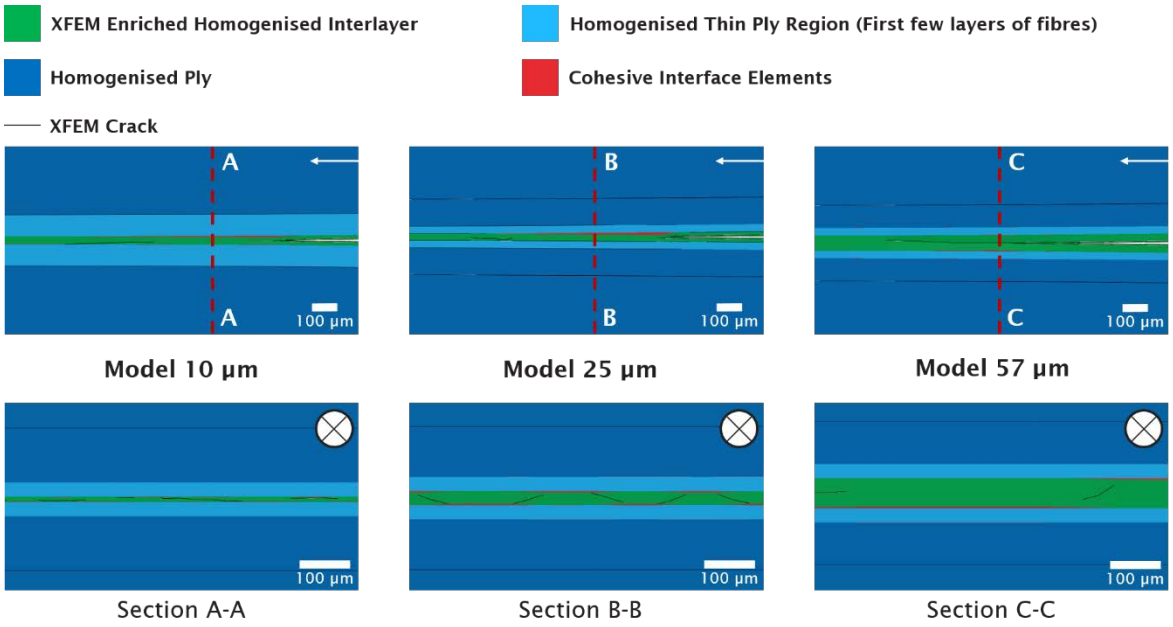

Figure 50 Comparison of different interlayer thickness models where the relative interface strength is 100% that of the interlayer. A section on the plane of symmetry is shown on the top row and the images show the damage immediately after the pre-imposed crack. In both the 10 µm and 25 µm thickness interlayer models the crack transitions to the interlayer-ply interface. In sections A-A and B-B interlayer crack forms, appearing to bridge between the cracks running along either interface on the opposing side of the interlayer. For the 57 µm thick interlayer model on the symmetry plane where the crack is propagating from right to left the interlayer crack does not transition, although there is evidence of damage to the lower interface which did not become dominant. In section C-C the oscillation between the upper and lower interface is less frequent and an oblique crack appears to be bridging between the upper and lower interface.

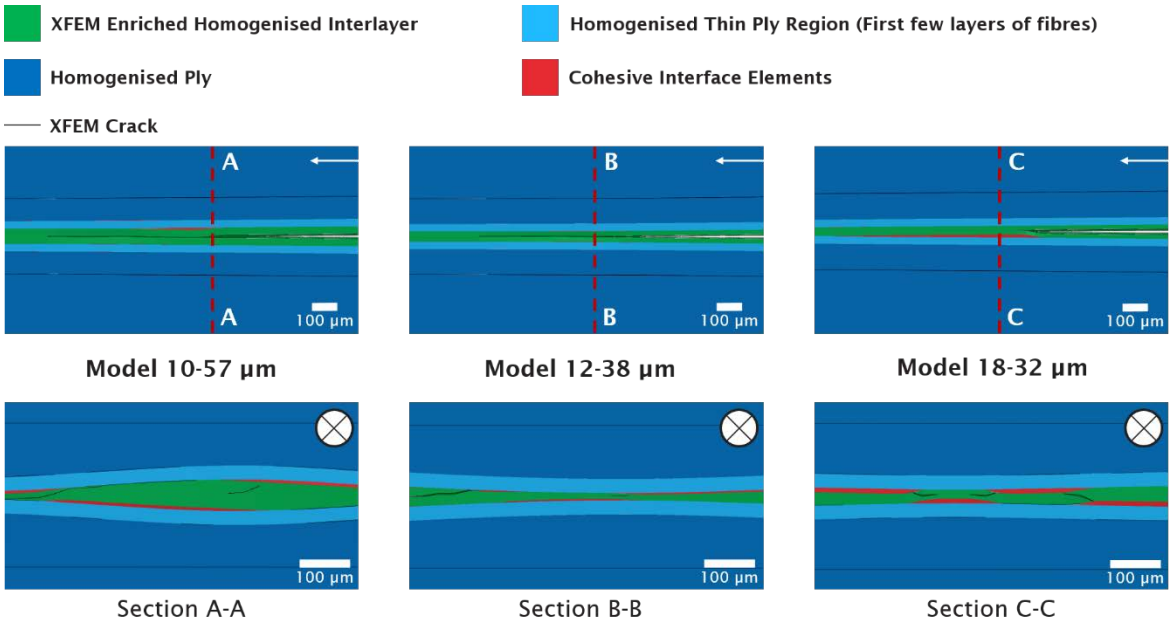

Figure 51 Comparison of different varying interlayer thickness models where the relative interface strength is 100% that of the interlayer. A section on the plane of symmetry is shown on the top row and the images show the damage immediately after the pre-imposed crack. In the top row of images where the crack is propagating from right to left it can be seen that on the symmetry plane, the crack remains in the interlayer for both the 10 – 57 µm and 12 – 38 µm varying thickness models respectively, where there is some damage in the upper interface of the former. In the 18 – 32 µm varying thickness model, the crack transitions to the lower interface. In sections A-A, B-B, and C-C the crack propagates along the upper and lower interlayer-ply interfaces with increasing frequency respectively, where interlayer cracks can be seen to bridge between them.

5.3.2 Crack Distribution

Progressive damage of elements using cohesive elements and the XFEM can be quantified using the stiffness degradation (SDEG), which is a measure of the load-carrying capacity of an element relative to its failure criteria ranging from 0 (no failure) to 1 (failed). In practice, this means a cohesive element which fails due to an applied normal stress of 100 MPa will see progressive degradation in its load-carrying capacity after that load has been applied. Hence, for an SDEG value of 0.9, the element would only be able to support a load equivalent to 10 MPa.

The schematic in Figure 52 is to give the reader a reference to interpret the results displayed subsequently in Figure 53 - Figure 63 which show the proportion of damage in each layer and the

load-point opening displacements at which the results have been reported. Figure 52 is not intended to be an exact depiction of the crack transition process but rather to give the reader a sense of chronology and context and are broadly in line with the results shown previously in Figure 38, Figure 39, and Figure 40 in Chapter 4: Figure 52a shows a schematic of a crack propagating in the direction of the fibres from right to left. Up to section A-A, the crack begins in the interlayer where low-level damage may occur at the adjacent interface. The reader may notice that the low-level damage depicted can overlap with the main crack, however, these regions do not degrade further or open. Between sections A-A and B-B the main crack has transitioned to the top interface. The oblique angle between the former crack in the interlayer and the now transitioned crack represents deviation through the interlayer, bridging between them. In this case, there is no overlap between the two fully opened (or damaged) crack regions. Further low-level/local damage can be observed in both the interlayer and top ply as the main crack propagates along the top interface in both the interlayer and top ply. As the crack propagates through section C-C it has transitioned to the top of the thin ply. As this is a three-dimensional problem one must also account for the orthogonal sections, as shown in Figure 52b – d, representing positions A-A, B-B, and C-C respectively. The intention is to illustrate how a crack may exhibit twisting and bifurcation across its width.

In the following section the proportion of partly or fully damaged elements, in each layer is compared for different geometric and material property combinations. Damaged elements are defined as elements which have an SDEG greater than 0, whereas, fully damaged elements are defined as elements that have lost over 90% of their load-carrying capacity, and are considered here to represent the fully developed crack path in each layer. For Figure 53 - Figure 63, only damage which has progressed from that of the pre-imposed starter crack is considered and the load-point opening displacement (δ) at which the results are reported is overlaid. The first graph (a) in each pair compares each model at a common converged timestep equating to a load opening displacement of 7.2 mm and a total crack extension of approximately 1 mm. The second graph in each pair (b) compares each model at their respective final converged timestep, not making them directly comparable as the crack length and element degradation is dependent on the last converged timestep. This gives a sense beyond that of the common converged timestep of the total damaged progression captured. This is because a more complex crack path in terms of cracking in multiple adjacent layers introduces convergence issues due to non-linearities introduced through a large number of elements softening due to traction-separation. The blue area represents the proportion of the total damaged elements which are located within the interlayer, whereas the orange, and yellow show the proportion in the bottom and top interlayer-fibre interface respectively, and finally the purple and green represent the proportion in the

bottom and top fibre interface several fibre diameters into the ply respectively. Significant differences between material property combinations are apparent, with an intuitively reasonable trend of increasing damage in the interlayer (or less damage transition out of the interlayer) with an increasingly strong interface relative to the interlayer. The variation in crack behaviour is seen to depend significantly on the interlayer geometry when the relative strength of the interface is equal to or less than that of the interlayer. In general, the proportion of total damage in the interlayer also increases as the interlayer thickness decreases, with the presence of tow gap-like features having a similar effect.

In terms of the fully developed crack when the relative strength of the interface is 80% or less than that of the interlayer, none of the crack remains within the interlayer but transitions to the interlayer-fibre interface. Furthermore, the thickest interlayer model (57 μm) retains the crack within the interlayer when the interface strength is at least 90% of that of the interlayer. This contrasts with all other geometry conditions, where the crack is retained in the interlayer only when there is no relative strength difference or the interface strength is greater. Additionally, it is also clear that the presence of tow gaps significantly impacts the proportion of the fully developed crack in each potential delamination layer. The presence of the tow gap appears to change the crack path, however, the exact effect is dependent on the interlayer geometry and material properties which is strongly suggestive of coupling between these variables.

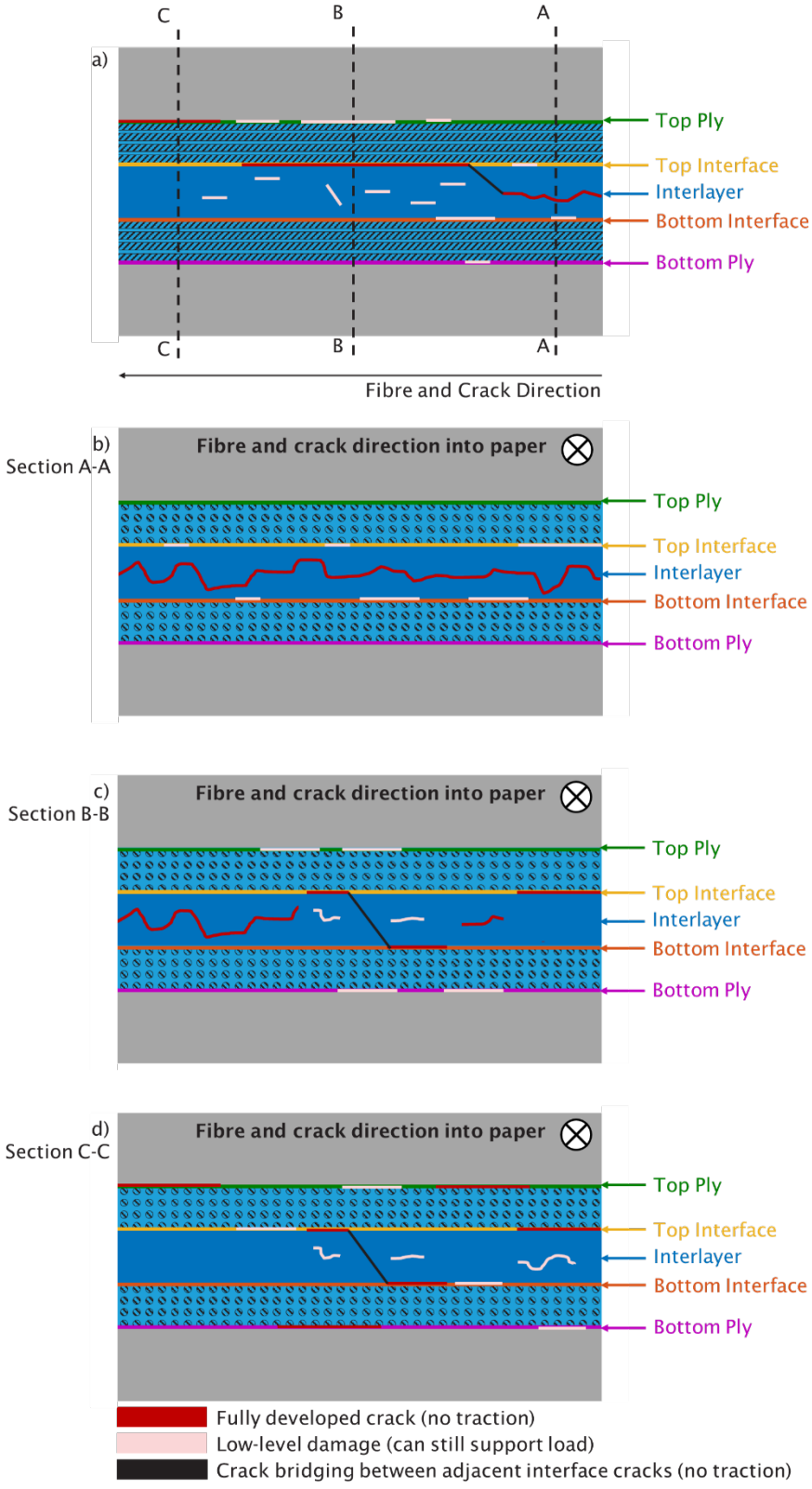

Figure 52 Schematic of crack and damage distribution in modelled volumes as an aid to interpreting the results in the following sections. It has been colour coded to match the legend used for the graphs displaying the proportion of the crack in each of the respective layers. This figure is broadly in line with the results shown previously in Figure 38, Figure 39, and Figure 40 in Chapter 4.

5.3.2.1 Interface Strength at 80% of Interlayer Strength

Figure 53 shows the proportion of damaged elements for each geometric condition when the relative strength of the interface and ply was 80% of the interlayer with and without the presence of tow gaps.

Figure 53a compares the models at a common converged timestep as mentioned previously. There is a clear migration of the damage out of the interlayer and to the upper and lower interface regions with a small amount of damage observed in the upper and lower ply regions. Without the presence of tow gaps the 10 µm thick interlayer shows the greatest proportion of damaged elements in the interlayer, albeit by only a small amount and there is no significant difference between the other geometry conditions apart from the varying 12 – 38 µm model which shows a small amount of damage within the ply layers. It can be seen that the presence of tow gaps makes little difference apart from in the thickest interlayer and the varying 10 – 57 µm geometry model where a greater proportion of the damage is observed in the interlayer.

Figure 53b compares the models at their respective final converged timesteps as similarly mentioned previously. Notably, a greater proportion of damage is observed in the ply without the presence of tow gaps in two of the varying interlayer thickness models (greater than one standard deviation from the mean). Whereas for the 10 – 57 µm varying geometry model and constant thickness 57 µm thickness model, a greater proportion of damage in the ply is observed with the presence of tow gaps and an increase in the damage distributed within the upper and lower ply.

Figure 54 shows the proportion of the fully developed crack within each potential delamination path. Similar to before, a) make a comparison at a common converged timestep and b) at each respective final converged timestep. These results illustrate that the entire crack for all models transitioned out of the interlayer after the pre-imposed interlayer crack, except for the varying 10 – 57 µm model with tow gaps, where a small proportion is retained.

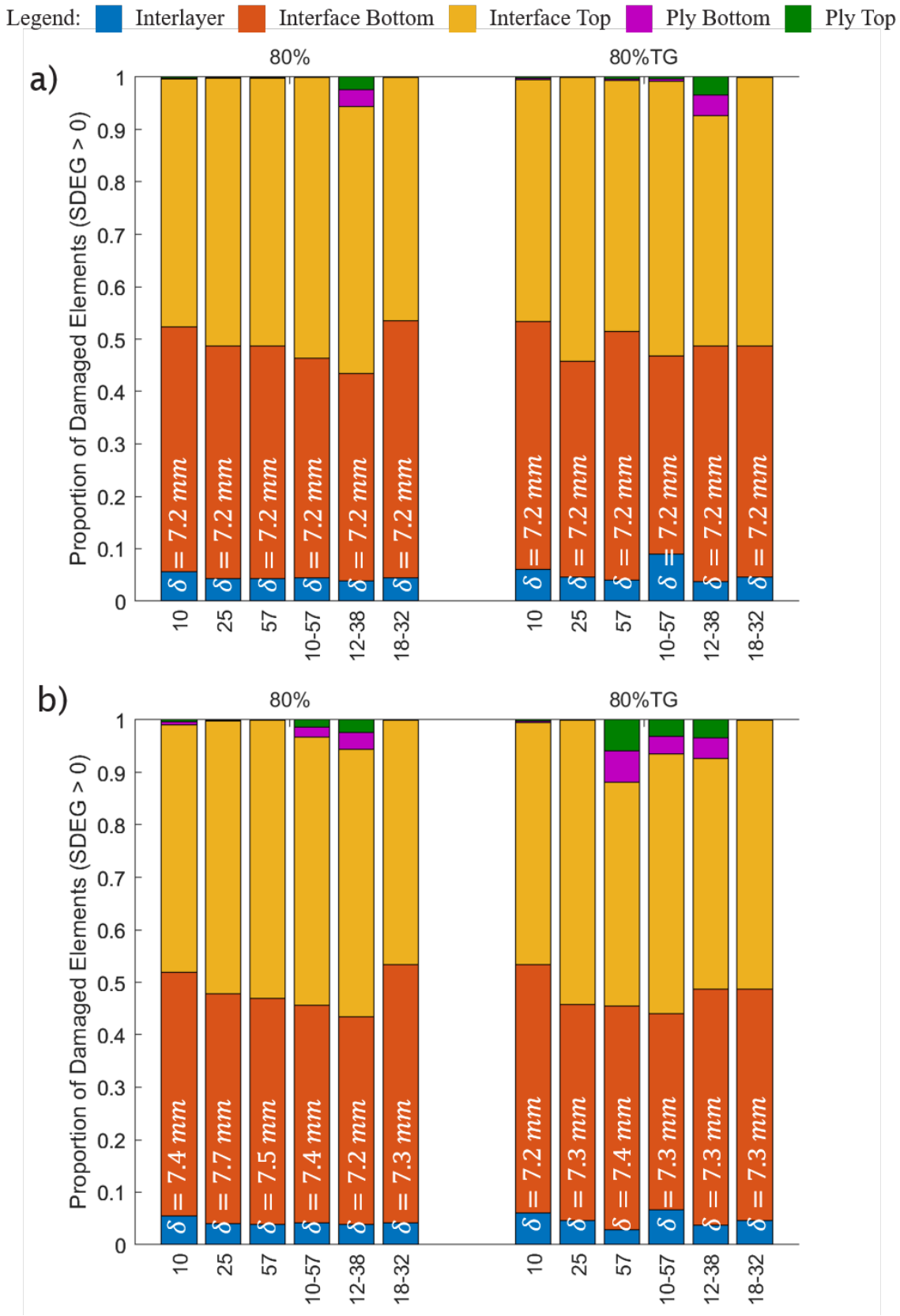

Figure 53 Proportion of damaged elements in each potential delamination path when the relative interface strength is 80% of that of the interlayer and SDEG > 0. a) Shows the proportion of the crack in each layer at a commonly converged timestep making the results directly comparable. The 10 µm thickness interlayer has the most damage

distributed in the interlayer. The presence of tow gaps notably increases the proportion of damage in the interlayer for the 10 – 57 µm varying interlayer thickness model. b) Shows the proportion of the crack at the respective final converged timestep for each model, therefore these proportions are not directly comparable with each other. The tow gaps appear to have a smaller effect on the crack path with an increase in damage in the interlayer in the 10 – 57 µm varying interlayer thickness model.

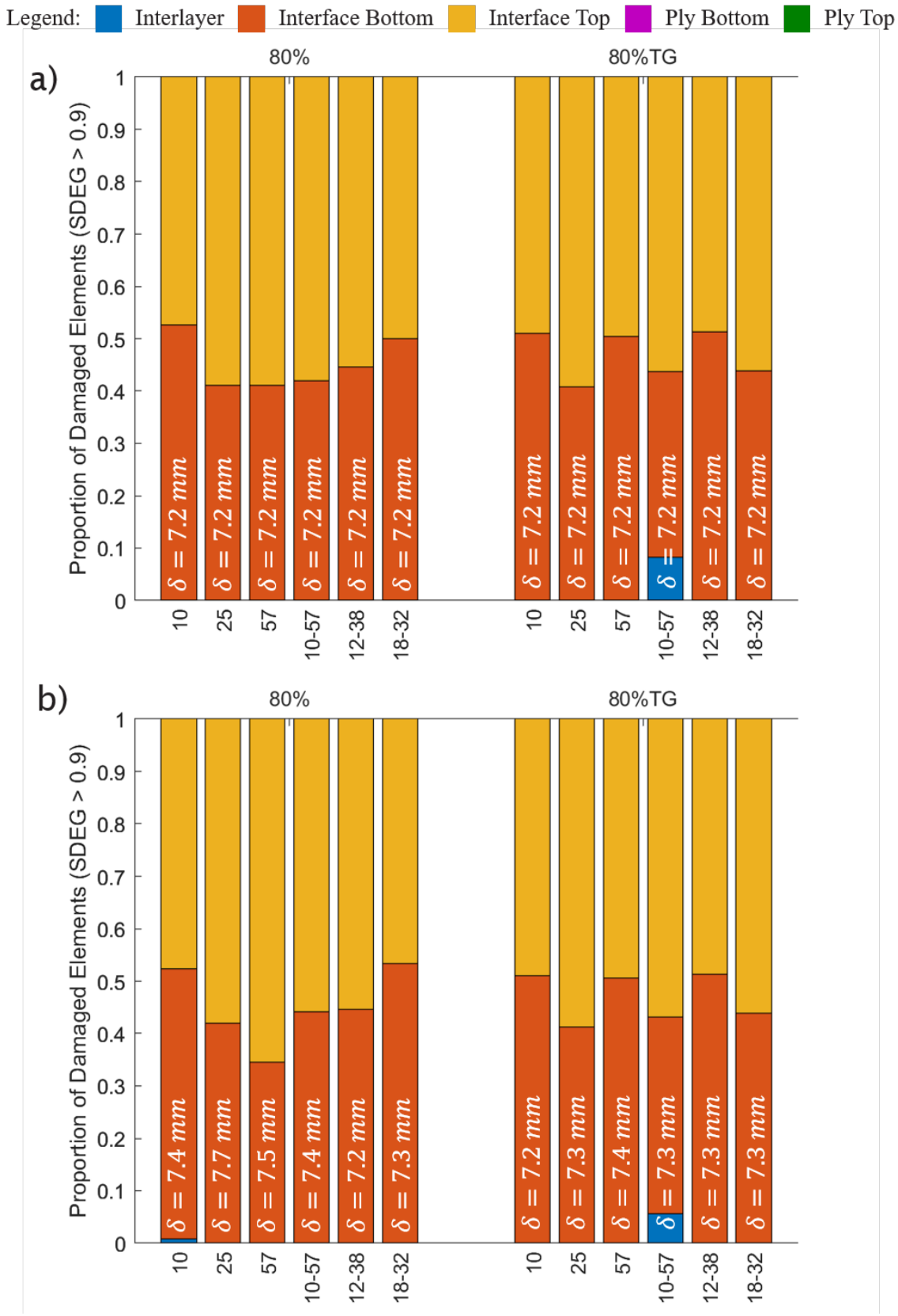

Figure 54 Proportion of damaged elements in each potential delamination path when the relative interface strength is 80% of that of the interlayer and SDEG > 0.9. a) Shows the proportion of the crack in each layer at a commonly converged timestep making the results directly comparable. In the absence of tow gaps the crack is distributed in the

interlayer-fibre interface, however, the presence of tow gaps facilitates a small proportion of the crack to be retained within the interlayer for the 10 – 57 µm varying thickness model. b) Shows the proportion of the crack at the respective final converged timestep for each model, therefore these proportions are not directly comparable with each other. The distribution of damage is similar to that mentioned above, however, a small fraction of the crack appears to have transitioned to the interlayer of the 10 µm thick model absent of tow gaps.

5.3.2.2 Interface Strength 90% of Interlayer Strength

Figure 55 shows the proportion of damaged elements for each geometric condition when the relative strength of the interface and ply was 90% of the interlayer with and without the presence of tow gaps.

Figure 55a compares the models at a common converged timestep as mentioned previously. Similar to before here is a clear migration of the damage out of the interlayer and to the upper and lower interface regions, however with little or no damage in the ply, with or without the presence of tow gaps. Without the presence of tow gaps the 57 µm thick interlayer shows the greatest proportion of damaged elements in the interlayer. The presence of tow gaps is seen to slightly increase the proportion of damage in the interlayer for all models, with the most significant increase being observed in the 10 – 57 µm varying thickness model.

Figure 55b compares the models at their respective final converged timesteps as similarly mentioned previously. The damage is seen to develop without the presence of tow gaps in the 10 – 57 µm varying thickness model, where the presence of tow gaps in this model reduces the proportion of damage in the ply. Whereas the presence of tow gaps for the 25 µm and 57 µm models increases significantly the proportion of damage within the ply.

Figure 56 shows the proportion of the fully developed crack within each potential delamination path. Similar to before a) makes a comparison at a common converged timestep and b) at each respective final converged timestep. In Figure 56a the fully developed crack can be seen to have fully transitioned to the upper and lower interface regions for the 10 µm and 25 µm thickness models without the presence of tow gaps. Notably for the 57 µm model without tow gaps, the crack remains fully within the interlayer. The varying thickness models see a decrease in the proportion of the fully developed crack within the interlayer as the amplitude decreases. The presence of tow gaps has a clear impact on the transition of the fully developed crack path reducing significantly the proportion in the interlayer for the 57 µm thickness model (from 100%

to ≈ 15%). In Figure 56b the continued transition of the crack to the interface is evident due to the reduced proportion of the total crack within the interlayer for most models, except for the 10 µm thickness interlayer model, where a small amount of interlayer failure occurs, and the 57µm model, where 100% interlayer failure occurs, unchanged from the common converged timestep represented in Figure 56b.

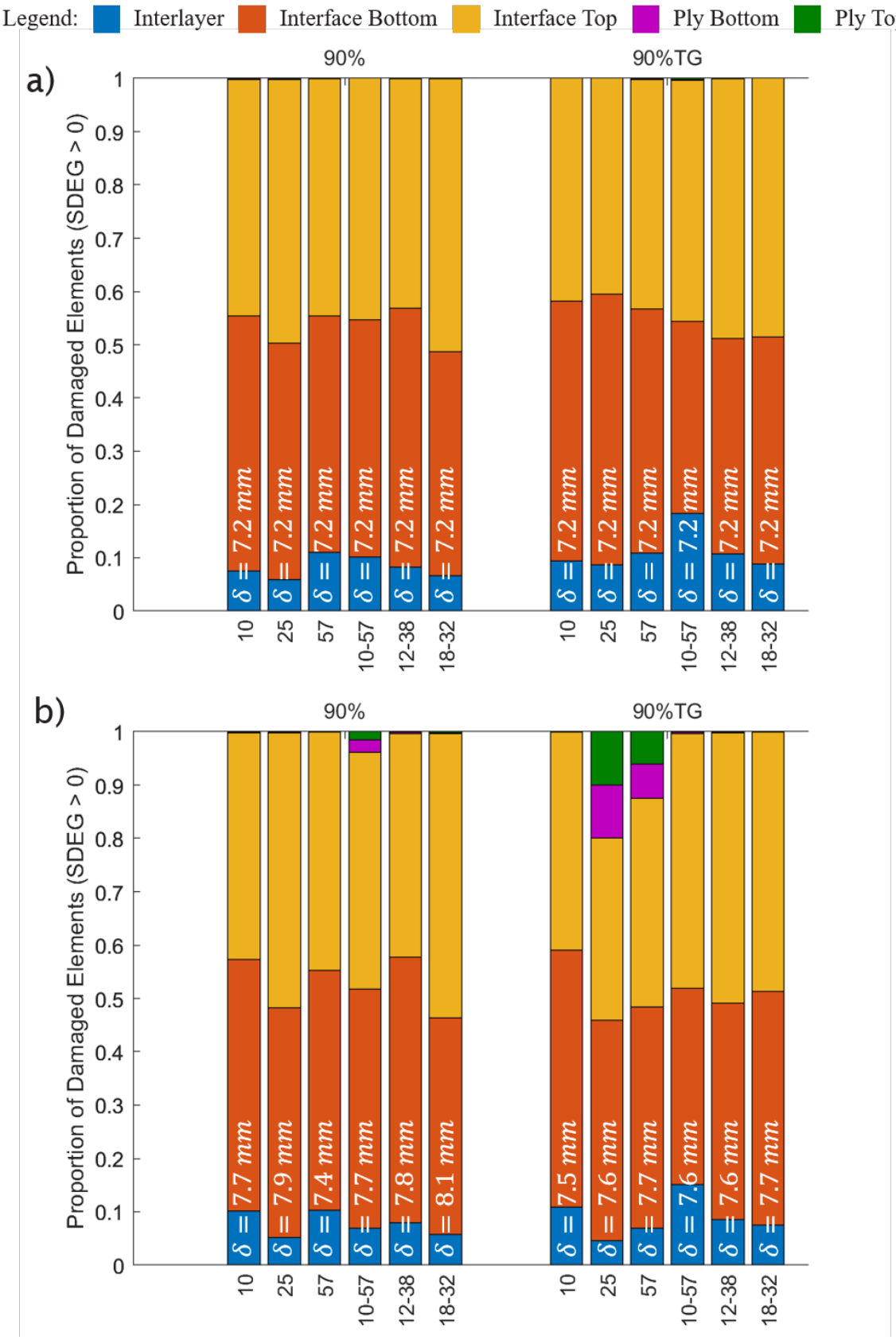

Figure 55 Proportion of damaged elements in each potential delamination path when the relative interface strength is 90% of that of the interlayer and SDEG > 0. a) Shows the proportion of the crack in each layer at a commonly converged timestep making the results directly comparable. In the absence of tow gaps, the most damage is

distributed in the interlayer for the 57 µm constant thickness model and the proportion decreases when variation is introduced and as the interlayer gets thinner. Notably, the model with the least damage distributed in the interlayer is the 25 µm interlayer thickness model. The presence of tow gaps increased the distribution of damage in the interlayer for all models, particularly the 10 – 57 µm varying interlayer thickness model b) Shows the proportion of the crack at the respective final converged timestep for each model, and therefore these proportions are not directly comparable with each other. The presence of tow gaps appears to enable damage to propagate in the top and bottom plies in two of the constant thickness geometry models.

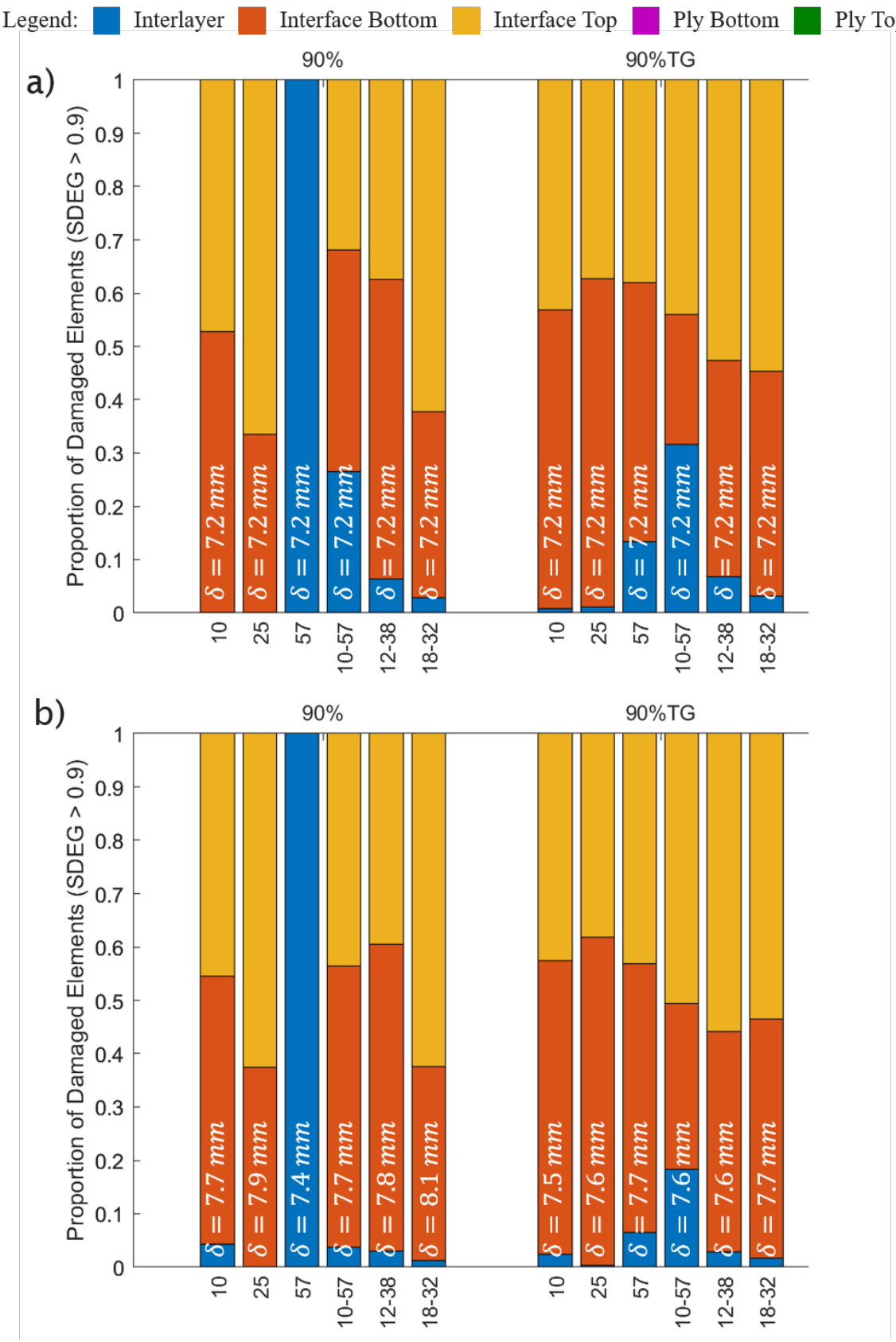

Figure 56 Proportion of damaged elements in each potential delamination path when the relative interface strength is 90% of that of the interlayer and SDEG > 0.9. a) Shows the proportion of the crack in each layer at a commonly converged timestep making the results directly comparable. In the absence of tow gaps the fully developed crack

remains entirely in the interlayer for the constant thickness 57 μm interlayer thickness model and a much smaller fraction remains in the interlayer for all the varying interlayer geometry models, whereas the thinner constant thickness interlayer models all see the crack transition out of the interlayer to the interlayer-fibre interfaces. The presence of tow gaps in the 57 μm constant thickness model significantly reduces the proportion of the crack in the interlayer by approximately 65 % b) Shows the proportion of the crack at the respective final converged timestep for each model, therefore these proportions are not directly comparable with each other. The crack remains entirely in the interlayer for the 57 μm thickness interlayer model, in the absence of tow gaps, however, the presence of tow gaps appears to facilitate a significant transition of the crack away from the interlayer.

5.3.2.3 Interface Strength 95% of Interlayer Strength

Figure 57 shows the proportion of damaged elements for each geometric condition when the relative strength of the interface and ply was 95% of the interlayer with and without the presence of tow gaps.

Figure 57a compares the models at a common converged timestep as mentioned previously. As seen in the previous models there is again a migration of the damage away from the interlayer, albeit to a lesser extent, with a greater proportion of the damage remaining within the interlayer region. There is very little damage distributed in the ply layers when no tow gaps are present for all geometries, however, when tow gaps are presented there is a marked increase in damage distributed in both the upper and lower ply layers for the 18 μm – 32 μm varying thickness interlayer.

Figure 57b compares the models at their respective final converged timesteps as similarly mentioned previously. For all models except for the 10 μm thickness model with no tow gaps, there is at least some damage distributed within the ply layers.

Figure 58 shows the proportion of the fully developed crack within each potential delamination path. Similar to before a) makes a comparison at a common converged timestep and b) at each respective final converged timestep. In Figure 58a it can again be seen that without the presence of tow gaps, the fully developed crack remains entirely in the interlayer for the 57 μm interlayer thickness model, however, the incorporation of tow gaps leads to a clearly greater proportion of interface failure. In Figure 58b it can be seen that with continued growth cracking increasingly migrates to the interface regions in all of the models.

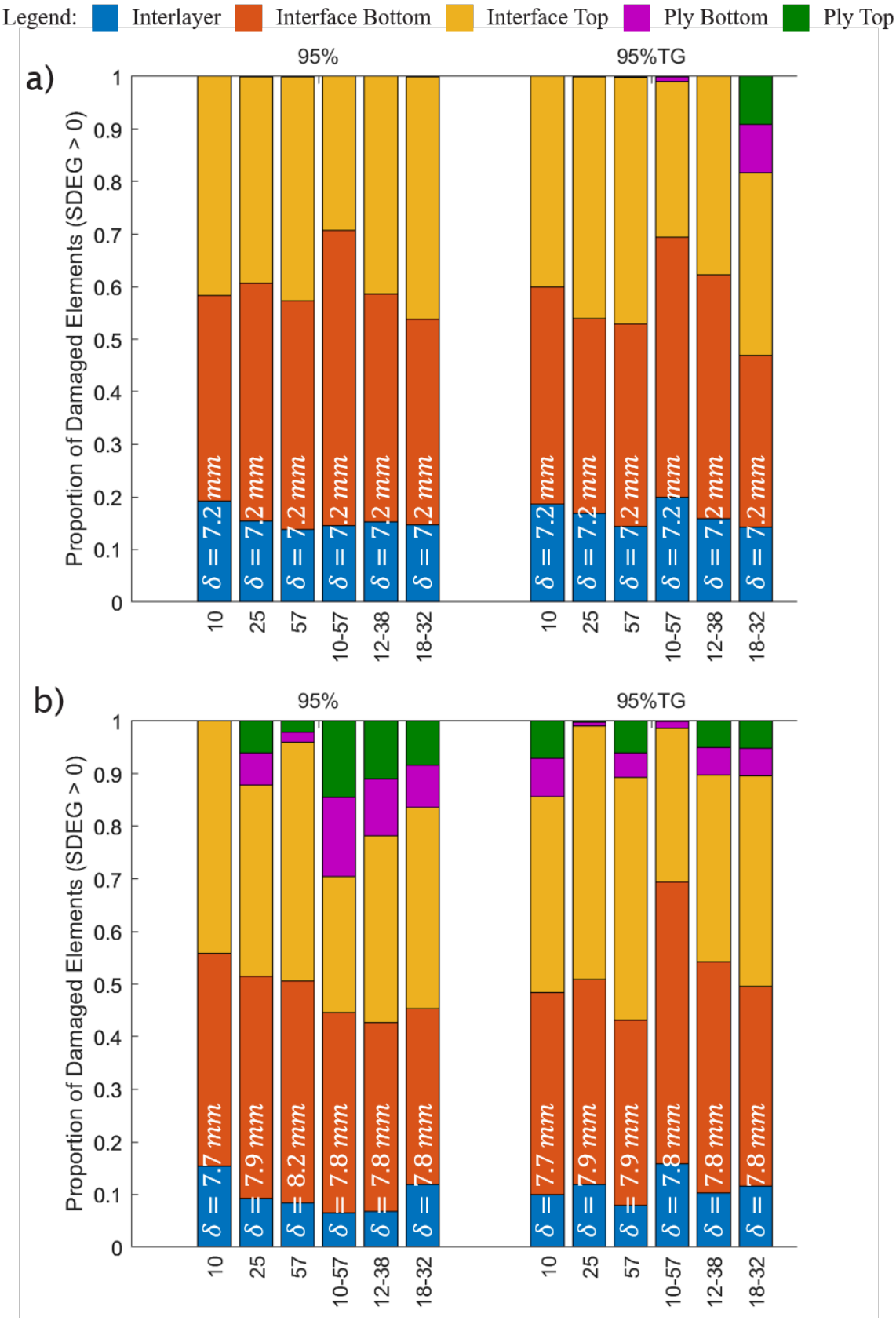

Figure 57 Proportion of damaged elements in each potential delamination path when the relative interface strength is 95% of that of the interlayer and SDEG > 0. a) Shows the

proportion of the crack in each layer at a commonly converged timestep making the results directly comparable. The thinner interlayer geometry models see the most damage distributed in the interlayer in the absence of tow gaps. The presence of tow gaps increases the distribution of damage in the interlayer for the 10 – 57 µm varying thickness interlayer. b) Shows the proportion of the crack at the respective final converged timestep for each model, therefore these proportions are not directly comparable with each other. Notably, there is a greater proportion of damage distributed in the upper and lower plies with and without and presence of tow gaps for the majority of models.

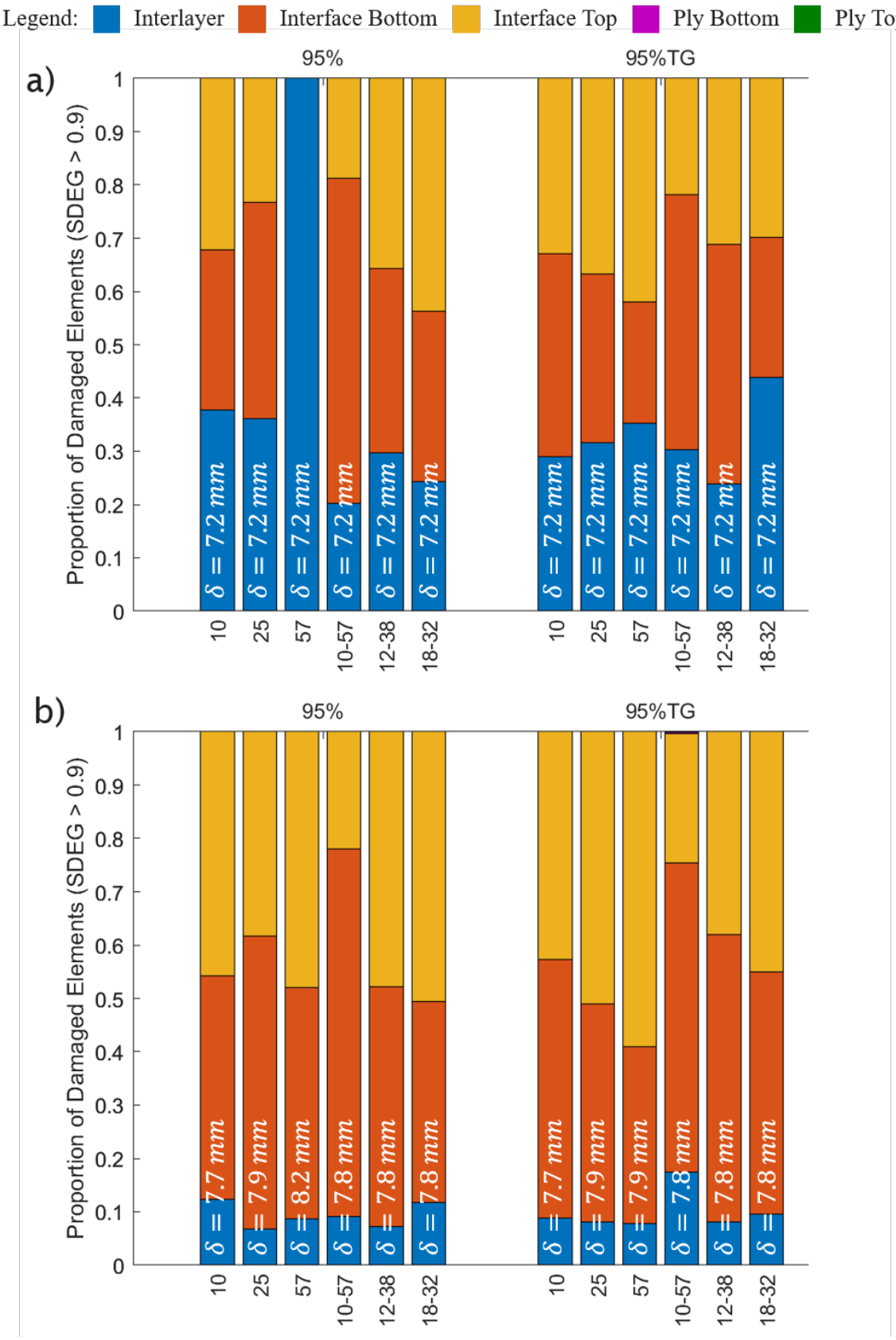

Figure 58 Proportion of damaged elements in each potential delamination path when the relative interface strength is 95% of that of the interlayer and SDEG > 0.9. a) Shows the proportion of the crack in each layer at a commonly converged timestep making the results directly comparable. A greater proportion of the crack is distributed in the

interlayer for all models, however, the majority of the crack remains in the interlayer-fibre interface, with the exception of the 57 µm interlayer thickness model absent of tow gaps. The presence of tow gaps reduces the proportion of the crack in the interlayer for the constant thickness geometry models and the for the varying thickness geometry models where the standard deviation is greater than one. b) Shows the proportion of the crack at the respective final converged timestep for each model, therefore these proportions are not directly comparable with each other. The crack appears to transition out of the interlayer in all models despite the strength of the interface is 95 % that of the interlayer for all models.

5.3.2.4 Interface Strength 100% of Interlayer Strength

Figure 59 shows the proportion of damaged elements for each geometric condition when the relative strength of the interface and ply was the same as that of the interlayer with and without the presence of tow gaps.

Figure 59a compares the models at a common converged timestep as mentioned previously. The observations of total damage distribution are similar to the trends in the previous cases, and the trend of a greater proportion of the total damage occurring within the interlayer continues, with similar observations being made in Figure 59b, however, it is notable that with the increase in crack opening displacement and therefore crack growth there is significantly more damage distributed in the top and bottom ply

Figure 60 shows the proportion of the fully developed crack within each potential delamination path. Similar to before a) makes a comparison at a common converged timestep and b) at each respective final converged timestep. In Figure 60a without tow gaps, the fully developed crack remains entirely in the interlayer. However, when tow gaps are present they significantly reduce the proportion of the crack in the interlayer for the 10 µm – 57 µm varying thickness model, with a lesser effect on the other geometry models. In Figure 60b it can be seen that with further crack propagation, there is still a transition from the interlayer to the upper and lower interface regions. It should be explicitly noted here that due to the convergence behaviours of each model, the proportions of the crack here are not comparable, but the main observation that cracks transition does still occur in all models is valid.

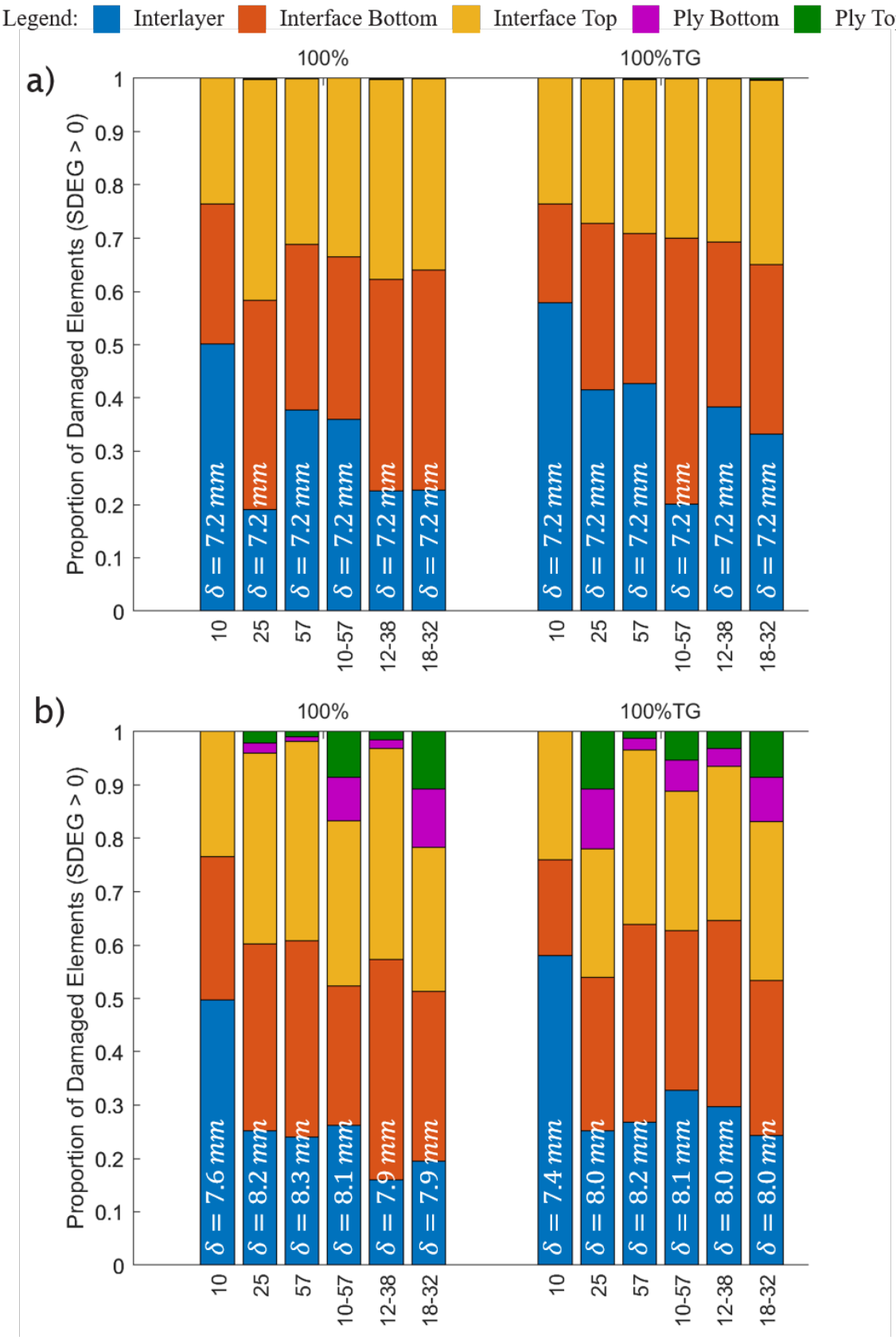

Figure 59 Proportion of damaged elements in each potential delamination path when the relative interface strength is equal to that of the interlayer and SDEG > 0. a) Shows the proportion of the crack in each layer at a commonly converged timestep making the results directly comparable. almost 50 % of the damage is distributed within the

interlayer of the 10 µm thickness interlayer model with the absence of tow gaps. When tow gaps are present the proportion of damage in the interlayer increases to around 55 %. The same trend is similarly seen in the other models except for the 10 – 57 µm varying thickness interlayer model where damage distribution within the interlayer decreased with the presence of tow gaps. b) Shows the proportion of the crack at the respective final converged timestep for each model, therefore these proportions are not directly comparable with each other. Notably, the proportion of damage in the interlayer increases in the presence of tow gaps for all models as well as damaged elements in the upper and lower ply in all models except for the 10 µm interlayer thickness model regardless of the presence of tow gaps.

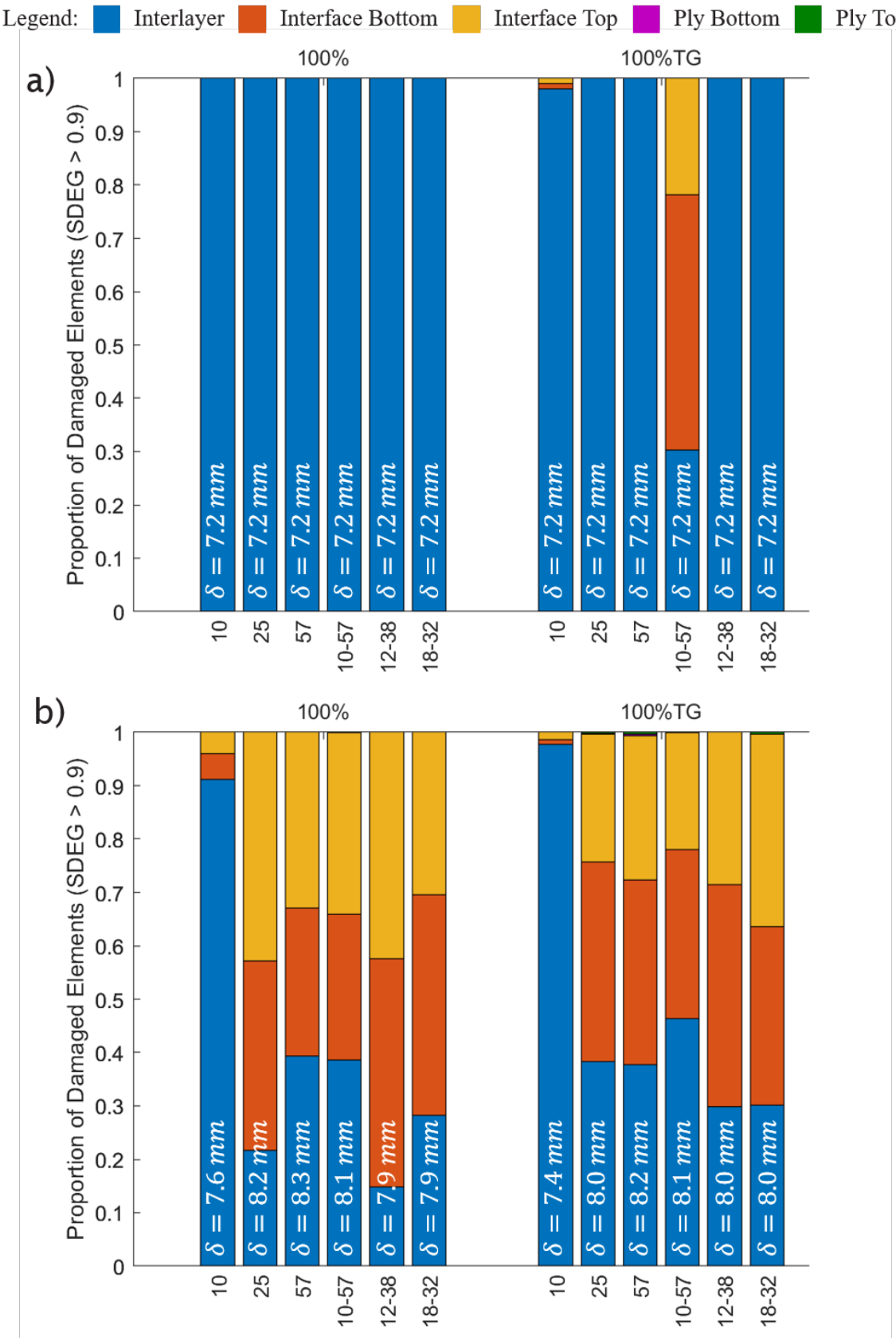

Figure 60 Proportion of damaged elements in each potential delamination path when the relative interface strength is equal to that of the interlayer and SDEG > 0.9. a) Shows the proportion of the crack in each layer at a commonly converged timestep making the results directly comparable. Absent of tow gaps, the crack remains in the interlayer

for all models. When tow gaps are present there is a limited transition of the crack to the interlayer-fibre interface for the 10 µm interlayer thickness model and a much more significant transition in the 10 – 57 µm varying thickness interlayer, where approximately 70 % of the crack has transitioned to the interface. b) Shows the proportion of the crack at the respective final converged timestep for each model, therefore these proportions are not directly comparable with each other. At the final converged timestep for each model, it is illustrated that for all interlayer geometry conditions when the relative strength of the interlayer and interface are equal, the crack transitions away from the interlayer.

5.3.2.5 Interface over Strength 100% of Interlayer Strength

Figure 61 shows the proportion of damaged elements for each geometric condition when the relative strength of the interface and ply was greater than that of the interlayer, however, the effect of tow gaps has not been analysed for these model conditions.

Figure 61a compares the models at a common converged timestep as mentioned previously. All damage is concentrated in the interlayer for all geometry conditions when the relative interface strength is greater than that of the interlayer. In contrast to the previous models, Figure 61b which compares the models at their respective final converged timestep shows a much more complex distribution of damage between all possible delamination layers, but the greatest proportion remains in the interlayer.

Figure 62 shows the proportion of the fully developed crack within each potential delamination path. Similar to before a) makes a comparison at a common converged timestep and b) at each respective final converged timestep. In Figure 62a the crack is seen to remain in the interlayer for all models. However, in Figure 62b there is some crack transition when the relative interface strength is 1.05 times that of the interlayer and no observed transition when the relative strength was 1.1 and 1.2 times that of the interlayer.

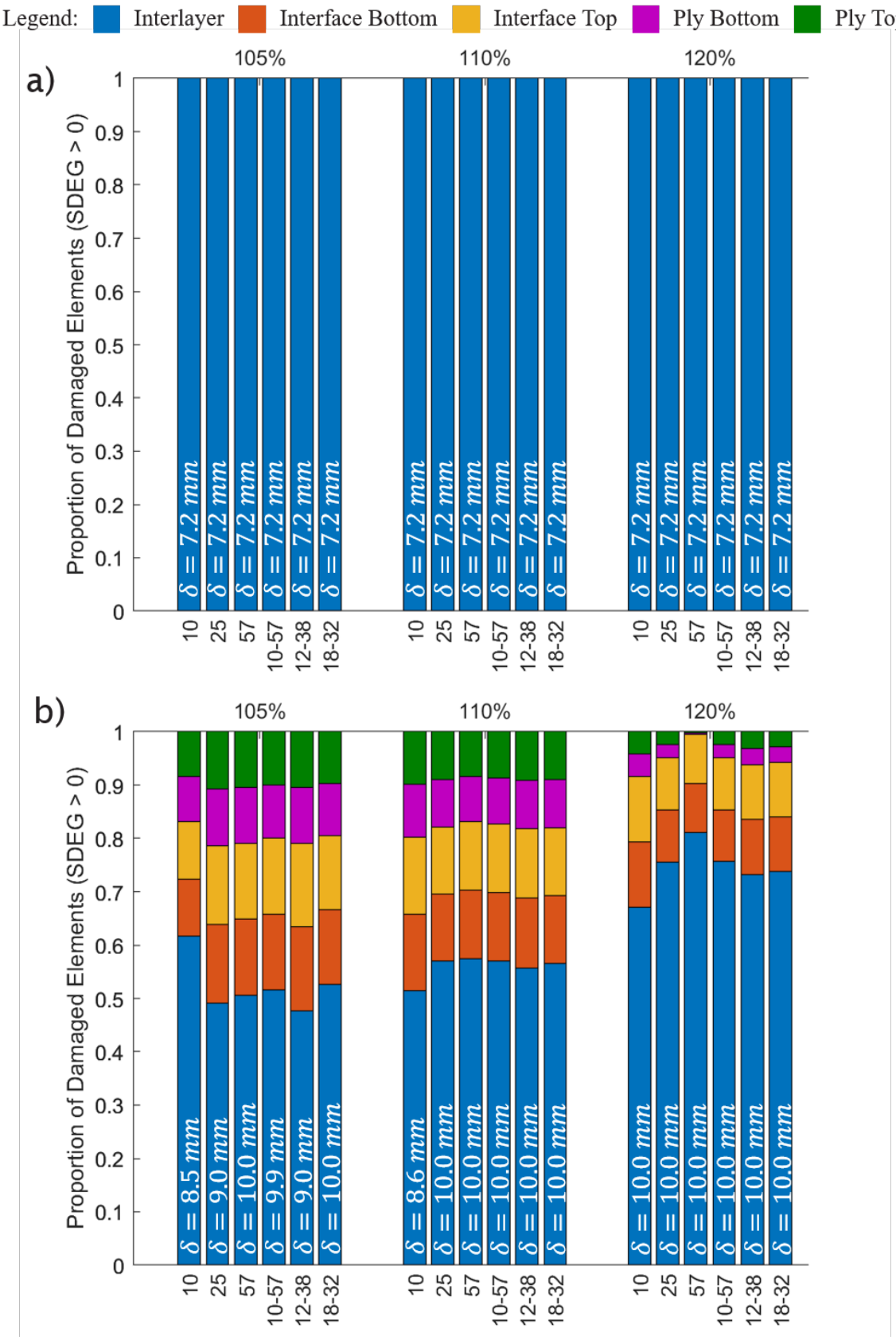

Figure 61 Proportion of damaged elements in each potential delamination path when the relative interface strength is 105%, 110% and 120% of that of the interlayer respectively and SDEG > 0. a) Shows the proportion of the crack in each layer at a commonly converged timestep making the results directly comparable. For all models, the

relative strength of the interface is greater than the interlayer and all damage remains in the interlayer for all interlayer geometries. b) Shows the proportion of the crack at the respective final converged timestep for each model, therefore these proportions are not directly comparable with each other. For all interlayer geometry models the damage becomes distributed within the interlayer with further load-point opening displacement there is a clear trend for all interlayer geometries that as the strength of the interface increases relative to the interlayer the proportion of damage distributed in the interlayer increases.

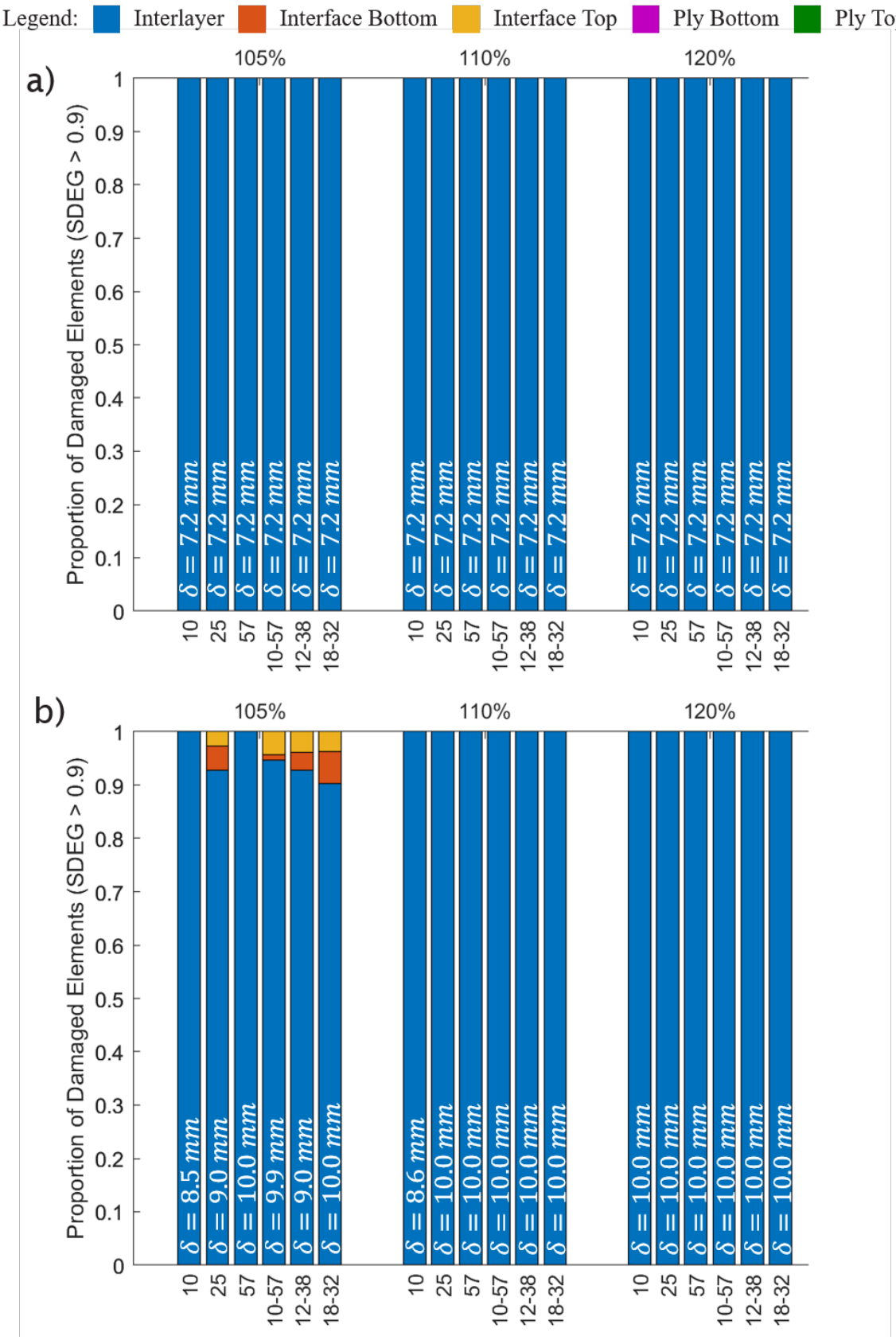

Figure 62 Proportion of damaged elements in each potential delamination path when the relative interface strength is 105%, 110% and 120% of that of the interlayer respectively and SDEG > 0.9. a) Shows the proportion of the crack in each layer at a commonly converged timestep making the results directly comparable. The crack remains in the

interlayer for all models. b) Shows the proportion of the crack at the respective final converged timestep for each model, therefore these proportions are not directly comparable with each other. A small proportion of the crack transitions to the interlayer-fibre interface when the strength of the interface is 1.05 times that of the interlayer for the final converged step of the 25 μm interlayer thickness model and all varying thickness models. When the strength of the interface is greater than 1.05 times the strength of the interlayer the whole crack remains in the interlayer for all models.

5.3.2.6 Stochastic Distribution of Interface and Interlayer Strength

Figure 63 shows the proportion of the crack at the final timesteps of the stochastic models (the cohesive properties of the progressive damage elements are assigned randomly) for all damage distributed (a) and for the distribution of the fully developed crack (b). These models have not been compared at equal timesteps due to the large difference in the convergence between the models which is reflective of the complexity of the crack path, hence comparing at a common timestep would not provide a fair reflection of the damage distribution between models. What is evident, however, is that the proportion of damaged elements and the proportion of fully damaged elements are much more consistent than in any of the previous models. There is also a significant proportion of the crack distributed in the upper and lower plies when only elements with an SDEG > 0.9 is considered, which is not seen in the results presented previously for the parameter sweep.

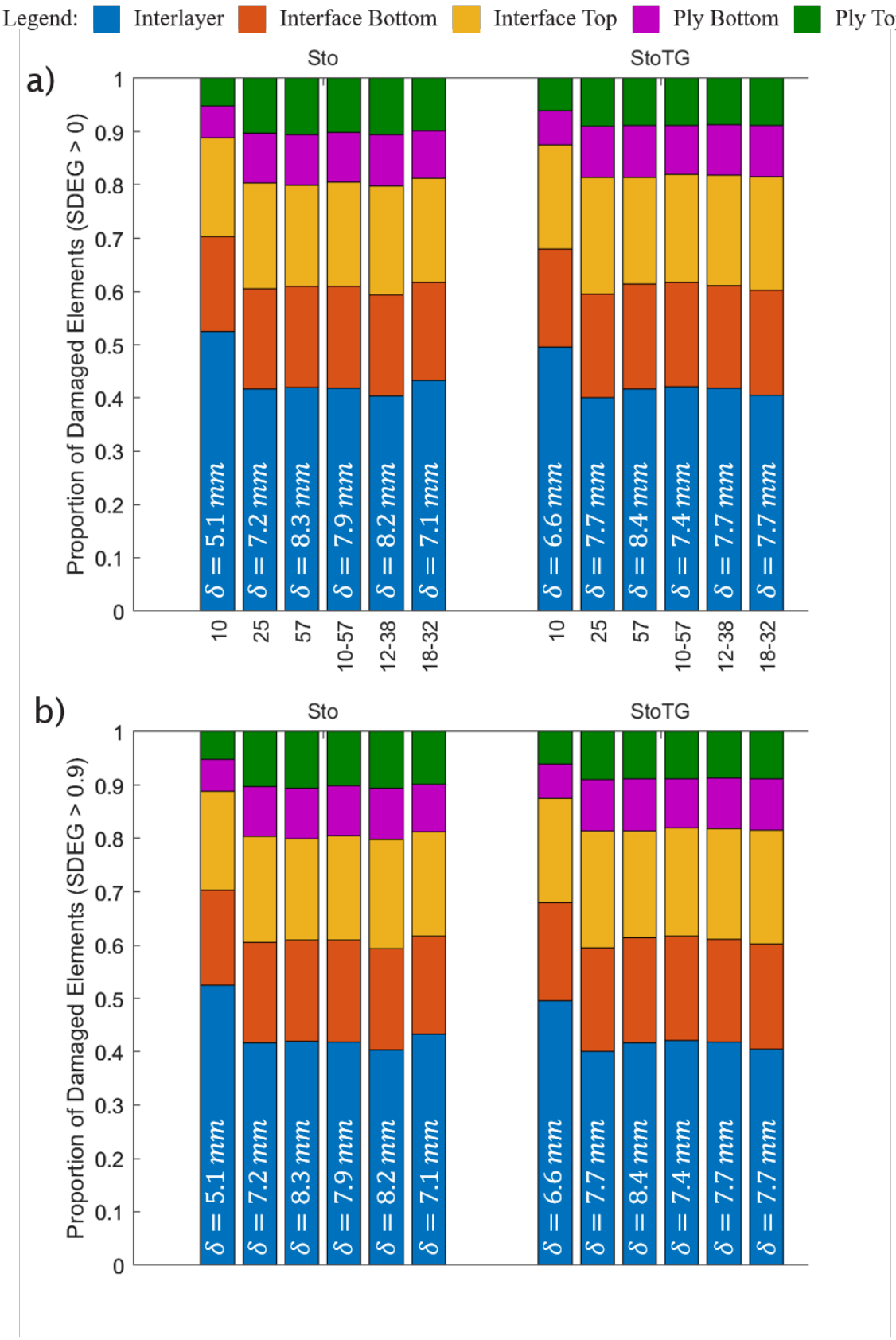

Figure 63 Proportion of damaged elements in each potential delamination path when the strength properties of the progressive damage elements in the interfaces and interlayer are stochastic. a) Shows the total proportions of elements with SDEG > 0 due to damage at the final timestep for each respective model. Therefore, models are not directly

comparable with each other. b) Shows the proportion of fully damaged elements being capable of supporting less than 90% of their original load-bearing capacity at the final timestep for each respective model. Therefore, models are not directly comparable with each other. It is noteworthy that for stochastic fracture properties, the distribution of the fully developed crack is similar to the total damage distribution. There is also little difference in damage distribution with or without the presence of tow gaps. Damage is distributed in all layers for all the models.

5.3.3 Change in Interlayer Toughness with Varying Interlayer Geometry

The apparent toughness for each geometric model when the relative strength of the interface was 120% of the interlayer crack initiation strength was calculated to evaluate whether the interlayer geometry has an appreciable effect on the delamination resistance of coupon This case was chosen as there was no crack transition away from the interlayer, the models displayed the best convergence behaviour and hence the effect of the interlayer thickness on its strength could be isolated. The toughness was calculated the same way it would be for a coupon undergoing Mode I delamination in a physical DCB test by using modified beam theory (MBT) as shown in Equation 5-5.

$$G_{IC} = \frac{3P\delta}{2b(a + |\Delta|)} \qquad 5\text{-}5$$

Where P is the opening force, δ is the load opening displacement, b is the full specimen width, a is the length of the crack from the load point, and $|\Delta|$ is determined as the point where the least squares fit intersects the x-axis of the plotted of the graph of the cube root of compliance ($C^{1/3}$) vs delamination length (a). The general response between all models is the same, i.e. no crack transition and the same R-curve shape, so the mean value of G_{IC} is directly comparable and the interlayer thickness/variation can be isolated. Figure 64 shows the mean G_{IC} plotted for each interlayer geometry condition and the error bars represent the standard error of the mean for each case. The standard error of the mean in this case provides a measure of the variation in the G_{IC} throughout crack propagation for each respective model. The largest variation in the mean toughness between models is 6.2% which is between the 57 µm thick interlayer model and the 10 µm to 57 µm varying thickness model. There is a slight decrease in toughness as the interlayer thickness increases for the constant thickness models. For the varying interlayer thickness models, toughness decreases slightly as the variation in thickness becomes less extreme.

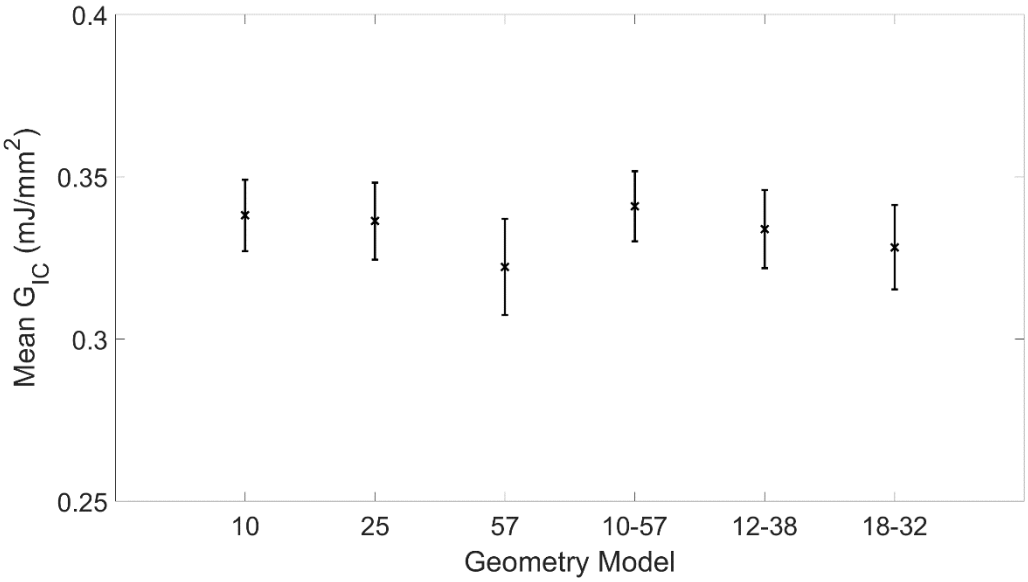

Figure 64 Variation in the apparent critical strain energy release rate for each geometric model when the interface stress is 120% of the interlayer strength, where the error bars represent the standard error of the mean.

5.3.4 Stochastic Influence on Rate of Crack Transition

A comparison of the load point opening displacement required for 25 % of the crack to transition out of the interlayer for each interlayer geometry condition where the cohesive properties vary stochastically from element-to-element is plotted in Figure 65. As the interlayer thickness increases a greater displacement is required to drive the crack out of the interlayer. The 57 µm model requires the largest opening and the 10 µm the least. It is also worth noting that the varying geometry models require a greater opening for the crack transition than the constant thickness interlayer model based on the mean interlayer thickness value (25 µm), however, require less than the 57 µm constant thickness interlayer model.

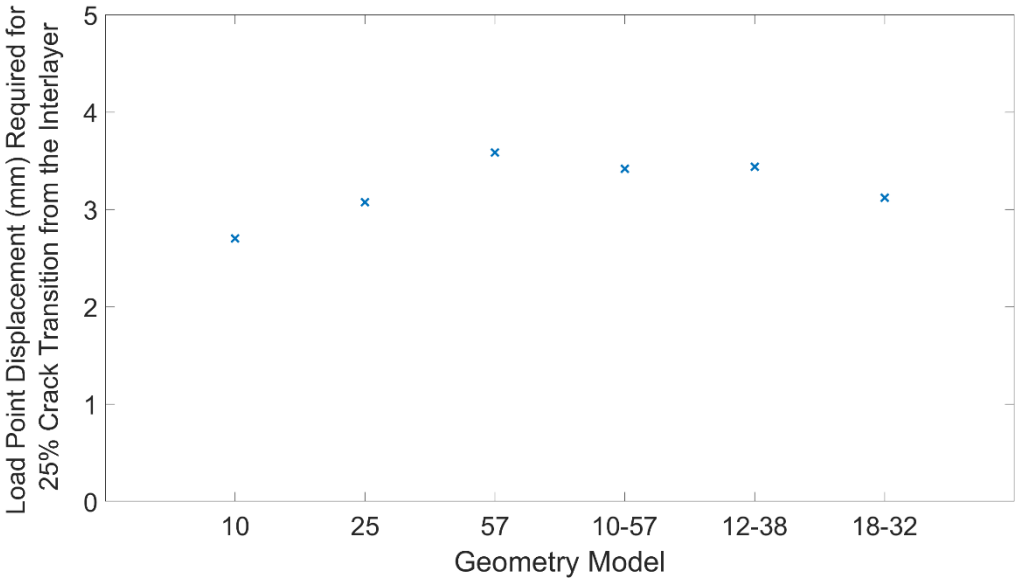

Figure 65 Load Point Opening displacement required for 25% of the crack to transition out of the interlayer

5.4 Discussion

5.4.1 Damage Distribution during Crack Propagation

Figure 53 to Figure 63 indicate that the single most important factor determining crack path is the relative values of the fibre/ply interface strength compared to the crack initiation strength in the interface. Relatively small variations in the relative strength of the interface, in the range of ±10%, lead to a transition from a crack remaining entirely within the interlayer to a crack path at the ply interfaces. This is consistent with the conclusions from Borstnar's earlier micromechanical modelling [49], but this must be confirmed at the scale of typical test specimens. It is also notable that over the range of parameters explored in this work, and with the modelling assumptions made, the crack only jumps into adjacent plies, which is likely to result in fibre-bridging, under limited circumstances, which is achieved if ply thickness varies in combination with the presence of tow gaps.

Regarding the influence of ply thickness, there is a marked difference in the distribution of damaged elements equating to all damage and those equating to a fully developed crack. In general, the thinnest interlayer model of 10 µm has a higher proportion of damage in the interlayer. However, in terms of fully damaged elements equating to a developed crack the proportion of the elements in the interlayer is significantly smaller and it is the thickest interlayer which leads to a greater fraction of the crack remaining in the interlayer for longer. To explain this behaviour, it is instructive to consider a volume around the crack tip as a process zone, as shown

schematically in Figure 66. The detailed micro mechanisms operating in the process zone are not important. However, it is reasonable to assume that the radius of the process zone is largely independent of the local microstructure. If it is considered that in Figure 66 all variables other than the interlayer thickness are equal, the distribution of damage around the crack tip can be assessed. In the thinner interlayer for case a) and case b), the process zone overlaps significantly with the interlayer and fibres. Whereas for the thicker interlayer in case c), and case d) there is no overlap when the crack is in the interlayer and very little overlap when the crack is in the ply. This means that in the thinner interlayer, there is more potential for the damage to be distributed in all layers, and microcracks can develop in the interlayer far more easily than in the thicker interlayer case, hence a higher proportion of the total damage is contained within the interlayer. However, this 'low-level' damage does not necessarily develop into a fully developed crack which could in part be due to hydrostatic stresses not allowing these cracks to open and hence shielding the main crack. This may in part explain the contrast between damage distribution and developed crack distribution.

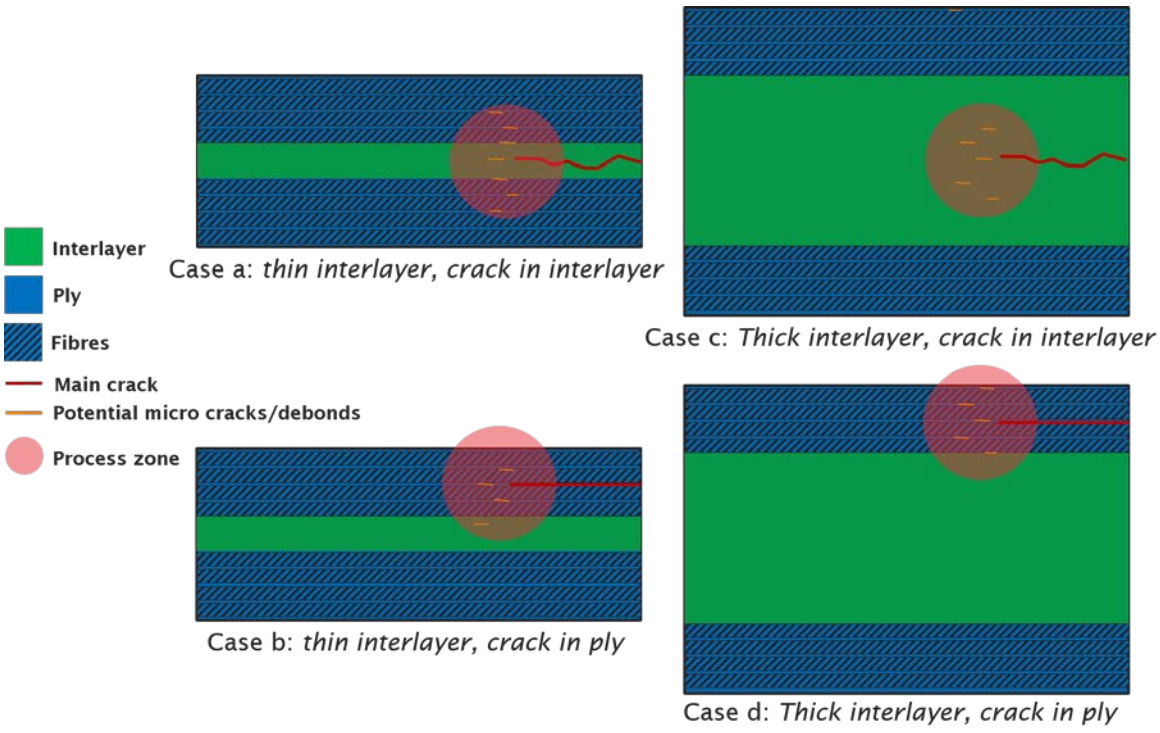

Figure 66 potential crack interaction with adjacent fibre-matrix interface regions, showing as the interlayer becomes thicker there may be less interaction with the fibres in the surrounding plies of the interlayer.

The inclusion of tow gaps in the model appears to have a similar effect as increasing the interaction between the potential delamination paths as seen. As is particularly evident when the cohesive strengths of the interlayer and interface regions are within 5 % of each other. Where the total damage distribution in the interlayer increases when the cohesive strength of the interlayer

less than 90% of that of the interface as shown particularly in Figure 53 and Figure 55. Their presence tends to increase the proportion of total damage in the interlayer. This could be due to the geometrical junction which is formed between all potential delamination μm paths. However, these effects are relatively modest when compared to the influence tow gaps can have on the fully developed crack path. No crack transition is seen out of the interlayer for an interlayer thickness of 57 μm when the relative strength of the interface is 90% of the interlayer or greater (in Figure 56, Figure 58, and Figure 60.). However, when tow gaps are introduced over 60% of the fully developed crack transitions at the commonly converged timestep (equivalent to a load point opening displacement of 7.2 mm) when the relative interface strength is 95% of that of the interlayer as shown in Figure 58. This effect seems to be compounded by two other variables, a thinner interlayer, and by variation in the interlayer thickness with the interlayer model varying from 10 – 57 exhibiting a significant crack path transition even when there is no relative strength difference between the interlayer and the interface.

5.4.2 Toughness Response with Increasing or Varying Interlayer Thickness

It is well known that the inclusion of toughening particles causes a thickening of the interlayer between plies which is thought to be dependent on particle volume fraction, distribution, and average size [122, 232-234, 238, 239]. However, there is not a clear consensus, nor any specific research on whether the thickness of the interlayer itself affects the toughness of the composite. There is an argument to be made that if the incorporation of toughening particles increases the toughness of the composite then any effect resulting from the architecture of the interlayer could be considered inconsequential. It could also be argued, however, that the interlayer thickness resulting from interleaving could be a significant variable in predicting, or biasing towards a particular toughening response mechanism. The results shown above support this assertion.

Firstly, it is useful to separate the concepts of initiation toughness and propagation toughness. Here the initiation toughness is used to refer to the measured G_{IC} value in the first few mm's of crack growth [240], whereas the propagation toughness refers to the resistance of the composite to further crack propagation where the toughness plateaus [241] and was considered as the mean value of the G_{IC} values in the final 25 mm of crack growth in the work presented by Borstnar [84]. Therefore, considering the initiation toughness of the composite Figure 64 shows a slight increase in G_{IC} with decreasing interlayer thickness. It also shows that the presence of interlayer thickness variation (about a mean thickness of 25 μm) also increases the G_{IC} value. Therefore, in practical terms, it would suggest that in a case similar to that presented by Hayes and Seferis [122] when the particle volume fraction is lower, the distribution of the particles and resulting interlayer thickness is of greater influence (in comparison with a higher volume fraction), a thinner

interlayer could cause an increased initiation toughness in this case, however, the effect is small and unlikely to be defining.

On the other hand, the delamination resistance response with increased crack opening and delamination propagation is also significant, with a flat or rising R-curve response desirable. The results presented give some insight into potential crack path scenarios and the potential toughening mechanisms arising from those crack path transitions. In the initial case considering the constant thickness interlayers, it is seen from the stacked bar charts in Figure 53 to Figure 63 that the thinner interlayer causes more interaction within the ply and results in more crack transition to the interlayer-fibre interface. It can also be seen in Figure 65 that the crack transition occurs in thinner interlayer models with a smaller load point opening displacement. Therefore, the modelling suggests that if the relative cohesive strength of the interface is equal to or less than that of the interlayer then a large proportion of the crack transitions to the interlayer-fibre interface in only 100 – 1000's of μm's of crack growth. The varying geometry models similarly promote crack transition to the interlayer-fibre interface. Furthermore, they also show a larger share of damage distribution in the ply than the constant thickness models.

The consequence of this crack transition will depend on the specific makeup of the composite material. However, several scenarios can be hypothesised. Firstly, the crack remains in the toughened interlayer. This appears most likely to occur for thicker, more uniform interlayers, with fewer tow gaps. Evidently, if a crack remains in the interlayer it will give rise to damage response mechanisms associated with such, *i.e.* particle-crack face bridging, crack pinning, particle-matrix debonding *etc*. This could lead to a small initial rise followed by self-similar crack propagation and flat R-curve behaviour but is unlikely to lead to a rising R-curve behaviour [78]. The second scenario is a transition to the interlayer fibre interface. If it is assumed that the fracture toughness of this interface is lower than the interlayer then this could lead to an initially decreasing R-curve [231]. The model suggests that this is most likely to occur in thin, constant thickness interlayers. Finally, a transition of the crack into the ply could occur. If oblique fibre-bridging is not induced then a case similar to the transition to the interlayer-fibre interface will result, with a decreasing R-curve. However, it is also possible that such a crack-path transition and weak fibre-resin interfaces could lead to fibre-bridging which can then cause significant toughening and a rising R-curve [23, 69]. This scenario is most likely to occur in a varying thickness interlayer, particularly if tow gaps are present. The modelling presented in this work predicts relatively low fractions of crack transition into the ply. In DCB coupons, this transition is seen more frequently, with resulting oblique fibre-bridging and significant changing R-curve behaviour. This suggests that other micromechanical factors may also be important, and could be considered in future modelling as well as microstructural characterisation. Relevant factors might include longitudinal

fibre waviness, ply and fibre-level residual stress, and mesoscale variations in effective interface strength from the surface fibres on a ply to those in the bulk which may require a multiscale modelling approach to explore.

5.5 Conclusions

This work presented has explored, using finite element progressive damage modelling, key mechanisms and interactions on a meso to macroscale which contributes to crack path transitions and toughening of a UD toughened epoxy composite system. A combined CZM and XFEM modelling approach provides an effective means to determine to crack path as a function of local geometry and material property variation. Key factors determining the transitions of the crack path were identified. This model builds upon previous work on the microscale by using a 3D DCB scale model and observing crack growth over 1000's of μm's and accounting for stochastic variability in cohesive properties. Simplifications are made to represent the interlayer's geometry and allow parametric variations to be explored. Individual fibres and toughening particles are not modelled explicitly. However, the current work agrees with previous findings as well as being in line with experimental observations

The transition of the crack from the interlayer to the fibre-matrix interface is found to be sensitive to the relative cohesive properties of the respective layers and ply/fibre interfaces. The meso geometry of the interlayer, particularly thickness variation, within the range observed experimentally, was shown to be a significant factor in determining the crack path. The interlayer's absolute and mean thickness determined the system's sensitivity to crack path transition for specific combinations of material properties. It has been shown that to increase the probability of the crack remaining in the interlayer, the interlayer geometry should be as thick as is allowable given other material and manufacturing constraints and should not be skewed negatively from the mean value to avoid the transition from the interlayer. Even when stochastic variations in cohesive properties are accounted for, the geometry of the interlayer still plays a role in controlling the crack path.

Overall this work demonstrates the power of combining *in situ* XCT observations with parametric modelling to explore the sensitivities of composite material response to geometric, microstructural and micromechanical property variations. It is an example of the utility of "data-rich mechanics". In turn, this allows for material and process optimisation and also has the potential to inform quality assurance and *in situ* inspection methods.

Chapter 6 Summary, Conclusions, and Further Work

This work has analysed crack path transitions in particle-toughened unidirectional continuous carbon fibre reinforced epoxy composite systems undergoing Mode I loading. The work uses a variety of methods to interrogate the mechanisms contributing to the transition from interlaminar to intralaminar crack growth. DCB tests were used to characterise the toughness response of a range of particle-toughened systems differing by either their particle type, fibre type or matrix type and surface fractography was used to identify dominant macroscale toughening mechanisms as well as observe differences in the rate and magnitude of crack transition with crack extension. XCT and SRCT were used to characterise the interlayer geometry and features which could contribute to the transition of the crack path. Finally, using the FEM a DCB specimen scale model was used to investigate the impact of mesoscale interlayer architecture and relative cohesive and adhesive interface strengths to identify trends and likely mechanisms contributing to the crack path during Mode I loading and hence the probable arising R-curve shape resulting from these toughening mechanisms.

6.1 Summary

6.1.1 DCB Testing and Toughness Characterisation:

The work presented in Chapter 3 compares the toughness response of six UD CFRP DCB specimens. Two samples are untoughened and vary by their matrix type, whereas the other four are toughened via the interlayering of thermoplastic toughening particles. These toughened systems differed by either their particle type, matrix type, or fibre type. DCB tests were carried out to determine the interlaminar fracture toughness of each material system. To compare the toughness of each material system a polynomial function was fitted to the data and the subsequent error of this fit was plotted. XCT was used to obtain an overview of each specimen, furthermore, OM and SEM were used to characterise the fracture surfaces.

The results clearly show that the G_{IC} lay within the range of error of each of the tested material systems, therefore, showing that there is no discernible benefit of incorporating toughening particles in terms of fracture initiation resistance. However, the differences between materials systems become more apparent with delamination growth. It appears that the inclusion of toughening particles can result in a flat delamination resistance curve if large-scale bridging is not present, however, if large-scale bridging is induced this can lead to a rising R-curve. The material system showing the highest SERR with crack propagation and rising R-curve was interlayered with

toughening particles and had an alternative fibre type which led to intralaminar crack transitions and large-scale fibre-bridging. The cross-sections of CT images show the formation of a distinct interlayer between plies which is not present in the untoughened systems. This observation is similarly reflected in the surface fractography of the samples using OM and SEM, where in particle-toughened systems there is a clear distinction between interlaminar and intralaminar fracture. Toughening mechanisms are also inferred through SEM imaging of the fracture surfaces with mechanisms such as fibre breaks, matrix microcracking, and river lines being dominant in untoughened systems; resin scarps, resin hackles, thermoplastic particles plastic deformation and pullout being dominant in particle-toughened systems.

The chapter shows that the choice of toughening particles (if any), fibre type, and matrix type play a direct role in determining the shape of the materials system R-curve reflecting the damage response mechanisms as a result. Although this chapter suggests a link between the formation of a non-uniform distinct interlayer and interlaminar to intralaminar crack path transition it has not been verified and at this stage remains speculative. The results also suggest that the dominant toughening response mechanisms arising from the inclusion of toughening particles such as particle matrix debonding and particle plastic deformation are not necessarily sufficient to create an increasing or even self-similar R-curve, and can in fact negatively impact the toughness response compared with untoughened systems. It also appears evident that to obtain a rising R-curve with appreciable crack propagation of mm's – cm's the toughening response mechanism must be of the same order of scale. For example, the materials system that showed an appreciable increase in toughness with crack propagation over 50 mm crack growth showed large-scale fibre-bridging in the wake of the crack bridging opening displacements in the order of mm's.

All in all this chapter looks in depth at the crack path during Mode I interlaminar fracture testing and the resulting damage response mechanisms. Dominant mechanisms are identified for each material system and linked explicitly to the shape of the materials system delamination resistance curve. It has also been found that there is a link between thermoplastic particle interlayering, interlayer thickness and geometry, and a speculated knock-on to the resulting crack path and hence dominant damage response mechanisms. Finally, the results challenge the assertion that it is damage response mechanisms directly related to the inclusion of toughening particles which are commonly reported such as particle yielding, particle deformation, particle crack face bridging *etc.* that lead to rising R-curves. Rather toughening particles can contribute to mechanisms which can lead to larger-scale toughening mechanisms such as large-scale bridging, given that the appropriate fibres are embedded in an appropriate matrix allowing such a mechanism to occur, because as this work shows it is not due exclusively to the inclusion of the toughening particles, but to a combination of factors. Hence, in the design of composite systems, a clear idea of the

toughening response over a particular length scale should be developed and appropriate toughening mechanisms which could lead to this behaviour should be identified.

6.1.2 *In situ* Observation of Crack Path Transitions:

In situ crack growth imaging of four proprietary particle-toughened materials systems was carried out under Mode I loading using a wedge opening method. Three samples from material system 4 were imaged using a laboratory-based XCT system and one material system was imaged at the European Synchrotron Research Facility at a voxel resolution of 5.2 µm and 0.65 µm for each imaging method respectively. The fracture surfaces of the samples were also imaged *ex situ* using both OM and SEM. Mechanisms such as interlaminar to intralaminar crack path transition were identified on the fracture surface of three samples. These regions were then mapped back to the XCT scans of the undamaged sample before crack propagation to investigate whether postulated interlayer features such as TARPs were evident or not.

In total ten interlaminar to intralaminar crack path transitions were mapped across three samples. All were found to be associated with either a TARP or tow gap. Furthermore, SEM provides evidence that the initial transition appears to be a localised event which begins around several fibres (approximately 20 – 30 µm's) in width. The surface fractography also reveals the frequency of such transitions appears to increase with crack propagation and also a lateral spread of the intralaminar crack as the crack length increases.

SRCT shows three slices through the cross-section of the specimen at the same frame during crack propagation. In the initial case, the entire crack in the FOV remains in the particle-toughened interlayer. However, after a crack propagation of a few mm's there appears to be a parallel intralaminar crack embedded in the adjacent fibres. With a further propagation of the crack of approximately 1 mm, the intralaminar crack appears to have become dominant and the intralaminar crack transition looks to have occurred within the FOV.

In keeping with the results of this chapter and related literature five mechanisms are proposed which could contribute to the crack path transition during Mode I loading. The proposed mechanisms are currently speculative however, there is evidence from the literature and the current work to support that there is thermoplastic toughening particle debonding from the matrix which contributes to the interlaminar crack propagation. It also appears that a secondary crack is able to initiate in the ply where, with further crack growth, it becomes dominant over the interlaminar crack. The work suggests that "mesostructure" variability of the interlayer influences the macroscopic crack path as well as provides valuable insights into the mechanisms contributing to interlaminar to intralaminar crack path transitions during Mode I loading.

6.1.3 Finite Element Modelling using Advanced Failure Modelling

Abaqus was used to model the delamination of an essentially standard 3D DCB specimen using solid elements, employing the XFEM and the CZM technique to simulate damage initiation and propagation. The model was designed to look at trends in crack path transitions with varying interlayer geometries, differing relative stress states between delamination paths and stochastic variation in the local cohesive properties. Interlayer geometry was based on values measured from XCT volumes, albeit simplified such that a good quality mesh could be obtained and the geometry could be varied systematically to test a wide range of conditions; such as constant thickness interlayers, varying thickness interlayers, and the inclusion of tow gaps.

The results of this chapter show a contrast in the distribution of low-level damage within the interlaminar and intralaminar layers and fully degraded elements (crack path) within the respective layers. There appears to be an increased distribution of damage between adjacent crack paths in thinner interlayers, where high stress around the crack tip induces damage in the adjacent layers, however, this does not necessarily correlate to transitions of the main crack, where for thicker interlayers the crack remains in the interlayer for a higher relative stress difference between competing delamination paths. It is also shown that the presence of tow gaps can be of particular detriment for a thick constant thickness interlayer causing crack transition where otherwise the entire crack would remain in the interlayer.

The variation in fracture toughness as a function of interlayer geometry is small compared to the change in interlayer thickness. In isolation it appears interlayer variation could contribute to a small increase in fracture toughness of the interlayer, however, such variations also increase intralaminar crack path transition when compared to a thicker constant thickness interlayer, which could lead to an overall drop in toughness given certain assumptions around damage response mechanisms.

6.2 Conclusions

The conclusions of this work have been outlined in detail within their respective chapters however, they are briefly summarised below:

- Crack path transitions from the particle-toughened interlayer to the ply occur in all material systems tested in this thesis. The rate at which that transition occurs as well as the relative effect this transition has on the delamination response varies between materials systems and depends upon the dominant resulting damage response mechanisms.

- Crack transitions away from the interlayer can lead to a falling delamination resistance response if the large-scale fibre-bridging is not induced and the toughness of the fibre-matrix interface is less than that of the particle-toughened interlayer. However, these transitions can also have little impact on the delamination response where there is no appreciable difference in the adhesive strength of the fibre matrix interface leading to a self-similar delamination response. Conversely, the crack transition can lead to a rising R-curve if it is accompanied by large-scale bridging which becomes the dominant damage response mechanism. In this case, the toughness increases while oblique fibre bridges build up in the wake of the crack, however, once the rate of creation is equal to the rate of breakage the rising curve flattens to give a self-similar response with further loading.
- So-called 'trigger' regions where the crack is seen to make the transition out of the particle interlayer to the fibre interface are associated with tow gap features and resin pocketed regions in the interlayer through the use of SEM and XCT.
- Transitions appear, in part, to be caused by secondary cracks which may initiate at the fibre interface concurrent to a crack in the interlayer. If the fracture energy required to propagate the secondary crack is less than the main crack it may itself become the dominant crack and propagate ahead of the initial crack, in turn, shielding the interlayer crack and causing it to arrest. This observation was made during *in situ* Mode I loading during SRCT. Furthermore, evidence of adjacent cracks running concurrently on either side of the interlayer at the fibre interfaces was also found and reported
- Five potential mesoscale mechanisms for crack transition associated with tow gaps have been identified in this research: (1) debonding of the toughening particle-matrix interface. (2) Interlaminar crack growth within the interlayer propagating through readily debonded particles ahead of the crack front. (3) lateral crack propagation into the ply where a crack in the interlayer around the tow gap could coalesce with fibre matrix debonds, later becoming the dominant crack growth mechanism. (4) crack turning, where the crack continuously propagates laterally into the ply adjacent to the tow gap with no overlap with the interlayer crack. (5) the intralaminar crack has become dominant and no damage is observed within the particle-toughened interlayer.
- The research clearly suggests that "mesostructure" variability influences the macroscopic crack path. If features which are commonly seen in particle-toughened composites such as tow gaps, resin pockets, and particle agglomerations could be more carefully controlled the crack path could equally be controlled. If the goal were to maintain a crack within the particle-toughened interlayer then reducing the presence of features such as tow gaps, increasing interlayer thickness and uniformity and improving fibre interface adhesion would go some way to increasing the crack propagation length until an effective transition

was to occur. However, it has also been seen that fibre-bridging mechanisms can provide significant toughening, and, so may be advantageous in certain circumstances hence it may be of interest to increase such transitions and improve the ability of fibres to debond and form effective fibre bridges.

- Critical relative strengths between the interlayer and fibre interfaces have been verified as a significant factor in determining crack path transitions where even a small decrease in the relative strength of the fibre interface can lead to significant transition over small propagation distances.
- The thickness and geometry of the interlayer have a minor influence on the *in situ* toughness of the interlayer demonstrated by crack growth analysis using XFEM.
- The presence of tow gaps appears to strongly influence the crack transition path during Mode I loading where the effect is most pronounced when the relative fibre interface strength is equal to, or greater, than that of the interlayer

6.3 Further Work

6.3.1 Linking Length Scales

Further work needs to be done to link previous observations on the microscale to the observations in this work on the macroscale as well as the mesoscale variations in interlayer thickness, comparable to the previously termed TARPs, which could be related to the distribution of toughening particles and the crack transition in particle-toughened systems. This work gives credence to the assertion that events which originate on the microscale do have a direct influence at larger length scales and even become significant and measurable during macroscale toughness tests. The three-dimensional nature of crack transition needs to be further explored and a definite link between length scales needs to be made to provide a better understanding of the dominant mechanisms involved in determining crack transitions and whether these factors can be better accounted for in material manufacturing and design processes. This may be achieved by a combination of numerical modelling and detailed computed tomography and fractography observations.

6.3.2 Isolating the Effect of Meso-Scale Interlayer Features On Delamination Path and Toughness

Several potential areas for future work can be identified from the observations of crack path transitions in this work. Firstly, a more deterministic study could be undertaken to investigate the impact of features such as TARPs and tow gaps by creating material systems that systematically adjust these variables such as their frequency and size. This would provide further insight into the mesoscale interlayer features and their impact on crack transitions. By challenging the conclusion from this work, a more robust understanding of the complex mechanistic interactions that occur during crack propagation could be obtained. Additionally, idealised mesoscale feature modelling could be conducted to better understand their role in crack propagation. This could provide a deeper understanding of the crack transition.

Furthermore, capturing the crack transition during *in-situ* imaging is challenging due to the dynamic nature of crack growth within particle-toughened systems, including stick-slip behaviour and sudden strain energy release. To overcome this challenge, the experimental setup could be modified to better control crack growth by clamping the specimen ahead of the crack tip and imaging at several load steps before, leading up to, and including the visual propagation of the crack. This modification would enable more precise and accurate data collection, providing

greater insight into the chronology and significance of particular damage response mechanisms leading to crack path transitions.

6.3.3 Expanding Modelling Capability

In summary, the present study has successfully demonstrated the use of a three-dimensional combined XFEM and CZM for modelling complex mechanistic interactions and identifying trends related to crack path transitions. However, there are still several potential areas for future work and expansion.

Firstly, it would be valuable to scale up the high-fidelity crack modelling to capture longer delamination lengths beyond a few millimetres. This could provide deeper insights into how the crack path develops and transitions under different loading conditions.

Secondly, extending the methodology to Mode II and mixed Mode I/Mode II loading tests would enable the identification of crack transition behaviour during various delamination tests. This could provide a more comprehensive understanding of the complex mechanistic interactions that occur during these loading conditions.

Thirdly, to obtain a better representation of the interlayer geometries, future work could look into modelling more realistic interlayer shapes and variations using a higher-resolution finite element model. This would complement the current macro-scale modelling work presented in this thesis and provide more accurate and precise results.

Furthermore, the modelling strategy employed in this study could be extended to angle ply lay-up and arbitrary loading cases. This extension would allow for the assessment of the applicability of the mechanistic understanding gained regarding the damage response mechanisms during Mode I loading of UD laminates under different loading conditions.

Overall, these future work areas have the potential to expand on the findings of this study and improve the understanding of the complex mechanistic interactions that occur during the delamination of composite materials.

Appendix A Delamination Resistance Experiments

A.1 Experimental Setup

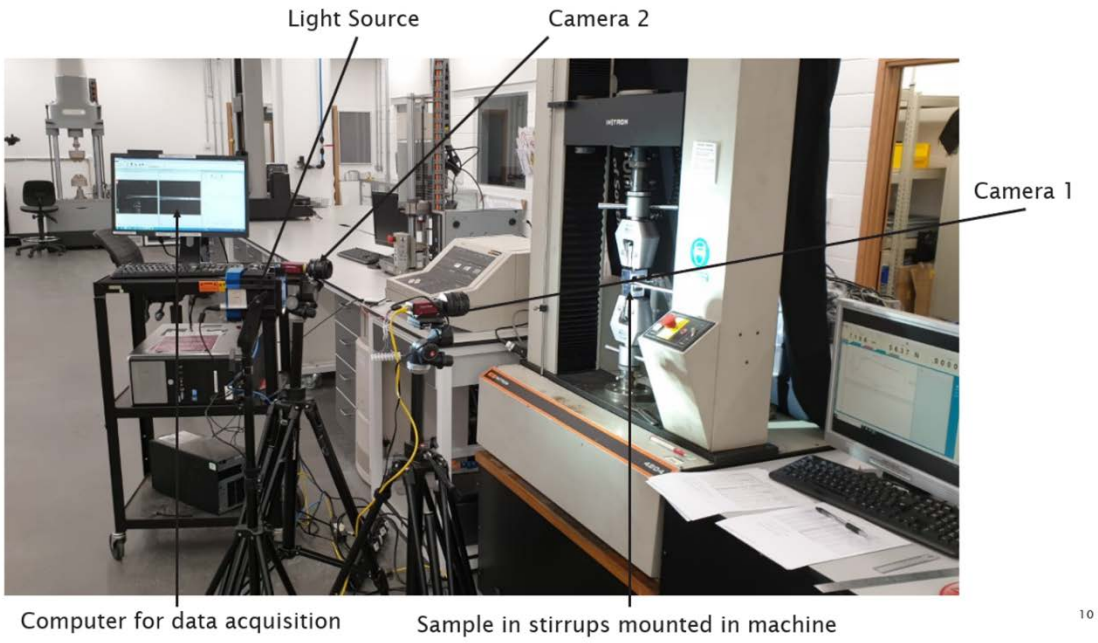

Figure A- 1 Data acquisition setup for DCB tests, showing cameras used to monitor crack growth.

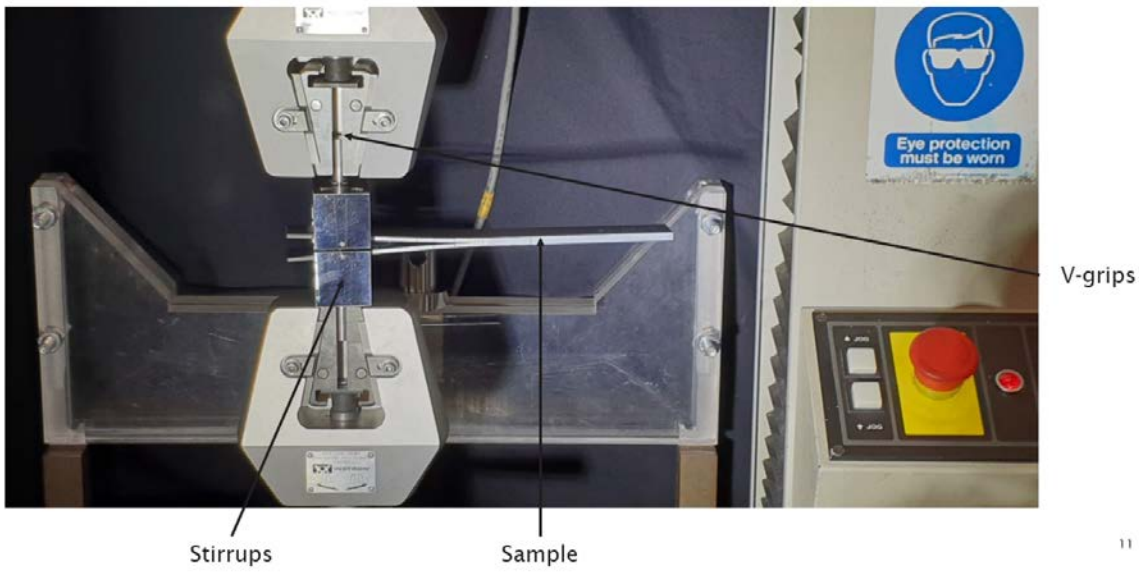

Figure A- 2 DCB sample mounted in electromechanical tensile test machine using v-grips and stirrups.

A.2 Delamination Resistance Plots

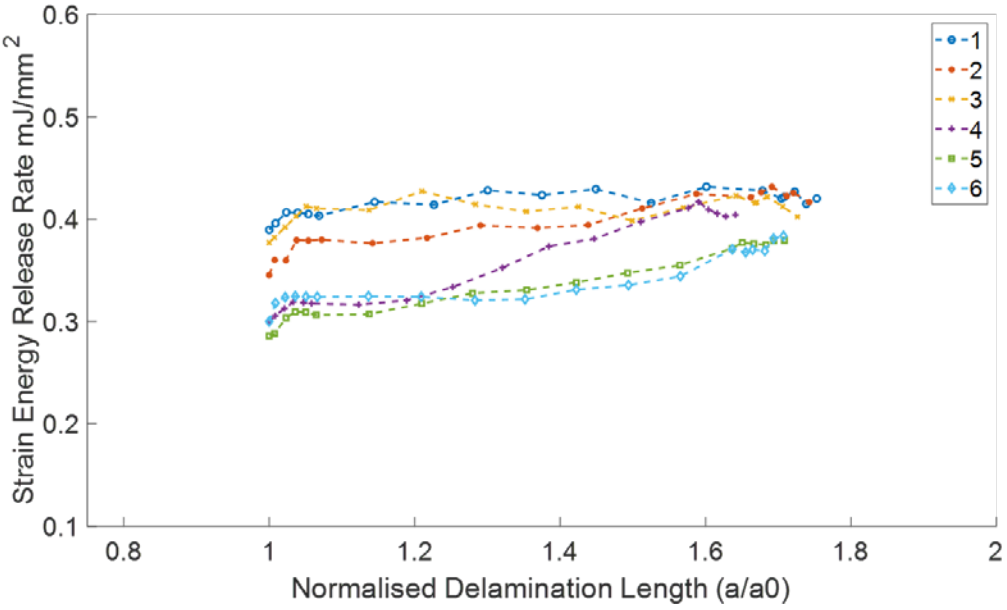

Figure A- 3 All R-curves for specimens tested in material system 1.

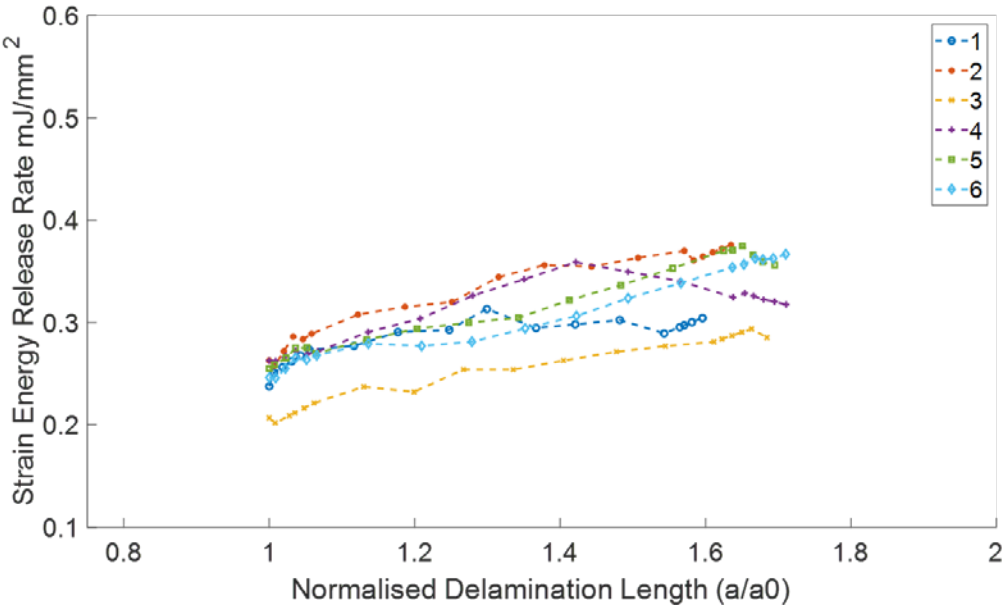

Figure A- 4 All R-curves for specimens tested in material system 2.

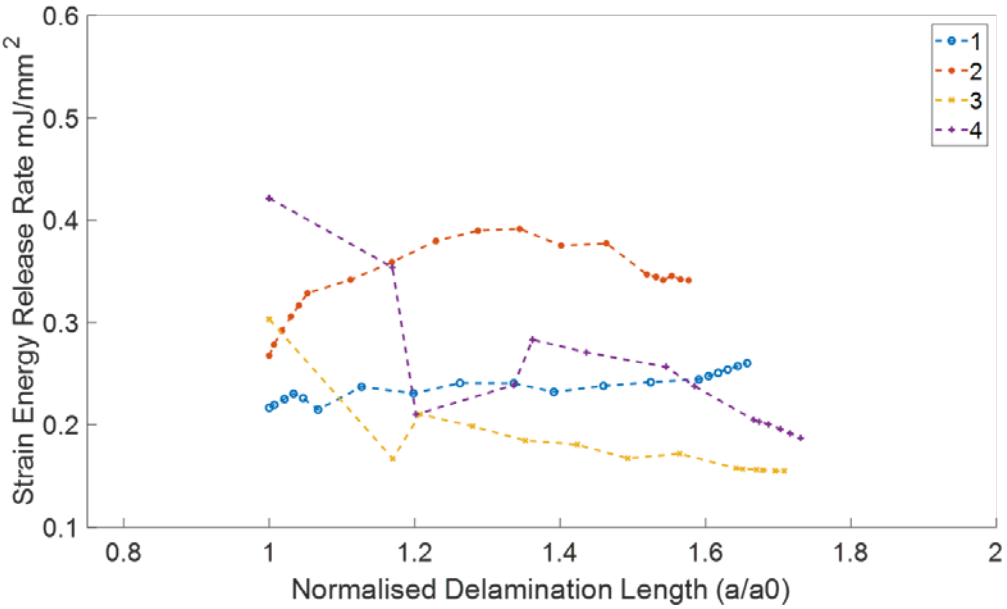

Figure A- 5 All R-curves for specimens tested in material system 3.

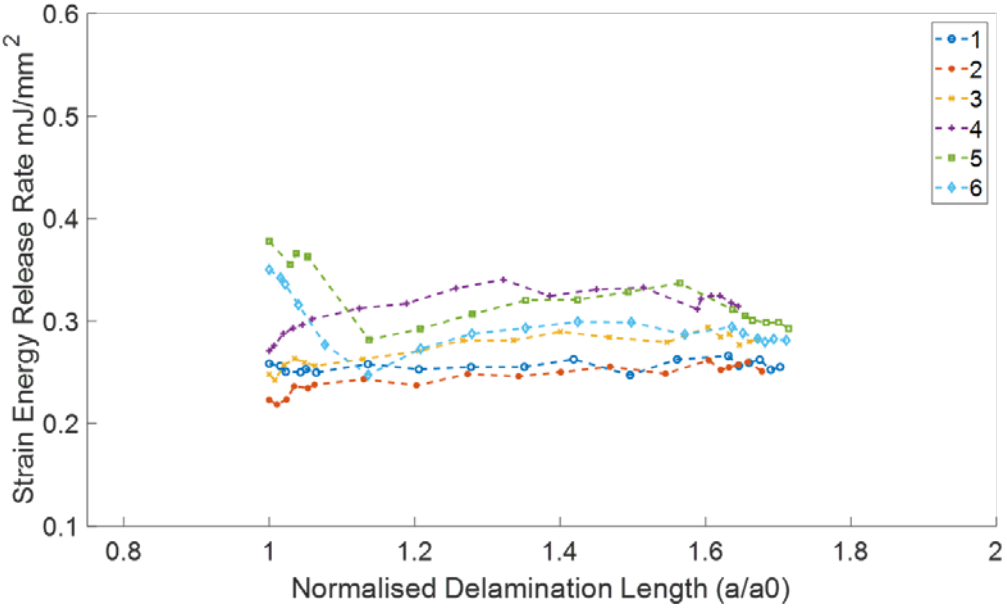

Figure A- 6 All R-curves for specimens tested in material system 4.

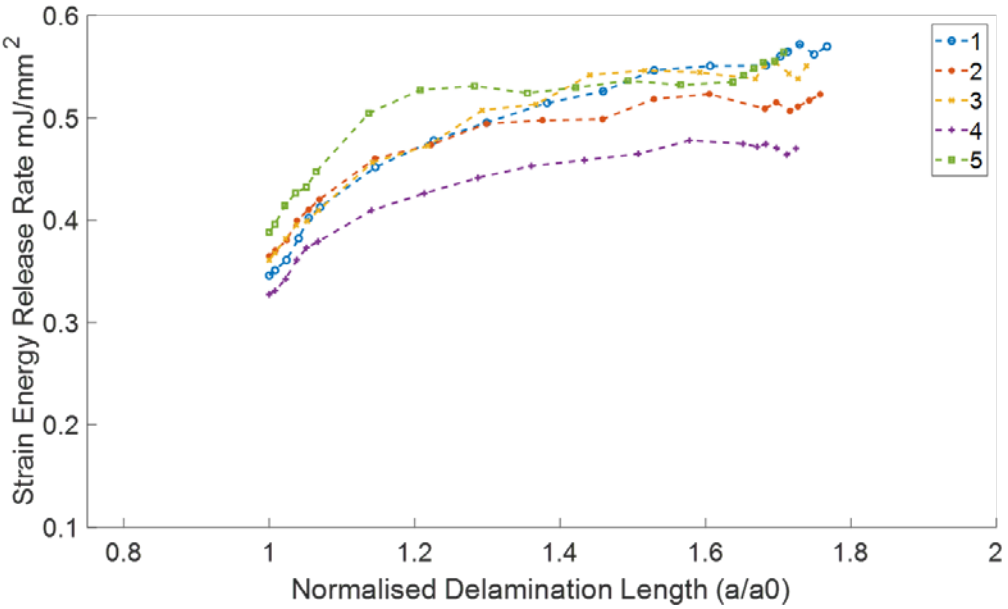

Figure A- 7 All R-curves for specimens tested in material system 5.

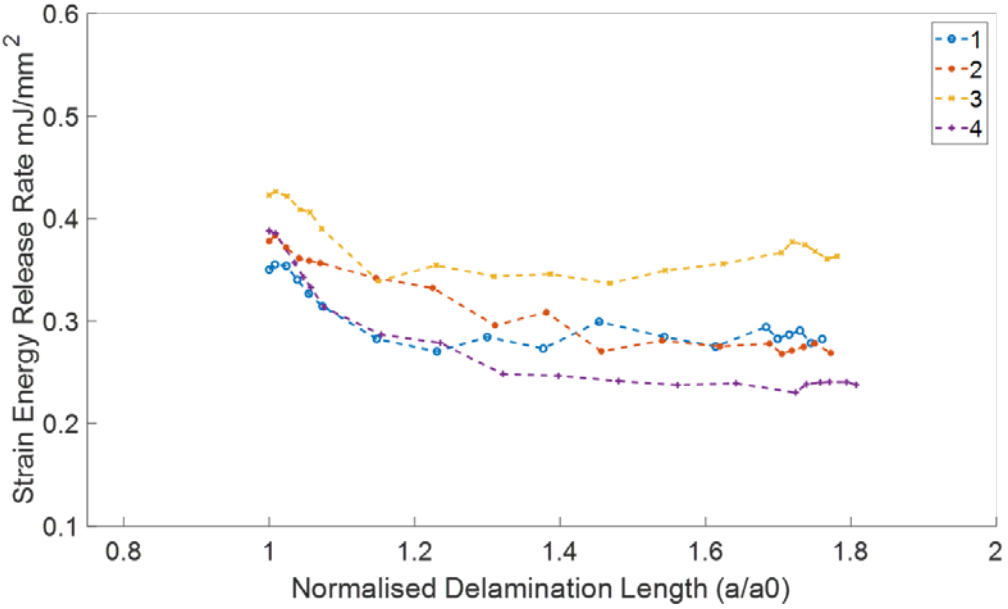

Figure A- 8 All R-curves for specimens tested in material system 6.

Appendix B *In situ* Investigation of Crack Path Transitions

B.1 Mapping Transition Regions

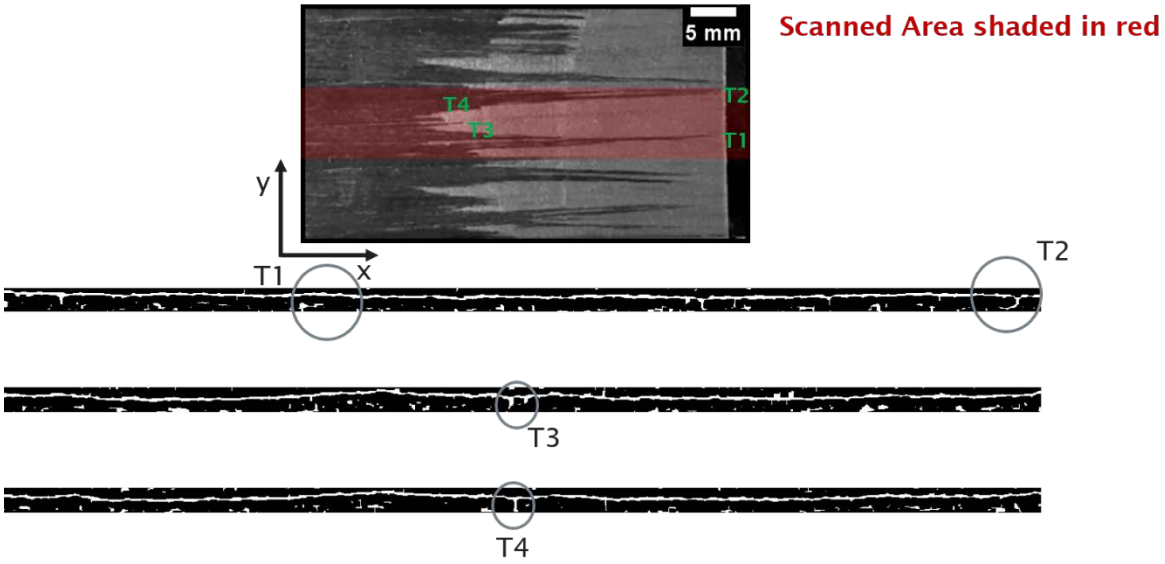

Figure B- 1 Example of mapped trigger regions to binarised interlayer image.

B.2 *In situ* Mode I loading Method

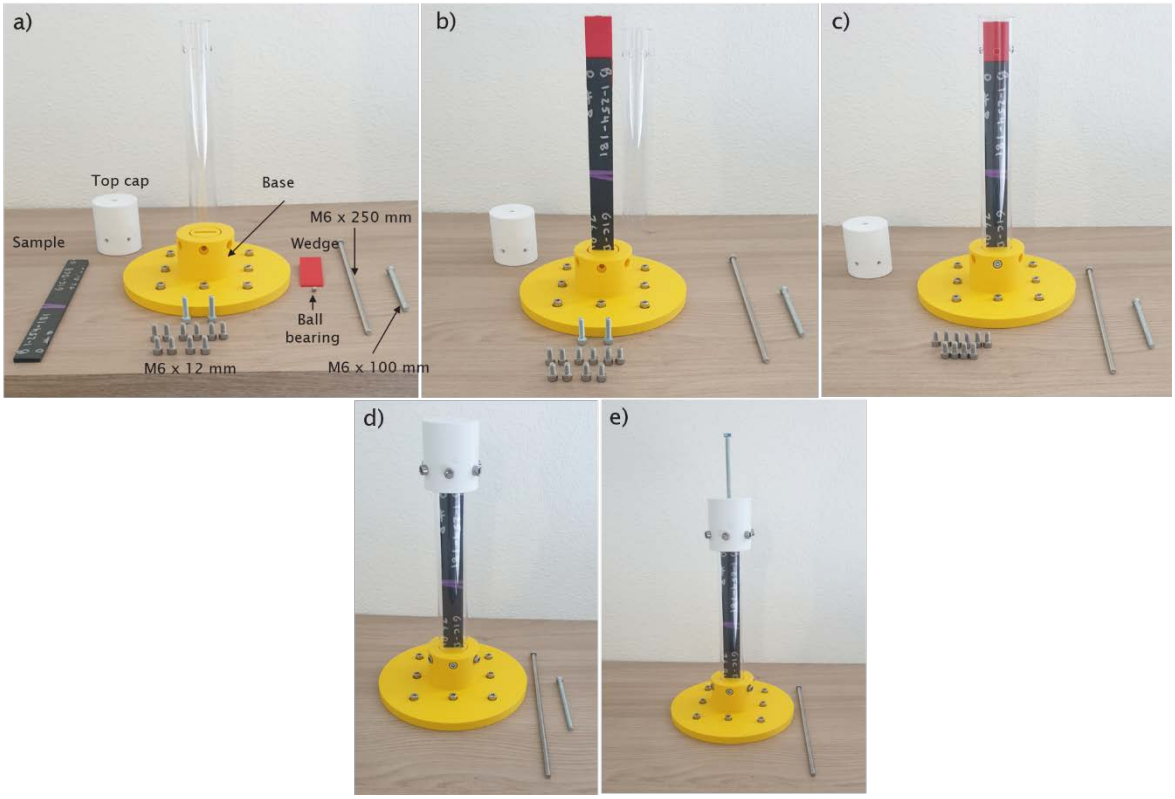

Figure B- 2 In situ rig used for ESRF experiments.

Appendix C Modelling of Crack Path Transitions

C.1 Obtaining Geometric Laminate Properties

1. Scan is aligned in-plane and out-of-plane
2. Pseudo flat-field correction (Gaussian blur subtraction 4 pixels)
3. Inverse image and carry out another pseudo flat-field correction (get rig of dark spot in the middle)
4. Average every 10 slices together (brings enhances interlayer and ply and reduces noise)
5. Enhance contrast (pixel saturation of 0.3%)
6. Median filter (4 pixels)
7. Copy and subtract value of ply (not including interlayer from image) then image subtraction of the two (gets rid of significant noise and distinguished interlayer by removing bright fringe
8. Threshold image and binarise, interlayer can now be effectively measure across whole volume including all plys in the measurement hence reducing error

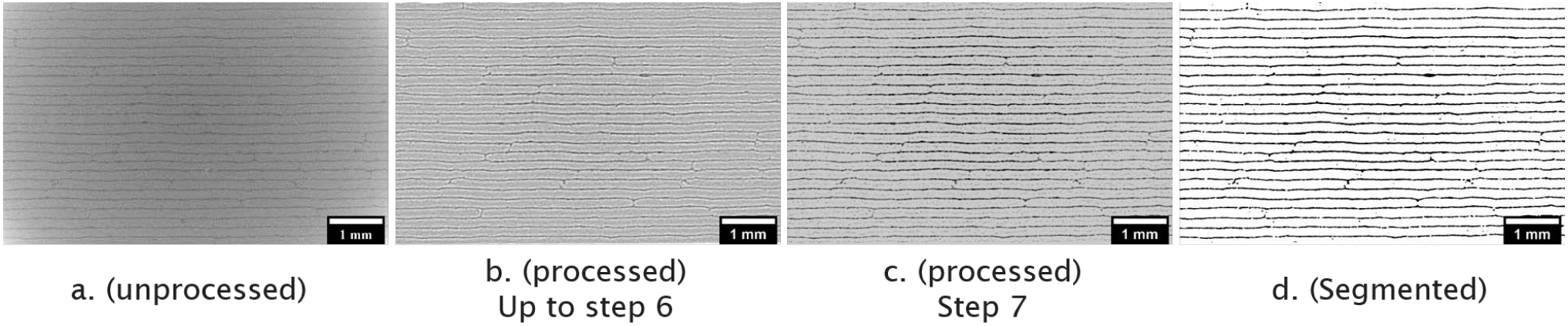

Figure C- 1 Cross-sectional XCT images of a particle-toughened carbon fibre reinforced polymer composite during sequential stages of image processing to binarise and measure the interlayer.

C.2 Mesh Independence Study

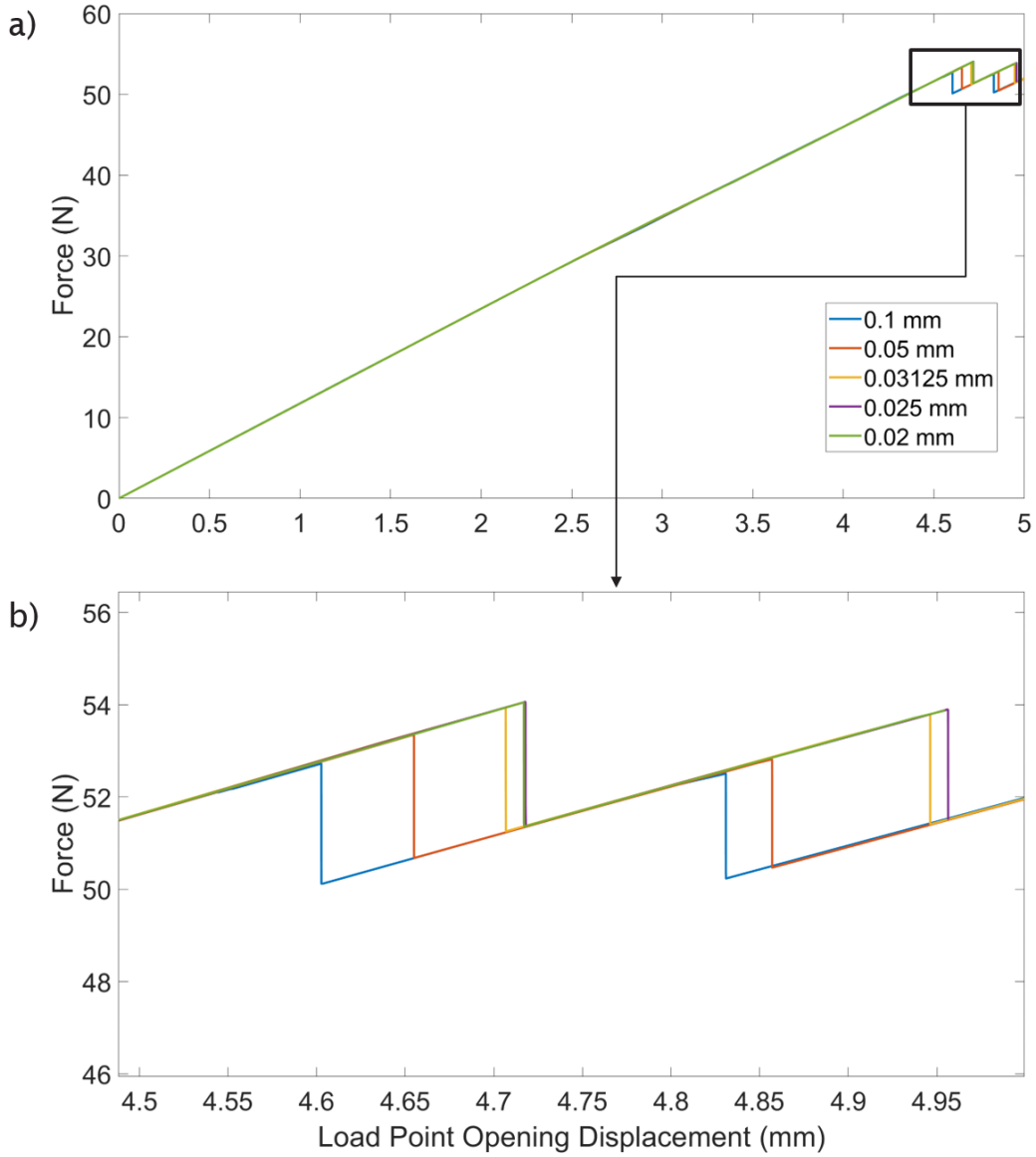

Figure C- 2 Mesh independence study of cohesive element length. a) the overall force-displacement response.b) shows the difference in force-displacement response on a zoomed in section where the crack begins to propagate.

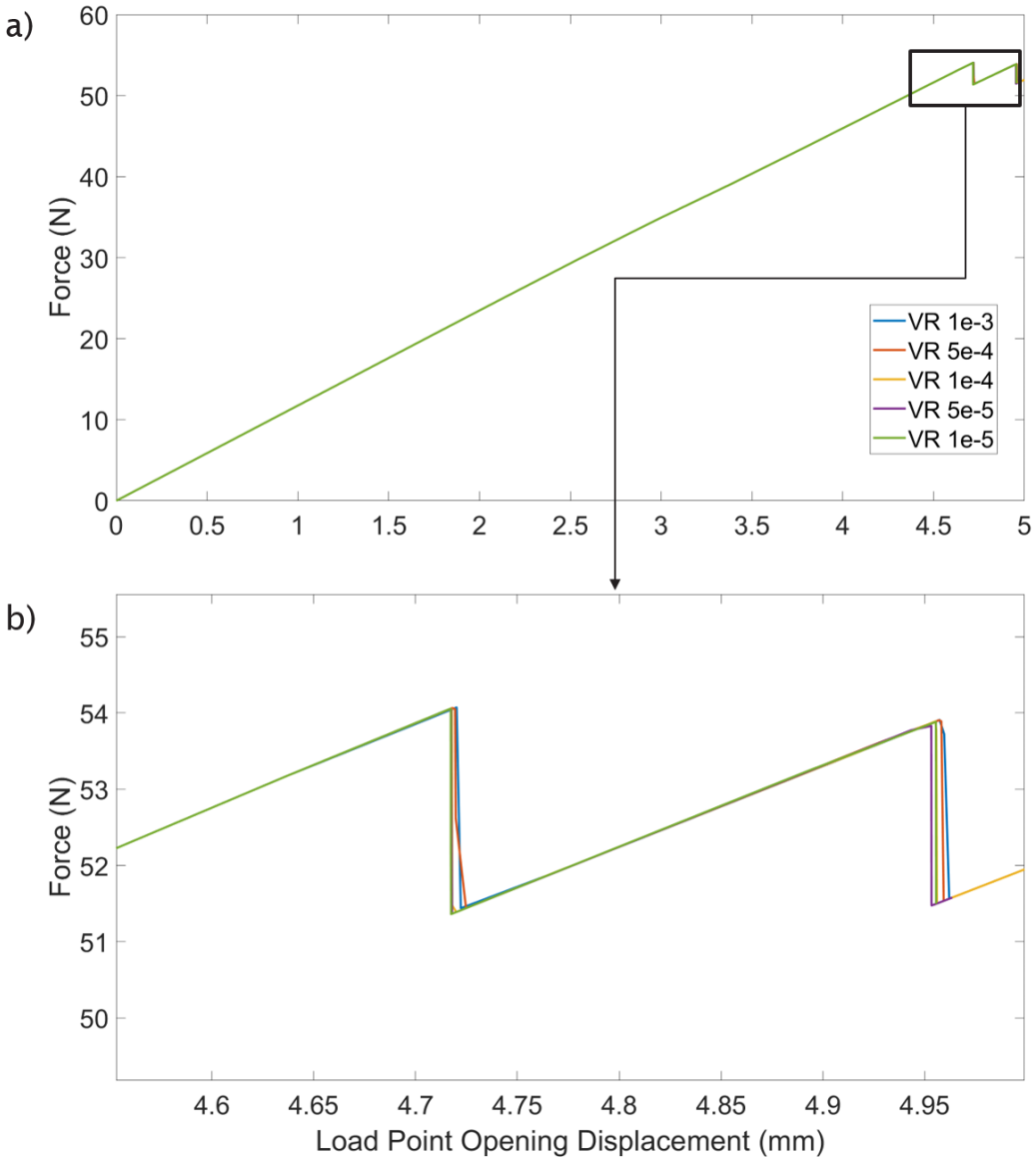

Figure C- 3 Mesh independence study using a mesh size of 0.03125 mm and a range of viscous regularisation values. a) shows the overall force-displacement response. b) shows a zoomed in section where the crack begins to propagate there is only a small difference is softening due to traction separation.

C.3 Example Scripts and Input Files to Reproduce Model

```
clc

rng('default'); % For reproducibility

R = rng;

prompt = 'Which data set is being
analysed format:\n Geometry(i.e.
15.5_51.5)x(+-)X%:\n ';
x = input(prompt,'s');
prompt2 = 'Enter percentage variation
in mean initiation stress from
interlayer, including sign (+/-):\n';
ms = input(prompt2); %percent (+ or -
variation for mean interface strength)
MIFS = 63 * ((ms/100)+1); %Mean
interface stress of upper and lower
interface
txt = '.txt';
%Create stochastic Abaqus Model
Alternate Version

%% Top cohesive and bottom

interfacecoh_el_numbers =
[250881:322560 322561:393344]; %Set
matrix associated with element
arrangement

Initiation_Stress_interface =
normrnd(MIFS,5,[1,length(interfacecoh_
```

Figure C- 4 Matlab code for generating stochastic parameters.

```
*Heading
** Job name: 18_32F_80 Model name: IM7_8552_Final_Model_18_32
** Generated by: Abaqus/CAE 2021.HF6
*Preprint, echo=NO, model=NO, history=NO, contact=NO
**
** PARTS
**
*Part, name=Bulk
*Node
      1,           5., -0.140499994,           0.
      2,           5., -0.140499994,          40.
      3,           5.,        -1.5,          40.
      4,           5.,        -1.5,           0.
      5,          -5., -0.140499994,          40.
      6,          -5.,        -1.5,          40.
      7,          -5.,        -1.5,           0.
      8,          -5., -0.140499994,           0.
      9,           5., -0.140499994,          45.
     10,           5.,        -1.5,          45.
     11,          -5., -0.140499994,          45.
     12,          -5.,        -1.5,          45.
     13,           5.,  0.140499994,          45.
     14,           5.,  0.140499994,          40.
     15,           5.,         1.5,          40.
     16,           5.,         1.5,          45.
     17,          -5.,  0.140499994,          40.
     18,          -5.,         1.5,          40.
     19,          -5.,         1.5,          45.
     20,          -5.,  0.140499994,          45.
     21,           5.,         1.5,         125.
     22,           5.,        -1.5,         125.
     23,          -5.,         1.5,         125.
```

Figure C- 5 Example Abaqus .input file for 18 - 32 micron varying interlayer thickness model, where the relative interface strength is 90% of the interlayer strength.

List of References

[1] J. Amankwah-Amoah, Stepping up and stepping out of COVID-19: New challenges for environmental sustainability policies in the global airline industry, Journal of Cleaner Production 271 (2020) 123000.

[2] S. Booth, C. Howarth, R. Ruparel, P. Swidlicki, What If...?: The Consequences, Challenges & Opportunities Facing Britain Outside EU, (2015).

[3] S. Capoccitti, A. Khare, U. Mildenberger, Aviation industry-mitigating climate change impacts through technology and policy, Journal of technology management & innovation 5(2) (2010) 66-75.

[4] J. Zhang, V.S. Chevali, H. Wang, C.-H. Wang, Current status of carbon fibre and carbon fibre composites recycling, Composites Part B: Engineering 193 (2020) 108053.

[5] G. Marsh, Airbus takes on Boeing with reinforced plastic A350 XWB, Reinforced Plastics 51(11) (2007) 26-29.

[6] S. Sankaran, K. Deshmukh, M.B. Ahamed, S.K. Khadheer Pasha, Recent advances in electromagnetic interference shielding properties of metal and carbon filler reinforced flexible polymer composites: A review, Compos., A, Appl. Sci. Manuf. (Netherlands) 114 (2018) 49-71.

[7] M. Drishti, S. Anthony, The Future of Carbon Fiber Composites, Lux Research, 2020.

[8] Airbus, Safe operations with composite aircraft, 2014.

[9] L. Zhu, N. Li, P.R.N. Childs, Light-weighting in aerospace component and system design, Propulsion and Power Research 7(2) (2018) 103-119.

[10] R.J. Tapper, M.L. Longana, A. Norton, K.D. Potter, I. Hamerton, An evaluation of life cycle assessment and its application to the closed-loop recycling of carbon fibre reinforced polymers, Composites Part B: Engineering 184 (2020) 107665.

[11] S. Pimenta, S.T. Pinho, Recycling carbon fibre reinforced polymers for structural applications: Technology review and market outlook, Waste Management 31(2) (2011) 378-392.

[12] A.T. Rhead, R. Butler, N. Baker, Analysis and Compression Testing of Laminates Optimised for Damage Tolerance, 18(1) (2011) 85-100.

[13] C.A.S. FAA, Advisory Circular (AC) 20-107B, Change 1 (2010).

[14] V. Dikshit, S.K. Bhudolia, S.C. Joshi, Multiscale Polymer Composites: A Review of the Interlaminar Fracture Toughness Improvement, Fibers 5(4) (2017) 38.

[15] D.J. Bull, A.E. Scott, S.M. Spearing, I. Sinclair, The influence of toughening-particles in CFRPs on low velocity impact damage resistance performance, Compos., A, Appl. Sci. Manuf. (Netherlands) 58 (2014) 47-55.

[16] M.J. Hinton, P.D. Soden, Predicting failure in composite laminates: the background to the exercise, Compos. Sci. Technol. (Netherlands) 58(7) (1998) 1001-1010.

[17] C.C. Chamis, F. Abdi, M. Garg, L. Minnetyan, H. Baid, D. Huang, J. Housner, F. Talagani, Micromechanics-based progressive failure analysis prediction for WWFE-III composite coupon test cases, J. Compos. Mater. (USA) 47(20-21) (2013) 2695-2712.

[18] M.J. Hinton, A.S. Kaddour, P.D. Soden, A comparison of the predictive capabilities of current failure theories for composite laminates, judged against experimental evidence, Compos. Sci. Technol. (Netherlands) 62(12) (2002) 1725-1797.

[19] M.J. Hinton, A.S. Kaddour, P.D. Soden, A further assessment of the predictive capabilities of current failure theories for composite laminates: comparison with experimental evidence, Compos. Sci. Technol. (Netherlands) 64(3) (2004) 549-588.

[20] M.J. Hinton, A.S. Kaddour, P.D. Soden, Evaluation of failure prediction in composite laminates: background to 'part C' of the exercise, Compos. Sci. Technol. (Netherlands) 64(3) (2004) 321-327.

[21] P.D. Soden, A.S. Kaddour, M.J. Hinton, Recommendations for designers and researchers resulting from the world-wide failure exercise, Compos. Sci. Technol. (Netherlands) 64(3) (2004) 589-604.

[22] A.S. Kaddour, M.J. Hinton, P.A. Smith, S. Li, The background to the third world-wide failure exercise, J. Compos. Mater. (USA) 47(20-21) (2013) 2417-2426.

[23] B.F. Sorensen, T.K. Jacobsen, Large-scale bridging in composites: R-curves and bridging laws, Compos. Pt. A-Appl. Sci. Manuf. 29(11) (1998) 1443-1451.

[24] G. Borstnar, M.N. Mavrogordato, L. Helfen, I. Sincla, S.M. Spearing, Interlaminar fracture micro-mechanisms in toughened carbon fibre reinforced plastics investigated via synchrotron radiation computed tomography and laminography, Compos. Pt. A-Appl. Sci. Manuf. 71 (2015) 176-183.

[25] S.C. Garcea, I. Sinclair, S.M. Spearing, In situ synchrotron tomographic evaluation of the effect of toughening strategies on fatigue micromechanisms in carbon fibre reinforced polymers, Compos. Sci. Technol. (Netherlands) 109 (2015) 32-39.

[26] D.J. Bull, S.M. Spearing, I. Sinclair, Observations of damage development from compression-after-impact experiments using ex situ micro-focus computed tomography, Compos. Sci. Technol. (Netherlands) 97 (2014) 106-114.

[27] A.E. Scott, M. Mavrogordato, P. Wright, I. Sinclair, S.M. Spearing, In situ fibre fracture measurement in carbon-epoxy laminates using high resolution computed tomography, Compos. Sci. Technol. (Netherlands) 71(12) (2011) 1471-1477.

[28] N.G. Ozdemir, T. Zhang, I. Aspin, F. Scarpa, H. Hadavinia, Y. Song, Toughening of carbon fibre reinforced polymer composites with rubber nanoparticles for advanced industrial applications, Express Polym. Lett. 10(5) (2016) 394-407.

[29] M. Zhang, Z. Guan, X. Wang, S. Du, Micro-Mechanical Analysis About Kink Band in Carbon Fiber/Epoxy Composites Under Longitudinal Compression, Appl. Compos. Mater. (Netherlands) 24(5) (2017) 1011-1028.

[30] S.C. Garcea, I. Sinclair, S.M. Spearing, Fibre failure assessment in carbon fibre reinforced polymers under fatigue loading by synchrotron X-ray computed tomography, Compos. Sci. Technol. (Netherlands) 133 (2016) 157-164.

[31] G. Borstnar, M.N. Mavrogordato, L. Helfen, I. Sinclair, S.M. Spearing, Interlaminar fracture micro-mechanisms in toughened carbon fibre reinforced plastics investigated via synchrotron radiation computed tomography and laminography, Compos., A, Appl. Sci. Manuf. (Netherlands) 71 (2015) 176-183.

[32] D. Kreculj, B. Rasuo, Review of impact damages modelling in laminated composite aircraft structures, Tehnicki Vjesnik 20 (2013) 485-495.

[33] L. Mishnaevsky, K. Branner, H.N. Petersen, J. Beauson, M. McGugan, B.F. Sørensen, Materials for Wind Turbine Blades: An Overview, Materials (Basel) 10(11) (2017) 1285.

[34] C. Bisagni, G. Di Pietro, L. Fraschini, D. Terletti, Progressive crushing of fiber-reinforced composite structural components of a Formula One racing car, Compos. Struct. 68(4) (2005) 491-503.

[35] M.S. Sohn, X.Z. Hu, J.K. Kim, L. Walker, Impact damage characterisation of carbon fibre/epoxy composites with multi-layer reinforcement, Composites Part B: Engineering 31(8) (2000) 681-691.

[36] A.C. Garg, Y.-W. Mai, Failure mechanisms in toughened epoxy resins—A review, Compos. Sci. Technol. (Netherlands) 31(3) (1988) 179-223.

[37] D. Hull, Y.B. Shi, Damage mechanism characterization in composite damage tolerance investigations, Compos. Struct. 23(2) (1993) 99-120.

[38] D.D.R. Cartié, P.E. Irving, Effect of resin and fibre properties on impact and compression after impact performance of CFRP, Composites Part A: Applied Science and Manufacturing 33(4) (2002) 483-493.

[39] M. de Freitas, L. Reis, Failure mechanisms on composite specimens subjected to compression after impact, Compos. Struct. 42(4) (1998) 365-373.

[40] G. Sala, Post-impact behaviour of aerospace composites for high-temperature applications: experiments and simulations, Composites Part B: Engineering 28(5) (1997) 651-665.

[41] D.J. Bull, S.M. Spearing, I. Sinclair, L. Helfen, Three-dimensional assessment of low velocity impact damage in particle toughened composite laminates using micro-focus X-ray computed tomography and synchrotron radiation laminography, Compos. Pt. A-Appl. Sci. Manuf. 52 (2013) 62-69.

[42] F.-K. Chang, H.Y. Choi, S.-T. Jeng, Study on impact damage in laminated composites, Mech. Mater. 10(1) (1990) 83-95.

[43] C. Bouvet, S. Rivallant, J.J. Barrau, Low velocity impact modeling in composite laminates capturing permanent indentation, Composites Science and Technology 72(16) (2012) 1977-1988.

[44] S. Agrawal, K.K. Singh, P.K. Sarkar, Impact damage on fibre-reinforced polymer matrix composite – A review, J. Compos. Mater. (USA) 48(3) (2013) 317-332.

[45] K. Naito, Y. Tanaka, J. Yang, Y. Kagawa, Tensile and flexural properties of single carbon fibres, Proceedings of the 17th International Conference on Composite Materials, ICCM-17, Edinburgh, UK, 2009, pp. 27-31.

[46] T.A. Sebaey, M. Bouhrara, N. O'Dowd, Fibre Alignment and Void Assessment in Thermoplastic Carbon Fibre Reinforced Polymers Manufactured by Automated Tape Placement, Polymers 13(3) (2021) 473.

[47] D. Carolan, A. Ivankovic, A.J. Kinloch, S. Sprenger, A.C. Taylor, Toughened carbon fibre-reinforced polymer composites with nanoparticle-modified epoxy matrices, J. Mater. Sci. 52(3) (2017) 1767-1788.

[48] S. Wicaksono, G.B. Chai, Life prediction of woven CFRP structure subject to static and fatigue loading, Compos. Struct. 119 (2015) 185-194.

[49] G. Borstnar, M.N. Mavrogordato, Q.D. Yang, I. Sinclair, S.M. Spearing, Crack path simulation in a particle-toughened interlayer within a polymer composite laminate, Compos. Sci. Technol. (Netherlands) 133 (2016) 89-96.

[50] D. Carolan, A. Ivankovic, A. Kinloch, S. Sprenger, A. Taylor, Toughened carbon fibre-reinforced polymer composites with nanoparticle-modified epoxy matrices, J. Mater. Sci. 52(3) (2017) 1767-1788.

[51] M. Ye, B. Yuan, Y. Hu, X. Hu, Compression-after-impact properties of carbon fiber composites with interlays of Aramid pulp micro-/nanofibers, Polym. Compos. n/a(n/a).

[52] X. Zhang, L. Hounslow, M. Grassi, Improvement of low-velocity impact and compression-after-impact performance by z-fibre pinning, Compos. Sci. Technol. (Netherlands) 66(15) (2006) 2785-2794.

[53] M. Siegfried, C. Tola, M. Claes, S.V. Lomov, I. Verpoest, L. Gorbatikh, Impact and residual after impact properties of carbon fiber/epoxy composites modified with carbon nanotubes, Compos. Struct. 111 (2014) 488-496.

[54] C. Soutis, Fibre reinforced composites in aircraft construction, Progress in Aerospace Sciences 41(2) (2005) 143-151.

[55] S. Abrate, Impact on composite structures, Cambridge university press2005.

[56] M.O.W. Richardson, M.J. Wisheart, Review of low-velocity impact properties of composite materials, Compos., A, Appl. Sci. Manuf. (Netherlands) 27(12) (1996) 1123-1131.

[57] C. Soutis, P.T. Curtis, Prediction of the post-impact compressive strength of cfrp laminated composites, Compos. Sci. Technol. (Netherlands) 56(6) (1996) 677-684.

[58] D.J. Bull, S.M. Spearing, I. Sinclair, Investigation of the response to low velocity impact and quasi-static indentation loading of particle-toughened carbon-fibre composite materials, Compos., A, Appl. Sci. Manuf. (Netherlands) 74 (2015) 38-46.

[59] L. Walker, M.-S. Sohn, X.-Z. Hu, Improving impact resistance of carbon-fibre composites through interlaminar reinforcement, Compos., A, Appl. Sci. Manuf. (Netherlands) 33(6) (2002) 893-902.

[60] D.J. Bull, S.M. Spearing, I. Sinclair, Image-enhanced modelling of residual compressive after impact strength in laminated composites, Compos. Struct. 192 (2018) 20-27.

[61] T.-W. Shyr, Y.-H. Pan, Impact resistance and damage characteristics of composite laminates, Compos. Struct. 62(2) (2003) 193-203.

[62] S.M. Spearing, I. Sinclair, Iop, The micro-mechanics of strength, durability and damage tolerance in composites: new insights from high resolution computed tomography, 37th Riso International Symposium on Materials Science, Iop Publishing Ltd, Bristol, 2016.

[63] D.J. Bull, L. Helfen, I. Sinclair, S.M. Spearing, T. Baumbach, A comparison of multi-scale 3D X-ray tomographic inspection techniques for assessing carbon fibre composite impact damage, Compos. Sci. Technol. (Netherlands) 75 (2013) 55-61.

[64] S.M. Lee, AN EDGE CRACK TORSION METHOD FOR MODE-III DELAMINATION FRACTURE TESTING, Journal of Composites Technology & Research 15(3) (1993) 193-201.

[65] A. Lopez-Menendez, J. Vina, A. Arguelles, S. Rubiera, V. Mollon, A new method for testing composite materials under mode III fracture, J. Compos. Mater. (USA) 50(28) (2016) 3973-3980.

[66] A. Lopez-Menendez, J. Vina, A. Arguelles, I. Vina, S. Rubiera, Analysis of mode III interlaminar fracture toughness of laminated composites using a novel testing device, Eng. Fract. Mech. 173 (2017) 55-63.

[67] Y. Ge, X. Gong, A. Hurez, E. De Luycker, Test methods for measuring pure mode III delamination toughness of composite, Polymer Testing 55 (2016) 261-268.

[68] V. Dikshit, S.K. Bhudolia, S.C. Joshi, Multiscale polymer composites: A review of the interlaminar fracture toughness improvement, Fibers 5(4) (2017).

[69] S.M. Spearing, A.G. Evans, The role of fiber bridging in the delamination resistance of fiber-reinforced composites, Acta Metallurgica et Materialia 40(9) (1992) 2191-2199.

[70] ASTM D5528, 5528-01: Standard Test Method for Mode I Interlaminar Fracture Toughness of Unidirectional Fiber-Reinforced Polymer Matrix Composites, Annual book of ASTM standards, 2001.

[71] BS ISO 15024:2001, Fibre-reinforced plastic composites. Determination of mode I interlaminar fracture toughness, GIC, for unidirectional reinforced materials., Fibre-reinforced plastic composites. Determination of mode I interlaminar fracture toughness, GIC, for unidirectional reinforced materials. (2002).

[72] M. Arai, Y. Noro, K.I. Sugimoto, M. Endo, Mode I and mode II interlaminar fracture toughness of CFRP laminates toughened by carbon nanofiber interlayer, Compos. Sci. Technol. (Netherlands) 68(2) (2008) 516-525.

[73] A. Kumar, S. Roy, Characterization of Fracture Properties of Nanographene Reinforced EPON 862 Polymer and their Carbon Fiber Composites, Destech Publications, Inc, Lancaster, 2015.

[74] A.B. Pereira, A.B. de Morais, Mode I interlaminar fracture of carbon/epoxy multidirectional laminates, Compos. Sci. Technol. (Netherlands) 64(13-14) (2004) 2261-2270.

[75] V.K. Srivastava, T. Gries, D. Veit, T. Quadflieg, B. Mohr, M. Kolloch, Effect of nanomaterial on mode I and mode II interlaminar fracture toughness of woven carbon fabric reinforced polymer composites, Eng. Fract. Mech. 180 (2017) 73-86.

[76] P.R. Thakre, D.C. Lagoudas, J.C. Riddick, T.S. Gates, S.J.V. Frankland, J.G. Ratcliffe, J. Zhu, E.V. Barrera, Investigation of the effect of single wall carbon nanotubes on interlaminar fracture toughness of woven carbon fiber-epoxy composites, J. Compos. Mater. (USA) 45(10) (2011) 1091-1107.

[77] Y. Gong, L.B. Zhao, J.Y. Zhang, Y.N. Wang, N. Hu, Delamination propagation criterion including the effect of fiber bridging for mixed-mode I/II delamination in CFRP multidirectional laminates, Compos. Sci. Technol. (Netherlands) 151 (2017) 302-309.

[78] F. Naya, G. Pappas, J. Botsis, Micromechanical study on the origin of fiber bridging under interlaminar and intralaminar mode I failure, Compos. Struct. 210 (2019) 877-891.

[79] S. Roy, A. Kumar, Effect of particle size on mixed-mode fracture of nanographene reinforced epoxy and mode I delamination of its carbon fiber composite, Compos. Struct. 181 (2017) 1-8.

[80] G. Borstnar, F. Gillard, M.N. Mavrogordato, I. Sinclair, S.M. Spearing, Three-dimensional deformation mapping of Mode I interlaminar crack extension in particle-toughened interlayers, Acta Mater. (Netherlands) 103 (2016) 63-70.

[81] F. Xu, H.Y. Liu, X.S. Du, An Analytical Model of Interlaminar Fracture of Polymer Composite Reinforced by Carbon Fibres Grafted with Carbon Nanotubes, Polymers 10(6) (2018) 15.

[82] K.C. Shekar, B.A. Prasad, N.E. Prasad, Strengthening in and fracture behaviour of CNT and carbon-fibre-reinforced epoxy-matrix hybrid composite, Sadhana-Acad. Proc. Eng. Sci. 41(12) (2016) 1443-1461.

[83] A.T. Seyhan, M. Tanoglu, K. Schulte, Mode I and mode II fracture toughness of E-glass non-crimp fabric/carbon nanotube (CNT) modified polymer based composites, Eng. Fract. Mech. 75(18) (2008) 5151-5162.

[84] G. Borstnar, Micro-mechanical contributions to interlaminar toughness in particle-toughened CFRPs, Faculty of Engineering and the Environment, University of Southampton, 2016.

[85] T. Hayashi, M. Endo, Carbon nanotubes as structural material and their application in composites, Composites Part B: Engineering 42(8) (2011) 2151-2157.

[86] M. Zamanian, M. Mortezaei, B. Salehnia, J.E. Jam, Fracture toughness of epoxy polymer modified with nanosilica particles: Particle size effect, Eng. Fract. Mech. 97 (2013) 193-206.

[87] H. Dodiuk, S.H. Goodman, Handbook of thermoset plastics, William Andrew2013.

[88] K.P. Unnikrishnan, E.T. Thachil, Toughening of epoxy resins, Designed Monomers and Polymers 9(2) (2006) 129-152.

[89] Q.D. Yang, D. Schesser, M. Niess, P. Wright, M.N. Mavrogordato, I. Sinclair, S.M. Spearing, B.N. Cox, On crack initiation in notched, cross-plied polymer matrix composites, 78 (2015) 314-332.

[90] T.L. Anderson, Fracture mechanics: fundamentals and applications, CRC press2005.

[91] R.J. Morgan, J.E. O'Neal, The microscopic failure processes and their relation to the structure of amine-cured bisphenol-A-diglycidyl ether epoxies, J. Mater. Sci. 12(10) (1977) 1966-1980.

[92] J. Mijović, J. Koutsky, Correlation between nodular morphology and fracture properties of cured epoxy resins, Polymer 20(9) (1979) 1095-1107.

[93] S. Yamini, R.J. Young, The mechanical properties of epoxy resins, J. Mater. Sci. 15(7) (1980) 1823-1831.

[94] C.S. Henkee, E.J. Kramer, Crazing and shear deformation in crosslinked polystyrene, Journal of Polymer Science Part B: Polymer Physics 34(17) (2003) 2825-2841.

[95] J. Lee, Role of inherent matrix toughness on fracture of glass bead filled epoxies, 41(23) (2000) 8375-8385.

[96] F. Awaja, S. Zhang, M. Tripathi, A. Nikiforov, N. Pugno, Cracks, microcracks and fracture in polymer structures: Formation, detection, autonomic repair, Progress in Materials Science 83 (2016) 536-573.

[97] I. Ashcroft, D. Hughes, S. Shaw, Mode I fracture of epoxy bonded composite joints: 1. Quasi-static loading, International Journal of Adhesion and Adhesives 21(2) (2001) 87-99.

[98] C.B.G. Brito, R.d.C.M.S. Contini, R.F. Gouvêa, A.S.d. Oliveira, M.A. Arbelo, M.V. Donadon, Mode I interlaminar fracture toughness analysis of Co-bonded and secondary bonded carbon fiber reinforced composites joints, Materials Research 20 (2017) 873-882.

[99] E.S. Greenhalgh, 4 - Delamination-dominated failures in polymer composites, in: E.S. Greenhalgh (Ed.), Failure Analysis and Fractography of Polymer Composites, Woodhead Publishing2009, pp. 164-237.

[100] T.H. Hsieh, A.J. Kinloch, K. Masania, A.C. Taylor, S. Sprenger, The mechanisms and mechanics of the toughening of epoxy polymers modified with silica nanoparticles, Polymer 51(26) (2010) 6284-6294.

[101] R. Bagheri, B. Marouf, R. Pearson, Rubber-Toughened Epoxies: A Critical Review, Journal of Macromolecular Science® Part C: Polymer Reviews (2009) 201-225.

[102] J.H. Hodgkin, G.P. Simon, R.J. Varley, Thermoplastic toughening of epoxy resins: a critical review, Polymers for Advanced Technologies 9(1) (1998) 3-10.

[103] S.-Y. Fu, X.-Q. Feng, B. Lauke, Y.-W. Mai, Effects of particle size, particle/matrix interface adhesion and particle loading on mechanical properties of particulate–polymer composites, Composites Part B: Engineering 39(6) (2008) 933-961.

[104] H. Chai, Deformation and fracture of particulate epoxy in adhesive bonds, Acta Metallurgica et Materialia 43(1) (1995) 163-172.

[105] R.A. Pearson, A.F. Yee, Influence of particle size and particle size distribution on toughening mechanisms in rubber-modified epoxies, J. Mater. Sci. 26(14) (1991) 3828-3844.

[106] R.A. Pearson, A.F. Yee, Toughening mechanisms in elastomer-modified epoxies, J. Mater. Sci. 21(7) (1986) 2475-2488.

[107] R. Bagheri, R.A. Pearson, Role of particle cavitation in rubber-toughened epoxies: II. Inter-particle distance, Polymer 41(1) (2000) 269-276.

[108] A.G. Evans, Z.B. Ahmad, D.G. Gilbert, P.W.R. Beaumont, Mechanisms of toughening in rubber toughened polymers, Acta Metallurgica 34(1) (1986) 79-87.

[109] Y. Huang, A.J. Kinloch, The sequence of initiation of the toughening micromechanisms in rubber-modified epoxy polymers, Polymer 33(24) (1992) 5338-5340.

[110] Y. Huang, A.J. Kinloch, Modelling of the toughening mechanisms in rubber-modified epoxy polymers, J. Mater. Sci. 27(10) (1992) 2763-2769.

[111] B.B. Johnsen, A.J. Kinloch, R.D. Mohammed, A.C. Taylor, S. Sprenger, Toughening mechanisms of nanoparticle-modified epoxy polymers, Polymer 48(2) (2007) 530-541.

[112] J. Hedrick, I. Yilg□R, G. Wilkes, J. McGrath, Chemical modification of matrix Resin networks with engineering thermoplastics, Polymer Bulletin 13(3) (1985).

[113] P. Judt, J.-C. Zarges, A. Ricoeur, H.-P. Heim, Crack path predictions in fiber reinforced composites, Procedia Structural Integrity 5 (2017) 769-776.

[114] J. Llorca, C. González, J.M. Molina-Aldareguía, J. Segurado, R. Seltzer, F. Sket, M. Rodríguez, S. Sádaba, R. Muñoz, L.P. Canal, Multiscale Modeling of Composite Materials: a Roadmap Towards Virtual Testing, Advanced Materials 23(44) (2011) 5130-5147.

[115] W.L. Tsang, A.C. Taylor, Fracture and toughening mechanisms of silica-and core–shell rubber-toughened epoxy at ambient and low temperature, J. Mater. Sci. 54(22) (2019) 13938-13958.

[116] S. Sprenger, M.H. Kothmann, V. Altstaedt, Carbon fiber-reinforced composites using an epoxy resin matrix modified with reactive liquid rubber and silica nanoparticles, Compos. Sci. Technol. (Netherlands) 105 (2014) 86-95.

[117] Y. Zeng, H.-Y. Liu, Y.-W. Mai, X.-S. Du, Improving interlaminar fracture toughness of carbon fibre/epoxy laminates by incorporation of nano-particles, Composites Part B: Engineering 43(1) (2012) 90-94.

[118] J. Yao, K. Niu, Y. Niu, T. Zhang, Toughening efficiency and mechanism of carbon fibre epoxy matrix composites by PEK-C, Compos. Struct. 229 (2019) 111431.

[119] A. Kinloch, R. Mohammed, A. Taylor, S. Sprenger, D. Egan, The interlaminar toughness of carbon-fibre reinforced plastic composites using 'hybrid-toughened'matrices, J. Mater. Sci. 41(15) (2006) 5043-5046.

[120] Y. Huang, W. Liu, Q. Jiang, Y. Wei, Y. Qiu, Interlaminar Fracture Toughness of Carbon-Fiber-Reinforced Epoxy Composites Toughened by Poly(phenylene oxide) Particles, ACS Applied Polymer Materials 2(8) (2020) 3114-3121.

[121] M. Yasaee, I.P. Bond, R.S. Trask, E.S. Greenhalgh, Mode I interfacial toughening through discontinuous interleaves for damage suppression and control, 43(1) (2012) 198-207.

[122] B.S. Hayes, J.C. Seferis, Influence of Particle Size Distribution of Preformed Rubber on the Structure and Properties of Composite Systems, 36(3) (2002) 299-312.

[123] S.K. Chan, I.S. Tuba, W.K. Wilson, On the finite element method in linear fracture mechanics, Eng. Fract. Mech. 2(1) (1970) 1-17.

[124] E.T. Wessel, W.G. Clark Jr, W.K. Wilson, Engineering methods for the design and selection of materials against fracture, WESTINGHOUSE RESEARCH LABS PITTSBURGH PA, 1966.

[125] M. Stern, E. Becker, R. Dunham, A contour integral computation of mixed-mode stress intensity factors, International Journal of Fracture 12(3) (1976) 359-368.

[126] E.F. Rybicki, M.F. Kanninen, A finite element calculation of stress intensity factors by a modified crack closure integral, Eng. Fract. Mech. 9(4) (1977) 931-938.

[127] R. Krueger, Virtual crack closure technique: history, approach, and applications, Appl. Mech. Rev. 57(2) (2004) 109-143.

[128] I. Raju, J. Crews Jr, M. Aminpour, Convergence of strain energy release rate components for edge-delaminated composite laminates, Eng. Fract. Mech. 30(3) (1988) 383-396.

[129] G. Formica, F. Milicchio, Crack growth propagation using standard FEM, Eng. Fract. Mech. 165 (2016) 1-18.

[130] D.S. Dugdale, Yielding of steel sheets containing slits, J. Mech. Phys. Solids (Netherlands) 8(2) (1960) 100-104.

[131] G.I. Barenblatt, The mathematical theory of equilibrium cracks in brittle fracture, Advances in applied mechanics 7(1) (1962) 55-129.

[132] S.R. Hallett, P.W. Harper, 2 - Modelling delamination with cohesive interface elements, in: P.P. Camanho, S.R. Hallett (Eds.), Numerical Modelling of Failure in Advanced Composite Materials, Woodhead Publishing2015, pp. 55-72.

[133] M.M. Abdel Wahab, 11 - Simulating mode I fatigue crack propagation in adhesively-bonded composite joints, in: A.P. Vassilopoulos (Ed.), Fatigue and Fracture of Adhesively-Bonded Composite Joints, Woodhead Publishing2015, pp. 323-344.

[134] A. Needleman, A continuum model for void nucleation by inclusion debonding, (1987).

[135] V. Tvergaard, J.W. Hutchinson, The relation between crack growth resistance and fracture process parameters in elastic-plastic solids, J. Mech. Phys. Solids (Netherlands) 40(6) (1992) 1377-1397.

[136] G.T. Camacho, M. Ortiz, Computational modelling of impact damage in brittle materials, Int. J. Solids Struct. 33(20-22) (1996) 2899-2938.

[137] P.H. Geubelle, J.S. Baylor, Impact-induced delamination of composites: a 2D simulation, Composites Part B: Engineering 29(5) (1998) 589-602.

[138] M. Heidari-Rarani, M. Sayedain, Finite element modeling strategies for 2D and 3D delamination propagation in composite DCB specimens using VCCT, CZM and XFEM approaches, Theoretical and Applied Fracture Mechanics 103 (2019) 102246.

[139] Y. Mi, M. Crisfield, G. Davies, H. Hellweg, Progressive delamination using interface elements, J. Compos. Mater. (USA) 32(14) (1998) 1246-1272.

[140] C.T. Sun, Z.H. Jin, Crack Tip Plasticity, Elsevier2012, pp. 123-169.

[141] A. Hillerborg, M. Modéer, P.-E. Petersson, Analysis of crack formation and crack growth in concrete by means of fracture mechanics and finite elements, Cement and concrete research 6(6) (1976) 773-781.

[142] Q. Yang, B. Cox, Cohesive models for damage evolution in laminated composites, International Journal of Fracture 133(2) (2005) 107-137.

[143] T. Belytschko, T. Black, Elastic crack growth in finite elements with minimal remeshing, International journal for numerical methods in engineering 45(5) (1999) 601-620.

[144] J.M. Melenk, I. Babuška, The partition of unity finite element method: Basic theory and applications, Computer Methods in Applied Mechanics and Engineering 139(1) (1996) 289-314.

[145] C.A. Duarte, J. Oden, A New Meshless Method To Solve Boundary-Value Problems, (1995).

[146] M. Holl, S. Loehnert, P. Wriggers, An adaptive multiscale method for crack propagation and crack coalescence, International Journal for Numerical Methods in Engineering 93(1) (2013) 23-51.

[147] M.R. Wisnom, F.-K. Chang, Modelling of splitting and delamination in notched cross-ply laminates, Compos. Sci. Technol. (Netherlands) 60(15) (2000) 2849-2856.

[148] D. Xie, A.M. Waas, Discrete cohesive zone model for mixed-mode fracture using finite element analysis, Eng. Fract. Mech. 73(13) (2006) 1783-1796.

[149] Z. Hashin, Failure criteria for unidirectional fiber composites, (1980).

[150] J.C. Brewer, P.A. Lagace, Quadratic stress criterion for initiation of delamination, J. Compos. Mater. (USA) 22(12) (1988) 1141-1155.

[151] M. Koc, F.O. Sonmez, N. Ersoy, K. Cinar, Failure behavior of composite laminates under four-point bending, J. Compos. Mater. (USA) 50(26) (2016) 3679-3697.

[152] A. De Luca, F. Caputo, A review on analytical failure criteria for composite materials, AIMS Materials Science 4(5) (2017) 1165-1185.

[153] Q.D. Yang, D. Schesser, M. Niess, P. Wright, M.N. Mavrogordato, I. Sinclair, S.M. Spearing, B.N. Cox, On crack initiation in notched, cross-plied polymer matrix composites, J. Mech. Phys. Solids (Netherlands) 78 (2015) 314-332.

[154] T.K. O'Brien, Characterization of delamination onset and growth in a composite laminate, Damage in composite materials: basic mechanisms, accumulation, tolerance, and characterization, ASTM International1982.

[155] R. Martin, Incorporating interlaminar fracture mechanics into design, Proceedings of the Institution of Mechanical Engineers, Part L: Journal of Materials: Design and Applications 214(2) (2000) 91-97.

[156] I. Raju, T. O'brien, Fracture mechanics concepts, stress fields, strain energy release rates, delamination initiation and growth criteria, Delamination behaviour of composites, Elsevier2008, pp. 3-27.

[157] S. Rinderknecht, B. Kroplin, A finite element model for delamination in composite plates, MECHANICS OF COMPOSITE MATERIALS AND STRUCTURES An INTERNATIONAL JOURNAL 2(1) (1995) 19-47.

[158] Y.-P. Liu, C.-Y. Chen, G.-Q. Li, A modified zigzag approach to approximate moving crack front with arbitrary shape, Eng. Fract. Mech. 78(2) (2011) 234-251.

[159] D. Xie, S.B. Biggers Jr, Strain energy release rate calculation for a moving delamination front of arbitrary shape based on the virtual crack closure technique. Part I: Formulation and validation, Eng. Fract. Mech. 73(6) (2006) 771-785.

[160] J.R. Reeder, A Bilinear Failure Criterion for Mixed-Mode Delamination, in: E.T. Camponeschi (Ed.), ASTM International, West Conshohocken, PA, 1993, pp. 303-322.

[161] J.R. Reeder, 3-D Mixed Mode Delamination Fracture Criteria-An Experimentalist's Perspective, (2006).

[162] S. Hashemi, A.J. Kinloch, G. Williams, Mixed-Mode Fracture in Fiber-Polymer Composite Laminates, in: T.K. Brien (Ed.), ASTM International, West Conshohocken, PA, 1991, pp. 143-168.

[163] J.D. Whitcomb, Analysis of instability-related growth of a through-width delamination, National Aeronautics and Space Administration, Langley Research Center1984.

[164] M.L. Benzeggagh, M. Kenane, Measurement of mixed-mode delamination fracture toughness of unidirectional glass/epoxy composites with mixed-mode bending apparatus, Compos. Sci. Technol. (Netherlands) 56(4) (1996) 439-449.

[165] M. Kenane, M.L. Benzeggagh, Mixed-mode delamination fracture toughness of unidirectional glass/epoxy composites under fatigue loading, Compos. Sci. Technol. (Netherlands) 57(5) (1997) 597-605.

[166] J. Williams, On the calculation of energy release rates for cracked laminates, International Journal of Fracture 36(2) (1988) 101-119.

[167] Z. Suo, J.W. Hutchinson, Interface crack between two elastic layers, International Journal of Fracture 43(1) (1990) 1-18.

[168] M. Conroy, A. Kinloch, J. Williams, A. Ivankovic, Mixed mode partitioning of beam-like geometries: A damage dependent solution, Eng. Fract. Mech. 149 (2015) 351-367.

[169] ASTM D7905 / D7905M-19e1, Standard Test Method for Determination of the Mode II Interlaminar Fracture Toughness of Unidirectional Fiber-Reinforced Polymer Matrix Composites, ASTM International, ASTM International, West Conshohocken, PA, 2019.

[170] ASTM D6671 / D6671M-19, Standard Test Method for Mixed Mode I-Mode II Interlaminar Fracture Toughness of Unidirectional Fiber Reinforced Polymer Matrix Composites, ASTM International, West Conshohocken, PA,, 2019.

[171] S.L. Donaldson, S. Mall, C. Lingg, The split cantilever beam test for characterizing Mode III interlaminar fracture toughness, Journal of Composites, Technology and Research 13(1) (1991) 41-47.

[172] S.M. Lee, An edge crack torsion method for mode III delamination fracture testing, Journal of Composites, Technology and Research 15(3) (1993) 193-201.

[173] V.K. Goyal, E.R. Johnson, C.G. Davila, Irreversible constitutive law for modeling the delamination process using interfacial surface discontinuities, Compos. Struct. 65(3-4) (2004) 289-305.

[174] M.F. Pernice, N.V. De Carvalho, J.G. Ratcliffe, S.R. Hallett, Experimental study on delamination migration in composite laminates, Compos., A, Appl. Sci. Manuf. (Netherlands) 73 (2015) 20-34.

[175] J. Ratcliffe, M. Czabaj, T. O'Brien, A test for characterizing delamination migration in carbon/epoxy tape laminates NASA, TM-2013-218028. NASA, 2013.

[176] J.G. Ratcliffe, N.V. DeCarvalho, Investigating delamination migration in composite tape laminates, (2014).

[177] X. Li, J. Chen, An extended cohesive damage model for simulating multicrack propagation in fibre composites, Compos. Struct. 143 (2016) 1-8.

[178] Q. Yang, M. Naderi, 10 - A new augmented finite element method (A-FEM) for progressive failure analysis of advanced composite materials, in: P.P. Camanho, S.R. Hallett (Eds.), Numerical Modelling of Failure in Advanced Composite Materials, Woodhead Publishing2015, pp. 265-308.

[179] Y. Xie, M. Koslowski, Numerical simulations of inter-laminar fracture in particle-toughened carbon fiber reinforced composites, Composites Part A: Applied Science and Manufacturing 92 (2017) 62-69.

[180] Y. Xie, Y. Mao, L. Sun, M. Koslowski, Local versus average field failure criterion in amorphous polymers, Modelling and Simulation in Materials Science and Engineering 23(2) (2015) 025004.

[181] A. Mubashar, I.A. Ashcroft, A.D. Crocombe, Modelling Damage and Failure in Adhesive Joints Using A Combined XFEM-Cohesive Element Methodology, The Journal of Adhesion 90(8) (2014) 682-697.

[182] L. Bouhala, A. Makradi, S. Belouettar, A. Younes, S. Natarajan, An XFEM/CZM based inverse method for identification of composite failure parameters, Computers & Structures 153 (2015) 91-97.

[183] F. Stuparu, D.M. Constantinescu, D.A. Apostol, M. Sandu, A Combined Cohesive Elements—XFEM Approach for Analyzing Crack Propagation in Bonded Joints, The Journal of Adhesion 92(7-9) (2016) 535-552.

[184] D. De Cicco, F. Taheri, Delamination Buckling and Crack Propagation Simulations in Fiber-Metal Laminates Using xFEM and Cohesive Elements, Applied Sciences 8(12) (2018) 2440.

[185] P.M. Wright, Investigation of damage in laminated carbon fibre composites using high resolution computed tomography, University of Southampton, 2011.

[186] J. Hsieh, Computed tomography: principles, design, artifacts, and recent advances, SPIE Bellingham, WA, 2009.

[187] M. Beister, D. Kolditz, W.A. Kalender, Iterative reconstruction methods in X-ray CT, Physica medica 28(2) (2012) 94-108.

[188] T.S. Smith, B.K. Bay, M.M. Rashid, Digital volume correlation including rotational degrees of freedom during minimization, Experimental Mechanics 42(3) (2002) 272-278.

[189] R.R. Hughes, B.W. Drinkwater, R.A. Smith, Characterisation of carbon fibre-reinforced polymer composites through radon-transform analysis of complex eddy-current data, Composites Part B: Engineering 148 (2018) 252-259.

[190] P. Cloetens, M. Pateyron-Salomé, J. Buffiere, G. Peix, J. Baruchel, F. Peyrin, M. Schlenker, Observation of microstructure and damage in materials by phase sensitive radiography and tomography, Journal of Applied Physics 81(9) (1997) 5878-5886.

[191] G. Davis, J. Elliott, Artefacts in X-ray microtomography of materials, Materials science and technology 22(9) (2006) 1011-1018.

[192] G.R. Davis, Image quality and accuracy in X-ray microtomography, Developments in X-ray Tomography II, International Society for Optics and Photonics, 1999, pp. 147-155.

[193] A.C. Kak, M. Slaney, Principles of computerized tomographic imaging, SIAM2001.

[194] R.A. Brooks, G. Di Chiro, Beam hardening in x-ray reconstructive tomography, Physics in medicine & biology 21(3) (1976) 390.

[195] P. Hammersberg, M. Mångård, Correction for beam hardening artefacts in computerised tomography, J. X-Ray Sci. Technol. (Netherlands) 8(1) (1998) 75-93.

[196] J. Rueckel, M. Stockmar, F. Pfeiffer, J. Herzen, Spatial resolution characterization of a X-ray microCT system, Applied Radiation and Isotopes 94 (2014) 230-234.

[197] E.A. Zwanenburg, D.G. Norman, C. Qian, K.N. Kendall, M.A. Williams, J.M. Warnett, Effective X-ray micro computed tomography imaging of carbon fibre composites, Composites Part B: Engineering 258 (2023) 110707.

[198] H. Zhang, C. Li, W. Dai, Y. Liu, S. Tian, W. Huang, D. Jia, D. He, Y. Zhang, Static compression testing CFRP single-lap composited joints using X-ray μCT, Compos. Struct. 234 (2020) 111667.

[199] E. Dilonardo, M. Nacucchi, F. De Pascalis, M. Zarrelli, C. Giannini, High resolution X-ray computed tomography: A versatile non-destructive tool to characterize CFRP-based aircraft composite elements, Compos. Sci. Technol. (Netherlands) 192 (2020) 108093.

[200] J. Teuwsen, S.K. Hohn, T.A. Osswald, Direct fiber simulation of a compression molded ribbed structure made of a sheet molding compound with randomly oriented carbon/epoxy prepreg strands—A comparison of predicted fiber orientations with computed tomography analyses, Journal of Composites Science 4(4) (2020) 164.

[201] N. Krajangsawasdi, F. Alvarez-Borges, K.M. Ball, M.N. Mavrogordato, I. Hamerton, B.K.S. Woods, D.S. Ivanov, M.L. Longana, DcAFF (Discontinuous Aligned Fibre Filament) – Mechanical properties investigation on multilayer 3D printed parts, Composites Part B: Engineering 264 (2023) 110903.

[202] L. Felsner, S. Hu, A. Maier, J. Bopp, V. Ludwig, G. Anton, C. Riess, A 3-D Projection Model for X-ray Dark-field Imaging, Scientific Reports 9(1) (2019) 9216.

[203] B. Powierza, C. Gollwitzer, D. Wolgast, A. Staude, G. Bruno, Fully experiment-based evaluation of few digital volume correlation techniques, Review of Scientific Instruments 90(11) (2019).

[204] E. Schöberl, C. Breite, A. Melnikov, Y. Swolfs, M.N. Mavrogordato, I. Sinclair, S.M. Spearing, Fibre-direction strain measurement in a composite ply under quasi-static tensile loading using Digital Volume Correlation and in situ Synchrotron Radiation Computed Tomography, Compos., A, Appl. Sci. Manuf. (Netherlands) 137 (2020) 105935.

[205] E. Schöberl, C. Breite, S. Rosini, Y. Swolfs, M. Mavrogordato, I. Sinclair, S.M. Spearing, A novel particle-filled carbon-fibre reinforced polymer model composite tailored for the application of digital volume correlation and computed tomography, J. Compos. Mater. (USA) 55(14) (2021) 1907-1934.

[206] R. Brault, A. Germaneau, J.-C. Dupré, P. Doumalin, S. Mistou, M. Fazzini, In-situ analysis of laminated composite materials by X-ray micro-computed tomography and digital volume correlation, Experimental Mechanics 53 (2013) 1143-1151.

[207] R. Olsson, Factors influencing the interlaminar fracture toughness and its evaluation in composites, NASA STI/Recon Technical Report N 93 (1992) 29076.

[208] I.K. Giannopoulos, K. Grafton, S. Guo, H. Smith, Damage tolerance of CFRP airframe bolted joints in bearing, following bolt pull-through failure, Composites Part B: Engineering 185 (2020) 107766.

[209] T. Sebaey, E. González, C. Lopes, N. Blanco, J. Costa, Damage resistance and damage tolerance of dispersed CFRP laminates: Design and optimization, Compos. Struct. 95 (2013) 569-576.

[210] W.S. Johnson, P.D. Mangalgiri, Investigation of fiber bridging in double cantilever beam specimens, Journal of Composites Technology & Research 9 (1987) 10-13.

[211] F. De Florio, Chapter 4 - Airworthiness Requirements, in: F. De Florio (Ed.), Airworthiness (Third Edition), Butterworth-Heinemann2016, pp. 37-83.

[212] L. Mishnaevsky, K. Branner, H.N. Petersen, J. Beauson, M. McGugan, B.F. Sørensen, Materials for wind turbine blades: an overview, Materials 10(11) (2017) 1285.

[213] T.H. Hsieh, A.J. Kinloch, K. Masania, J.S. Lee, A.C. Taylor, S. Sprenger, The toughness of epoxy polymers and fibre composites modified with rubber microparticles and silica nanoparticles, J. Mater. Sci. 45(5) (2010) 1193-1210.

[214] M. Yasaee, I.P. Bond, R.S. Trask, E.S. Greenhalgh, Mode I interfacial toughening through discontinuous interleaves for damage suppression and control, Compos., A, Appl. Sci. Manuf. (Netherlands) 43(1) (2012) 198-207.

[215] N.K. Fritz, R. Kopp, A.K. Nason, X. Ni, J. Lee, I.Y. Stein, E. Kalfon-Cohen, I. Sinclair, S.M. Spearing, P.P. Camanho, B.L. Wardle, New interlaminar features and void distributions in advanced aerospace-grade composites revealed via automated algorithms using micro-computed tomography, Compos. Sci. Technol. (Netherlands) 193 (2020) 108132.

[216] P. Feraboli, A. Masini, Development of carbon/epoxy structural components for a high performance vehicle, Composites Part B: Engineering 35(4) (2004) 323-330.

[217] T. Allen, S. Ahmed, W. Hepples, P.A. Reed, I. Sinclair, M. Spearing, A comparison of quasi-static indentation and low-velocity impact on composite overwrapped pressure vessels, J. Compos. Mater. (USA) 52(29) (2018) 4051-4060.

[218] D. Bull, I. Sinclair, S. Spearing, L. Helfen, Composite laminate impact damage assessment by high resolution 3D X-ray tomography and laminography, (2011).

[219] V. Kostopoulos, A. Baltopoulos, P. Karapappas, A. Vavouliotis, A. Paipetis, Impact and after-impact properties of carbon fibre reinforced composites enhanced with multi-wall carbon nanotubes, Compos. Sci. Technol. (Netherlands) 70(4) (2010) 553-563.

[220] W.J. Cantwell, J. Morton, Detection of impact damage in CFRP laminates, Compos. Struct. 3(3) (1985) 241-257.

[221] O.T. Topac, B. Gozluklu, E. Gurses, D. Coker, Experimental and computational study of the damage process in CFRP composite beams under low-velocity impact, Compos., A, Appl. Sci. Manuf. (Netherlands) 92 (2017) 167-182.

[222] W.J. Cantwell, J. Morton, The impact resistance of composite materials — a review, Composites 22(5) (1991) 347-362.

[223] G.A. Schoeppner, S. Abrate, Delamination threshold loads for low velocity impact on composite laminates, Compos., A, Appl. Sci. Manuf. (Netherlands) 31(9) (2000) 903-915.

[224] R.B. Ladani, A.R. Ravindran, S. Wu, K. Pingkarawat, A.J. Kinloch, A.P. Mouritz, R.O. Ritchie, C.H. Wang, Multi-scale toughening of fibre composites using carbon nanofibres and z-pins, Compos. Sci. Technol. (Netherlands) 131 (2016) 98-109.

[225] A.P. Mouritz, Review of z-pinned composite laminates, Compos., A, Appl. Sci. Manuf. (Netherlands) 38(12) (2007) 2383-2397.

[226] B.F. Sørensen, T.K. Jacobsen, Large-scale bridging in composites: R-curves and bridging laws, Composites Part A: Applied Science and Manufacturing 29(11) (1998) 1443-1451.

[227] C.A. Schneider, W.S. Rasband, K.W. Eliceiri, NIH Image to ImageJ: 25 years of image analysis, Nature methods 9(7) (2012) 671.

[228] A. Kyrieleis, V. Titarenko, M. Ibison, T. Connolley, P.J. Withers, Region-of-interest tomography using filtered backprojection: assessing the practical limits, J. Microsc. (UK) 241(1) (2011) 69-82.

[229] P. Cloetens, M. Pateyron-Salomé, J.Y. Buffière, G. Peix, J. Baruchel, F. Peyrin, M. Schlenker, Observation of microstructure and damage in materials by phase sensitive radiography and tomography, Journal of Applied Physics 81(9) (1997) 5878-5886.

[230] A. Mirone, E. Brun, E. Gouillart, P. Tafforeau, J. Kieffer, The PyHST2 hybrid distributed code for high speed tomographic reconstruction with iterative reconstruction and a priori knowledge capabilities, Nuclear Instruments and Methods in Physics Research Section B: Beam Interactions with Materials and Atoms 324 (2014) 41-48.

[231] M. Hojo, S. Matsuda, M. Tanaka, S. Ochiai, A. Murakami, Mode I delamination fatigue properties of interlayer-toughened CF/epoxy laminates, Compos. Sci. Technol. (Netherlands) 66(5) (2006) 665-675.

[232] E.N. Gilbert, B.S. Hayes, J.C. Seferis, Interlayer toughened unidirectional carbon prepreg systems: effect of preformed particle morphology, Compos., A, Appl. Sci. Manuf. (Netherlands) 34(3) (2003) 245-252.

[233] D. Stevanovic, S. Kalyanasundaram, A. Lowe, P.-Y. Jar, Mode I and mode II delamination properties of glass/vinyl-ester composite toughened by particulate modified interlayers, Compos. Sci. Technol. (Netherlands) 63(13) (2003) 1949-1964.

[234] F. Gao, G. Jiao, Z. Lu, R. Ning, Mode II Delamination and Damage Resistance of Carbon/Epoxy Composite Laminates Interleaved with Thermoplastic Particles, J. Compos. Mater. (USA) 41(1) (2007) 111-123.

[235] A. Turon, C.G. Dávila, P.P. Camanho, J. Costa, An engineering solution for mesh size effects in the simulation of delamination using cohesive zone models, Eng. Fract. Mech. 74(10) (2007) 1665-1682.

[236] M. Jalalvand, G. Czél, M.R. Wisnom, Numerical modelling of the damage modes in UD thin carbon/glass hybrid laminates, Compos. Sci. Technol. (Netherlands) 94 (2014) 39-47.

[237] M. Jalalvand, H. Hosseini-Toudeshky, B. Mohammadi, Numerical modeling of diffuse transverse cracks and induced delamination using cohesive elements, Proceedings of the Institution of Mechanical Engineers, Part C: Journal of Mechanical Engineering Science 227(7) (2013) 1392-1405.

[238] J.Z. Liang, Estimation of Interlayer Thickness in Inorganic Particulate-Filled Polymer Composites, Journal of Thermoplastic Composite Materials 24(6) (2011) 777-788.

[239] J. Zhang, T. Lin, X. Wang, Electrospun nanofibre toughened carbon/epoxy composites: Effects of polyetherketone cardo (PEK-C) nanofibre diameter and interlayer thickness, Compos. Sci. Technol. (Netherlands) 70(11) (2010) 1660-1666.

[240] S.K. Bhudolia, P. Perrotey, S.C. Joshi, Mode I fracture toughness and fractographic investigation of carbon fibre composites with liquid Methylmethacrylate thermoplastic matrix, Composites Part B: Engineering 134 (2018) 246-253.

[241] P. Compston, P.-Y.B. Jar, P. Burchill, K. Takahashi, The transfer of matrix toughness to composite mode I interlaminar fracture toughness in glass-fibre/vinyl ester composites, Appl. Compos. Mater. (Netherlands) 9 (2002) 291-314.